Application of novel corrections for quantification of ^{123}I SPECT

Colin McMillan Brown
MEng, MSc

Submitted in fulfilment of the requirements for the degree of Doctor of Philosophy (PhD)

Department of Clinical Physics and Bioengineering
College of Medical, Veterinary and Life Sciences
Graduate School
University of Glasgow

March 2018

Abstract

Introduction

The quantification of clinical images provides a useful adjunct to visual assessment in the differentiation of disease processes. In nuclear medicine imaging, the accurate quantification of Single Photon Emission Computed Tomography (SPECT) data is challenging due to limited spatial resolution and the corrections required for photon attenuation and scatter.

Specific radionuclides used in SPECT imaging, such as Iodine-123 (^{123}I), pose additional challenges to quantification due to their complex decay schemes. ^{123}I has a predominantly low-energy photon emission of 159keV. However, ^{123}I also has high-energy emissions which, due to septal penetration, are detected within the imaging window. Consequently, absolute quantification of ^{123}I SPECT is not current clinical practice and remains a specialist task.

A novel reconstruction correction scheme has been developed by Hermes Medical Solutions which incorporates Monte Carlo simulation of photon interactions in both the patient and the detector system. This Collimator and Detector Response Modelling (CDRM) algorithm has the potential to enhance image quality and, therefore, the quantitative accuracy of ^{123}I SPECT studies. This thesis aims to optimise ^{123}I SPECT quantification using advanced reconstruction algorithms and, furthermore, to assess the clinical applications of these optimised techniques.

Method

With the ultimate aim of optimising quantification of ^{123}I SPECT, work was undertaken to assess SPECT spatial uniformity, spatial resolution, contrast recovery, noise and scatter suppression. This work was used to specify the optimum collimator and reconstruction parameters required for accurate quantification.

Using these parameters, absolute quantification was then assessed for accuracy with regard to neurology and oncology studies. The utility of Standardised Uptake Values (SUVs) was evaluated in ^{123}I-DaTSCAN patient studies. Furthermore, human observer studies were used to verify the findings of the quantitative assessment.

Results

Phantom studies demonstrated that Low Energy High Resolution (LEHR) collimators provide superior image quality for neurology applications where spatial resolution is essential. However, when imaging the torso, this work showed that Medium Energy General Purpose (MELP) collimators, with advanced reconstruction, can improve contrast recovery, noise characteristics and scatter suppression when compared with LEHR data.

The accuracy of quantifying activity concentration for neurology studies was optimised using the novel CDRM correction scheme (measured activity concentration within ±10% of true concentration). However, the accuracy of quantification in torso studies was shown to vary with lesion location in the Field of View (FOV). Therefore, neurology studies were identified as the best candidates for absolute quantification.

In a subsequent evaluation of patient studies, measuring the mean SUV of the putamen in ^{123}I-DaTSCAN studies marginally outperformed Hermes Medical Solutions BRASS™ automated analysis application with regard to the differentiation of normality. Direct quantitative assessment has the advantage that it removes the requirement for a normal database.

Furthermore, the evaluation of clinical patient ^{123}I-DaTSCAN studies by human observers demonstrated almost perfect agreement in diagnosis for the novel CDRM reconstruction correction scheme (Kappa coefficient=0.913). Image quality for the CDRM scheme rated significantly higher than current clinical practice (p-value<0.01).

The torso phantom observer study suggested that optimised reconstruction of MELP data demonstrated superior image quality and lesion detectability when compared with LEHR reconstructions.

Conclusions

For ^{123}I-mIBG oncology studies, including quantification of serial studies, data should be acquired with MELP collimators and reconstructed with advanced corrections for attenuation, scatter and depth-dependent spatial resolution. However, quantification of ^{123}I SPECT body section images for inter-patient comparison is not feasible due to variable accuracy with lesion location in the FOV.

Absolute quantification of ^{123}I-DaTSCAN studies, acquired with LEHR collimators, can be performed routinely with sufficient accuracy using the novel CDRM algorithm.

Table of Contents

List of Tables

List of Figures

Acknowledgements

“Thank you sir for the millions of words
That you've handed me down and you've told me to learn.”
— Ray Davies, Education, 1975

Firstly, my thanks to Dr Gerry Gillen for his unwavering commitment to this project. I appreciate not only the extensive knowledge and experience that Gerry has provided as principal supervisor, but also recognise the personal sacrifices made in supporting this thesis. Thanks also to my second supervisor, Dr Alice Nicol, who has always been eager to contribute with her expertise and wisdom throughout.

This thesis (and my sanity) would be much less coherent without the invaluable input of Dr Caroline Findlay and Dr Mary-Frances Dempsey. Your words of support and criticism have been equally indispensable. Also, many thanks to Mairi Kemp for proof-reading what must have often seemed like a foreign language document.

I would like to express my gratitude to all of those in the West Glasgow Nuclear Medicine department that have often gone to extra efforts in finding me spare camera time, spare radioactivity and, perhaps most importantly, have spared a friendly ear to my woes over the years. In particular, I wish to thank Tracy Todd, Dr Dave Colville, Dr John Shand and Dr Ed Kalkman for their essential input and enthusiasm in assisting my research. Thanks also to Clare McKeown (PhD pending) with whom I look forward to having far fewer physics related conversations in the future.

"Lean on me, when you're not strong"
— Bill Withers, Lean On Me, 1972

I am eternally grateful for the support of my wife, Ailsa. In spite of being a “PhD widow” while I have been busy pondering physics, she has been resolute in championing each step forward and, more importantly, kept me going whenever I took a step backwards. Ailsa, without a doubt, I am the Luckiest.

I wish to thank my mother and father, Jennifer and Sandy, and my sister Yvonne for their patience, understanding and support throughout the entirety of my studies.

Caleb — my apologies. Let's hang out sometime, just you and me.

"And you're so much like me … I'm sorry."
— Ben Folds, Still Fighting It, 2002

Author's Declaration

I declare that this thesis represents my own work except where referenced to others.

I declare that this thesis does not include work forming part of a thesis presented successfully for another degree.

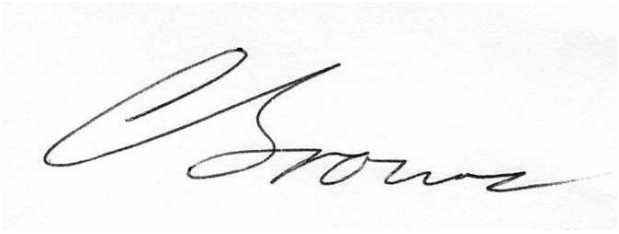

Colin Brown

March 2018

Abbreviations

^{57}Co	Cobalt-57
^{123}I	Iodine-123
^{131}I	Iodine-131
2D	Two Dimensional
3D	Three Dimensional
^{99m}Tc	Technetium-99m
AAPM	American Association of Physicists in Medicine
AFROC	Alternative FROC
aPS	atypical Parkinsonian Syndrome
AUC	Area Under the Curve
BV	Background Variability
CC	Calibration Coefficient
CCR	Cold Contrast Recovery
CDRM	Collimator and Detector Response Modelling
CF	Calibration Factor
CFOV	Central Field of View
CI	Confidence Interval
CNR	Contrast to Noise Ratio
COV	Coefficient of Variation
CR	Contrast Recovery
CT	Computed Tomography
DaT	Dopamine Transporter
DLB	Lewy body-type Dementia
EANM	European Association of Nuclear Medicine
EARL	EANM Research 4 Life
ECG	Electrocardiography
ENC-DAT	European Database of ^{123}I-FP-CIT (DaTSCAN) SPECT scans of healthy controls
ET	Essential Tremor
FBP	Filtered Back Projection
FL	False Localisation
FLR	False Localisation Rate
FN	False Negative
FOM	Figure of Merit

FOV	Field of View
FP	False Positive
FPF	False Positive Fraction
FROC	Free-response ROC
FWHM	Full Width at Half Maximum
FWTM	Full Width at Tenth Maximum
HCR	Hot Contrast Recovery
IEC	International Electrotechnical Commission
IPEM	Institute of Physics and Engineering in Medicine
IR	Image Roughness
LEHR	Low Energy High Resolution
LEUHR	Low Energy Ultra High Resolution
LLF	Lesion Location Fraction
LMEGP	Low to Medium Energy General Purpose
LPHR	Low Penetration High Resolution
LSF	Line Spread Function
LUT	Look Up Table
MEGP	Medium Energy General Purpose
MELP	Medium Energy Low Penetration
MLEM	Maximum Likelihood Expectation Maximum
MRI	Magnetic Resonance Imaging
MUR	Measured Uptake Ratio
NaI(Tl)	Thallium doped Sodium Iodide
NC	No Corrections
NEMA	National Electrical Manufacturers Association
NET	Neuroendocrine Tumour
OOSC	Object Only Scatter Correction
OSEM	Ordered Subset Expectation Maximisation
PD	Parkinson Disease
PET	Positron Emission Tomography
PMT	Photomultiplier Tube
PS	Parkinsonian Syndrome
PSF	Point Spread Function
RE	Residual Error
RMS	Root Mean Squared

ROC	Receiver Operating Characteristic
ROI	Region of Interest
ROR	Radius of Rotation
RORO	Radius of Rotation Offset
RR	Resolution Recovery
RSS	Residual Sum of Squares
SBR	Specific Binding Ratio
SD	Standard Deviation
SE	Standard Error
SF	Scatter Fraction
SNM	Society of Nuclear Medicine
SNR	Signal to Noise Ratio
SOI	Structure of Interest
SPECT	Single Photon Emission Computed Tomography
SPM	Statistical Parametric Mapping
SUSI	Specific Uptake Size Index
SUV	Standardised Uptake Value
TEW	Triple Energy Window
TN	True Negative
TNF	True Negative Fraction
TP	True Positive
TPF	True Positive Fraction
TUR	True Uptake Ratio
UFOV	Useful Field of View
UI	Uptake Indice
VOI	Volume of Interest
VXHR	Vantage eXtra High Resolution

Chapter 1: Introduction

In an ageing population, the incidence of neurodegenerative disease, cancer and heart disease is increasing. Early and accurate diagnosis of disease enables the determination of the most appropriate therapy, which may then improve patient well-being while also reducing the burden on the health service. Gamma camera imaging facilitates non-invasive mapping of radiopharmaceuticals administered to patients for diagnosis of these disease processes. Tomographic gamma camera imaging allows a 3-dimensional representation of the radionuclide distribution. This representation can greatly enhance image interpretation as it improves image contrast and allows overlapping objects to be differentiated.

Quantifying gamma camera Single Photon Emission Computed Tomography (SPECT) data could offer further advances in the management of patients. Specifically, in the diagnostic setting, quantification can be used with serial scans for the assessment of response to therapy, for differentiation of neurodegenerative diseases, for measuring cerebral and myocardial blood flow, and for pre-surgical assessment of lobar function in lung imaging [1]. Furthermore, in oncologic radionuclide therapy, patient-specific dosimetry can be planned using radionuclide quantification [2]. However, accurate quantification is challenging due to the corrections required for photon attenuation and scatter. Furthermore, certain radionuclides used in SPECT imaging, such as Iodine-123 (^{123}I), pose additional challenges due to their complex decay schemes. As a result, routine quantification of ^{123}I SPECT is not current clinical practice and remains a specialist task.

The aim of this thesis is to investigate the quantification of ^{123}I SPECT and its application in routine clinical practice using commercially available software.

1.1 Gamma Camera Technology

The basic concepts proposed by Hal Anger in 1958 still form the basis of today's modern gamma cameras. However, there have been major developments in tomographic imaging due to advances in mathematics and computing.

Gamma camera detectors incorporate a Thallium doped Sodium Iodide (NaI(Tl)) scintillation crystal for imaging radionuclides with photon emissions with energy in the range 80-300keV [3]. Photons incident on the crystal produce light which is detected using an array of Photomultiplier Tubes (PMTs). The outputs from the PMTs are digitised by an analogue-to-digital converter and are then passed to position logic boards which determine the location of each scintillation event. A pulse height analyser sums the signal from the analogue-to-digital converters, which results in an energy signal. Energy selection is necessary for imaging because it provides a means to discriminate against photons that have scattered between source and detector and have, therefore, lost their positional information. Scatter in the photopeak can be reduced by choosing a relatively narrow pulse height window. Only photons that undergo no scatter or small-angle scatter will be accepted. A modern gamma camera has an energy resolution of 9-10% at 140keV, the energy of the commonly used radionuclide Technetium-99m (^{99m}Tc) [3].

Modern gamma cameras are typically multi-headed systems. Rotating the camera heads around the patient's body allows acquisition of projections through 360°. These projections are reconstructed to produce tomographic images for manipulation in three dimensions (3D). Tomographic imaging overcomes the fundamental problem of acquiring planar two-dimensional (2D) images of 3D distributions; overlying or underlying structures may obscure the object of interest.

Photons emitted from a radioactive source are random events with respect to time, which is a major source of noise in radionuclide imaging [4]. The photons, or 'counts', detected follow a Poisson distribution. Following this distribution, the standard deviation of counts detected is equal to the square root of the measured counts. Each pixel must have a sufficient number of counts to achieve an acceptable Signal-to-Noise Ratio (SNR). Detecting a larger number of counts requires a longer acquisition time. There is, therefore, an inherent trade-off between the acquisition time and an acceptable level of noise in an image.

1.2 SPECT Imaging

Rotating the gamma camera heads around a 3D object acquires a planar image at each angle. These are called projections because they represent 2D parallel projections of the 3D source distribution. Figure 1.1 shows an example of a SPECT acquisition.

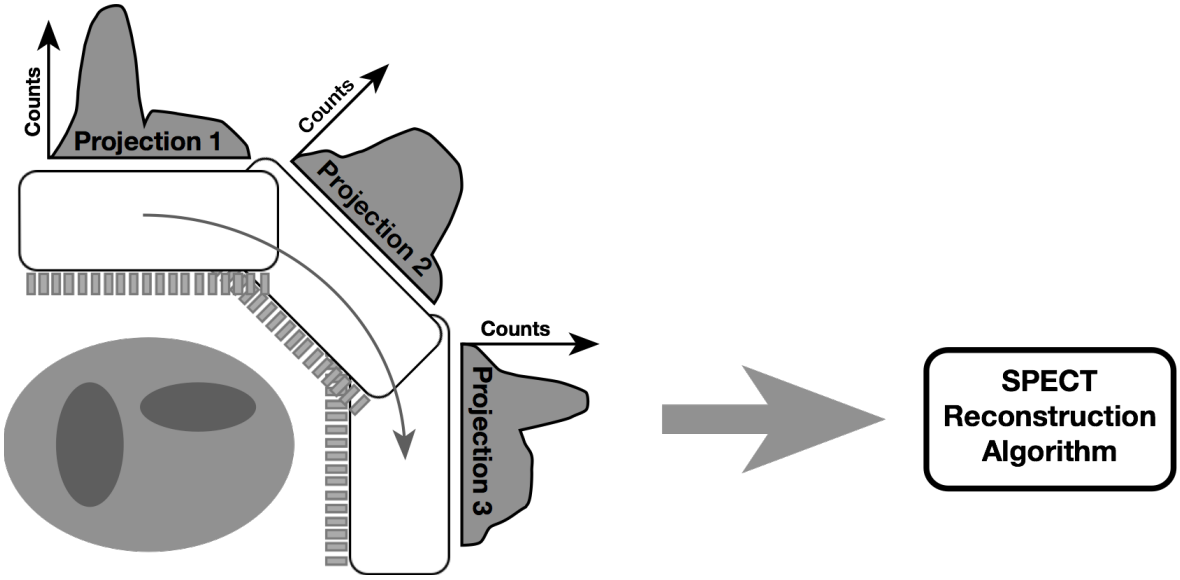

Figure 1.1: SPECT acquisition of multiple projections

The projections can be used to generate a 3D source distribution within the patient using an appropriate reconstruction algorithm. Although the process of acquiring a set of 360° projection images is relatively straightforward, reconstructing the corresponding activity distribution within the object is more complex. The two most commonly used methods of SPECT reconstruction are Filtered Back Projection (FBP) and iterative reconstruction.

1.2.1 Filtered Back Projection

Due to its relatively simple implementation, FBP has, until recently, been the most common method of SPECT reconstruction on commercial nuclear medicine computer systems. The approach for reconstructing images using FBP is to take the 2D planar images from different angles around the source and project the data from each element in the acquisition back across the image matrix. This method provides an approximation of the source distribution. However, an obvious artefact of this basic back projection method is blurring as projections are distributed along the entire projection line rather than simply at the source location. Mathematically, the reconstructed image is the true image convolved with a $1/r$ blurring function, where r is the distance from the centre of a point source [3]. Performing a Fourier Transform of the projection data allows multiplication with a ramp filter in the frequency domain. This multiplication has the effect of deconvolving the blurring function from the back projection.

A disadvantage of incorporating a ramp filter into the FBP process is that it leads to the amplification of high spatial frequencies. This increase, in turn, results in the amplification of high-frequency noise. For this reason, images reconstructed by FBP usually have the ramp filter modified by a smoothing filter to suppress the enhancement of high spatial frequencies. This filtering reduces noise but can also reduce spatial resolution. Therefore, the smoothing filter chosen for FBP reconstructions critically influences the compromise between noise and resolution [5]. Dewaraja [2] does not recommended the use of FBP reconstruction where accurate quantification is desirable due to its rudimentary nature. Rather, for quantification, iterative reconstruction is recommended [2], which can incorporate corrections for image degrading effects.

1.2.2 Iterative Reconstruction

Iterative reconstruction has been available for many years. However, only recent advances and reduced cost of the required computing power has established its use in routine clinical practice [5]. The iterative reconstruction process starts with a simple estimate of a transaxial activity distribution and forward projects this to determine what the corresponding projection images would be. A comparison of estimated projections and acquired projections is made based on a cost function. The initial estimate can then be repeatedly adjusted based on this comparison for a predetermined number of iterations (Figure 1.2).

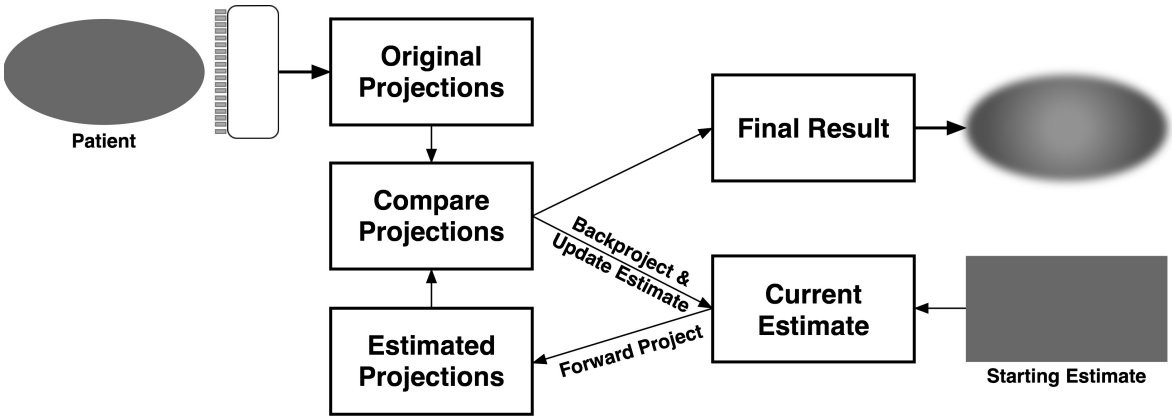

Figure 1.2: Flowchart of iterative reconstruction method
A comparison of the original projections and a forward projection of the current estimate is made based on a cost function. The current estimate is then updated. This method repeats for a predetermined number of iterations.

The forward projection process introduces the $1/r$ blurring already described with FBP. However, the forward projected estimate data is compared with the acquired data back projected. Therefore, the blurring only affects the correction image and will not affect the accuracy of the updating estimate, which becomes the resultant image. Unlike FBP, a

ramp filter is not necessary in the absence of the 1/*r* blurring artefact in this resultant image. Therefore, the choice of a smoothing filter for iterative reconstruction is not as critical as it is for FBP. Assuming the forward projection process represents an accurate model of the real gamma camera acquisition, then the iterative reconstruction method can correct for effects such as attenuation and poor collimator resolution. This improved reconstruction algorithm, therefore, has the potential to be a useful tool for SPECT quantification.

An aim of iterative reconstruction software is rapid convergence to an acceptable solution in a small number of iterations. One such algorithm, the Maximum Likelihood Expectation Maximum (MLEM) method, is widely used [6]. MLEM uses the ratio between the acquired and estimated projections to obtain a correction image. Then the current estimate and correction image are multiplied.

Subsequent work by Hudson [7] demonstrated acceleration of the MLEM technique by dividing projection data into subsets. This method is known as Ordered Subsets Expectation Maximisation (OSEM). OSEM is currently the method of choice implemented by most commercial systems [8]. Dividing the projections into subsets allows an acceleration of processing equivalent to the number of subsets. For example, an OSEM reconstruction with 10 iterations and 10 subsets is considered to be equivalent to an MLEM reconstruction with 100 iterations, performed in approximately 1/10th of the time. Therefore, the OSEM reconstruction method performs 100 “equivalent iterations”.

1.2.3 Quantification

Quantification of activity concentration can be an extremely useful tool in the interpretation of clinical studies [1]. The two most common methods of quantification currently used in SPECT imaging are relative quantification and absolute quantification [9]. In this thesis, “relative quantification” refers to a measure of uptake in relation to a suitable reference region. “Absolute quantification” refers to a direct measure of activity concentration with corrections made for degrading factors such as scatter, attenuation and resolution loss [9]. There does exist a third method of quantification, physiological quantification, which converts absolute quantification into physiological parameters. This technique requires kinetic modelling of the activity measurements and is outwith the scope of this thesis.

A reconstruction algorithm must incorporate various corrections to enable accurate quantification of SPECT studies. The three most significant system limitations which require correction are [1]:

- scattered photons
- photon absorption
- limited spatial resolution and variable spatial resolution with distance

The effect of each of these on quantification accuracy will be explored further.

1.2.3.1 Scatter

Parallel hole lead collimators are used to define the direction of the detected photon emissions. The collimator is used in combination with a narrow energy window to reduce the number of non-primary photons included in the image. There are four photon interactions with the imaging system (Figure 1.3):

- Primary photons (Figure 1.3A) emitted from the object of interest do not interact with the object or detection system and are detected within the photopeak window.
- Scattered photons (Figure 1.3B) in the photopeak window have scattered within the object of interest and have changed direction such that they travel parallel with the collimator.
- Collimator scatter (Figure 1.3C) is the result of photons detected in the photopeak window which have changed direction within the lead septa.
- Septal penetration (Figure 1.3D) is the result of photons detected in the photopeak window which have travelled through one or more of the collimator septa without interaction.

In this thesis the term “scatter” refers to photons detected in the photopeak window which have interacted with the object of interest (Figure 1.3B). “Septal penetration” refers to photons detected in the photopeak window which have interacted with the collimator and detector system, including backscatter from detection electronics (Figure 1.3C and 1.3D).

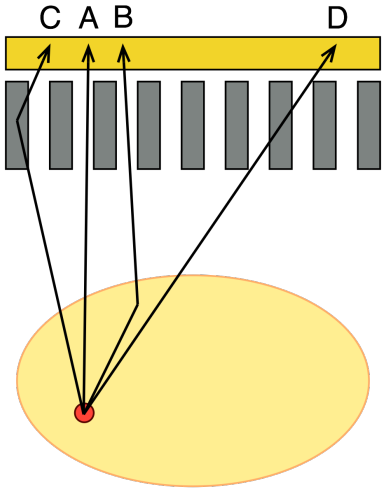

Figure 1.3: Schematic of photon interactions
Includes A) primary photons which travel parallel to the collimator holes, B) scatter within the object of interest, C) scatter within the collimator and D) septal penetration

Thicker collimator septa reduce the amount of septal penetration. However, they also reduce the efficiency of the imaging system by covering the sensitive area of the detector. A compromise is necessary between collimator efficiency and septal penetration. Typically ~5% septal penetration is accepted for the specified energy range of the collimator [3, 5, 10].

Scatter correction can be applied either before or during reconstruction. Section 2.3.2 describes methods for performing scatter correction.

1.2.3.2 Attenuation

Attenuation is a process by which some photons fail to reach the detector because they interact in the patient or collimator. Photoelectric absorption dominates at low-energies while Compton scatter interactions dominate at energies greater than 100keV for the range of energies used diagnostically. Photoelectric absorption and Compton scatter result in a loss of counts from the image, an effect which is greatest for organs deep within the patient. Therefore, deep structures will demonstrate less activity in them than is actually present [8]. Projections acquired from an unknown distribution of attenuating materials degrade quantification accuracy. Section 2.3.1, therefore, describes methods of correction for attenuation.

1.2.3.3 Spatial Resolution

The spatial resolution of an imaging system is the minimum distance to distinguish two separate sources when they are close together [11]. The finite size of the image produced by a perfect point source describes this characteristic [5]. The 2D representation of a point source is called the Point Spread Function (PSF). Resolution is usually measured in terms of the Full-Width at Half-Maximum (FWHM) of a profile through the PSF [5, 12].

The system resolution is a combination of the geometric resolution of the collimator and the intrinsic resolution of the detector. The geometric resolution of the collimator is optimal at the surface of the collimator and deteriorates with distance from the collimator. The decrease in spatial resolution with increasing distance from the collimator is demonstrated in Figure 1.4, which highlights the greater source acceptance angle with distance from the detector [10].

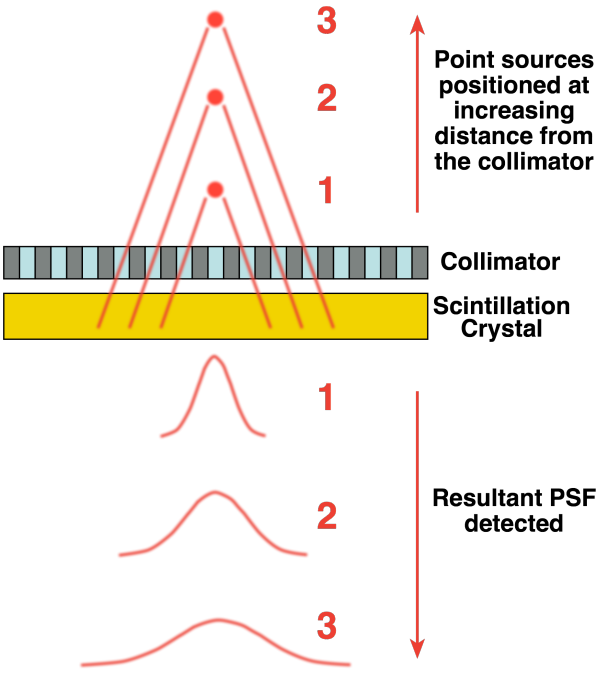

Figure 1.4: Point Spread Function (PSF) with distance from the collimator

A model can be incorporated into the reconstruction algorithm to correct for this variable spatial resolution with distance from the detector using known dimensions of the collimator (i.e. hole length and diameter). This method, known as Resolution Recovery (RR), is described in more detail in Section 2.4.

In addition to scatter, attenuation and spatial resolution corrections, Bailey [1] recommends that for accurate quantification the reconstruction algorithm also needs to:

- maintain linearity with activity concentration
- be able to calibrate the data in units of activity concentration (kBq/ml)
- account for radioactive decay during the acquisition process

Commercially available reconstruction algorithms now contain many of the required corrections to make quantification of SPECT studies part of routine clinical practice. Absolute quantification of SPECT images using ^{99m}Tc has become more widely used for a range of studies [1]. Kangasmaa [13] and Koral [14] investigated the variability of gamma camera calibration for SPECT absolute quantification for ^{99m}Tc and Iodine-131 (^{131}I) respectively. However, consistency of calibration for ^{123}I quantification has not been considered. ^{123}I has been less explored as it is a much more challenging radionuclide due to its complex emission scheme. Quantification would, however, be extremely useful in clinical applications such as neurology (^{123}I-DaTSCAN™) and oncology (^{123}I-mIBG).

1.3 ^{123}I SPECT Imaging

^{123}I has a physical half-life of 13.2h and primary photon emission at 159keV. The physical characteristics and chemical properties of ^{123}I make it a suitable radionuclide for nuclear medicine planar scintigraphy and SPECT [8]. The energy of the primary photon emission is suitable for the scintillation crystals of current gamma cameras, which are efficient detectors of photons in the 80-300keV range [3]. ^{123}I labelled radiopharmaceuticals are currently being used as imaging agents to investigate several disease processes. These will be detailed further in Section 1.3.3.

1.3.1 ^{123}I Energy Spectrum and Practical Limitations

^{123}I labelled radiopharmaceuticals are used widely in clinical applications due to their attractive physical and chemical characteristics. The radiation dose to the patient is low due to minimal charged particle emission and short physical half-life. While the primary emitted photon energy of 159keV is suitable for gamma camera imaging, ^{123}I also emits higher energy photons. There is a significant proportion of photons emitted between 440 and 625keV (2.4%) and a further 0.15% between 625 and 784keV. The attenuation coefficient in lead for these high-energy photons is about ten times lower than for the 159keV photons [15] resulting in a substantial proportion of high-energy photons penetrating the collimator septa. This septal penetration leads to a significant increase in the apparent sensitivity of low-energy gamma camera collimators [16].

Large volume sources increase the proportion of scatter. This increase is due to the high-energy photons having a higher probability of scatter interaction and septal penetration than absorption. The result is a proportional increase in the number of high-energy photons that undergo Compton scattering and are subsequently accepted by the photopeak window compared to the 159keV photons. Some authors have recommended the use of medium-energy collimators, especially when quantification is required [16, 17]. However, when high spatial resolution is necessary, as for neurology SPECT, Low Energy High Resolution (LEHR) collimators, supported by scatter correction, are used [16, 18]. Section 2.1 reviews collimator selection for ^{123}I imaging.

1.3.2 Effect of High Energy Emissions on the ^{123}I Photopeak

Medium-energy collimators allow only a small proportion of septal penetration from high-energy photons (Figure 1.5a). Low-energy collimators change the spectrum detected in such a way that some high-energy photons penetrate the collimator and, due to scatter, are detected in the 159keV energy window (Figure 1.5b) [19]. Despite the small proportion

of high-energy photons (about 2.5%), their higher probability of scatter interaction rather than absorption makes their detection efficiency greater compared with 159keV photons. This efficiency makes their relative contribution to the detected photons very important.

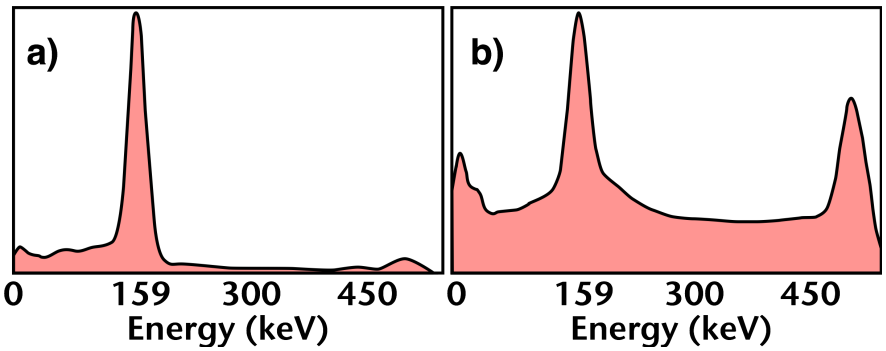

Figure 1.5: The spectra of ^{123}I in air with (a) medium-energy and (b) low-energy collimators (from Dobbeleir [19])

The proportion of high-energy photons detected as a result of septal penetration reduces as the distance from the source to collimator is increased. This reduction is a consequence of the photon flux of high-energy photons reducing with distance. The photon flux of low-energy photons also reduces with distance. However, the acceptance angle of the parallel hole collimator increases, resulting in a consistent sensitivity with distance. Review of the area under the curve of the PSF shown in Figure 1.5 demonstrates this relationship. The amplitude of the PSF reduces as the width increases.

The complex emission scheme of ^{123}I makes quantification particularly challenging. A simple correction for scatter of primary photons within the object of interest will not account for the high-energy emissions detected as a result of scatter or septal penetration [20, 21]. Studies using Monte Carlo simulation suggest detection of high-energy emissions in the low-energy photopeak to be 49-54% of all detected photons when using low-energy collimators [22-25]. This proportion is dependent on the distance from the detector.

1.3.3 Clinical Uses of ^{123}I

The fields of neurology, endocrinology, oncology and cardiology use ^{123}I labeled radiopharmaceuticals for imaging. Optimising image quality and providing accurate quantification to aid visual diagnosis has significant potential benefit. This section will outline common clinical applications of ^{123}I imaging and, in doing so, highlight clinical aims for the investigations performed in this thesis.

1.3.3.1 Neurology

Imaging Dopamine Transporters (DaT), which are responsible for reuptake of dopamine, is the most common use of ^{123}I in the field of neurology. Cocaine derivatives bind with high affinity to DaT and are therefore ideal candidates for radiopharmaceuticals. FP-CIT, β-CIT, IPT and PE2I are common ^{123}I cocaine analogues. Of predominant clinical importance is ^{123}I-FP-CIT (DaTSCAN™). DaTSCAN™ was licensed for use in Europe and the United States in 2001 and 2011 respectively [26]. The indication for DaTSCAN™ is for detecting loss of functional dopaminergic neurone terminals in the striatum of patients with clinically uncertain Parkinsonian Syndromes (PS).

DaT imaging can provide crucial evidence about whether a patient has Parkinson Disease (PD) or Atypical PS (aPS) and can help differentiate Essential Tremor (ET) and Lewy body-type Dementia (DLB) from PS [27]. In cases of PD, the nerve fibres connected to the posterior putamen are affected earlier and more markedly than those to the anterior putamen and caudate. In this situation, imaging would show reduced radiopharmaceutical uptake in the striatum of PD patients. The reduced uptake progresses from the posterior to the anterior putamen, and finally the caudate. In the early stages of disease, a marked asymmetry of striatal binding is evident, with a more pronounced loss in the striatum contralateral to the clinically more affected limbs

Although the visual analysis of SPECT images is, in general, suitable for clinical assessment, the accurate quantification of striatal uptake might increase sensitivity and reliability of the technique. This improvement may help in early diagnosis, follow-up, and resulting treatment response of PD [28]. Relative quantification is suggested in the European imaging guidelines [27] as an aid to reporting. The recent availability of a large-scale reference database, which allows age-related reference values to be defined, has consolidated this approach [26, 29]. Dickson [30] established reconstruction parameters for relative quantification of ^{123}I-DaTSCAN™. However, advanced reconstruction algorithms now incorporate depth-dependent Resolution Recovery (RR) as standard. Dickson's study did not include this correction and, therefore, additional evaluation is necessary. Furthermore, Dickson’s investigation did not consider novel methods of scatter correction or absolute quantification of activity concentration.

The volume of each striatum is ~11.2ml [31]. This volume is relatively small for SPECT imaging. Differentiation of structures and their integrity is highly dependent on sufficient image quality. For example, detecting small structures in the presence of noise requires

adequate spatial resolution and recovery of object contrast. Therefore, optimisation of image quality based on spatial resolution, contrast and noise metrics is essential.

There are also radiopharmaceuticals available for imaging postsynaptic receptors. The most widely available radiopharmaceuticals are ^{123}I-IBZM and ^{123}I-epidepride. However, reports show that postsynaptic imaging alone is not highly sensitive [32] and will, therefore, not be discussed further.

1.3.3.2 Oncology: Neuroendocrine Tumours

Imaging with ^{123}I-m-Iodobenzylguanidine (mIBG) allows the detection, localisation, staging and follow-up of Neuroendocrine Tumours (NETs) and their metastases. NETs are rare tumours that develop in cells of the neuroendocrine system. Common NET indications for ^{123}I-mIBG imaging include phaeochromocytomas, neuroblastomas and paragangliomas. Tumour uptake can be studied to aid dosimetric evaluation in the planning of high activity radionuclide ^{131}I-mIBG therapy. Accurate estimation of dose, tumour volume and number of focal mIBG uptake sites enables evaluation of tumour response to therapy [33, 34]. Accurate quantification and optimised image quality can, therefore, play vital roles for both personalised planning of radionuclide therapy and the evaluation of tumour response to therapy.

1.3.3.3 Endocrinology and Cardiology Applications of ^{123}I

The thyroid and parathyroid glands form part of the body's endocrine system and produce hormones that provide important regulatory functions. Iodine is a key component of hormones produced and secreted by the thyroid gland. Therefore, iodine actively concentrates in the thyroid. ^{123}I imaging is useful for determining the status of thyroid nodules as "hot" or "cold" in reference to the relative accumulation of radiopharmaceutical. Nearly 20% of cold nodules are malignant whereas few neutral and almost no hot nodules are malignant, so the uptake status of a suspicious nodule is very important [35]. Planar quantitative measurements of the thyroid can be performed to calculate the iodine uptake for the diagnosis of hyperthyroidism and hypothyroidism. Although it has been shown to be useful [36-38], SPECT imaging is not common in the assessment of thyroid disorders and, therefore, will not be discussed further. Imaging in thyroid cancer studies uses both ^{123}I and ^{131}I. Locally, ^{131}I is the radionuclide chosen for these studies. Therefore, in this thesis there will be no substantial reference to the use of ^{123}I in thyroid oncology.

Parathyroid imaging, using a dual-isotope (^{123}I and ^{99m}Tc) technique, is not used for diagnosis of hyperparathyroidism. Typically patients will have had their diagnosis confirmed from blood sampling. The purpose of SPECT imaging is to localise hyperfunctioning parathyroid glands before surgery. Therefore, quantification is not a critical component of the imaging protocol. However, localisation of small objects before surgery requires optimised image quality.

Disease states, such as congestive heart failure and myocardial ischemia, adversely affect cardiac sympathetic function. The neurotransmitter of the cardiac sympathetic system is nor-adrenaline. The presynaptic nerve terminal stores ^{123}I-mIBG which has diffused into the synaptic space, in a manner similar to that of norepinephrine [39]. Therefore, ^{123}I-mIBG is retained and localised in myocardial sympathetic nerve endings. Current practice involves planar imaging for assessment of Heart-to-Mediastinal uptake ratio and myocardial washout rate. These studies are not performed locally, therefore, they are not discussed further.

1.4 Aim of the Thesis

The aim of this thesis is to investigate:

- the optimisation of advanced SPECT reconstruction parameters with regard to quantification of ^{123}I
- quantification of activity concentration for ^{123}I SPECT for routine clinical use using third party software
- the clinical application of optimised reconstruction parameters with regard to quantification and image quality

1.5 Outline of the Thesis

This thesis will begin by outlining the current state of the art of ^{123}I SPECT acquisition, reconstruction techniques, methods of image analysis and methods of quantification in Chapter 2.

Chapter 3 details an evaluation of planar imaging performance. Chapters 4-8 describe the optimisation of SPECT reconstruction parameters via practical phantom experiments. The outcome of these investigations, including recommended reconstruction parameters, will be summarised in Chapter 9.

Calibration of a gamma camera for relative quantification is performed in Chapter 10, and for absolute quantification in Chapter 11. The latter calibration is followed by an assessment of quantitative accuracy. Chapter 12 will investigate the application of the absolute quantification technique for routine clinical use.

A human observer study of both phantom and patient data was performed to evaluate the application of optimised reconstruction parameters for visual assessment of ^{123}I SPECT imaging. Chapter 13 describes this investigation.

Finally, the thesis will conclude in Chapter 14 with a summary of findings, detailing methodological issues of the work performed and opportunities for future evaluations.

Chapter 2: Literature Review

The aim of this thesis is to investigate quantification of ^{123}I SPECT and its application in routine clinical practice using commercially available software. As described in Chapter 1, quantification of ^{123}I SPECT is challenging and optimisation involves consideration of many factors. The aim of this Chapter is to individually review the specialised corrections which are available to enable accurate SPECT quantification, thereby presenting the necessary background and justification for the work undertaken in this thesis.

The importance in collimator choice for ^{123}I SPECT acquisition will be covered. The choice of corrections, and how they should be applied to this data to facilitate accurate quantification, will then be discussed, and the ability to recover spatial resolution of SPECT data will be introduced. Finally, the way in which SPECT image data can be assessed and measured will be reviewed.

2.1 ^{123}I Collimator Choice

Radionuclide energy is the most important factor in selecting the collimator [3]. Collimators are design to achieve less than 5% septal penetration at the rated energy of use. Above this rated energy, the proportion of septal penetration becomes too large for acceptable images [5].

Once a radionuclide energy is known, a collimator with higher resolution or higher sensitivity can be chosen. For SPECT quantification, Rosenthal [40] recommends using the collimator with the highest spatial resolution. However, although ^{123}I has a primary emission at 159keV, for which low-energy collimators are suitable, the photopeak window accepts a proportion of the higher energy emissions. These detections are a result of high-energy photons losing energy due to scatter in the object of interest, scatter within

the collimator, and backscatter from the hardware beyond the scintillation crystal. Therefore, for ^{123}I SPECT, low-energy collimators are not an automatic choice.

A clear approach to reducing the problem of high-energy septal penetration is to make use of a collimator with thicker septa or longer bores. However, altering the collimator dimensions can have detrimental effects on spatial resolution. The additional complexity of high-energy emissions detected in the low-energy photopeak of ^{123}I acquisitions has provided a consistent debate over the choice of collimator and, as such, is typically influenced by clinical need.

2.1.1 History of Collimator Choice

The complex emission scheme of ^{123}I has led to opposing recommendations for collimator choice when acquiring ^{123}I clinical studies. In the 1970s, it was acknowledged that LEHR collimators of the time were not appropriate for minimising septal penetration. At that time, McKeighen [41] recommended pinhole collimators while Bolmsjo [15] recommended medium-energy collimators.

Bolmsjo demonstrated that LEHR collimators suffered a loss of low-frequency signal compared to medium-energy collimators, although medium-energy collimators had a poorer response at high spatial frequencies (Figure 2.1).

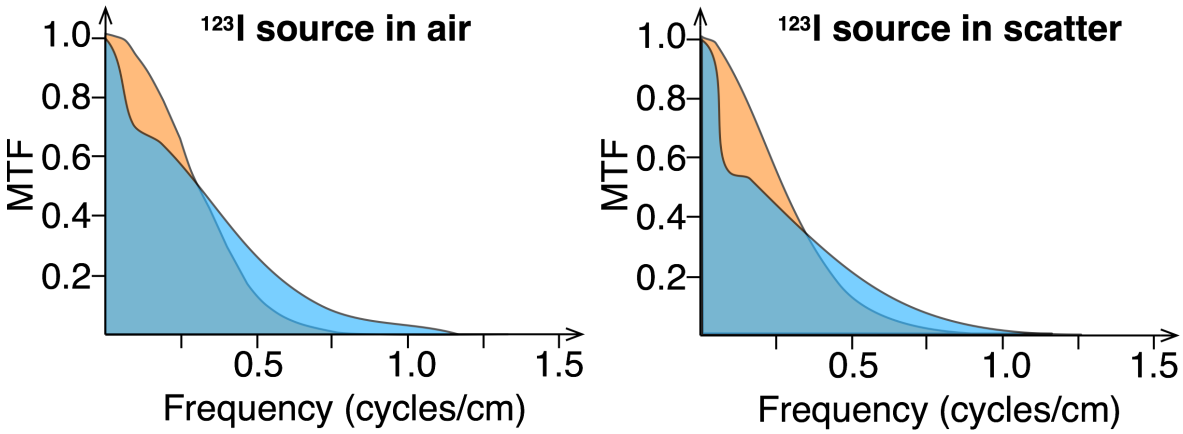

Figure 2.1: Modulation Transfer Function of an LEHR (blue) and a medium-energy (orange) collimator for ^{123}I in air (left) and in scatter (right) [15]

Bolmsjo concluded that the medium-energy collimator had “superior statistical accuracy per unit time”. This finding suggests medium-energy collimators may be preferred when quantification is necessary, although accurate quantification is dependent on the spatial frequency of the object.

There was further support for the choice of medium-energy collimators throughout the 1980s and 90s [16, 19, 42], particularly for specific clinical quantitative tasks such as the measurement of brain or myocardium activity ratios [17], and striatal uptake ratios [43].

In contrast to these publications, Müeller recommended LEHR collimators for ^{123}I brain imaging as early as 1986 [44]. Müeller showed higher resolution, even at a cost of a reduction in sensitivity, yielded significant improvements for brain SPECT. Furthermore, Madsen suggested in 1992 that the optimal spatial resolution for ^{123}I brain studies should be a Full Width at Half Maximum (FWHM) of 8-9mm [45]. Typically, a FWHM <9mm is only achieved with the use of LEHR collimators.

In 1999, Dobbeleir [19] recommended the use of medium-energy collimators for ^{123}I acquisition. However, the author noted the utility of LEHR collimators when including correction for scatter and septal penetration. In the following decade, publications described improvements in the clinical use of LEHR collimators with novel correction methods which included deconvolution of septal penetration [46] and energy window downscatter correction [20, 47] (described further in Section 2.3.2).

Recent clinical practice guidelines suggest the use of LEHR collimators for neuroreceptor and transporter imaging [27, 48, 49], mIBG tumour imaging [34], and pheochromocytoma and paraganglioma imaging [50]. In addition to clinical procedure guidelines, there has been an ongoing movement towards the standardisation of ^{123}I-DaTSCAN™ imaging across Europe. This has included a methodology for the calibration of a gamma camera for ^{123}I SPECT which uses LEHR collimators for acquistion [51].

A current procedure guideline which recommends medium-energy collimators is for cardiac sympathetic imaging [52]. This recommendation is due to the reliable performance of medium-energy collimators for quantification.

Recently, Maebatake [53] supported the use of LEHR collimators for ^{123}I DaT imaging in spite of the author's results, which demonstrated improved quantification using medium-energy collimators compared to low-energy collimators (with a statistically significant difference). Additionally, Lagerburg [21] suggests that for ^{123}I SPECT medium-energy collimators more accurately replicate known contrast ratios than low-energy collimators.

The studies by Maebatake and Lagerburg demonstrate that, in spite of clinical practice guidelines describing the use of LEHR collimators for ^{123}I SPECT, there remains interest in

the use of medium-energy collimators, particularly for a quantitative approach. Furthermore, recent advances in reconstruction correction schemes may reduce the influence of scatter and septal penetration for LEHR collimators and improve the spatial resolution of medium-energy collimators. These advances may improve image quality and quantitative accuracy for both collimators. Therefore, it is important to revisit the issue of preferred collimator choice for ^{123}I SPECT with the addition of these algorithms.

2.1.2 Manufacturer Variation in Collimator Design

A further complication in the ongoing debate concerning collimator choice is the variation in design between manufacturers. This is recognised in the European Association of Nuclear Medicine (EANM) clinical practice guidelines for ^{123}I-mIBG tumour imaging [34] which, although explicitly suggesting the use of LEHR collimators, states that: “Given the variability in collimator characteristics and design from different manufacturers, the choice of collimator … should therefore be left to the individual nuclear medicine department.”

Each manufacturer’s LEHR and medium-energy collimators typically have unique dimensions. One aim of collimator design is to achieve less than 5% septal penetration at the rated energy of use [5]. The hole length and septal thickness can be altered to achieve this aim, such that:

$$W > \frac{3}{\mu}$$ **Equation 2.1 [5]**

where W is the path length through the septum in cm and μ is the attenuation coefficient of the collimator material (cm^{-1}). A long hole length increases the path length through the septum (W) and allows the septal thickness to be kept small. In a comparison of current vendor collimator dimensions, the variation in composition between hole length and septal thickness is apparent (Table 2.1).

Name:	Siemens	GE	Philips	Siemens	GE	Philips	Siemens	GE	Philips
	LEHR			LPHR	LEUHR	VXHR	MELP	MEGP	
Hole Length (mm)	24.05	35	32.8	35	40	54	32.84	58	48
Septal Thickness (mm)	0.16	0.2	0.152	0.2	0.2	0.152	0.66	1.05	1.143

Table 2.1: Dimensions of low and medium-energy collimator designs from three main vendors

Collimator description: Low Energy High Resolution (LEHR), Low Penetration High Resolution (LPHR), Low Energy Ultra High Resolution (LEUHR), Vantage eXtra High Resolution (VXHR), Medium Energy Low Penetration (MELP) and Medium Energy General Purpose (MEGP)

The design of the Philips Vantage eXtra High Resolution (VXHR) collimator trades long hole length for thinner septa whereas the Siemens LEHR has a shorter hole length but thicker septa. Recent vendor comparison work has shown the shorter hole length of the Siemens LEHR collimator makes it susceptible to a higher proportion of septal penetration from ^{123}I than for GE and Philips low-energy collimators [54, 55]. Furthermore, Maebatake [53] has demonstrated that the Siemens LEHR collimator had a lower accuracy than GE low-energy collimators for quantification of ^{123}I DaT SPECT.

As Siemens LEHR collimators are the most susceptible to septal penetration, they present the greatest challenge to advanced reconstruction correction schemes and, therefore, they will be the focus of this thesis.

2.1.3 Custom Collimator Designs

Bespoke collimator designs and novel hardware solutions can address some of the issues associated with ^{123}I acquisitions. For example, Lee [56] used a multi-pinhole collimator with 20 apertures for brain SPECT while Park [57] used a dedicated high-sensitivity cardiac gamma camera for striatal quantification in brain SPECT. Although both studies report positive results, they rely upon dedicated task-specific hardware. The majority of nuclear medicine departments will rely on more generalised hardware options. Therefore, custom collimator designs will not be considered in this thesis.

2.1.4 Conclusions from Review of Collimator Choice for ^{123}I

The majority of current imaging guidelines recommend the use of LEHR collimators for ^{123}I. However, guidelines for cardiac sympathetic imaging and studies evaluating quantification recommend medium-energy collimators. This inconsistency in collimator

choice demonstrates the ongoing complexity of imaging ^{123}I. In practice, the ideal approach will be dependent on both the clinical application and the availability of manufacturers' hardware. What is clear from the literature is the significant impact of high-energy emissions which, if not removed using hardware (i.e. medium-energy collimators), has to be corrected to achieve accurate quantification.

One of the aims of this thesis is to investigate a novel third-party reconstruction algorithm which corrects for septal penetration of low-energy collimators. Siemens LEHR collimators are particularly susceptible to ^{123}I septal penetration. The investigation will, therefore, focus on these collimators. Comparison will be made with results for the Siemens MELP collimators, which is a commonly available hardware option for reducing septal penetration.

2.2 Acquisition and Iterative Reconstruction Parameters

This Section will outline the acquisition and reconstruction parameters which are used commonly throughout this thesis.

2.2.1 Acquisition Parameters

This section will introduce SPECT acquisition parameters. The choice of matrix size and number of projection angles described in this Section will be used as the standard method for SPECT acquisition throughout this work unless stated otherwise.

2.2.1.1 Acquisition Matrix Dimensions and Zoom

A 128x128 square acquisition matrix is used extensively throughout this research work. This dimension was chosen because Hermes Medical Solutions iterative reconstruction algorithm (Hybrid Recon™), which is used throughout this thesis, is restricted to a maximum matrix size of 128x128. Hermes Medical Solutions have chosen this upper limit as iterative reconstruction of SPECT data can be computationally intensive, particularly with the addition of novel correction techniques [58].

The linear sampling distance is determined by a combination of the matrix size and the acquisition zoom applied. The linear sampling distance sets a theoretical limit on the planar spatial resolution of projection data up to a maximum frequency known as the Nyqvist frequency, which is the frequency represented by twice the pixel width [5]. The Siemens Symbia gamma camera, which will be introduced in Section 3.2, has a pixel width of 4.8mm with a 128x128 matrix and no acquisition zoom applied. This mode of

acquisition is used clinically for SPECT imaging of body sections to ensure there is no truncation of anatomy. For neurology applications, a zoom is applied. Locally, an acquisition zoom of 1.45 is applied for clinical ^{123}I-DaTSCAN™ studies, which results in a pixel width of 3.3mm. As the spatial resolution for neurology SPECT is recommended by Madsen [45] as a FWHM of 8-9mm, the 3.3mm pixel width conforms with guidelines from the EANM for ^{123}I DaT imaging [27] of “one-third to one-half of the expected resolution”.

In this thesis, a further acquisition zoom of 2.0 is used in the assessment of SPECT spatial resolution (Chapter 5). The zoom of 2.0 results in a pixel width of 2.4mm, which is a suitable acquisition zoom that can be applied without truncating phantom data. Furthermore, the pixel size conforms with National Electrical Manufacturers Association (NEMA) recommendations of <2.5mm for the measurement of SPECT spatial resolution.

2.2.1.2 Projection Angles Acquired Over 360°

Previously, there has been some debate over the number of projection angles required over 360° to ensure suitable angular sampling. For example, Hutton [59] responded to a review of quantitative SPECT by Rosenthal [40] to clarify the projections necessary to suitably sample an object. Hutton’s method suggests 126 angles are required to provide appropriate angular sampling of a circular object 20cm in diameter. A similar method for determining the necessary projections is described by Cherry [3] and Lawson [5] which determines ~190 angles are necessary to sample a circular object 20cm in diameter.

However, these historical methods relate to Filtered Back-projection (FBP) reconstruction and do not apply to iterative reconstruction. Lawson [5] provides a mathematical proof which suggests iterative reconstruction requires half the projections necessary for FBP reconstruction. A review by Takahashi [60] confirms this proposal by demonstrating no loss of SPECT spatial resolution whether 30, 60 or 120 projection angles were used over 360°.

Local clinical ^{123}I SPECT acquisitions include 128 projections per 360°. Consequently, the number of projections acquired clinically provides suitable angular sampling for SPECT with iterative reconstruction and, as such, will be used as standard throughout this thesis.

2.2.2 Convergence of Iterative Reconstruction

The Maximum Likelihood Expectation Maximum (MLEM) iterative reconstruction algorithm, initially proposed by Shepp [6] and outlined in Section 1.2.2, converges with

increasing iterations to a maximum likelihood that the image estimates the emission data. Stamos [61] describes the convergence of the image estimate as being dependent on both the object and the amplification of noise with increasing iterations. Therefore, Llacer [62] proposed a stopping rule based on image deterioration from noise amplification. However, other metrics have also been used to determine convergence. For example, Liow [63] used the convergence of spatial resolution while Dickson [30] used the convergence of uptake ratios. Therefore, the determination of convergence is task specific.

A common aim of Chapters 5-8 will be to assess the convergence of the iterative reconstruction algorithm, with regard to spatial resolution, contrast recovery, noise and scatter suppression respectively. Convergence is also dependent on the reconstruction algorithm and will, therefore, be assessed with advanced correction schemes.

2.2.2.1 Projection Angles per Subset

Hudson [7] proposed a method to accelerate the iterative reconstruction algorithm by dividing the number of SPECT projections acquired into subsets of projections. This acceleration technique is known as an Ordered Subset Expectation Maximum (OSEM) algorithm. The MLEM "equivalent iterations" can be determined by multiplying the OSEM iterations by subsets [64]. The factor of acceleration achieved is equal to the number of subsets [7]. For example, two subsets would be twice as fast as an MLEM reconstruction, and four subsets would be four times faster. Therefore, to reduce reconstruction time, the projection data should be divided into as many subsets as possible, while projections should equally divide into subsets [7].

Although reducing reconstruction time is beneficial, quantitative results may be affected by dividing projections into a large number of subsets such that each subset has limited content. Hutton [65] demonstrated that data reconstruction with subsets consisting of only a few projections resulted in an overestimation of contrast when compared with a non-accelerated MLEM reconstruction. A review of acquisition and reconstruction parameters for SPECT quantification by Dewaraja [2] suggests "a reasonable compromise between speed and reconstruction quality is to have at least four projections per subset, although for noisy data (e.g. < 50k counts per slice) more projections per subset should be used". Although Hutton [65] describes a qualitative evaluation of images with four projections per subset as "virtually identical" to reconstructions for equivalent iterations, a more conservative approach should be taken when accurate quantitative measures are

essential. Therefore, work in this thesis will use a minimum of eight projections per subset, following recommendations by Dewaraja [2] for low-count data.

2.2.3 Conclusions

A 128x128 acquisition matrix will be used extensively throughout this thesis. Where appropriate, finer linear sampling will be achieved by applying an acquisition zoom. 128 projections will be acquired per 360°. Iterative reconstruction will be accelerated using an OSEM algorithm with a minimum of 8 projections per subset.

A theme of practical work in this thesis will be the evaluation of the convergence of image quality metrics for advanced iterative reconstruction correction schemes.

2.3 Attenuation and Scatter Correction Review

As outlined in Section 1.2.3, for accurate quantification of SPECT data, it is essential to include attenuation and scatter correction in the image reconstruction process. This Section describes commonly used and advanced methods for performing attenuation and scatter correction. The Section will conclude by identifying the methods of attenuation and scatter correction for subsequent investigation.

Attenuation describes photons that are not detected because they undergo an interaction in the patient. Scatter describes photons which are detected after undergoing Compton scatter in the patient, leading to a gain in counts in the wrong location. It is usual to treat attenuation and scatter independently even though both result from the same Compton interactions.

A review of SPECT scatter correction by Hutton [66], an investigation into the absolute quantification of SPECT by Ritt [10] and a review of SPECT quantification by Bailey [1] agree that appropriate correction for both attenuation and scatter is necessary for quantification and should be performed in combination.

2.3.1 Attenuation Correction Techniques

Attenuation is the process by which some photons will fail to reach the detector because they interact in the patient. Photoelectric absorption or Compton scatter result in a loss of counts from the image. At diagnostic radionuclide energies (such as ^{99m}Tc to ^{131}I, which range from 140 to 364keV respectively) the photons have a higher probability of undergoing Compton scatter in the attenuating material [67].

The effect of attenuation is greatest for organs deep within the patient. The result is that deep structures will appear to have less activity in them than they do [8]. Attenuation correction attempts to counteract this effect by increasing counts that come from deep within the patient. For most methods of attenuation correction, the reconstruction algorithm needs a map which details the distribution of attenuating material in the patient.

The linear attenuation coefficient, μ, which is a measure of the fraction of photons lost in each centimetre of tissue, characterises the attenuation of photons in different tissues [8]. For higher density materials, such as bone, the attenuation coefficient is higher to reflect the greater loss of photons per centimetre. Conversely, low-density materials such as air have a lower attenuation coefficient to reflect fewer attenuated photons per centimetre. The linear attenuation coefficient also varies with the energy of the incident photon. The higher the photon energy, the lower the probability of attenuation per centimetre, and hence there is a lower attenuation coefficient. The linear attenuation coefficients for common radionuclides in water (tissue equivalent) and bone are given in Table 2.2 [67].

Radionuclide	Energy (keV)	Water (cm^{-1})	Bone (cm^{-1})
Technetium-99m (^{99m}Tc)	**140**	0.149	0.294
Iodine-123 (^{123}I)	**159**	0.138	0.273
Iodine-131 (^{131}I)	**364**	0.099	0.172

Table 2.2: Linear attenuation coefficients for water (tissue equivalent) and bone density [67] for various radionuclide emission energies

An attenuation map represents the spatial distribution of linear attenuation coefficients for the object of interest [68]. The methods for generating the attenuation map belong to two main classes: transmissionless and transmission based. Transmissionless correction methods estimate distribution using either a manually determined boundary of attenuation coefficients, conjugate counting of opposing views or segmented Magnetic Resonance Imaging (MRI) data.

Zaidi's review of the use of attenuation maps in emission tomography [68] suggests the assumption of transmissionless attenuation maps is only appropriate for brain studies. In brain studies, it is straightforward to determine an outline of the skull and to assume that the attenuation coefficient is the same everywhere inside. Additionally, automated methods can allow for a certain thickness of higher attenuation material to be added to account for the skull [68]. However, Zaidi suggests uniform attenuation correction would

be inadequate for the chest due to the combination of lungs, soft tissue and bone where a single attenuation coefficient is no longer appropriate [9, 68]. In this imaging scenario, an internal map of attenuation coefficients would be required and would be different for each patient [5]. Furthermore, Van Laere's comparison of transmissionless and transmission based attenuation correction for brain perfusion studies [69] notes that single attenuation coefficients determined experimentally with phantoms do not extrapolate directly for application in clinical data.

In areas of inhomogeneous attenuation, direct methods of measurement must be used to generate the attenuation map. To date, measured transmission data is the most accurate attenuation correction technique [9, 68, 70]. A transmission based approach utilises radionuclide scanning or appropriately scaled Computed Tomography (CT) scans acquired either separately or sequentially on multimodality imaging systems. The methods for transmission based correction vary in complexity, accuracy, computation time required [9] and cost of hardware [71].

Zaidi [9] suggests that transmission based non-uniform attenuation correction can provide more accurate attenuation maps than transmissionless techniques and that correction using these maps allows accurate quantification [40, 72]. However, Zaidi's observer study of brain imaging [73, 74] showed no significant difference in subjective image quality between images reconstructed with transmissionless and non-uniform attenuation maps.

2.3.1.1 Radionuclide Transmission

Radionuclide transmission methods often incorporate a transmission source positioned directly opposite a detector which rotates with the gantry. When radionuclide sources are used to acquire the transmission data, photon statistical noise from the transmission scan can propagate through the reconstruction process, affecting the quality of the images [9]. Although radionuclide transmission maps provide a patient specific outline and attenuation map, Van Laere [69] demonstrated quantification was no more accurate than uniform transmissionless attenuation maps.

2.3.1.2 CT Attenuation Maps

In 1989, Fleming [75] showed that CT data could be used to improve the accuracy of SPECT data by generating a patient-specific attenuation map. Recent technology has allowed hybrid type cameras to become commonplace, with SPECT-CT systems becoming more widespread in nuclear medicine departments. The CT images do not need to be of diagnostic quality. Therefore, a gamma camera which incorporates a low dose,

low-resolution CT scanner in the same gantry is suitable. In these systems, the range of X-ray energies transmitted has an average energy somewhat lower than common radionuclides. However, the CT value for each pixel in the image can be used to characterise whether it is composed of air, tissue or bone. The attenuation coefficient at any other energy can be determined by extrapolation [8].

Although extrapolation of attenuation coefficients to radionuclide energies is well established, the scenario with ^{123}I is complicated by the range of emissions. The map of attenuation coefficients is scaled to the predominant 159keV emission energy. However, this method overestimates the attenuation coefficients of the higher energy emissions. An overestimation in attenuation coefficient will result in an over amplification of detected photons in this region.

A study by Lange [76] does not recommend CT attenuation correction for ^{123}I-DaTSCAN™ imaging due to the additional radiation dose to the patient for a negligible difference in interpretation. However, this is in contrast with Maebatake [53], Lapa [77] and Yokoyama [78] who agree that CT attenuation correction gives more accurate quantification for ^{123}I-DaTSCAN™ studies.

Care must be taken to ensure that SPECT and CT data are suitably registered. Warwick [70] found the CT attenuation correction was more accurate compared to transmissionless attenuation correction in phantom work. However, the author described that patient brain SPECT studies with subtle misregistration resulted in inferior quantification compared to transmissionless corrections [70].

With regard to combined attenuation and scatter correction, Hutton's investigation of attenuation correction of cardiac SPECT [79], noted “… the scatter problem has become more prominent since the artefacts introduced by scatter can be more serious after correction for non-homogeneous attenuation is performed”. Therefore, Zaidi [68], Greaves [8], Hesse [80] and Hutton [66] agree that reconstruction with CT attenuation must also include scatter correction.

2.3.1.3 Conclusions from Review of Attenuation Correction

The use of CT-based attenuation correction maps will be used extensively throughout this thesis. This will address one of the aims, the provision of quantification. When CT attenuation correction is applied, scatter correction must also be employed [8, 66, 68, 80].

2.3.2 Scatter Correction Techniques

Scatter and septal penetration detected within the primary photopeak degrades image contrast. Techniques for scatter correction either aim to minimise the proportion of scatter detected or to correct for the presence of scatter. The aim of this section is to detail the two methods of scatter correction used extensively in this thesis: measured scatter and modelled scatter distribution. However, these two methods will be described following a summary of alternative approaches to scatter correction.

2.3.2.1 Summary of Alternative Approaches

This Section reviews methods of scatter correction that are not used in this thesis. However, a summary of their methodology establishes a platform for describing the two methods that were selected for evaluation. Therefore, the aim of this Section is to summarise alternative methods of scatter correction and describe their weaknesses.

Asymmetric Energy Window

In Hutton's recent review of SPECT scatter correction [66], the author describes that the simplest technique to minimise the proportion of scatter detected is to select an asymmetric photopeak energy window. An asymmetrical energy window is suited for monoenergetic radioisotopes such as ^{99m}Tc. However, asymmetric photopeak energy windows are not appropriate for radionuclides like ^{123}I with complex emission schemes which include high-energy downscatter.

Spectral Methods

Methods which incorporate extensive spectral analysis and modelling rely on recording precise energy information for all detected events and fitting the energy spectrum of events detected in each pixel. Despite the high accuracy of these corrections, and with the advantage of appropriately compensating for scatter coming from out-of-field activity, their implementation requires full list-mode acquisition. This method includes the simultaneous acquisition of data in a large number (>10) of energy windows, which is not commonly available on commercial systems [66].

Appropriate Attenuation Coefficient

A crude form of scatter correction is to reduce the amount of attenuation correction, thereby restoring fewer counts. An example of this is reducing the attenuation coefficient from the theoretical narrow beam value to a measured broad beam value [8]. The approach does not compensate for the spatial distribution of the object-dependent effects

of scatter and so does not remove photons that are at a ‘wrong’ location. Therefore, the method only works satisfactorily for a reasonably uniform source distribution [8].

Filtering

Hutton’s review of SPECT scatter correction [66] describes the historical use of FBP filters to provide some compensation for scatter. For example, Metz and Wiener filters are designed to deliver a degree of point spread function compensation that includes scatter. The problem with these filters is their assumption of a constant object-independent point spread function, which is not true. As a result, these are no longer commonly used.

Modifying a Reconstruction Probability Matrix

As the probability of Compton scattering at any given angle is known, it is possible to calculate the probability that photons originating in a particular image voxel will scatter into any projection bin. The appropriate element of the projection matrix is assigned this probability. This method requires knowledge of the distribution of scattering material in the patient with, for example, an attenuation map. This additional complexity increases the computational overhead [8]. As the scatter estimate is object-dependent, based on the distribution of tissue densities, it is therefore unique to each patient.

Hutton [66] points out that this approach can only allow for scatter sources within the field of view of the camera. In the case of an out-of-field ‘hot’ source, a scatter measurement technique may be a better approach. In these circumstances, Greaves [8] suggests it is better to use a measured scatter distribution from the patient than projection matrix manipulation.

2.3.2.2 Measured Scatter

For realistic scatter correction, it is necessary to determine the amount of scatter in an individual image. This amount will depend on the distribution of activity within the patient, the distribution of scattering material and the range of scattering angles accepted. A reasonable estimate of the scatter contribution within the image obtained from the photopeak energy window can be derived from one or more adjacent energy windows.

Data from a scatter image acquired by an energy window positioned just below the photopeak can be multiplied by a scaling factor to account for energy window width and placement outside of the photopeak. The scatter image can then be subtracted from the photopeak image to give a scatter corrected image. Lower energy scatter windows are commonly used for correction of single energy emission radionuclides such as ^{99m}Tc.

Many commercial systems implement this dual energy window scatter correction technique due to its simplicity and effectiveness [8].

The main disadvantage with the dual energy window approach is that the spatial distribution of scatter differs as a function of both the loss of energy and the different order of scatter. The primary window contains photons largely with small deflection angles and first order scatter, whereas a wide lower energy window will measure photons with a larger deflection angle and higher order scatter. The correction, therefore, removes a pattern of larger angle and higher order scatter from the photopeak, which is not representative of low angle first order scatter locations. This method is limited further as the uniformity correction is dependent on the higher energy primary window [66].

An alternative method for the measurement of scatter uses a triple energy window (TEW). This method sets two narrow scatter windows: one immediately below the photopeak window and the other immediately above it. The contribution of scatter to the photopeak window can then be estimated by linear interpolation between the low and high scatter windows. The corrected image is the photopeak image minus the average of the two scatter window images [8, 81, 82]. Investigations of measured scatter correction methods for ^{123}I imaging by Small [20] and Lagerburg [21] suggest LEHR collimator acquisitions must include downscatter correction from an upper energy window for the accurate measurement of contrast ratio.

The main disadvantage of the TEW technique is the noise amplification that arises due to the acquisition of relatively low counts in the narrow scatter windows. Hutton [66] notes that "… in low count situations the presence of negative values in scatter corrected projections can lead to serious artefacts". Furthermore, as Geeter observed [17], subtracting the scatter image from the photopeak window image dramatically increases the noise level. Narita [83] also suggests TEW has a much poorer SNR than alternative scatter correction methods. Wider scatter windows could reduce noise, but the estimated distribution of scatter will be more biased.

For practical purposes, methods based on the use of several energy windows have a definite appeal, despite their limitations, since they permit direct estimation of scatter from low and high-energy emissions [66]. Therefore, as an effective and commonly used technique, the TEW method will be used extensively throughout this thesis.

2.3.2.3 Modelling Scatter Distribution

Simulation studies [84, 85] have shown that accurate modelling of the full 3D spatial scatter response is superior with regard to noise properties (contrast-to-noise ratio as a function of iteration number) compared to the use of energy window-based measured scatter correction. This finding holds, even if the window-based scatter estimate is noise-free, which is better than can be achieved in practice [66]. Methods for modelling scatter distribution include:

- *Analytical:* this method uses complex equations that allow an exact calculation of scatter [66]. These models are often restricted to the modelling of first order scatter.
- *Transmission-Dependent Convolution Subtraction:* estimates scatter based on a convolution of the photopeak counts by the assumption that the scatter point response is a mono-exponential function. Estimated scatter is subtracted from the photopeak counts or incorporated in the reconstruction modelling.
- *Object Shape or Slab Derived Estimation:* whereby scatter is estimated based on experimental work or simulation, tabulating scatter functions at various depths behind a slab of water. The functions for uniform objects of different shapes can be accurately estimated.
- *Fast Monte Carlo Scatter Estimation:* A full Monte Carlo simulation can be applied, rather than a simplified model, to estimate scatter. Given knowledge of the distribution of attenuation coefficients, the scatter distribution for individual sources of activity can be estimated accurately.

Full estimation of scatter for an individual patient was traditionally considered too computationally demanding to be useful. However, recent work in optimising Monte Carlo methods has demonstrated that it is feasible to compute scatter estimates in sufficient time to be practical for inclusion in image reconstruction [58, 84-86]. Monte Carlo-based methods of scatter correction have been reported to provide a more accurate scatter correction than energy window-based methods [66, 86].

As well as correction for scatter within the patient, Monte Carlo methods have been developed to model the effects of septal penetration [87]. This approach has particular appeal in the context of ^{123}I as the high-energy downscatter and photopeak are independently modelled to include interactions in the patient, collimator and detector system. Hutton [66] notes the combination of multi-energy and detector modelling has the potential to significantly improve the diagnostic quality of multi-energy radionuclides which have traditionally been considered inferior.

2.3.2.4 Conclusions from Review of Scatter Correction Methods

Monte Carlo modelling of primary and high-energy photons within the patient and detector system provides the most promising approach for the complex emission scheme of ^{123}I, especially in regard to LEHR acquisition. The inclusion of Collimator and Detector Response Modelling (CDRM) into Monte Carlo simulation of photons has the potential to provide the most accurate correction method for SPECT imaging of ^{123}I. As such, the following reconstruction correction schemes will form the basis of investigation in this thesis:

- CDRM scatter correction, accessed under a research agreement with Hermes Medical Solutions ahead of commercial release
- Object Only Scatter Correction (OOSC), which simulates scatter within the patient at the photopeak energy. OOSC is a Monte Carlo scatter correction algorithm commercially available from Hermes Medical Solutions which has proven accurate for scatter correction of ^{99m}Tc cardiac studies [58]
- TEW scatter correction, which is the most commonly used clinical scatter correction technique for LEHR ^{123}I imaging [21, 30, 31, 66]

The CDRM, OOSC and TEW scatter correction methods will be applied to data acquired with LEHR collimators. With regard to medium-energy collimator acquisitions, Lagerburg [21] demonstrated explicit corrections for high-energy septal penetration are not necessary for accurate recovery of image contrast. Therefore, CDRM and TEW scatter correction methods were not applied to data acquired with medium-energy collimators.

2.4 Resolution Recovery Review

As outlined in Section 1.2.3.3, the gamma camera has a finite resolution, and that resolution deteriorates with source distance from the collimator. As gamma camera collimators have known dimensions such as hole length, hole diameter and septal thickness, the acceptance angle of photons can be determined. Furthermore, the distance of the collimator from the centre of rotation is known. Therefore, reconstruction algorithms can model the projection of photons, with the width of the projection ray increasing with distance from the detector [8]. The correction may be depth-dependent or depth-independent subject to the complexity of the correction algorithm. This section will describe the motivations for Resolution Recovery (RR) and outline the method used extensively throughout this thesis to perform the correction.

2.4.1 Motivations for Resolution Recovery

A clear motivation for correction of collimator blurring is to improve image quality. O'Mahoney [88] describes RR as improving image quality through reduced partial volume effect, higher image contrast and lower levels of noise. This improvement may provide the option to reduce the amount of activity administered to patients. Therefore, this approach is of particular interest in areas where dose reduction is paramount. For example, Sheehy [89] and Stansfield [90] have demonstrated that use of RR in SPECT reconstruction can reduce the exposure of paediatric patients undergoing ^{99m}Tc-DMSA and ^{99m}Tc-MDP bone scans respectively.

Alternatively, if RR improves image quality, then acquisition time can be reduced. Reduced acquisition time is of particular interest in the field of nuclear cardiology where Venero [91], DePuey [92], Kangasmaa [93] and Armstrong [94] have investigated using reduced-time acquisitions reconstructed with RR.

2.4.1.1 Resolution Recovery for Improving Quantification

The use of RR to correct for collimator blurring improves spatial resolution and partial volume effect. Enhanced spatial resolution improves the accuracy of quantification of object size and activity concentration. A simulation study of iterative reconstruction for quantification by Müller [95] suggested a minimum system resolution of approximately 0.4 times the object diameter was necessary to allow accurate estimation of object size and activity. In Warwick's investigation on RR of brain SPECT studies [70], the author advises that any SPECT quantification task should include correction for collimator blurring. Kalantari [96] similarly suggests that using RR results in more accurate quantification.

However, RR algorithms have limitations. For example, O'Mahoney described significant overestimation of small sources (20-30mm) [88]. Sohlberg demonstrated Gibb's ringing artefacts using Hermes Medical Solutions implementation of depth-dependent RR [97]. Similarly, in Armstrong's investigation of quantification using Siemens xSPECT reconstruction software [98], Gibb's ringing artefact was responsible for the underestimation of activity concentration of a 28mm sphere. The ringing artefacts are produced by the RR algorithm trying to recover fine detail lost due to the low spatial resolution of the gamma camera. Erlandsson's review of RR [99] suggests that "… reversing the effects of [partial volume effect] usually lead to noise-amplification or image artefacts".

2.4.2 Resolution Recovery via Probability Matrix Adjustment

Hermes Medical Solutions implement depth-dependent RR in their iterative reconstruction algorithm by probability matrix adjustment.

The gamma camera's finite resolution deteriorates with distance both within and between slices. Determining the point spread function of the camera allows 3D modelling of correction for the loss of spatial resolution. The projection matrix can be modified to take account of the probability that photons originating from slightly off the projection ray can still reach a given projection bin.

The FWHM of the Gaussian-shaped PSF will increase with increasing distance from the collimator. However, this can be easily measured or calculated if the dimensions of the collimator (hole diameter and length) are known. If the dimensions of the collimator and the distance of the patient from the collimator are known, the projection matrix can incorporate the image blurring caused by limited resolution [8]. Although this technique works in theory, in practice the process is still limited by image noise, and so RR cannot produce images with perfect resolution. Nevertheless, the resultant images are improved when compared to those produced by other reconstruction techniques [8].

2.4.3 Conclusions from Review of Resolution Recovery

Reconstructions performed in this thesis use Hermes Medical Solutions implementation of depth-dependent RR. The algorithm uses the probability matrix adjustment method described in Section 2.4.2. Collimator dimensions detailed in the Siemens Technical Specifications document [100] allowed point spread function modelling.

2.5 Indices for Optimisation of Reconstruction Parameters

The aim of optimising SPECT reconstruction parameters in this thesis is to improve quantitative accuracy and to enhance image quality for observers. Publications optimising SPECT image reconstruction have performed evaluation with a number of image quality metrics, including:

- Spatial resolution
- Contrast
- Noise
- Contrast-to-Noise Ratio (CNR)
- Residual Error (RE)

Therefore, this Section will review these metrics for assessing image quality. One of the aims of this thesis is to produce ^{123}I SPECT images with a high degree of quantitative accuracy. This review further aims to identify the utility of these measures as they relate to ^{123}I SPECT quantification.

2.5.1 Spatial Resolution

Spatial resolution is the minimum distance between two points in an image that can be detected [11]. Spatial resolution is commonly quantified from the Full-Width at Half-Maximum (FWHM) of the Line Spread Function (LSF) [12], a measure that has been described as matching human perception of spatial resolution [101]. As well as being an important image quality metric, spatial resolution is also interconnected with quantitative accuracy. Work by both Kojima [102] and Müller [95] suggest a minimum system resolution of approximately 0.4 times the object diameter was necessary to allow accurate estimation of object size and activity. Therefore, optimisation of spatial resolution is a key metric in achieving accurate quantification.

Spatial resolution has previously been used as a metric to justify the choice of collimator and acquisition energy windows for ^{123}I imaging. Optimisation work by Bolmsjo [15] measured the LSF to establish the ideal collimator and energy window for the acquisition of planar ^{123}I images. Bolmsjo concluded that an LEHR converging collimator demonstrated the smallest FWHM (11.2mm), while energy window widths investigated did not influence spatial resolution.

Similarly, Rault [47] measured the spatial resolution of ^{123}I SPECT data to determine the ideal collimator choice. Rault recommended LEHR collimators reconstructed with TEW scatter correction, based on a FWHM of 7.9mm for the LEHR collimator compared with 13.4mm for the medium-energy collimator.

Various authors have used the convergence of the FWHM to determine a cut-off point for iterative reconstruction. Liow's simulation study [63] characterised the convergence of SPECT FWHM and found that, depending on the size of objects, the global spatial resolution may not have fully converged until 200 iterations. However, Norberg [103] challenges Liow's theoretical approach to convergence based on FWHM by suggesting "the optimisation process must be done for every clinical examination". This statement is evidenced by Brambilla [64] who recommends 80 iterations for ^{99m}Tc cardiac SPECT, Olsson [104] who recommends 195 iterations for ^{99m}Tc brain SPECT and Norberg who

suggested at least 60 iterations for ^{99m}Tc lung SPECT, all based on FWHM measurements.

Spatial resolution measurements have also been used to assess advances in reconstruction algorithms. Bouwens [105] simulation study compared iterative reconstruction variants incorporating RR by evaluating the error in measured to known FWHM of a point source. Bouwens found that both MLEM and OSEM converged at 40 iterations. Similarly, Knoll [106] used a line source phantom to evaluate advanced reconstructing algorithms for ^{99m}Tc SPECT supplied by GE, Siemens and Philips. Knoll determined that advanced algorithms which incorporate RR and scatter correction minimised the FWHM at 75-80 iterations.

To date, there has been no investigation of ^{123}I SPECT spatial resolution which assesses the inclusion of advanced corrections for depth-dependent RR, CT attenuation correction and Monte Carlo scatter correction in the reconstruction algorithm. An aim of this thesis, therefore, will be to determine convergence of system spatial resolution for ^{123}I SPECT to enable accurate quantification.

2.5.2 Contrast

Cherry [3] defines contrast as: “the ratio of signal change of an object of interest, such as a lesion, relative to signal level in surrounding parts of the image”. Cherry further details that factors affecting contrast will also affect observer detectability, making contrast a key metric in the assessment of image quality. Contrast Recovery (CR) describes how accurately a reconstructed image represents a known uptake to background contrast ratio.

As with spatial resolution, evaluating CR allows assessment of acquisition and reconstruction parameters to enable optimisation of image quality. Rault’s [47] investigation of collimator choice for ^{123}I SPECT measured CR in reconstructed data. Rault concluded that ^{123}I, acquired with LEHR collimators and corrected with TEW scatter correction, had higher CR than medium-energy collimator data. A simulation study by Crespo [24] demonstrated that additional correction with RR improved ^{123}I SPECT CR.

The outcome of an optimisation study based on CR convergence is dependent on the object under investigation and is, therefore, task specific. This is demonstrated by the variation in published recommendations based on CR convergence. In Liow’s simulation study [63] the author suggests CR converges for SPECT reconstruction at 200 iterations,

whilst Grootjan [107] suggests convergence of CR at 96 iterations. Dickson reported convergence in uptake ratio (a surrogate for CR) of ^{123}I at 96 iterations using a striatal brain phantom. However, the reconstruction algorithm used by Dickson did not incorporate advanced corrections such as depth-dependent RR or Monte Carlo scatter correction.

CR typically refers to Hot CR (HCR). HCR is the ratio of detected contrast to true contrast on a scale of 0-1, with a result of 1 indicating complete recovery of the known contrast. However, Cold CR (CCR) can also be measured. CCR is the ratio of counts in a cold region to counts in a background region on a scale of 0-1, with a result of 1 indicating complete recovery of a photopenic region. CCR is suggested by Graham [12] for routine SPECT quality control. Additionally, Brambilla [64] measured CCR in the evaluation of RR in the reconstruction of ^{99m}Tc SPECT. Brambilla found that CCR took longer to converge than HCR and was, therefore, essential in determining optimum imaging parameters.

The use of the NEMA International Electrotechnical Commission (IEC) Body phantom has, more recently, become commonplace for measuring SPECT CR [98, 106-108]. However, the phantom has yet to be used with regard to ^{123}I SPECT. Therefore, this thesis will investigate both HCR and CCR using the NEMA IEC Body phantom to examine convergence for ^{123}I SPECT reconstruction, with the aim of optimising image contrast.

2.5.3 Noise

Noise is a general term for an unwanted signal. A signal may suffer from noise during capture, storage, transmission, processing, or conversion [109]. Noise also describes signals that are random and, therefore, carry no useful information. With regard to gamma camera imaging, noise most commonly refers to statistical noise present in acquired data [8].

Noise present in planar imaging follows Poisson statistics of counts acquired and is easy to establish. However, determining noise for tomographic imaging is much more complex. The intensity level for each pixel depends on computations from multiple projections which involve virtually all other pixels in the image [3]. Two methods used to describe noise in tomographic images are Image Roughness (IR) and Background Variability (BV).

IR is a measure of how noise varies from pixel-to-pixel in a reconstructed volume [110]. Most simply, IR can be measured by taking the counts in a large Region of Interest (ROI) or Volume of Interest (VOI) and dividing the standard deviation by the mean. Brambilla [64] has shown a linear relationship of increasing IR with iterations for ^{99m}Tc SPECT. Knoll

[106] used IR to show that advanced iterative reconstruction algorithms could be used to reduce IR for ^{99m}Tc SPECT compared with conventional iterative reconstruction. A study by van Gils [111] demonstrated IR in ^{131}I SPECT imaging could be reduced by incorporating RR in the reconstruction algorithm.

Bailey [112] showed that the IR of ^{99m}Tc SPECT, reconstructed with FBP, varied with count density with a 1/√counts Poisson relationship. However, Schmidtlein [113] determined this was not the case for iterative reconstruction in Positron Emission Tomography (PET) imaging due to nonlinearity of the algorithm. The relationship between IR and count density for ^{123}I SPECT with complex iterative reconstruction is not known.

Background Variability (BV) relates to how noise varies region-to-region within an image [110]. BV is the Coefficient of Variation (COV) of the means between multiple ROI or VOIs. For example, Grootjans [107] determined BV for ^{99m}Tc SPECT as the COV of the means from 60 ROIs. The author showed that BV reduces when the reconstruction algorithm includes RR, and also when count density increases. BV indicates how consistent or otherwise noise is in an image. However, it does not indicate noise magnitude. Therefore, BV should not be taken on its own and should be considered alongside IR [114].

2.5.4 Contrast to Noise Ratio (CNR)

Statistical noise can impair the detection of a lesion even when the size of an object is substantially larger than the limiting spatial resolution of the image, especially if the object has low contrast [3]. To detect a lesion or other object in an image, the observer must be able to distinguish between the lesion and the noise generated contrast patterns in background areas. Therefore, determining the Contrast-to-Noise-Ratio (CNR) of an image is a useful indicator of detectability.

A visual means to assess the relationship between contrast and noise in an image is a simple contrast-noise curve. This method was used by Gantet [115] in a simulation study which compared standard OSEM with two implementations of RR reconstruction. Reconstructions which included RR were shown to have similar CR and reduced noise (IR).

CNR is one of a number of metrics that can be used to assess SPECT image quality. For example, in ^{131}I SPECT imaging, van Gils [111] demonstrated higher CNR for reconstructions of the NEMA IEC Body phantom which included RR and Monte Carlo scatter correction than in those without correction. Furthermore, van Gils demonstrated

CNR maximised at 10-15 iterations, dependent on the correction scheme. Using a similar method of analysis for ^{99m}Tc SPECT, Grootjans [107] demonstrated the relationship between CNR and count density for advanced reconstruction algorithms from multiple vendors, again with the NEMA IEC Body phantom.

Oloomi [108] investigated CNR of ^{99m}Tc SPECT reconstructions of both a cardiac phantom and the NEMA IEC Body phantom. Oloomi found a consistently higher CNR for reconstructions which included attenuation and scatter correction than in uncorrected reconstructions of the NEMA phantom. The cardiac phantom demonstrated higher CNR with combined attenuation correction and a novel scatter correction method than alternative methods.

To the author's knowledge, there have been no evaluations of the CNR properties of advanced ^{123}I SPECT reconstruction schemes. Therefore, this thesis will follow the methods of van Gils, Grootjans and Oloomi for measuring the CNR of ^{123}I SPECT reconstructions using the NEMA IEC Body phantom.

2.5.5 Residual Error

Residual Error (RE) is a measure of counts in a region within the object of interest that should be devoid of counts. Residual Error differs from CCR in that CCR measurements are of a region with density similar to tissue which will give rise to scatter events. RE is measured in a region of low density and, therefore, assesses the effectiveness of attenuation and scatter corrections in SPECT reconstruction. Although originally proposed for PET quality control [116], the measurement was used by van Gils [111] to compare TEW and Monte Carlo scatter correction of ^{131}I SPECT. Van Gils found the RE metric useful for comparing scatter correction methods where septal penetration exists, concluding that the Monte Carlo scatter correction approach minimised RE. Therefore, RE can be considered particularly applicable to ^{123}I SPECT which suffers from septal penetration of low-energy collimators. The reconstruction correction scheme which minimises RE should indicate the most appropriate method of correction for septal penetration. With accurate attenuation and scatter correction, the RE of a cold region in the centre of hot phantom should tend towards 0%.

2.5.6 Summary of Indices for Optimisation of Reconstruction Parameters

Table 2.3 summarises the use of the image quality measures described in this Section.

Author (year)	Isotope	Spatial Resolution	Contrast Recovery	Noise	CNR	RE
Bolmsjo (77)	^{123}I	✔				
Kojima (89)	^{99m}Tc	✔				
Liow (93)	—	✔	✔			
Bouwens (01)	—	✔				
Bailey (05)	^{99m}Tc			✔		
Brambilla (05)	^{99m}Tc	✔	✔	✔		
Gantet (06)	^{123}I				✔	
Koral (07)	^{131}I		✔			
Norberg (07)	^{99m}Tc	✔				
Olsson (07)	^{99m}Tc	✔				
Rault (07)	^{123}I	✔	✔			
Crespo (08)	^{123}I		✔			
Knoll (12)	^{99m}Tc	✔		✔		
Oloomi (13)	^{99m}Tc		✔		✔	
Armstrong (16)	^{99m}Tc		✔			
Grootjans (16)	^{99m}Tc		✔	✔	✔	
van Gils (16)	^{131}I			✔	✔	✔

Table 2.3: Summary of the use of image quality measures described in this Section

Table 2.3 illustrates that no single study provides a comprehensive assessment of image quality metrics for ^{123}I SPECT. Therefore, an aim of this thesis is to perform such an assessment of ^{123}I SPECT image quality with the inclusion of advanced corrections. This evaluation will be performed based on the metrics described in this Section. The outcome of the investigation will inform collimator choice for acquisition and recommend preferred reconstruction parameters for visual assessment and quantification.

2.6 Quantification of Radionuclide Uptake

Relative and absolute quantification are the two forms of quantification used in tomographic nuclear medicine that are the focus of this thesis. Relative quantification of ^{123}I SPECT is commonplace in neurology [29, 31, 117] and cardiology [46, 118]. However, absolute quantification is more challenging. Reconstruction algorithms that contain the required corrections now overcome many of the challenges associated with absolute quantification.

Quantification of the most common radionuclide for imaging, ^{99m}Tc, is being adopted in routine clinical practice for a range of studies [1]. However, additional challenges remain for the accurate quantification of ^{123}I SPECT due to its complex emission scheme. This Section will describe methods of performing relative and absolute quantification and will review developments in the field.

2.6.1 Methods of Relative Quantification

Relative quantification is the ratio between a region of uptake and a reference region. However, relative quantitative measurements can be achieved by a number of approaches. This Section will describe the most clinically relevant, including automated approaches to measuring uptake ratios.

2.6.1.1 Specific Uptake Determination

The simplest method of relative quantification is a straightforward ratio of uptake to non-specific uptake. An example of this was the study by Ortega [119] of 183 movement disorder patients undergoing ^{123}I-DaTSCAN™ imaging. The investigation aimed to establish Uptake Indices (UI) between areas of specific activity and areas of non-specific activity. Ortega showed that a UI threshold of 1.44 resulted in a high degree of diagnostic accuracy in the differentiation of neurodegenerative Parkinson Disease.

Chen [46] applied a similar approach in ^{123}I-mIBG SPECT cardiology. Chen used a Heart-to-Mediastinal ratio, analogous with UI, when investigating deconvolution of septal penetration with a cardiac torso phantom. Chen then used the measure to distinguish patients with heart failure from normal controls [118].

2.6.1.2 Large ROIs/VOIs and the "Southampton Method"

Manual ROI analysis, such as the previous method by Ortega, includes substantial partial volume effect and operator-dependent variability [9]. Techniques have been introduced to reduce partial volume effect and operator variability through the use of larger ROIs/VOIs. For example, Crespo [24] used a large ROI for the quantification of ^{123}I DaT SPECT. ROIs were drawn using a high-resolution CT which was registered to the SPECT data. ROIs were then automatically expanded on the SPECT dataset to ensure the inclusion of all the activity that has spread outside the physical volume of the structures due to partial volume effect.

Combined work by Fleming [120, 121] and Tossici-Bolt [31] aimed to address both partial volume effect and inter-operator variability. The author's methods introduced both automation to region drawing and a Standardised Uptake Size Index (SUSI) for ^{123}I-DaTSCAN™ analysis. The technique is more commonly known as the Southampton Method.

The Southampton Method uses large ROIs/VOIs to compensate for partial volume effect. Following the method, transverse slices containing the striatum are summed together. The operator then places two large geometric shapes, one over each striatum. The large region ensures all the counts from the striatum outside the physical volume of the structure are measured to account for partial volume effect. Additionally, the use of regular geometric VOIs reduces operator positioning errors [120]. Appendix A includes a detailed description and a simple example of the Southampton Method.

2.6.1.3 Automated Relative Quantification

Striatal Uptake

Specific Binding Ratio (SBR), as described by Gilland in 1994 [33], has been used to evaluate ^{123}I SPECT striatal uptake as recommended by the Society of Nuclear Medicine (SNM) in 1995 [40]. This method has been integrated into commercially available automated applications, for example, Hermes Medical Solutions BRASS™ [29, 122], the open source Bas-Gan [123], and GE's DaTQUANT [124]. Furthermore, these software applications have been developed for automation of region drawing and comparison of the SBR of clinical studies with a normal database.

Creating a database of clinically normal investigations allows comparison of clinical studies with a probabilistic atlas with normal ranges for each voxel. In 2010, the EANM's Research 4 Life (EARL) group completed a project to create a "European Database of ^{123}I-FP-CIT (DaTSCAN™) SPECT scans of healthy controls (ENC-DAT)" [125]. This database of 137 normal volunteers has been incorporated into Hermes Medical Solutions BRASS™ application and the analysis of this database for SBR has determined gender and age-related declines [29, 126]. The same age-related declines have been demonstrated using the open source BasGan, which has been developed by the Italian Association of Nuclear Medicine [123].

Additionally, Dickson [30] has used the automated SBR analysis performed by BRASS™ as a metric for optimising ^{123}I SPECT reconstruction. Automatic SBR analysis is now a

common approach used in efforts to standardise striatal uptake measurements in European centres [117].

2.6.2 Quantification of Absolute Activity Concentration

Although relative quantification has been used extensively throughout Europe, a weakness of this approach is a dependence on a suitable reference region. Reference regions are typically areas of non-specific tracer uptake. These regions will be of relatively low count density and, therefore, noisy. Accuracy in any uptake ratio will be dependent on the noisy reference region. Furthermore, Zaidi [9] suggests performing automated quantitative analysis should be approached with care as DaT imaging, for example, can contain inadequate anatomical landmark information needed for automated algorithms.

An alternative to the relative quantitative approach is a direct measurement of activity concentration. This method of absolute quantification requires suitable calibration of the gamma camera. Setup is, therefore, more complicated compared to relative quantification. Despite this complexity, there has been a recent interest in the utility of absolute quantification for clinical applications [1, 127]. As a result, common nuclear medicine vendors have developed software suitable for absolute quantification. Hermes Medical Solutions market SUV-SPECT® [13], Siemens have introduced xSPECT™ [98], and GE have developed Q.Suite software (originally for PET quantification) for analysis of SPECT data.

The measurement of absolute activity concentration is achieved by calibration of a gamma camera. Calibration involves imaging a known activity concentration. The sensitivity of the camera can be used to determine a Calibration Factor (CF). In subsequent studies, counts in a region can be multiplied by the CF to convert to activity concentration in kBq/ml.

Some authors have used planar imaging to determine camera sensitivity [128-130]. Although planar calibration is simple to implement, Dewaraja [2] notes that its application to SPECT patient data must include perfect correction for scatter and attenuation. This condition is difficult to achieve and, therefore, direct calibration measurements with SPECT data acquisition are more reliable. Authors who calibrate for absolute quantification with SPECT data [98, 131-133] acquire a phantom with uniform activity and ensure the reconstruction parameters and corrections applied match those used clinically.

The accuracy of SPECT quantification of activity concentration is varied. In Bailey's review of quantitative SPECT [1], the author notes errors of up to 20% in activity concentration estimates in the literature. With regard to ^{123}I SPECT, Iida [134] performed a multi-centre evaluation of the accuracy of absolute quantification using a uniformly filled cylindrical phantom. Iida measured a consistent 12% underestimation in activity concentration with novel scatter correction and attenuation correction applied across a range of cameras. Iida attributed this underestimation to a line source method of calibration and, therefore, the difference in geometry between the phantom used for calibration and the phantom used for assessment of accuracy.

A phantom simulation study of ^{123}I brain SPECT by Crespo demonstrated an underestimation of 20-40% depending on the reconstruction algorithm. Interestingly, however, Crespo also noted the accuracy of activity concentration improves to ~5% when the Southampton Method was used to remove partial volume effect from the measurement. Crespo's results contrast with those of Du [135] who demonstrated a <2% error in ^{123}I brain phantom imaging. However, Du's study used specialist research software for reconstruction which included an MRI scan for anatomical information.

Kangasmaa [13] has shown consistent Calibration Factor (CF) determination of gamma cameras for ^{99m}Tc quantification with third party software. However, the accuracy and consistency of ^{123}I SPECT absolute quantification with commercially available software is unknown.

2.6.2.1 Standardised Uptake Values

Absolute quantification of activity concentration depends on the time of uptake following injection of radiopharmaceutical and the volume of distribution in the patient. The variability of these parameters between studies, therefore, means that activity concentration measurements cannot be used for comparison of inter-patient studies or even for intra-patient serial scans.

Converting activity concentration to Standardised Uptake Values (SUVs) normalises between patient studies. SUVs are simple to calculate and are commonplace in the evaluation of clinical PET-CT studies [136]. Bailey's recent review of quantification [127] discusses the methods for determining SUVs and their potential application in routine clinical SPECT. An SUV in g/ml can be calculated using Equation 2.2.

$$SUV = \frac{ActCon}{(InjAct_{DC}/BM)}$$ **Equation 2.2**

where *ActCon* is the activity concentration in kBq/ml within an ROI or VOI, $InjAct_{DC}$ is the injected activity in kBq decay corrected to the time of imaging and *BM* is the body mass of the patient in g [136]. Body mass is used as a surrogate for volume of distribution.

Although a simple calculation, the optimal method for the measurement of SUVs has been the subject of debate. Three commonly used options are SUV_{mean}, SUV_{max} and SUV_{peak} [137-140]. For determining SUV_{mean}, *ActCon* in Equation 2.2 is the mean voxel value from all of the voxels in a given ROI/VOI. Measurements made using SUV_{mean} are susceptible to partial volume effect if the extent of the ROI/VOI has been chosen to match the boundary of an object of interest. SUV_{max} avoids partial volume effect by using the maximum voxel value in an ROI/VOI. However, SUV_{max} is sensitive to noise [138, 141]. SUV_{peak} is a measure of the average SUV within a small, fixed-size ROI/VOI centred on a high-uptake region [137]. Therefore SUV_{peak} is less sensitive to noise compared with SUV_{max} and is less susceptible to partial volume effect compared with SUV_{mean}. However, Vanderhoek [138] has highlighted that SUV_{peak} is sensitive to the size and shape of the region defined as the peak. Therefore, consistent use of the same SUV_{peak} definition is required to ensure the measure is applicable.

Bailey's review [1] of clinical applications for quantitative SPECT suggested that, although feasible, routine clinical measurement of SUVs is not yet commonplace. Bailey states: "… cooperation between researchers developing the methodology required for quantitative SPECT and manufacturers will allow its wider introduction for clinical use". Consequently, recent publications by Kangasmaa [13] and Armstrong [98] have shown software packages from Hermes Medical Solutions and Siemens Healthcare respectively to be viable for SUV quantification of ^{99m}Tc SPECT. Use of SUVs will likely proliferate in SPECT imaging as vendors continue to expand distribution of product offerings. However, the viability of SUVs with ^{123}I SPECT is unexplored.

2.7 Conclusions

This Chapter has reviewed the main factors affecting optimisation of ^{123}I SPECT imaging.

Considering collimator choice, there is further work to be performed for ^{123}I SPECT optimisation, particularly with regard to advanced Monte Carlo scatter correction

algorithms. This Chapter has introduced the Monte Carlo CDRM and OOSC methods, and described the traditional TEW scatter correction method. These three methods will be used extensively throughout investigations in this thesis. CT attenuation correction and Resolution Recovery (RR) will be applied in conjunction with the scatter correction methods.

This Chapter has shown that assessing the final image is not straightforward. Iterative reconstruction of SPECT data is context dependent and established measurement protocols do not exist for advanced algorithms. The metrics introduced in this Chapter will be used with regard to optimising reconstruction parameters, whereby:

- Full Width Half Maximum (FWHM) measurements will be used to characterise spatial resolution in Chapter 5
- Hot Contrast Recovery (HCR) and Cold Contrast Recovery (CCR) will be used to investigate contrast recovery in Chapter 6
- Image Roughness (IR) and Background Variability (BV) will be used to describe noise in Chapter 7
- Contrast to Noise Ratio (CNR) will be used to evaluate the relationship between contrast and noise in Chapter 7
- Residual Error (RE) will be used to assess the effectiveness of scatter correction and attenuation correction in Chapter 8

Likewise, the challenges with quantification of SPECT data have been discussed. Chapter 10 will describe calibration of a gamma camera for relative quantification. Chapter 11 describes calibration of absolute quantification, with an assessment of the accuracy of activity concentration measurements. The clinical application of quantification via SUVs will be compared with current relative quantitative approaches in Chapter 12.

Chapter 3: ^{123}I Planar System Performance

3.1 Introduction

This Chapter assesses ^{123}I planar system performance. SPECT projections are a series of short duration planar images. Therefore, the production of high-quality SPECT images is dependent on the planar performance of the system.

Techniques for assessing gamma camera performance are well established [142-144]. Typically, ^{99m}Tc imaging performance is evaluated during camera acceptance testing or routine quality control due to its widespread use. Therefore, gamma camera performance using ^{99m}Tc is well understood.

However, characterising planar performance is important for all radionuclides, particularly for radionuclides with complex decay schemes, such as ^{123}I. The high-energy emissions of ^{123}I are known to introduce distance-dependent effects on sensitivity and scatter fraction when imaged with low-energy collimators [20]. Therefore, before embarking on tomographic imaging, it is critical that the planar performance of the system being used is understood.

In this Chapter, the planar performance of a Siemens Symbia T2 gamma camera for imaging ^{123}I was investigated. An evaluation was made of the following planar imaging characteristics critical for accurate SPECT quantification:

- spatial resolution
- scatter fraction
- sensitivity
- count rate response
- spatial uniformity

The aim of this work is to understand how ^{123}I can affect imaging performance. This work will provide the foundation for the subsequent Chapters in this thesis and, importantly, will contribute to the ultimate goal of optimising ^{123}I SPECT image quantification.

3.2 Siemens Symbia T2: Hybrid SPECT-CT Gamma Camera

A Siemens Symbia T2 dual-headed gamma camera was used throughout this thesis (Figure 3.1). The Siemens Symbia T2 has a two slice diagnostic CT scanner which allows sequential SPECT-CT imaging. Table 3.1 presents key specifications of the gamma camera.

Figure 3.1: Siemens Symbia T2 gamma camera

Parameter	Specification
Field of View (FOV)	53.3x38.7cm
Crystal Thickness	9.5mm
Photomultiplier Tubes (PMTs)	59 (hexagonal array)
Intrinsic Spatial Resolution (FWHM in CFOV)*	<3.8mm
Intrinsic Energy Resolution*	<9.9%
System Spatial Resolution in Air (LEHR collimator, FWHM at 10cm)*	7.4mm
System Spatial Resolution with Scatter (LEHR collimator, FWHM at 10cm)*	8.7mm
Maximum Count Rate	310kcps
System Planar Sensitivity (LEHR at 10cm)*	91cps/MBq
System Planar Sensitivity (MELP at 10cm)**	140cps/MBq
Reconstructed Spatial Resolution (Centre)*	<11.4mm
Average Auto-contour Distance	1.1cm

Table 3.1: Siemens Symbia T2 key technical specifications [100]
(*) indicates measured with ^{99m}Tc (140keV), (**) indicates measured with Indium-111 using dual photopeak acquisition (171keV and 245keV)

The patient table has an integrated collimator exchanger containing a set of Siemens BiCore™ Low Energy High Resolution (LEHR) and Medium Energy Low Penetration (MELP) collimators. Table 3.2 describes the specifications for these collimators.

Parameter	LEHR	MELP
Number of Holes (x1000)	148	14
Hole Length (mm)	24.05	40.64
Septal Thickness (mm)	0.16	1.14
Hole Diameter (mm)	1.11	2.94
Septal Penetration (%)	1.5*	1.2**

Table 3.2: Siemens BiCore™ specifications for LEHR and MELP collimators [100] (*) indicates measured with ^{99m}Tc (140keV), (**) indicates, measured with Gallium-67 (predominantly 93keV, 184keV, and 300keV)

3.3 Assessment of Siemen Symbia ^{123}I Planar System Spatial Resolution

Accurate quantification requires sufficient spatial resolution. A simulation study by Müller [95] suggested a minimum system resolution of approximately 0.4 times the object diameter was required to accurately estimate object size and activity concentration.

With regard to ^{123}I imaging, LEHR collimators are more susceptible to high-energy septal penetration than medium-energy collimators. However, medium-energy collimators typically have poorer spatial resolution. Furthermore, planar spatial resolution is known to degrade with distance from the detector. The aim of this work was to characterise planar spatial resolution with distance from the Symbia T2 gamma camera with Siemens LEHR and MELP collimators, and to compare findings with published results for ^{123}I.

3.3.1 Planar Spatial Resolution Methods and Materials

3.3.1.1 Line Source Phantom

Following guidelines from the Institute of Physics and Engineering in Medicine (IPEM) Report 111 on quality control of gamma cameras [144], two 30cm long, 22 gauge needles with a nominal internal diameter of 0.4mm, were used as line sources. The line sources contained an ^{123}I activity concentration of 74MBq/ml. One line source was parallel with the x-axis, and one was parallel with the y-axis.

3.3.1.2 Acquisition Parameters

The line sources were imaged in air using both LEHR and MELP collimators. IPEM report 111 [144] suggests data is acquired at distances of 0cm, 5cm and 10cm from the detector. However, as data may be acquired at greater distances in clinical practice, in this

investigation, the line sources were imaged at distances ranging from 1-30cm in 5cm increments.

The acquisition matrix was set to 256x256 with a zoom of 2.6, resulting in a square pixel width of 0.9mm, less than the 1mm maximum pixel width recommended by Bolster [142]. Images contained 100k counts per line source.

The planar spatial resolution was measured with and without Triple Energy Window (TEW) scatter correction. To perform scatter correction, upper and lower scatter windows were positioned on either side of the main photopeak, according to the method by Ichihara [82]. This approach resulted in the following energy window acquisition scheme:

- Photopeak: 143-175keV (159keV±10%)
- Lower Scatter: 135-143keV (5% of 159keV)
- Upper Scatter: 175-183keV (5% of 159keV)

The image used for scatter correction (C_{scat}) was calculated using Equation 3.1 [82]:

$$C_{scat} = 2 \times (C_{lower} + C_{upper}) \qquad \textbf{Equation 3.1}$$

where C_{lower} is the image acquired in the lower scatter window and C_{upper} is the image acquired in the upper scatter window. The TEW corrected image is achieved by subtracting C_{scat} from the primary photopeak acquisition.

3.3.1.3 Image Analysis

The Full-Width Half-Maximum (FWHM) was measured using a 16-pixel wide profile across both line sources. Line profiles of the sources contained at least 10^3 counts [142-144]. Profiles were positioned twice in both the x- and y-direction and mean values measured.

Due to the small number of measurements, the normality of data cannot be proven. Therefore, Chebyshev's theorem [145, 146], a non-parametric method for small datasets, was used to assess measurement error. The theorem does not suggest a level of probability. Rather it assures that at least 75% of any distribution of data is within plus or minus twice the Standard Error (SE). The more normal the distribution of data under test, the closer the theorem tends to a 95% probability. The standard error was determined using Equation 3.2.

$$SE = SD/\sqrt{n}$$ **Equation 3.2**

where *SD* is the Standard Deviation of the spatial resolution measurement and *n* is the number of measurements. Error bars were included on results where 2xSE≥1mm.

3.3.2 Planar Spatial Resolution Results

At the detector surface, the planar spatial resolution of the data acquired with LEHR and MELP collimators is approximately equal (4.6±0.3mm and 4.7±0.6mm respectively). However, as distance increases, the spatial resolution of MELP data degrades more than that of the LEHR data, due to the wider hole diameter of the former (Figure 3.2).

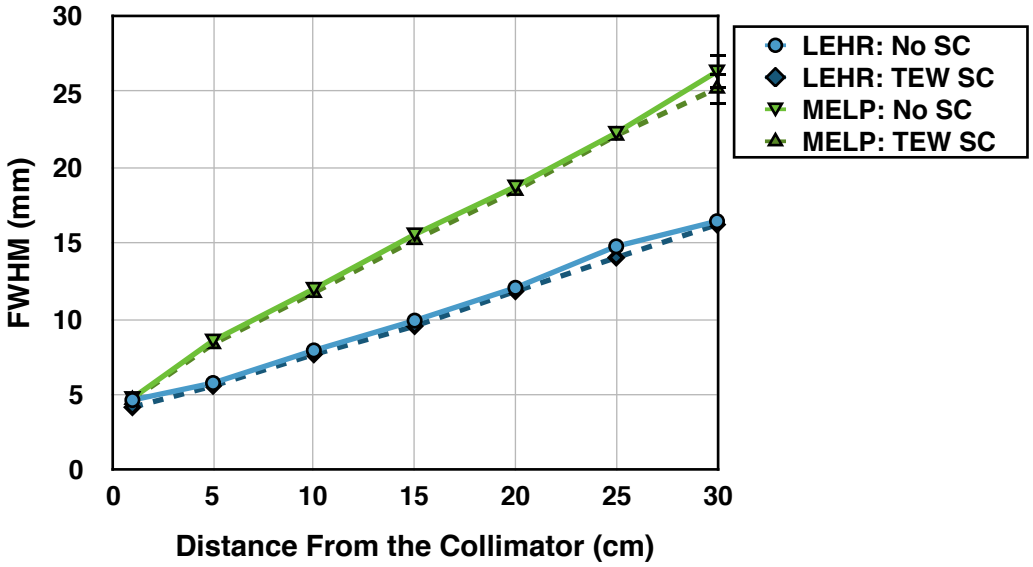

Figure 3.2: Planar spatial resolution (FWHM)
Measured with ^{123}I line sources at varying distance from the collimator surface with and without scatter correction (SC). Error bars are shown where 2*SE≥1mm.

Detection of scattered photons in gamma cameras typically affects the tails of the PSF rather than at the height of the FWHM [147]. Therefore, as anticipated, TEW scatter correction has a negligible impact on the FWHM results for both collimators.

3.3.3 Planar Spatial Resolution Discussion

The Siemens Symbia planar spatial resolution measurements presented here are comparable with the assessment of ^{123}I by Inoue [42] where the spatial resolution of Siemens collimators at distances of 5cm to 50cm from the detector were measured. A comparison of results is shown in Table 3.3. Inoue's results are approximated based on interpretation of figures in the publication.

	LEHR		MELP	
Distance	**No SC**	**Inoue**	**No SC**	**Inoue**
5cm	5.8cm	~6.5cm	8.6cm	~9.0cm
10cm	7.9cm	~8.5cm	12.0cm	~12.0cm
20cm	12.0cm	~12.5cm	18.7cm	~19.5cm
30cm	16.5cm	~17.0cm	26.3cm	~26.5cm

Table 3.3: Planar spatial resolution FWHM for ^{123}I (with and without scatter correction (SC)) comparing results from this investigation with published results by Inoue [42]

Further spatial resolution results published for ^{123}I have been acquired using alternative manufacturers' gamma cameras. Larsson [25] performed a simulation study of GE collimators and measured ^{123}I planar spatial resolution at 10cm in air from the detector. Larsson determined a FWHM of ~7mm and ~9.5mm for LEHR and MELP collimators respectively. These results compare with a FWHM of 7.9±0.3mm and 12.0±0.7mm measured in this investigation for LEHR and MELP collimators respectively. The GE collimators differ from Siemens collimators in that both GE collimators have a longer hole length, thus reducing the angle of acceptance and improving spatial resolution.

Similarly, Dobbeleir [19] measured ^{123}I planar spatial resolution at 10cm in air from Trionix collimators. Dobbeleir measured a FWHM of 7.4mm and 10.1mm for LEHR and medium-energy collimators respectively. The dimensions of the Trionix collimators used by Dobbeleir are unknown. However, as with Larsson's results, the 2mm difference in spatial resolution measured using medium-energy collimators can presumably be explained by variation in design.

Small [20] measured FWHM with ^{123}I point sources in scatter material at a distance of 10cm. Small measured a FWHM of 10.9mm for low-energy collimators and 14.0mm for medium-energy collimators using a GE Camstar XC/T gamma camera. Small noted downscatter correction of sources in scatter material does not improve FWHM measurements. This intuitive result was also demonstrated in the current investigation with the application of TEW scatter correction.

System spatial resolution is more often quoted with reference to ^{99m}Tc. Intrinsic spatial resolution improves with increasing energy [3, 148]. However, the primary emission energy of ^{99m}Tc (140keV) and ^{123}I (159keV) are sufficiently close to allow comparison. Kappadath [149] measured the inter-camera consistency of extrinsic spatial resolution on Siemens Symbia cameras as 4.4mm with ^{99m}Tc sources and LEHR collimators.

Kappadath does not describe the method of measurement. However, presuming measurements were made at the collimator surface in air, Kappadath's result is comparable with the 4.6±0.3mm FWHM measured at 1cm from the collimator surface in this investigation.

3.3.4 Planar Spatial Resolution Conclusions

The Siemens Symbia ^{123}I planar spatial resolution measurements are consistent with published findings, including distance effects [19, 20, 25]. As anticipated, it was shown that TEW scatter correction of ^{123}I did not improve spatial resolution, as measured by the FWHM.

3.4 Scatter Fraction

Photons detected in the photopeak energy window are a combination of primary photons, scattered photons and septal penetration. Scatter Fraction (SF) refers to the proportion of photons in the photopeak energy window which have scattered in the object or detector system. These non-primary photons reduce image contrast and adversely affect quantification. SF has been estimated to be as high as ~50% for ^{123}I using Monte Carlo simulation [23, 150]. Therefore, it is important to perform a practical assessment of SF for the Siemens Symbia system.

The aim of this Section is to assess SF by measuring the detected photons on either side of the main photopeak window. These measurements allow estimation of scatter in the photopeak window.

^{123}I images acquired with low-energy collimators are affected by a relatively high proportion of septal penetration. Medium-energy collimators have thicker septa and longer hole length which makes them less susceptible to septal penetration and, thus, should have a smaller SF. This assumption was assessed for the Siemens Symbia gamma camera with LEHR and MELP collimators. As high-energy emissions of ^{123}I introduce a distance-dependence, particularly for low-energy collimators, the SF was assessed at a range of distances from the detector.

3.4.1 Scatter Fraction Method

Images of the two line sources, previously described in Section 3.3.1.1, were acquired using the TEW scheme at a distance of 1-30cm from the collimator surface. SF can be expressed as a percentage by comparing the estimate of scattered photons using the

TEW approach (Equation 3.1) to the total number of photons detected in the photopeak. SF was calculated using Equation 3.3.

$$SF = 100x(\frac{C_{scat}}{C_{pp}}) \qquad \textbf{Equation 3.3}$$

where C_{scat} is the counts in the scatter windows normalised to the width of the photopeak window (Equation 3.1) and C_{pp} is the counts in the photopeak energy window.

3.4.2 Scatter Fraction Results

At a distance of 1cm from the detector, the SF was shown to be 49.8% and 14.2% for the LEHR and MELP collimator acquisitions respectively. While the proportion of scatter photons detected in the photopeak reduces with distance from both collimators, it was more obvious for LEHR data (Figure 3.3).

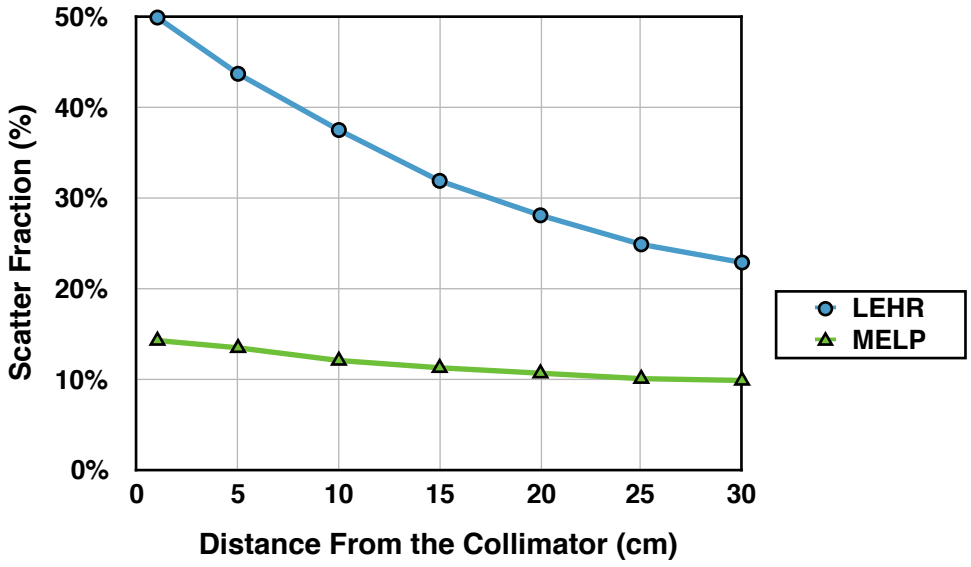

Figure 3.3: Estimated proportion of scatter in the photopeak window for LEHR and MELP acquisitions of two ^{123}I line sources

The reduction in SF with distance is due to the proportion of high-energy photons reducing with distance. From a point source, the reduction would follow the inverse square law. However, in this instance, demonstration of the inverse square law is complicated by the use of extended line sources and the combined effect of non-penetration and penetrating low and high-energy photons, both changing with distance.

3.4.3 Scatter Fraction Discussion

In this study, the estimated proportion of counts in the Siemens Symbia photopeak which results from scatter has been measured to be as high as 49.8% for LEHR and 14.2% for MELP. This practical measurement agrees with previous Monte Carlo simulation by Cot

[150] and Tanaka [23]. At 2mm from the detector surface, Tanaka estimated a 54% and 10% SF for LEHR and medium-energy collimators respectively, the dimensions of which are not given. Cot estimated the SF with distance to be 48.6%, 36.7% and 27.3% at 5cm, 15cm and 25cm respectively from a simulated collimator with a similar septal thickness and hole diameter as the Siemens LEHR, but with a longer hole length, which should reduce septal penetration. These simulation values are comparable with the 43.6%, 31.8% and 24.8% measured in this investigation. This finding suggests the TEW technique provides a reasonable estimation of the proportion of scattered photons detected in the photopeak energy window for this source distribution.

Dobbeleir [19] measured the SF of ^{123}I in air, 10cm from the detector, as 34.7% for Trionix LEHR collimators. Although less than the SF determined in this investigation (37.4% at 10cm), the author estimated scatter using a single lower energy window which would underestimate the influence of high-energy septal penetration.

To optimise spatial resolution in the clinical setting, the source should be imaged as close to the detector as possible. Therefore, the maximum SF of 49.8% measured in this evaluation demonstrates the extent of the scatter correction task required for ^{123}I SPECT reconstruction with LEHR collimators.

3.4.4 Scatter Fraction Conclusions

Septal penetration of ^{123}I high-energy emissions results in a relatively large SF for low-energy collimators compared with medium-energy collimators. For sources close to the surface, the SF can be as high as 50% for the Siemens LEHR collimator.

The SF reduces with distance from both collimators. A consequence of this effect will be a variable sensitivity with distance, which will affect sensitivity based absolute quantification.

3.5 Relative Sensitivity

System sensitivity is defined as the count rate detected by the camera system for a source of known radioactivity and is expressed in counts/second/MBq source activity [142, 143]. The sensitivity of the camera is a critical measure to quantify activity concentrations in reconstructed SPECT data.

Ideally system sensitivity should be independent of the distance of the source from the detector for parallel hole collimators. However, as shown with Scatter Fraction (SF)

results, this may not be the case for ^{123}I. As such, the sensitivity of low and medium-energy collimators with distance was investigated. Furthermore, for comparison, the relative sensitivity of both ^{123}I and ^{99m}Tc was evaluated, the latter of which is less susceptible to septal penetration of low-energy collimators. As high-energy septal penetration may be detected distant from the source position, the relative sensitivity of these two radionuclides was investigated for increasing proportions of the Field of View (FOV).

3.5.1 Relative Sensitivity Methods

3.5.1.1 Relative Sensitivity with Distance

Following the method by Small [20], sensitivity of the Siemens Symbia gamma camera to ^{123}I sources was measured at distance relative to the sensitivity at 5cm from the detector. Relative sensitivity was determined with acquisitions of the line sources described in Section 3.3.1.1, which were imaged in air 5-30cm from the detector in 5cm increments with LEHR and MELP collimators.

The total counts in each planar acquisition was used to determine relative sensitivity.

3.5.1.2 Relative Sensitivity Across the Field of View

To provide an assessment of the contribution of high-energy septal penetration across the FOV, sensitivity was measured by imaging relatively focal radionuclide sources.

The relative sensitivity of ^{123}I and ^{99m}Tc was evaluated with vials positioned 10cm from the detector surface. A vial of ^{123}I and a vial of ^{99m}Tc which contained comparable activities (28.8MBq and 33.0MBq respectively), chosen to minimise dead time effects, were used to compare relative sensitivity of the gamma camera to these two radionuclides. The vials were acquired in air with LEHR and MELP collimators. A 256x256 matrix with a pixel size of 2.4mm was used. Data were acquired with the TEW scheme described in Section 3.3.1.2.

As high-energy septal penetration may be detected distant from the source position, the relative sensitivity of these two radionuclides was investigated for increasing proportions of the FOV. A 16 pixel wide (38.4mm) square ROI was positioned over the vial. This size of ROI approximately matches the diameter of the vial. The ROI width was increased in increments of sixteen pixels (38.4mm) to measure relative sensitivity over an increasingly larger proportion of the FOV. Figure 3.4 shows ROI placement.

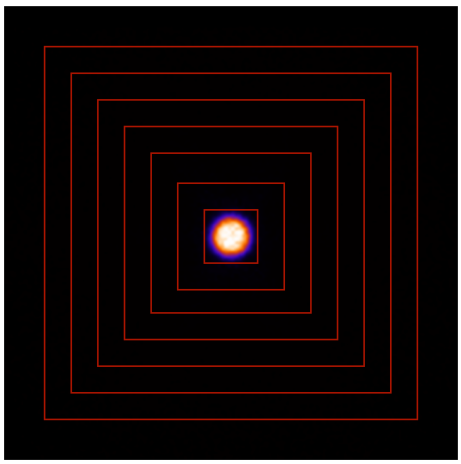

Figure 3.4: Placement of square ROIs on an image of an ^{123}I source acquired with LEHR collimators

3.5.2 Relative Sensitivity Results

3.5.2.1 Relative Sensitivity with Distance Results

Figure 3.5 shows that the relative sensitivity of a Siemens Symbia to ^{123}I line sources decreases as distance from the collimator surface increases.

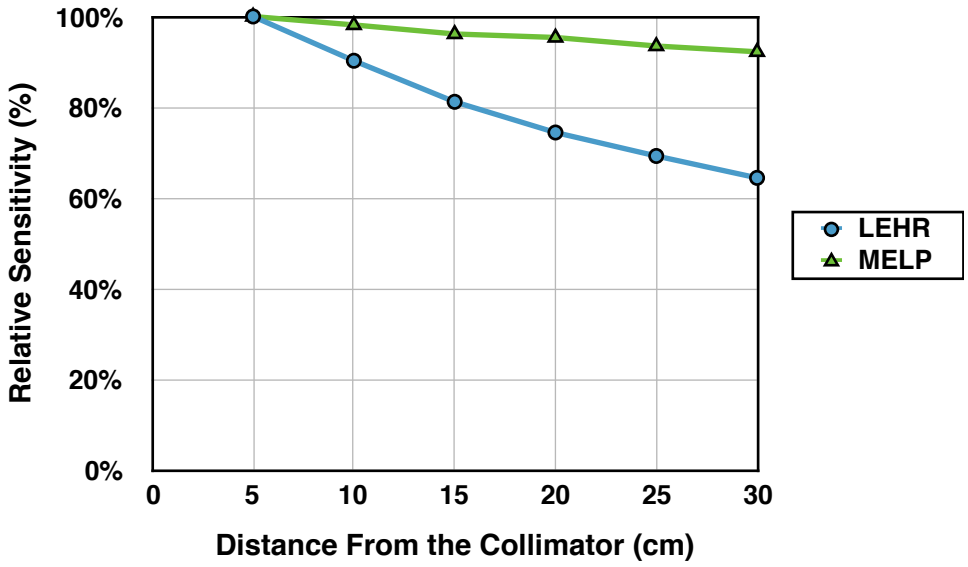

Figure 3.5: Relative sensitivity of a Siemens Symbia to an ^{123}I line source with distance from LEHR and MELP collimators

The relative sensitivity of the LEHR collimator reduces to 64.4% at 30cm. The reduction in relative sensitivity suggests that the sensitivity close to the detector is overestimated due to a higher proportion of septal penetration from high-energy emissions, as was demonstrated by the Scatter Fraction measurements in Section 3.4.2.

The relative sensitivity of the MELP collimator reduces to 92.2% at 30cm which indicates that these collimators are less susceptible to septal penetration.

3.5.2.2 Relative Sensitivity Across the Field of View

With increasing ROI size, the sensitivity of the detector to an ^{123}I source at 10cm in air, relative to the source measured with a 16 pixel wide square ROI, is shown in Figure 3.6.

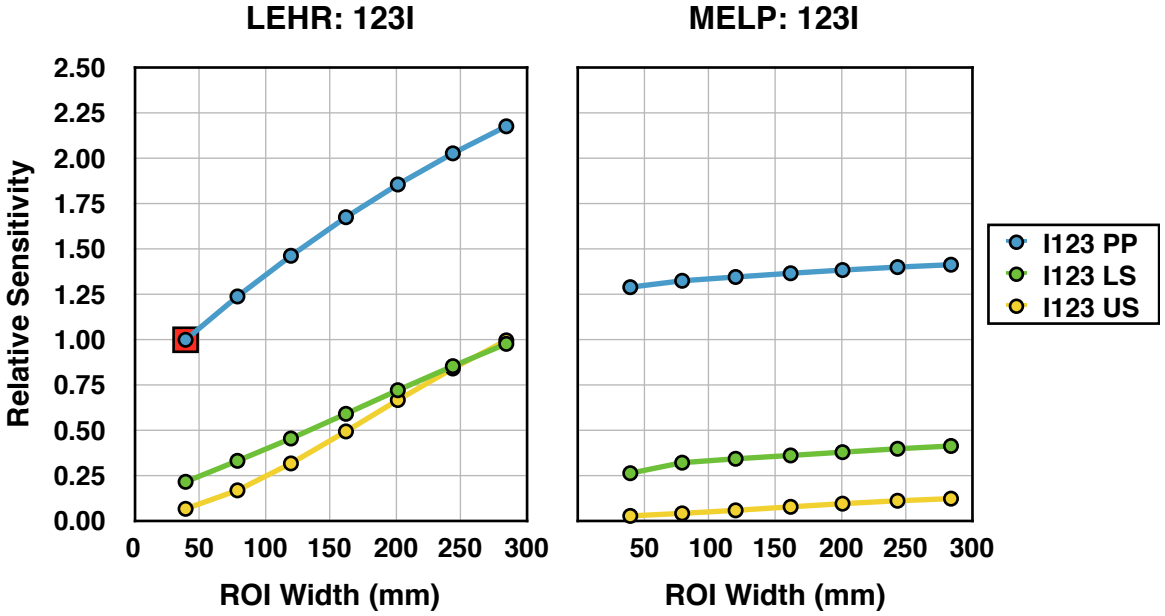

Figure 3.6: Relative sensitivity of a Siemens Symbia with increasing ROI width to ^{123}I with LEHR (left) and MELP (right) collimators
Photopeak (PP), Lower Scatter (LS) and Upper Scatter (US) results are relative to LEHR sensitivity with a 38.4mm wide ROI (red square)

The MELP collimator has a photopeak relative sensitivity of 1.29 for a 38.4mm ROI. This result confirms expectations of higher sensitivity with MELP collimators. However, as the width of the ROI increases, the photopeak relative sensitivity of LEHR collimators increases at a faster rate than for MELP collimators. At an ROI width of ~100mm, the relative sensitivity of the LEHR collimator becomes larger than that of the MELP collimator. With an ROI width of 284mm, the LEHR collimator has a relative sensitivity of 2.17 which is greater than the MELP relative sensitivity of 1.41.

The increase in relative sensitivity is due to the inclusion of counts as a result of high-energy septal penetration. This inclusion of septal penetration distant from the source location is further demonstrated by the increase in relative sensitivity of the upper scatter window. In comparison, an increase in relative sensitivity is not demonstrated by either collimator for ^{99m}Tc (Figure 3.7).

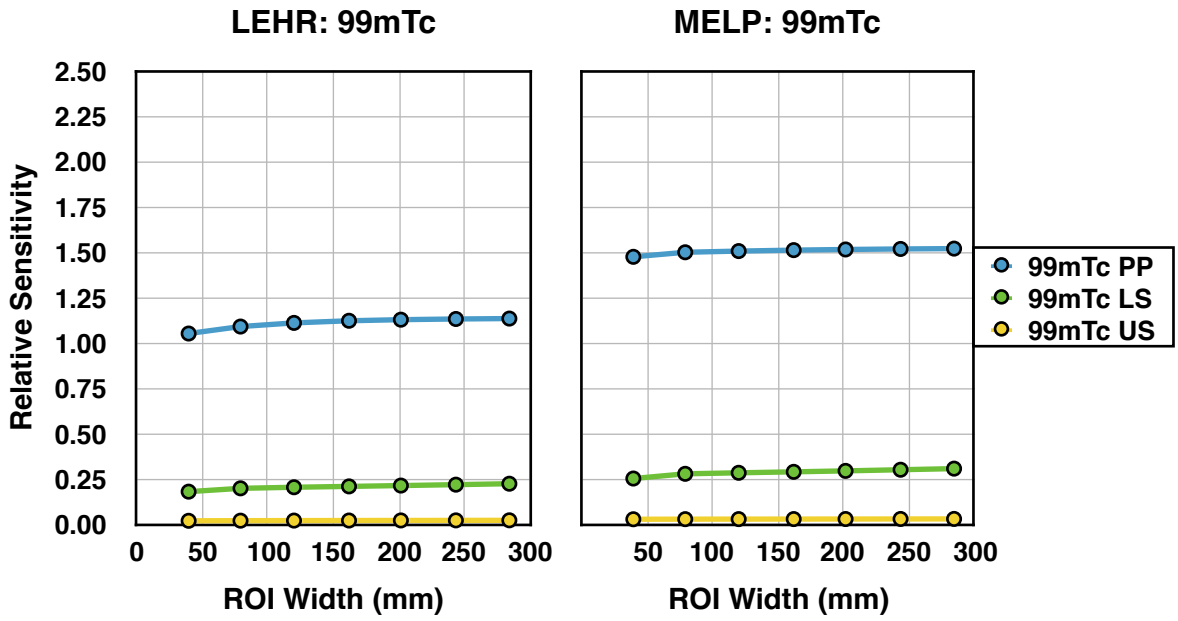

Figure 3.7: Relative sensitivity of a Siemens Symbia with increasing ROI width to ^{99m}Tc with LEHR (left) and MELP (right) collimators
Photopeak (PP), Lower Scatter (LS) and Upper Scatter (US) results are relative to ^{123}I LEHR sensitivity with a 38.4mm wide ROI (red square: Figure 3.6)

As anticipated, the MELP collimator has higher photopeak relative sensitivity for ^{99m}Tc than the LEHR collimator for all widths of ROI. The relative sensitivity of the upper scatter window is less than 0.05 for both collimators and all widths of ROI, as would be expected for a mono-energetic radionuclide.

3.5.3 Relative Sensitivity Discussion

The results of the relative sensitivity evaluations illustrate the dependence of sensitivity based on the distance of the source from the camera head. Sources close to the camera demonstrate higher detector sensitivity than those at a greater distance. This finding is due to the septal penetration of higher energy photons which contribute an increasingly smaller proportion of counts to the image with distance.

The relative sensitivity of the LEHR and MELP collimators to ^{123}I reduces more quickly with distance than published values by Small [20], who performed a similar investigation using a GE Camstar XC/T gamma camera with LEGP collimators. For example, at 20cm from the detector the relative sensitivity of the Siemens LEHR system had reduced by 25.6% while the GE LEGP system reduced by ~18%. The greater reduction in relative sensitivity with distance of the Siemens LEHR compared to the GE LEGP collimators is due to the larger hole diameter of the GE collimator, which provides greater sensitivity to true photopeak detections.

The results of this and Small's study demonstrate that the reduction in relative sensitivity with distance from a low-energy collimator is typical in ^{123}I imaging. In addition, the evaluation of relative sensitivity versus region size in this study has shown that the full FOV of the detector is more sensitive using LEHR collimators compared to MELP collimators. At the maximum region width investigated (284mm), the MELP collimator was 35.0% less sensitive than the LEHR collimator. A simulation study of Siemens collimators by Larsson [25] suggested the full FOV (larger than the ROI width used here) sensitivity of MELP collimators to ^{123}I is approximately 46% less than for LEHR.

3.5.4 Relative Sensitivity Conclusions

The sensitivity of Siemens LEHR collimators is variable with distance due to high-energy septal penetration. As such, quantitative accuracy will vary with the source to detector distance due to reliance on sensitivity measurements. Therefore, clinical studies with a fixed Radius of Rotation (ROR) where LEHR collimators are recommended, such as neurology studies, may be the most suitable candidates for accurate absolute quantification.

The sensitivity of MELP collimators is less variable with distance and is, therefore, potentially more appropriate for clinical SPECT studies with a variable source to detector distance (contoured orbits).

3.6 Count Rate Response

Count rate response describes the linearity of the gamma camera sensitivity over a range of activity in the Field of View (FOV). It is important to identify activity levels where the count rate performance of the camera begins to be adversely affected. Identifying this level is important as accurate quantification of activity concentration will similarly be affected by impaired count rate performance. For example, a patient acquisition with relatively high activity in the FOV may result in a reduction in count rate per MBq, thereby underestimating activity concentration. Consequently, quantification of an avid lesion would be underestimated.

The count rate response of the gamma camera to ^{123}I will differ from ^{99m}Tc as ^{123}I acquisitions will include more counts detected per unit of activity, due to the addition of high-energy septal penetration. This effect will be more pronounced for low-energy collimators and will vary with distance, as indicated by the Scatter Fraction (Section 3.4.2) and relative sensitivity results (Section 3.5.2). Therefore, the effect on count rate response

of the gamma camera to a range of ^{123}I activities and distance from a low-energy collimator was investigated.

3.6.1 Count Rate Response Method

A best practice method for measuring count rate response is to allow a high activity concentration source to decay in the FOV, performing multiple acquisitions throughout decay [142, 143]. As ^{123}I has a half life of 13.2h, it is impractical to carry out this setup in a busy clinical department. An alternative method is to gradually increase activity in the FOV [142, 143]. This technique was followed by acquiring images of vials containing concentrations of ^{123}I from 4MBq to 900MBq.

Data were acquired for 60s using the Siemens Symbia T2 gamma camera with LEHR collimators. Vials were imaged at distances of 0-30cm from the collimator surface in 5cm increments. Data were background corrected with an initial 60s acquisition with no sources in the FOV. A Capintec CRC-25R radionuclide calibrator was used to measure the ^{123}I activity in the vials.

The recommended method of measuring count rate involves applying a region around the object of interest only [142, 143]. However, a relatively high proportion of ^{123}I counts detected by the camera with low-energy collimators is from high-energy septal penetration, as demonstrated by relative sensitivity results in Section 3.5.2. A region encompassing only the object of interest would ignore a considerable proportion of counts detected outwith the object. Therefore, a novel approach was used by including the total number of counts detected in the planar acquisitions. The count rate in *cps/MBq* was determined using Equation 3.4.

$$CountRate = \frac{Counts}{60 x Activity(MBq)} \qquad \textbf{Equation 3.4}$$

3.6.2 Count Rate Response Results

The count rate performance of the Siemens Symbia T2 with LEHR collimators tends towards a horizontal profile as activity in the Field of View (FOV) reduces (Figure 3.8).

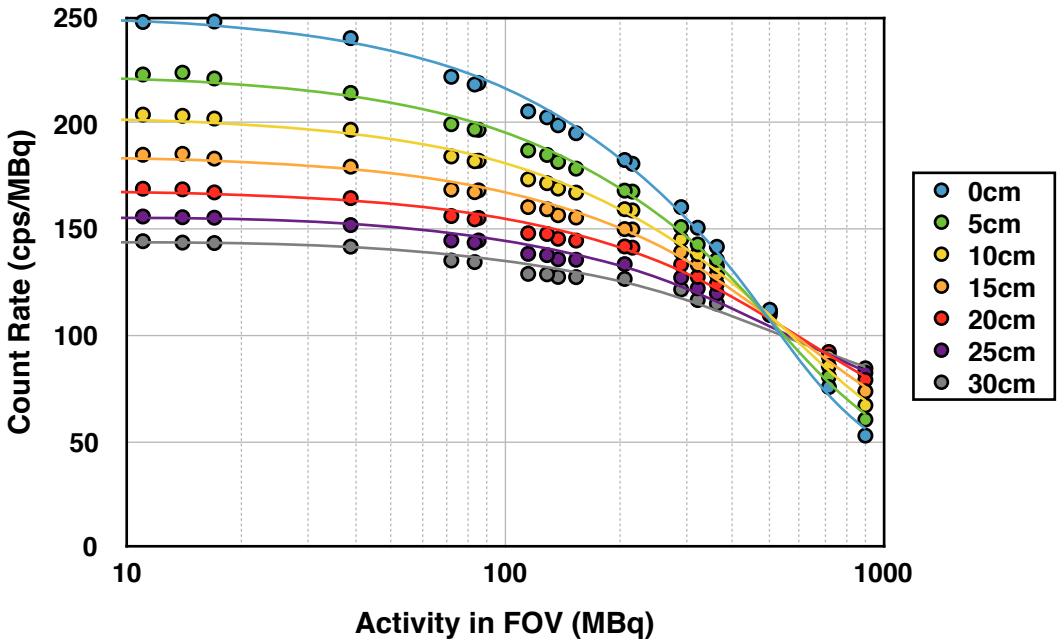

Figure 3.8: Count rate of a Siemens Symbia T2 to ^{123}I with varying source distance 2nd order polynomial trendlines are projected over data points.

The sources positioned at a larger distance from the collimator exhibit a lower count rate and the most horizontal profile for activities less than 100MBq. The sources close to the collimator have a higher proportion of counts resulting from septal penetration from high-energy emissions. Therefore, the count rate of the ^{123}I sources measured close to the collimator is higher. This finding indicates that the detector suffers greater dead-time effect from high activity sources close to the LEHR collimator.

The count rate decreases with activity greater than 100MBq at all distances from the collimator, due to detector dead-time. With approximately 500MBq in the FOV, all profiles converge. With activities larger than 500MBq the order of count rate with distance from the collimator is reversed. Sources close to the detector demonstrate a sharper roll off than sources at a distance due to a higher proportion of septal penetration in the photopeak window.

3.6.3 Count Rate Response Discussion

The varying count rate response of the Siemens Symbia to ^{123}I with distance from the LEHR collimator will degrade the precision of clinical quantification. For example, the count rate at 30cm for a low activity source is 42% less than the same source 0cm from the collimator surface. For SPECT studies involving a contoured, non-circular orbit, the distance from the source to collimator is variable throughout the study. Therefore, the sensitivity of the camera for a given projection will similarly be variable. This variability would be the case, for example, for clinical ^{123}I-mIBG SPECT studies. However, ^{123}I-

DaTSCAN™ studies have a fixed Radius of Rotation (ROR). For a fixed ROR, a constant sensitivity from a focal source can be assumed. However, this assumption may not hold for a distributed source.

Nevertheless, a local audit of 30 consecutive ^{123}I-DaTSCAN™ patient studies was performed. The data were acquired using a Siemens Symbia gamma camera with LEHR collimators and demonstrated a mean ROR of 15.3cm with a range of 13-17cm. The activity present in the FOV for an ^{123}I-DaTSCAN™ acquisition can be estimated to be ~54MBq, based on ^{123}I-DaTSCAN™ standardisation work by Tossici-Bolt and Dickson [31, 51, 125]. Count rates for activities less than or equal to 54MBq at 15cm from the collimator are relatively horizontal. This horizontal profile allows the gamma camera planar sensitivity for patient studies to be estimated as ~180cps/MBq at a distance of 15cm.

It should be noted that, in this experiment, the planar count rate was measured from a concentrated and relatively focal source of ^{123}I. In the clinical environment, a distributed source would have a horizontal count rate profile for higher activities than demonstrated in this investigation.

3.7 Planar Spatial Uniformity

Planar spatial uniformity can be considered to be the single most important performance parameter for routine quality control of a gamma camera [5, 142]. All camera corrections must be sufficiently applied to achieve acceptable uniformity. Any change in uniformity is, therefore, a very sensitive indication of a change in camera performance. Uniformity is, however, a non-specific indication of what is wrong [5].

Uniform data acquisition is essential for the production of high-quality SPECT images. Reconstruction algorithms amplify planar non-uniformities and this amplification factor can be as high as 30 towards the centre of the Field of View (FOV) [3].

Gamma camera manufacturers routinely use the same collimator uniformity correction maps applied to ^{99m}Tc studies for a range of different radionuclides. Correcting camera non-uniformity for ^{123}I with a correction map intended for ^{99m}Tc use appears a reasonable approach considering their similar photopeak (159keV and 140keV respectively). However, septal penetration of ^{123}I high-energy emissions influences acquisitions, particularly when using low-energy collimators. This high-energy contamination can degrade spatial uniformity, as previously demonstrated by Hsu [151]. Spatial uniformity could be improved by using a dedicated ^{123}I collimator correction map [152]. However, the

Siemens Symbia gamma camera does not allow the use of alternative radionuclide correction maps [153, 154]. Alternatively, TEW scatter correction is a simple method to implement which may correct the non-uniformities that result from high-energy septal penetration.

In this investigation, intrinsic uniformity of ^{99m}Tc and ^{123}I was compared. Subsequently, an investigation was carried out to determine the effectiveness of using a ^{99m}Tc collimator correction map for imaging ^{123}I. Extrinsic spatial uniformity of an ^{123}I flood phantom was evaluated for LEHR and MELP collimators. Furthermore, a ^{99m}Tc flood phantom was acquired with LEHR collimators for comparison.

3.7.1 Planar Spatial Uniformity Methods

An intrinsic calibration and collimator correction maps for LEHR and MELP collimators were acquired before the evaluation to ensure optimum uniformity during the investigation. The intrinsic calibration was performed by suspending a ~1MBq ^{99m}Tc point source from a source holder between the camera heads. The automated Siemens workflow uses the point source to tune the gains of the Photo-multiplier Tubes (PMTs) of both detectors. A 200M count intrinsic correction map was acquired. The Siemens system applies a curve correction algorithm to account for the proximity of the source to the detector [153].

The Siemens Symbia applies a collimator correction map based on a Cobalt-57 (^{57}Co) flood source acquisition. A correction map of 200M counts is acquired, and this generic collimator map is used to correct all radionuclides by scaling the acquisition to the primary photopeak energy [153, 154].

3.7.1.1 Energy Windows for Acquisition

The energy window scheme to allow TEW scatter correction was used for all ^{123}I acquisitions. A single ±10% photopeak window, centred on 140keV, was applied to the ^{99m}Tc acquisition. Table 3.4 summarises the energy windows used for acquisition.

	^{123}I	^{99m}Tc
Photopeak	159keV±10%	140keV±10%
Lower Scatter	139±4keV	—
Upper Scatter	179±4keV	—

Table 3.4: Energy window acquisition parameters for ^{123}I and ^{99m}Tc

3.7.1.2 Intrinsic Uniformity

The intrinsic uniformity of the gamma camera for ^{99m}Tc and ^{123}I was measured using 0.1ml point sources of 24.0MBq and 18.5MBq respectively. The sources were aligned with the centre of the gamma camera FOV at a distance of ~350cm from the uncollimated camera head. The detector has a diagonal dimension of 65.8cm [100]. Therefore, the source distance was equal to 5.3 times that of the diagonal, which is approximately the distance recommended by Lawson to minimise curvature effects [5]. Following the setup recommended by Lawson [5], data were acquired to 10M counts in a 64x64 matrix. The count rate of the ^{99m}Tc and ^{123}I sources was 11.4kcps and 7.0kcps respectively, which is less than the 20kcps as recommended by IPEM and NEMA [143, 144] to reduce dead time effects.

3.7.1.3 Extrinsic (System) Uniformity

System uniformity was assessed using a rectangular flood phantom, which covers the whole FOV and ensures a uniform flux of gamma photons. The flood phantom was alternately filled with ~100MBq ^{123}I and ^{99m}Tc. The ^{123}I flood phantom was acquired using LEHR and MELP collimators. The ^{99m}Tc flood phantom was acquired with LEHR collimators. The flood was positioned between both camera heads for simultaneous acquisition. The flood source was 13cm from one detector and 3cm from the other detector. These were the minimum distances achievable. Images were acquired to 100M counts into a 64x64 matrix. The count rates of the acquisitions were 17kct/s, 12kct/s, and 10kct/s for the ^{123}I LEHR, MEGP and ^{99m}Tc LEHR acquisitions respectively, which is less than the 20kct/s maximum rate suggested by NEMA [143].

3.7.1.4 Analysis of Uniformity

Intrinsic and extrinsic image data were measured using Hermes Medical Solutions automated HQUAL application, which calculates integral uniformity, differential uniformity and the uniformity index.

Integral Uniformity

Integral uniformity is a measure of how good the uniformity is over the whole FOV. Integral uniformity is defined as:

$$\text{Integral Uniformity} = \frac{C_{\max} - C_{\min}}{C_{\max} + C_{\min}} \times 100\% \qquad \textbf{Equation 3.5}$$

where C_{max} and C_{min} are the counts in the maximum and minimum pixels values respectively.

Differential Uniformity

Differential uniformity is a measure of how rapidly uniformity changes over a small distance in the worst part of the FOV. It is assessed by looking at the difference in counts between two pixels that are close together. A group of five adjacent pixels in a row is examined, and differential uniformity is determined as:

$$\text{Differential Uniformity} = \frac{C_H - C_L}{C_H + C_L} \times 100\% \qquad \textbf{Equation 3.6}$$

where C_H is the highest count in the group of five pixels and C_L is the lowest count. It is repeated for all groups of five adjacent pixels in every row of the image and then repeated for adjacent pixels in columns of the image. The largest value is the reported differential uniformity.

Uniformity Index

The uniformity index is more sensitive to global changes in the image than integral uniformity [5, 155]. The uniformity index was initially proposed by Cox [156] and is defined as:

$$\text{Uniformity Index} = COV \times \sqrt{1 - \left(\frac{SD^2}{C_{mean}}\right)^{-1}} \qquad \textbf{Equation 3.7}$$

where C_{mean} is the mean count per pixel and COV is the Coefficient of Variation expressed as the Standard Deviation as a percentage of the mean count. The uniformity index corrects the measured SD by subtracting the expected SD due to Poisson noise [5, 155].

The measurements were made on the Useful Field of View (UFOV) and the Central Field of View (CFOV), which is 75% of the UFOV.

Further to determining quantitative measures of uniformity, a ten pixel wide horizontal and vertical line profile was used for visual assessment of uniformity.

3.7.2 Planar Spatial Uniformity Results

3.7.2.1 Intrinsic Uniformity Results

The intrinsic uniformity images showed no obvious artefacts or indication of any gross non-uniformity. A key finding of the intrinsic uniformity results in Table 3.5 is that the measurements of ^{123}I and ^{99m}Tc are comparable. Therefore, with no collimator present both radionuclides, corrected with the same ^{99m}Tc intrinsic calibration, demonstrate the same intrinsic uniformity performance.

Measure	Region	^{123}I D1 (D2)	^{99m}Tc D1 (D2)
Integral Uniformity	UFOV	3.2 (5.0)	4.2 (5.1)
	CFOV	2.6 (4.4)	2.8 (3.9)
Differential Uniformity	UFOV	2.2 (2.8)	2.3 (2.9)
	CFOV	2.0 (2.8)	2.0 (2.9)
Uniformity Index	UFOV	1.0 (1.8)	1.4 (1.6)
	CFOV	0.7 (1.6)	0.9 (1.4)

Table 3.5: Siemens Symbia intrinsic uniformity of Detector 1 (D1) and Detector 2 (D2) for ^{123}I and ^{99m}Tc radionuclides

Quantitative measures of uniformity were comparable with a previously published assessment of Siemens Symbia technical specifications using ^{99m}Tc. Kappadath [149] measured integral and differential uniformity in the UFOV as 4.5% and 2.6% respectively using ^{99m}Tc.

3.7.2.2 Extrinsic Uniformity Results

Extrinsic uniformity results of the ^{123}I flood phantom, acquired with the LEHR collimators, suggest less uniform images than ^{123}I images acquired with MELP collimators or ^{99m}Tc with LEHR collimators (Table 3.6). The extrinsic uniformity results of the ^{123}I LEHR images range from being greater by a factor of 2.4 for differential uniformity (CFOV) to 4.9 for integral uniformity (UFOV) compared to the ^{123}I MELP data.

Measure	Region	^{123}I LEHR No SC D1 (D2)	^{123}I LEHR TEW D1 (D2)	^{123}I MELP D1 (D2)	^{99m}Tc LEHR D1 (D2)
Integral Uniformity	UFOV	16.3 (13.4)	7.5 (5.3)	3.4 (2.9)	2.0 (2.1)
	CFOV	8.4 (6.9)	4.7 (4.6)	2.3 (2.5)	1.4 (2.0)
Differential Uniformity	UFOV	5.9 (5.6)	3.9 (3.4)	1.3 (1.4)	1.1 (1.8)
	CFOV	3.3 (3.3)	3.2 (3.4)	1.3 (1.4)	0.9 (1.8)
Uniformity Index	UFOV	6.3 (5.4)	3.0 (2.3)	1.3 (1.1)	0.7 (0.8)
	CFOV	3.5 (2.9)	2.1 (2.3)	1.1 (0.9)	0.6 (0.8)

Table 3.6: Siemens Symbia extrinsic uniformity results of Detector 1 (D1) and Detector 2 (D2) for ^{123}I and ^{99m}Tc
Detector 1 was 13cm from the source while Detector 2 was 3cm from the source. LEHR data was assessed with and without TEW Scatter Correction (SC).

Kappadath [149] proposed action levels for Siemens Symbia systems of <5.3% and <3.2% for integral and differential uniformity respectively. The uniformity results of ^{123}I with LEHR collimators in this investigation are outside these action levels. Extrinsic uniformity is improved with the addition of TEW scatter correction of ^{123}I LEHR data. However, the results with TEW correction still demonstrate less uniform images than the ^{123}I MELP and ^{99m}Tc LEHR acquisitions. Furthermore, following scatter correction, uniformity results remain outside the action levels proposed by Kappadath.

The non-uniform nature of ^{123}I planar acquisition is shown by horizontal and vertical line profiles (Figure 3.9). The ^{123}I LEHR acquisitions exhibit an increase of counts towards the centre of the FOV compared to the edges. This appearance is in contrast with the ^{99m}Tc acquisition which demonstrates a relatively flat profile.

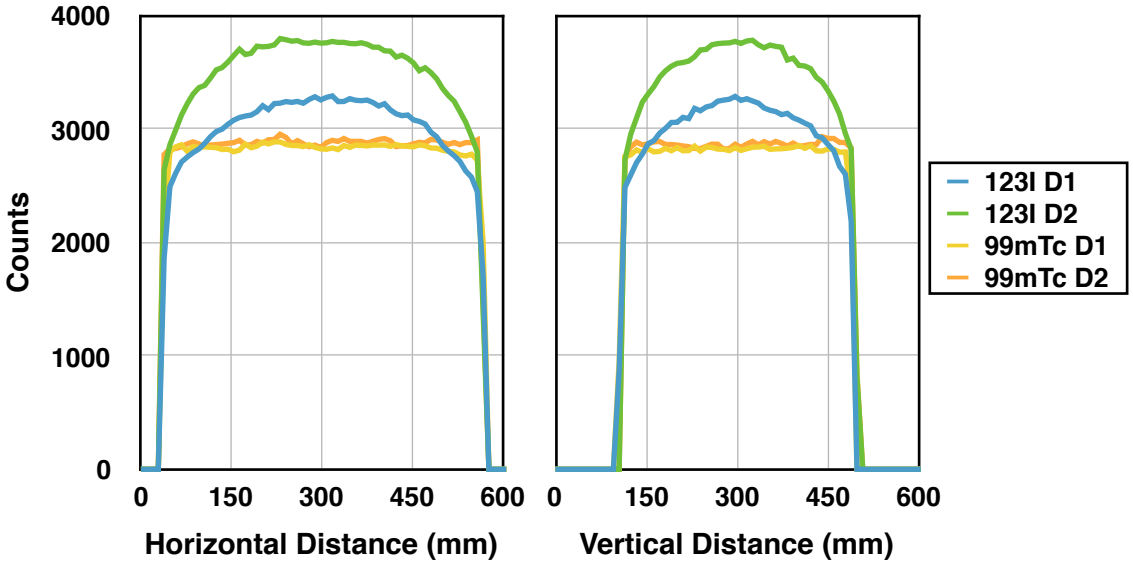

Figure 3.9: Line profiles in the x direction (left) and y direction (right) Detector 1 (D1) and Detector 2 (D2) for a uniform ^{123}I and ^{99m}Tc flood source acquired with LEHR collimators

The varying sensitivity of ^{123}I with distance from the collimator explains the difference in amplitude between the line profiles from each detector. As the collimators were not equidistant for the acquisition of the uniform flood phantom, with detector one at 13cm and detector two at 3cm, it would be anticipated that the latter would acquire a greater number of counts in the same time. In the case of ^{99m}Tc, sensitivity is relatively consistent with distance from the collimator [3, 5].

Visual inspection of the planar images demonstrates the severity of non-uniformity of ^{123}I acquired with LEHR collimators (Figure 3.10). The images confirm the pattern of non-uniformity that was suggested by the line profiles.

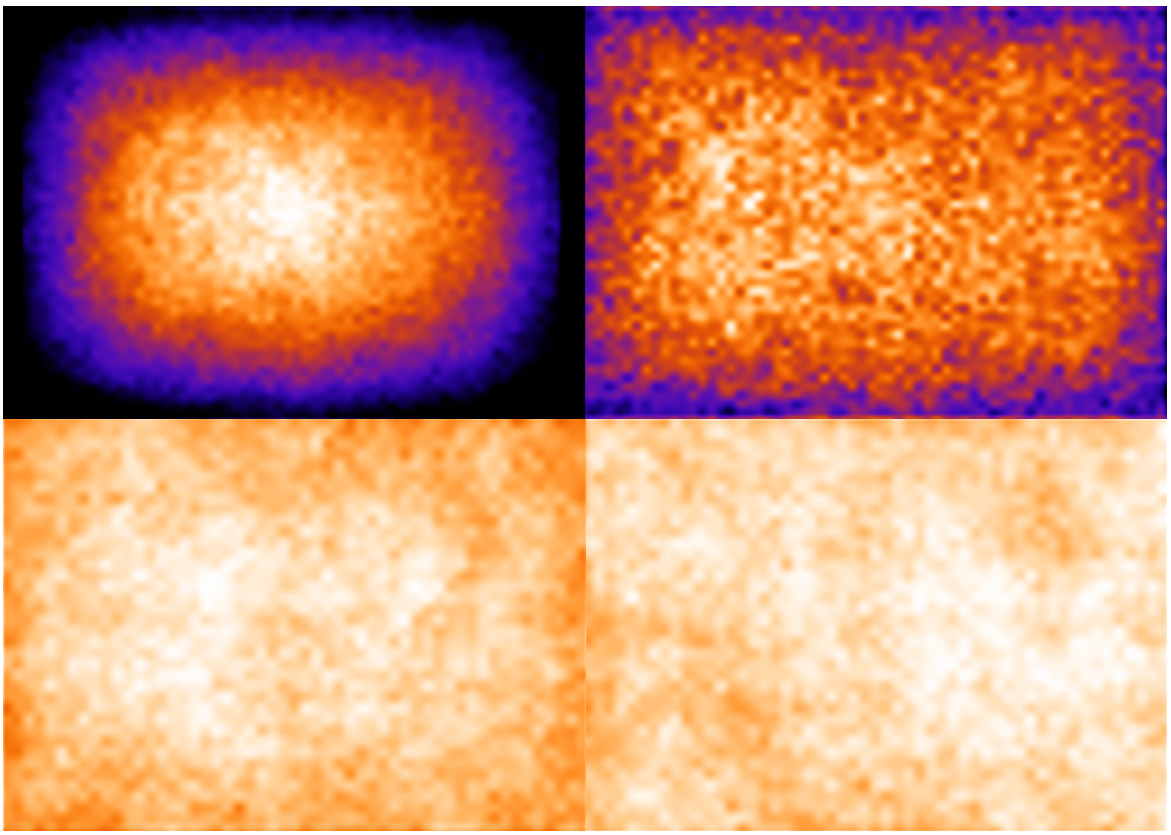

Figure 3.10: Planar acquisitions of the flood source ^{123}I with LEHR collimators (top left), ^{123}I with LEHR collimators and TEW correction (top right), ^{123}I with MEGP collimators (bottom left) and ^{99m}Tc with LEHR collimators (bottom right)

The ^{123}I LEHR image including TEW scatter correction is more uniform than the uncorrected image. However, a difference in appearance remains between the TEW scatter correction, and the ^{123}I MELP and ^{99m}Tc LEHR acquisitions. This difference is in part due to inaccuracies in the TEW corrected image towards the edges of the FOV and also due to the greater noise per pixel. The TEW image has had 50.7% of counts removed as a result of the correction process. This subtraction introduces greater variability per pixel. Consequently, the uniformity index of the TEW corrected image is more than double that of the ^{123}I MELP and ^{99m}Tc LEHR acquisitions.

3.7.3 Planar Spatial Uniformity Discussion & Conclusions

Quantitative measures and visual inspection demonstrate that uncorrected ^{123}I data acquired with LEHR collimators are grossly non-uniform. An ^{123}I specific collimator correction map would not optimise clinical uniformity as the correction applied would be highly dependent on the phantom dimensions and distance from the collimator. Therefore, applying a collimator correction map with an ^{123}I flood source would not be appropriate for correcting an object other than the flood source itself.

This investigation showed that TEW correction of the acquired ^{123}I flood with LEHR collimators improved uniformity. However, uniformity measures of the resultant images remained at least double the ^{123}I MELP and ^{99m}Tc LEHR acquisitions. This finding is due to an imperfect correction, particularly towards the edges of the FOV, and also due to the subtraction of a significant proportion of counts from the photopeak and, therefore, greater variability per pixel.

3.8 Planar Characterisation Conclusions

Spatial resolution measurements provide confidence that the system performs as reported in the literature. Similarly, the spatial uniformity of ^{123}I acquired with MELP collimators and ^{99m}Tc acquired with LEHR collimators are in agreement with published figures for a Siemens Symbia system.

Evaluation of the scatter fraction, sensitivity, count rate response and spatial uniformity of planar ^{123}I has demonstrated a dependence on distance from the detector. This dependence is particularly evident for low-energy collimators and, therefore, is confirmation that the cause is high-energy septal penetration. Consequently, subsequent investigations in this thesis will compare ^{123}I SPECT data acquired with both LEHR and MELP collimators. Reconstruction methods investigated will include a Monte Carlo scatter correction algorithm for LEHR acquisitions, which incorporates simulation of high-energy photons in the collimator and detector system, in the hope that this novel correction will mitigate the poor response of the planar measurements.

Chapter 4: SPECT Spatial Uniformity

Chapter 3 demonstrated the relatively poor planar spatial uniformity of ^{123}I acquisitions using Siemens LEHR collimators compared with medium-energy collimator acquisitions. Therefore, one of the aims of this Chapter is to evaluate the performance of SPECT spatial uniformity for both Siemens LEHR and MELP collimators. This assessment will include advanced SPECT reconstruction correction schemes to review their effect on ^{123}I uniformity for the first time.

4.1 Introduction

A localised region of non-uniformity in planar acquisitions, as a result of planar sensitivity variations, will appear at the same place in all angles of projection data. The amplitude of this artefact is significantly amplified in SPECT images and will manifest in reconstructed images in the shape of a ring [5]. An example of this, based on the acquisition of a uniform cylinder, is shown in Figure 4.1.

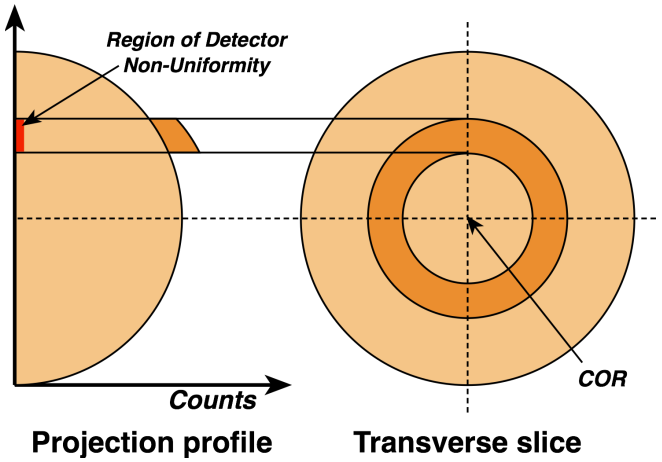

Figure 4.1: Example of a localised spatial non-uniformity in projection data (left) This non-uniformity appears at the same location in all projections, which results in a ring appearance in reconstructed transverse images (right) [5] which surrounds the Centre of Rotation (COR).

If planar uniformity is acceptable, then it follows that SPECT uniformity will be sufficient, assuming uniformity with acquisition angle is consistent, and the reconstruction algorithm is operating correctly. Therefore, evaluation of SPECT uniformity is performed relatively infrequently with a visual inspection of transverse slices to detect ring artefacts or any gross errors [5, 12, 144]. Consequently, quantitative assessment of SPECT uniformity is not considered essential for routine quality control of a gamma camera [142, 143] and, in any case, such an assessment does not evaluate the uniformity of the whole detector Field of View (FOV), only the area in which a phantom is positioned.

With regard to ^{123}I SPECT acquired with low-energy collimators, rather than localised detector non-uniformities from variations in planar sensitivity, a pattern of gross non-uniformity in planar projections is known (see Section 3.7.2). An investigation of low-energy collimators for ^{123}I SPECT by Macey [16] demonstrated that these planar non-uniformities lead to significant artefacts in transverse images. An example of the propagation of ^{123}I planar non-uniformity to transverse images is shown in Figure 4.2.

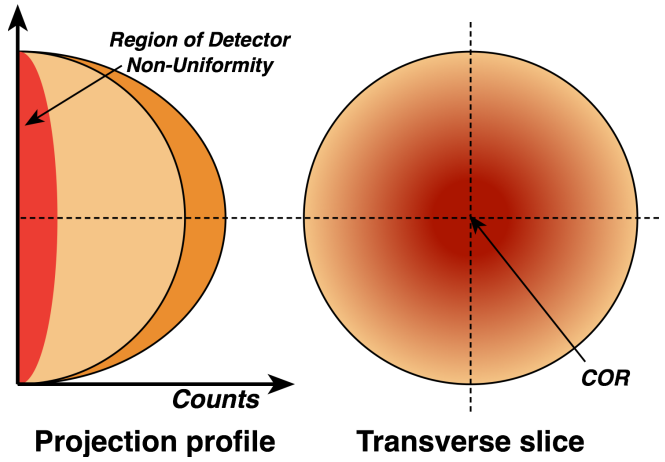

Figure 4.2: Example of global non-uniformity that affects all projection data (left) In this example, all projections will have a consistently increased count value in the centre, which would cause an overestimation of counts towards the Centre of Rotation (COR) of the transverse image (right).

As a gross non-uniformity has been demonstrated for planar acquisition of ^{123}I, it is important to evaluate the impact on SPECT uniformity. It is also useful to assess whether novel reconstruction correction techniques can be used to reduce the detrimental effect on images of this planar non-uniformity. Therefore, in this Chapter, the assessment of the spatial uniformity of a cylindrical phantom has been used to evaluate the accuracy of attenuation and scatter correction for ^{123}I SPECT. The assessment is of particular importance with regard to quantification.

Relative quantification of ^{123}I-DaTSCAN™ images has become routine in the clinical setting, in part due to widespread access to a European normal database [29]. Patient data acquired without correction for non-uniformity may overestimate or underestimate the Specific Binding Ratios (SBRs), potentially affecting their comparison with the normal database.

The Society of Nuclear Medicine (SNM) [49] recommend acquisition of data using low-energy collimators with an ^{123}I extrinsic uniformity calibration for DaT SPECT. The SNM describes this correction as being a more rigorous approach than ^{57}Co or ^{99m}Tc flood sources [49]. Unfortunately, on a Siemens Symbia gamma camera, a radionuclide-specific uniformity map is not supported [153, 154]. For the Siemens Symbia, all extrinsic uniformity corrections are scaled from a ^{57}Co or ^{99m}Tc flood source acquisition. The user must accept that planar ^{123}I acquisitions with low-energy collimators contain gross non-uniformities. In this instance, to prevent amplification of artefacts in SPECT data, a reconstruction correction scheme for these known artefacts should be employed.

The Triple Energy Window (TEW) technique is a method of scatter correction which may reduce non-uniformities in ^{123}I SPECT images. The planar evaluation demonstrated that, although TEW scatter correction improves uniformity, it is applied at the expense of noise. Increased noise in raw SPECT projections results in further amplification of noise by an iterative reconstruction algorithm. Therefore, TEW correction may not be the most appropriate method for correction of ^{123}I SPECT with low-energy collimators.

Alternative methods for scatter correction include Monte Carlo modelling. Of these, the Object Only Scatter Correction (OOSC) algorithm corrects for photons in the object of interest within the FOV. The Collimator and Detector Response Modelling (CDRM) algorithm additionally simulates high-energy scatter and septal penetration of the low-energy collimator. The following work was undertaken to evaluate which scatter correction technique is the optimum method for reducing non-uniformities in ^{123}I SPECT.

Siemens low-energy collimators are considered more susceptible to septal penetration than other vendors due to shorter hole length and thinner septa [54, 55]. Medium-energy collimators are less susceptible to high-energy septal penetration and were shown in Section 3.7.2 to have superior planar uniformity to LEHR collimators. Therefore, the uniformity of ^{123}I SPECT for both Siemens LEHR and MELP collimators will be assessed. Additionally, ^{123}I SPECT uniformity was assessed for data acquired with Philips VXHR

collimators, a low-energy collimator which features longer bores to reduce septal penetration.

An aim of the investigation was to recommend a best practice approach to acquire and reconstruct ^{123}I data for a Siemens Symbia system which minimises SPECT spatial non-uniformities. This aim will be addressed by intermediate aims which will assess:

- the impact of poor planar uniformity on ^{123}I SPECT imaging
- the effect of novel reconstruction correction schemes on SPECT uniformity
- the suitability of collimators to reduce septal penetration, as indicated by SPECT spatial uniformity

4.2 Methods and Materials

SPECT uniformity was assessed using a cylindrical phantom. The cylindrical phantom (diameter of 20.9cm and height of 18.2cm) was filled with ~74MBq of ^{123}I. The activity was chosen to ensure the count rate during acquisition was below 20kcts/s, as recommended by Lawson [5] to reduce dead time effects.

4.2.1 Acquisition of the Cylindrical Phantom

The cylindrical phantom was acquired using a Siemens Symbia T2 with LEHR and MELP collimators. The count rates were 5.6kcts/s and 4.0kcts/s respectively, which were sufficiently below the 20kcts/s count rate to reduce dead time effects. The phantom was also acquired using a Philips Forte gamma camera with VXHR collimators, with a count rate of 3.3kcts/s. Collimator dimensions are described in Table 4.1.

	Length (mm)	Diameter (mm)	Septal Thickness (mm)
Siemens LEHR	24.1	1.11	0.16
Siemens MELP	32.8	2.07	0.66
Philips VXHR	54.0	2.03	0.15

Table 4.1: Dimensions for Siemens LEHR, MELP and Philips VXHR collimators

An acquisition matrix with a 1.45 zoom was used, resulting in a pixel size of 3.3mm and 3.2mm for the Symbia and Forte acquisitions respectively. This zoom was chosen to match clinical ^{123}I-DaTSCAN™ studies. Projections were acquired using a 15cm Radius of Rotation (ROR) and three energy windows for the TEW scatter correction technique, as previously described in Section 3.3.1.2.

A relatively long 6-hour acquisition was used to evaluate spatial uniformity with low noise. The extended acquisition resulted in a data set containing 221M, 172M and 134M counts in the photopeak window of the LEHR, MELP and VXHR acquisitions respectively.

A CT was acquired using the Siemens Symbia which was used for attenuation correction and Monte Carlo simulation of photons for the OOSC and CDRM scatter correction algorithms. The CT data was, therefore, spatially registered to the LEHR and MELP SPECT acquisitions. However, as the Philips system does not feature a sequential CT scanner, the same CT data was applied to the Philips VXHR acquisition using manual rigid translational registration.

Parameter	Value
Matrix	128x128
Zoom	1.45
Pixel Size	3.3mm
Projections	128
Time per Projection	6min
Radius of Rotation	15cm
Orbit	Circular
Photopeak	159keV±10%
Scatter Windows	Lower: 138±4keV Upper: 178±4keV
CT mA	35mA
CT kVp	130kVp
CT Reconstruction Slice Width	3.3mm

Table 4.2: SPECT-CT acquisition parameters of the uniform cylindrical phantom

4.2.2 Reconstruction of the Cylindrical Phantom

This section will introduce SPECT reconstruction parameters. The parameters detailed for the Resolution Recovery (RR) and scatter correction algorithms in this Section will be used as standard throughout this thesis.

This Section also describes the correction schemes which will be evaluated extensively throughout this thesis and detail the parameters for their use.

The advanced OOSC and novel CDRM scatter correction algorithms were investigated for ^{123}I SPECT reconstruction. Additionally, data were reconstructed with the TEW technique, which is a commonly used method for ^{123}I scatter correction.

The correction schemes investigated were chosen based on recommendations in the literature and on combinations of corrections that are allowed by the reconstruction software. For example, as described in Chapter 2, CT attenuation correction should not be used without scatter correction. Additionally, OOSC and CDRM cannot be applied without a map of attenuation coefficients. Furthermore, the CDRM algorithm cannot be employed without RR. Consequently, the reconstruction correction schemes described in Table 4.2 were applied to all LEHR acquisitions:

Correction Scheme Name	Resolution Recovery	Attenuation Correction	Scatter Correction
NC(L)	No Corrections (NC)		
RR(L)	✔	—	—
OOSC(L)	✔	CT	OOSC
TEW(L)	✔	CT	TEW
CDRM(L)	✔	CT	CDRM

Table 4.3: Reconstruction correction schemes applied to data acquired with low-energy collimators
The reconstruction of data acquired with low-energy collimators is indicated with (L).

The Philips VXHR data was not reconstructed with CDRM as the collimator model was not available from the software developer.

An aim of TEW and CDRM scatter correction methods is to correct the septal penetration of low-energy collimators from high-energy emissions. The MELP collimator is less susceptible to these emissions relative to the LEHR collimator, as demonstrated by planar measurements in Chapter 3. Therefore, the MELP collimator acquisitions were not reconstructed with TEW or CDRM, on the presumption that these corrections would only provide a relatively small improvement. Consequently, the reconstruction correction schemes described in Table 4.4 were applied to the MELP acquisition.

Correction Scheme Name	Resolution Recovery	Attenuation Correction	Scatter Correction
NC(M)	No Corrections (NC)		
RR(M)	✔	—	—
OOSC(M)	✔	CT	OOSC

Table 4.4: Reconstruction correction schemes applied to data acquired with medium-energy collimators
The reconstruction of data acquired with medium-energy collimators are indicated with (M)

The collimator dimensions for distance-dependent RR modelling were taken from Siemens and Philips technical specifications (Table 4.4). A Radius of Rotation Offset (RORO) parameter adjusts the detector distance for the additional distance from the collimator surface to the crystal surface. For Siemens system, this is equivalent to the hole length plus an additional 0.7cm [157].

Parameter	LEHR	MELP	VXHR
Hole Diameter (cm)	0.111	0.294	0.203
Hole Length (cm)	2.41	4.06	5.40
Radius of Rotation Offset (cm)	3.11	4.76	5.40
Detector Resolution @ 140keV (cm)	0.38		0.34
Energy Resolution @ 140keV (%)	9.9		10.0

Table 4.5: Siemens and Philips collimator and gamma camera specifications used for reconstruction parameters [100]

Similarly, the parameters for Monte Carlo scatter correction are taken from Siemens technical specifications [100] and recommendations from the reconstruction algorithm software developer [158-160] (Table 4.5).

Parameter	Value
Energy resolution at 140keV (%)	9.9
Simulated photons	100k
Update iterations	2
Downscatter photons	100k

Table 4.6: Monte Carlo scatter correction reconstruction parameters
The energy resolution is taken from manufacturer's technical specifications [100]. Simulated photons, update iterations and downscatter photons are taken from recommendations of the software developer [158-160]

All SPECT data were reconstructed without post-filtering.

In this investigation of SPECT spatial uniformity, all acquisitions of the cylindrical phantom were reconstructed with 96 OSEM iterations (6 iterations, 16 subsets) based on recommendations by Dickson [30] for convergence of ^{123}I SPECT relative quantification.

4.2.3 Analysis of SPECT Uniformity

As stated earlier, SPECT spatial uniformity is not assessed quantitively as part of routine quality control checks as it is assumed SPECT uniformity will be adequate as long as planar uniformity is acceptable. Therefore, an established protocol for measuring SPECT uniformity does not exist and variable methods are used in the literature. In this study, two methods were used: the Coefficient of Variation (COV) and line profile analysis.

4.2.3.1 Coefficient of Variation

The Coefficient of Variation (COV) is commonly used to assess image uniformity [12, 71, 161-163]. The COV is the standard deviation divided by the mean counts in a region, expressed as a percentage. In this investigation, COV was measured by placing a large cylindrical Volume of Interest (VOI) in the centre of the cylindrical phantom. The VOI was 15cm in diameter and ten transverse slices in length (3.3cm) resulting in a total volume of 583ml.

4.2.3.2 Line Profiles and the Residual Sum of Squares

Line profile analysis allows a visual assessment of uniformity and is recommended by Graham [12] for quantification of SPECT performance. In this investigation, line profiles were generated by the summation of a 12-pixel wide profile across twelve transverse reconstructed slices, giving a profile width and depth of ~40mm, in accordance with the methodology of Graham [12].

Additionally, a Figure of Merit (FOM) was determined from the line profiles for error quantification. The Residual Sum of Squares (RSS) determines the error of a measurement compared to a known model [164]. This approach has previously been used by Li [165] to quantify the error in image reconstruction. In this investigation, the model used for error quantification was the known boundary of the phantom, which contained uniform activity. The pixels within the boundary of the phantom were determined using the spatially registered CT data. The line profiles were normalised to the mean amplitude within this boundary. The RSS error was calculated using Equation 4.1 [164].

$$RSS = \sum_{i=1}^{n} (NC_i - PNC_i)^2 \qquad \textbf{Equation 4.1}$$

where NC_i is the i^{th} value of measured Normalised Counts and PNC_i is the i^{th} value of Predicted Normalised Counts which, for the uniform model, is equal to 1.

4.3 Spatial Uniformity Results

4.3.1 Coefficient of Variation Results

Lower COV indicates less variation in pixel values, which reflects better uniformity. Considering the Siemens Symbia LEHR data, COV varied from 6.6-18.7%, with RR(L) producing the best and TEW(L) producing the worst uniformity, as shown in Figure 4.3.

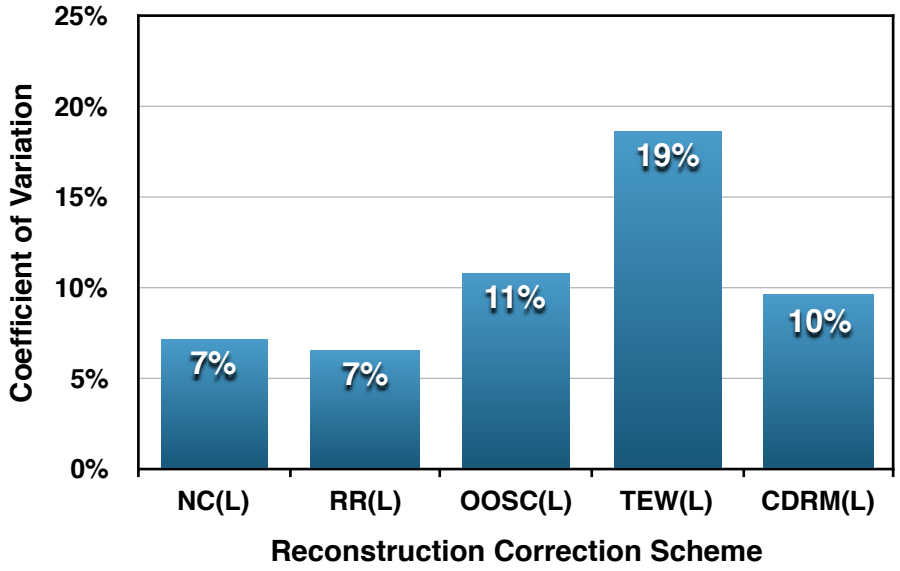

Figure 4.3: Coefficient of Variation (COV) for reconstruction of Siemens LEHR data Data were reconstructed with the No Corrections (NC), Resolution Recovery (RR), Object Only Scatter Correction (OOSC), Triple Energy Window (TEW) and Collimator and Detector Response Modelling (CDRM) correction schemes.

It is unsurprising that the RR(L) reconstruction has a lower COV (6.6%) than the NC(L) reconstruction (7.2%) due the inherent “smoothing” that RR introduces [25, 30]. However, the relatively small difference in COV between these correction schemes may be within measurement error, which is unknown as these results were generated from a single high count acquisition.

Of note, the COV of the RR(L) reconstructions is less than that for the reconstructions which also include attenuation and scatter correction. These additional corrections should improve uniformity by compensating for absorbed photons at depth. Of those schemes

which include attenuation and scatter correction, the CDRM images had the lowest COV (9.6%).

The TEW(L) reconstruction demonstrates the highest COV of the LEHR data (18.7%). This result is unsurprising as the TEW method subtracts a significant proportion of counts from the planar projections before reconstruction. Therefore, the TEW data has considerably higher variation between pixels than reconstructions with Monte Carlo scatter correction applied (OOSC(L) and CDRM(L)).

In comparison, the Siemens MELP reconstructions varied in COV form 6.0-17.9% and the Philips VXHR varied from 10.1-25.6% (Figure 4.4).

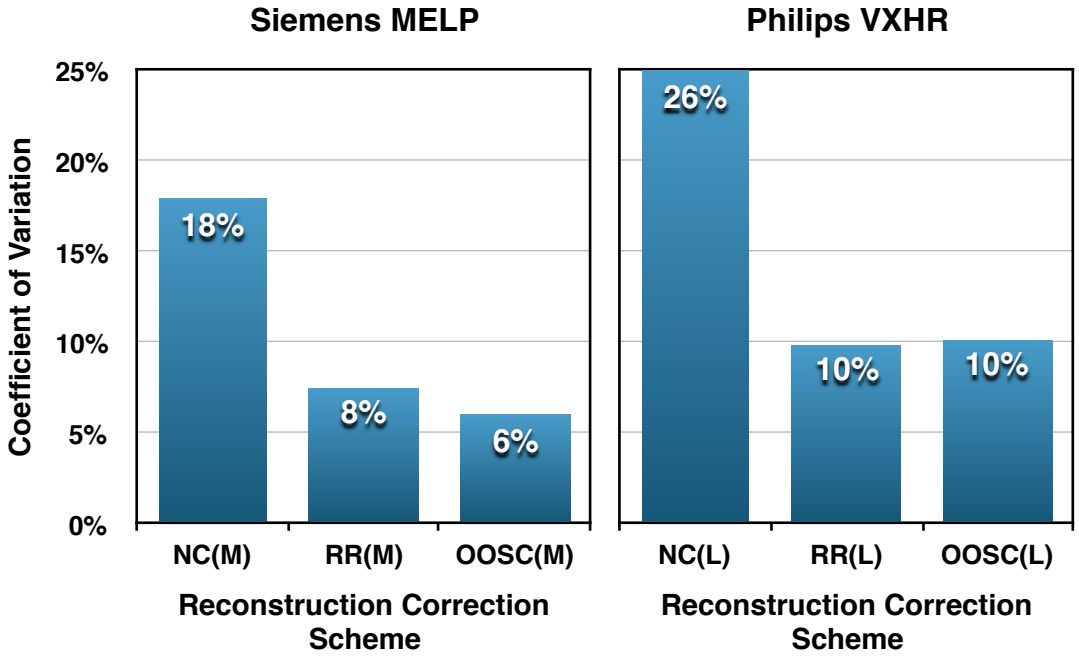

Figure 4.4: Coefficient of Variation (COV) for reconstruction of Siemens MELP and Philips VXHR

Data were reconstructed with the No Corrections (NC), Resolution Recovery (RR) and Object Only Scatter Correction (OOSC) correction schemes. MELP and VXHR data were not reconstructed with TEW and CDRM.

The OOSC(M) data had the lowest COV (6.0%) of all the methods investigated. This finding suggests that SPECT spatial uniformity is optimised with a hardware approach to reducing septal penetration, combined with the OOSC correction scheme.

In contrast with the Siemens LEHR data, the addition of attenuation and scatter correction to MELP data reduced the COV from 7.5% to 6.0%.

The Philips VXHR collimator has a marginally lower COV than the equivalent Siemens LEHR reconstruction when OOSC is applied (10.1% versus 10.9%). This difference would

suggest acquisitions using the longer hole length of the VXHR collimators results in a smaller proportion of high-energy septal penetration than the LEHR collimators. However, as stated previously, the measurement error is unknown as these results were generated from a single high count acquisition. Therefore, the relatively small difference indicates that both low-energy collimator options are impaired by high-energy septal penetration.

4.3.2 Line Profiles and the Residual Sum of Squares Results

4.3.2.1 Line Profiles and the Residual Sum of Squares for the Siemens Symbia LEHR Collimators

To describe the effect that additional corrections have on spatial uniformity, the structure of this Section will be to compare line profiles with supplementary corrections. Therefore, the order of this Section will be to present line profiles of Siemens LEHR data reconstructed:

- with and without Resolution recovery (RR)
- with and without attenuation and scatter correction
- with attenuation correction and scatter correction for high-energy septal penetration

Quantitative comparison of the line profiles will be made using the Residual Sum of Squares (RSS) error.

The line profiles for data acquired with LEHR collimators and reconstructed with and without RR demonstrated a relatively flat profile (Figure 4.5).

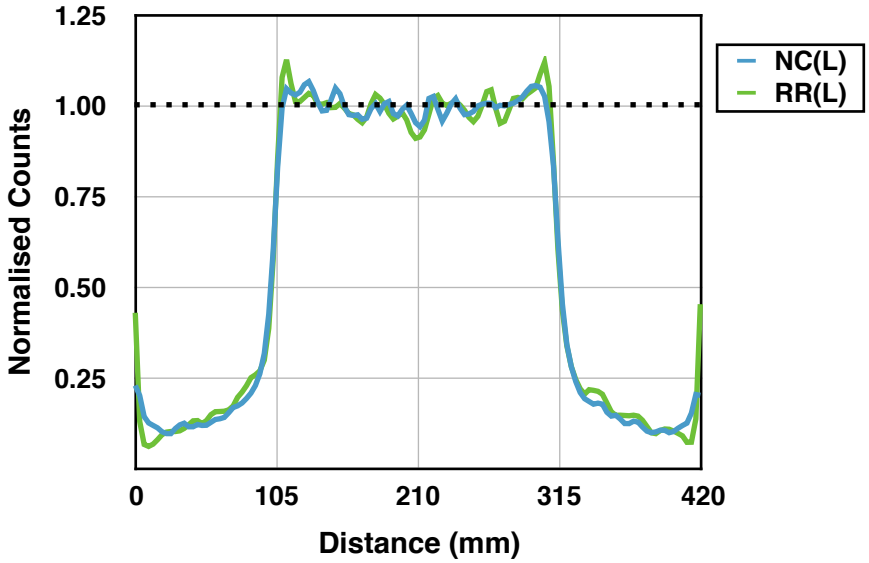

Figure 4.5: Line profiles of Siemens LEHR data reconstructed with and without Resolution Recovery

The reconstruction correction scheme with No Corrections (NC(L)) and with depth-dependent Resolution Recovery (RR(L)) applied is shown. Line profiles are normalised to the mean count value within the phantom boundary

Both NC(L) and RR(L) profiles are flatter in appearance than would be expected without correction for attenuation. Photons from the centre of the phantom have a lower probability of being detected by the camera as there is a higher probability of absorption. Therefore, it was anticipated that there would be fewer counts detected centrally when attenuation correction is not applied. However, the anticipated concave line profile was not observed and, therefore, this appearance was investigated further.

The flat appearance can be explained by the presence of high-energy emissions from ^{123}I. With increasing depth in water, the theoretical proportion of high-energy emissions relative to low-energy emissions increases (Figure 4.6). These high-energy emissions can be detected in the low-energy photopeak following scatter in the collimator and, in this example, flattens the profile across the phantom. This explanation would also support the relatively low COV measurement for LEHR data reconstructed with No Corrections (NC) and with RR applied (Figure 4.3).

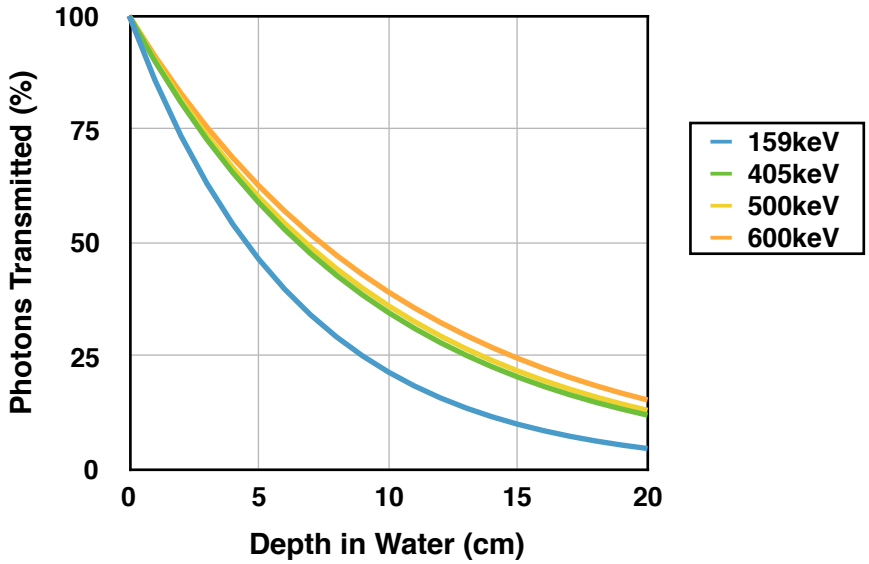

Figure 4.6: Theoretical graph of photons transmitted with thickness in tissue equivalent material [166]
The graph demonstrates that higher energy photons have a greater probability of being transmitted from depth in tissue equivalent material compared with low-energy photons. For example, at 10cm depth the proportion of 600keV photons transmitted is double that of 159keV photons

The circumstances leading to the relatively flat profile shown in Figure 4.5 are specific to the size of the object being imaged and to the particular acquisition. Planar investigations in Chapter 3 demonstrated ^{123}I sensitivity is dependent on the distance from the detector. Using a larger Radius Of Rotation (ROR) during acquisition in this investigation would reduce the proportion of high-energy emissions detected in the photopeak. Similarly, a collimator with thicker septa and longer bores would prevent a greater proportion of septal penetration and, thus, result in the anticipated concave profile.

A reconstruction of the upper scatter window (Figure 4.7), although noisy, is indicative of the distribution of high-energy photons in the photopeak window. The line profile demonstrates the greater proportion of counts detected in the centre of the phantom compared with the extremities, resulting in the compensation of absorbed low-energy photons.

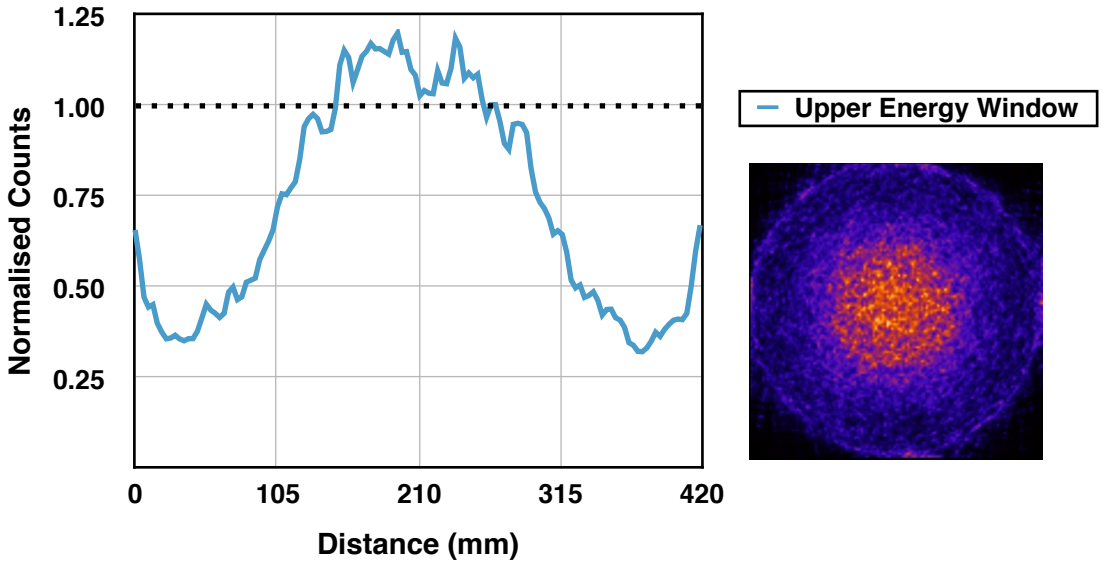

Figure 4.7: Line profile and transverse slice of a reconstruction of the upper energy window with No Corrections (NC(L)) applied
Line profiles are normalised to the mean count value within the phantom boundary

Figure 4.8 compares the line profile of Siemens LEHR reconstructions with and without attenuation and scatter correction (OOSC(L) and RR(L) respectively).

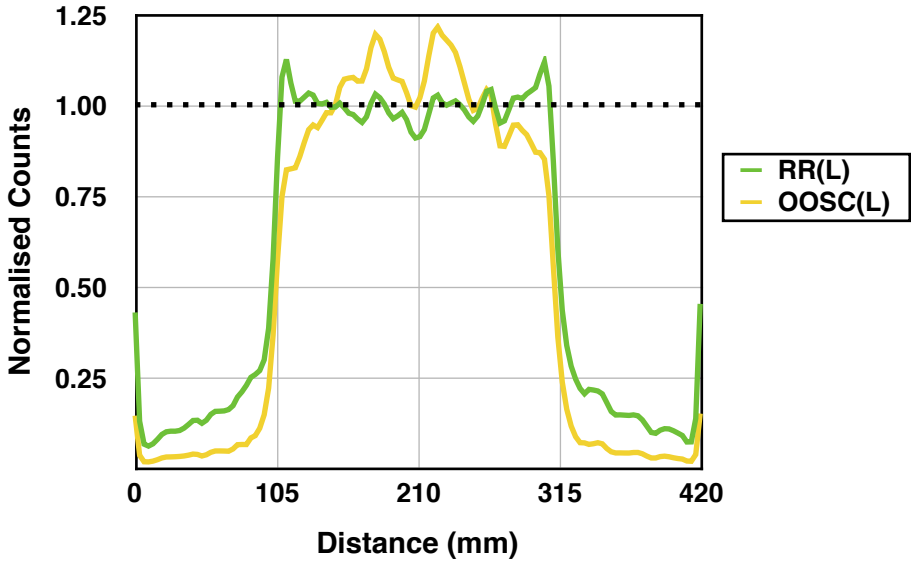

Figure 4.8: Line profiles of Siemens LEHR data reconstructed with and without attenuation and scatter correction
The reconstruction correction scheme with depth-dependent Resolution Recovery (RR(L)) and with Object Only Scatter Correction (OOSC(L)) applied is shown. Line profiles are normalised to the mean count value within the phantom boundary.

The OOSC(L) correction scheme transforms the relatively flat uncorrected profile into a convex profile. The process of attenuation correction amplifies counts in the centre of the phantom relative to the edges. In this example, the resulting profile overestimates the counts in the centre. Overestimation of photons in the centre of the phantom will result in inaccurate and non-uniform quantification across the object of interest.

The line profiles for Siemens LEHR data reconstructed with correction for high-energy septal penetration (TEW(L) and CDRM(L)) are shown in Figure 4.9.

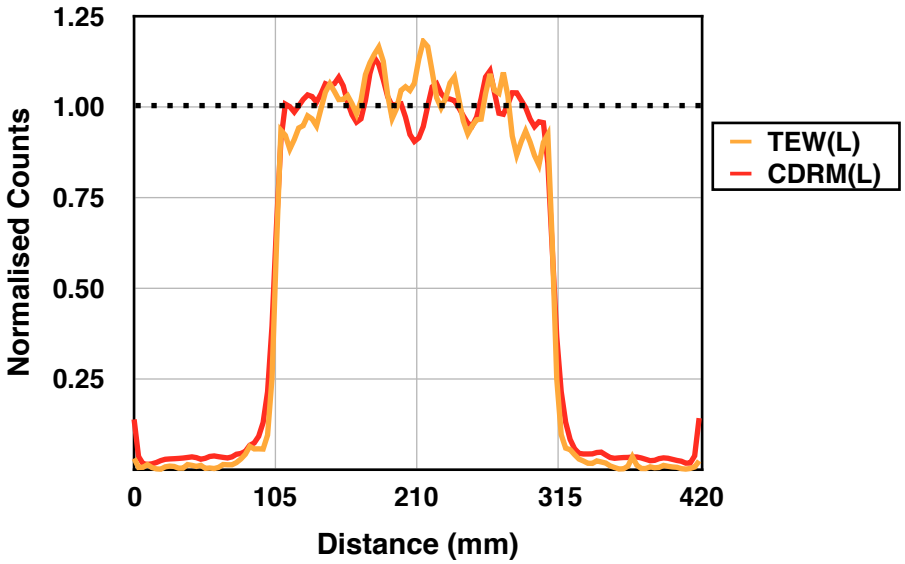

Figure 4.9: Line profiles of Siemens LEHR data reconstructed with correction for high-energy photons
The reconstruction correction scheme with Triple Energy Window (TEW(L)) and Collimator and Detector Response Modelling (CDRM(L)) applied is shown. Line profiles are normalised to the mean count value within the phantom boundary

The TEW(L) and CDRM(L) correction schemes visibly improve uniformity over the OOSC(L) method, particularly towards the edges of the phantom volume. The CDRM(L) reconstruction appears to most accurately represent the uniform phantom.

Visual assessment of the line profiles suggest that the NC(L) and RR(L) reconstructions have sufficient spatial uniformity, which is due to the coincidental compensation of absorbed low-energy photons by high-energy emissions. However, it should be noted that these reconstruction schemes, which do not include attenuation and scatter correction, are quantitatively inaccurate. For example, Figure 4.10 shows that, although the line profile for the NC(L) reconstruction appears uniform, it has considerably less counts than the CDRM(L) correction scheme. Figure 4.10 further demonstrates the overestimation of counts in the centre of the phantom using the OOSC(L) correction scheme.

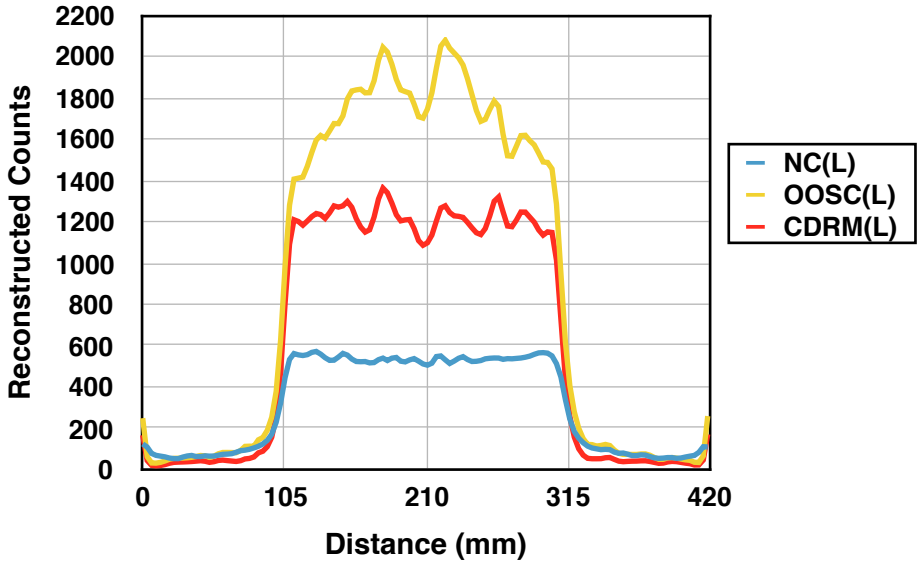

Figure 4.10: Line profiles of Siemens LEHR data which compares the absolute reconstructed counts for the NC(L), OOSC(L) and CDRM(L) correction schemes
Line profiles for reconstructions with No Corrections (NC(L)), Object Only Scatter Correction (OOSC(L)) and Collimator and Detector Response Modelling (CDRM(L)) are shown.

The findings from the qualitative assessment of the line profiles are mirrored by quantification of inaccuracy compared to the model profile, as indicated by the normalised RSS error (Figure 4.11).

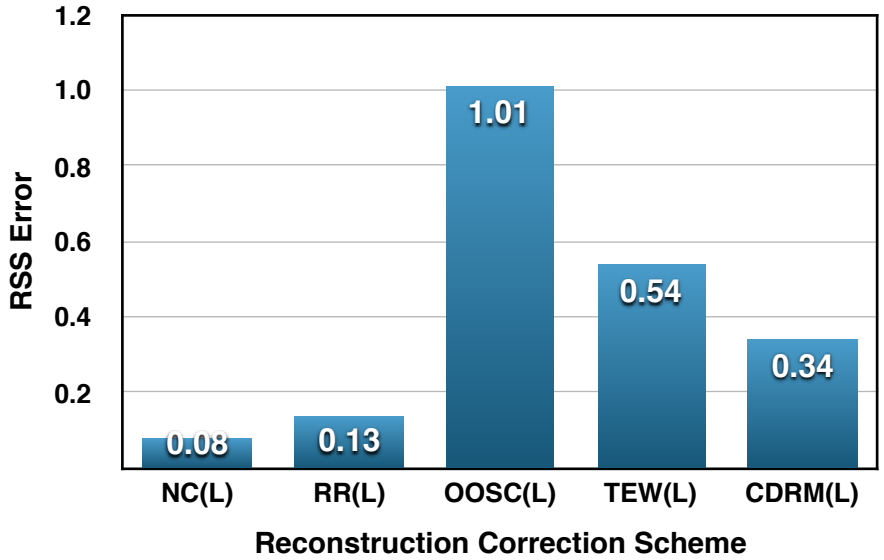

Figure 4.11: The Residual Sum of Squares (RSS) error for reconstructions of Siemens LEHR data

The NC(L) and RR(L) reconstructions, which have no attenuation or scatter correction, have the lowest RSS error. However, this is an artefactual result based on high-energy septal penetration which has compensated for low-energy photon absorption. The CDRM(L) correction scheme has the lowest RSS error of the three reconstruction

correction schemes which include attenuation and scatter correction (OOSC, TEW and CDRM).

Visual inspection of transverse slices (Figure 4.12) confirms the findings of the qualitative assessment and quantitative measurements.

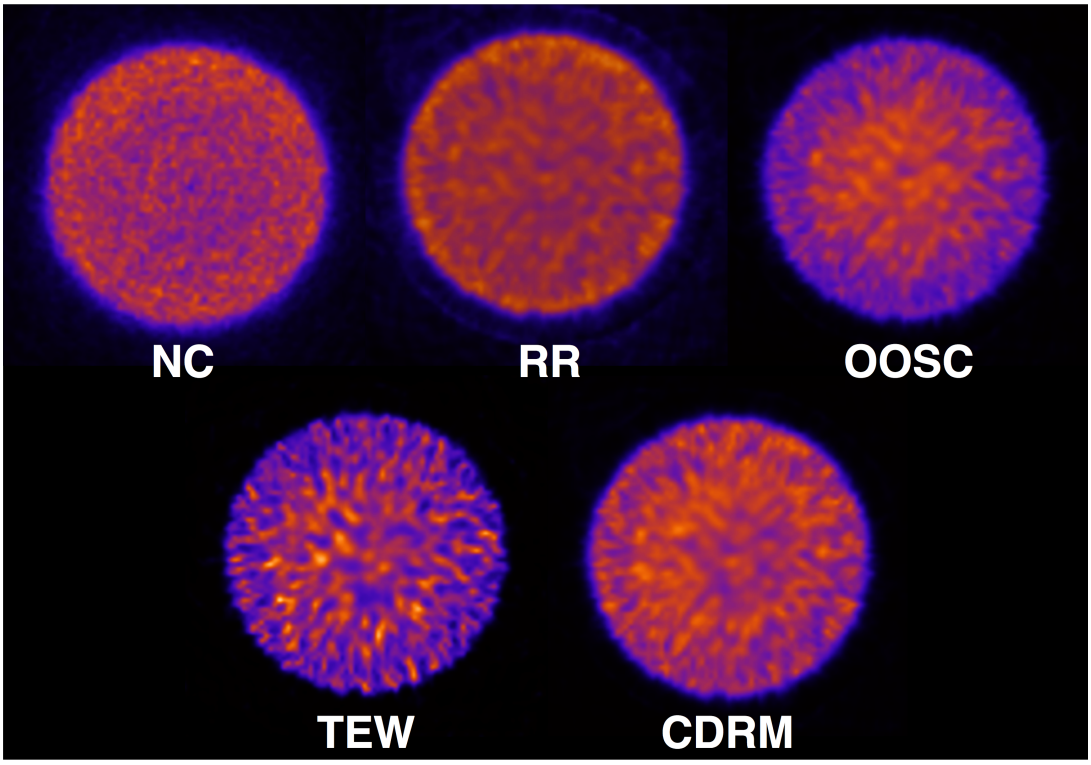

Figure 4.12: An example transverse slice of the uniform cylindrical phantom Siemens LEHR data reconstructed with NC(L) (top left), RR(L) (top middle), OOSC(L) (top right), TEW(L) (bottom left) and CDRM(L) (bottom right)

The NC(L) and RR(L) reconstructions appear relatively uniform, as the line profiles suggest. The transverse slice of the OOSC(L) reconstruction has more counts towards the centre of the phantom compared with the edge of the phantom, again as line profiles demonstrated (Figure 4.8). The counts in the middle of the phantom have been increased by attenuation and scatter correction compared to the NC(L) and RR(L) reconstructions.

Both the TEW(L) and CDRM(L) reconstructions, which include attenuation and scatter correction, appear more uniform than the OOCS(L) reconstruction. This appearance is a result of more accurate scatter correction. The TEW(L) reconstruction appears to be noisier than the CDRM(L) reconstruction. This finding was indicated by the poorer COV measurements of the TEW(L) data compared with the CDRM(L) data (Figure 4.3). The noisier TEW(L) reconstruction is unsurprising due to the significant proportion of counts subtracted from the acquired SPECT projections before reconstruction. This appearance was also demonstrated in the previous Chapter's investigation of planar uniformity.

4.3.2.2 Residual Sum of Squares for the Siemens Symbia MELP Collimators

Medium-energy collimators are less susceptible to high-energy septal penetration than low-energy collimators. This assumption is confirmed by the anticipated concave appearance of MELP reconstructions without attenuation correction (Figure 4.13).

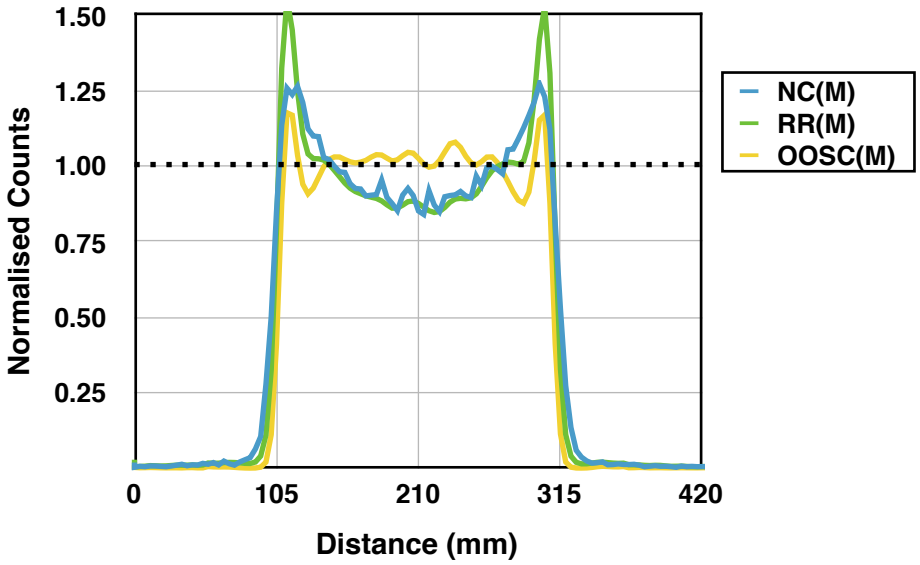

Figure 4.13: Line profiles of Siemens MELP data
Data reconstructed with No Corrections (NC(M)), depth-dependent Resolution Recovery (RR(M)) and Object Only Scatter Correction (OOSC(M)) applied are shown. Line profiles are normalised to the mean count value within the phantom boundary

Applying RR(M) sharpens the edges of the phantom, and smooths the profile compared to NC(M). When the OOSC(M) correction scheme is applied, the uncorrected concave appearance has been flattened. Both the RR(M) and OOSC(M) profiles suggest a ringing artefact at the edges of the phantom. This appearance is visibly apparent in transverse slices (Figure 4.14).

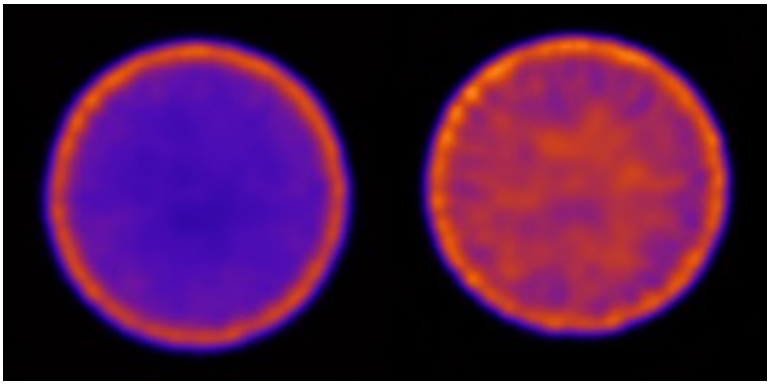

Figure 4.14: Ringing artefact at cylindrical phantom edges
Artefact demonstrated on MELP data reconstructed with RR(M) (left) and OOSC(M) (right)

The appearance of a Gibbs ringing artefact has been known to affect reconstructions incorporating RR [97]. The poorer spatial resolution of the MELP collimator planar projection data, as demonstrated in the previous Chapter, may increase susceptibility to

this ringing artefact compared to the LEHR collimator [167, 168]. However, it is unlikely that the sharp activity gradient at the edge of the phantom would be encountered clinically and, therefore, such severe ringing should not be present in routine clinical practice.

As with the LEHR data, visual assessment of normalised line profiles does not appropriately describe the difference in quantitative accuracy between reconstruction schemes with and without attenuation and scatter correction. Therefore, Figure 4.15 presents line profiles for MELP data in units of absolute reconstructed counts.

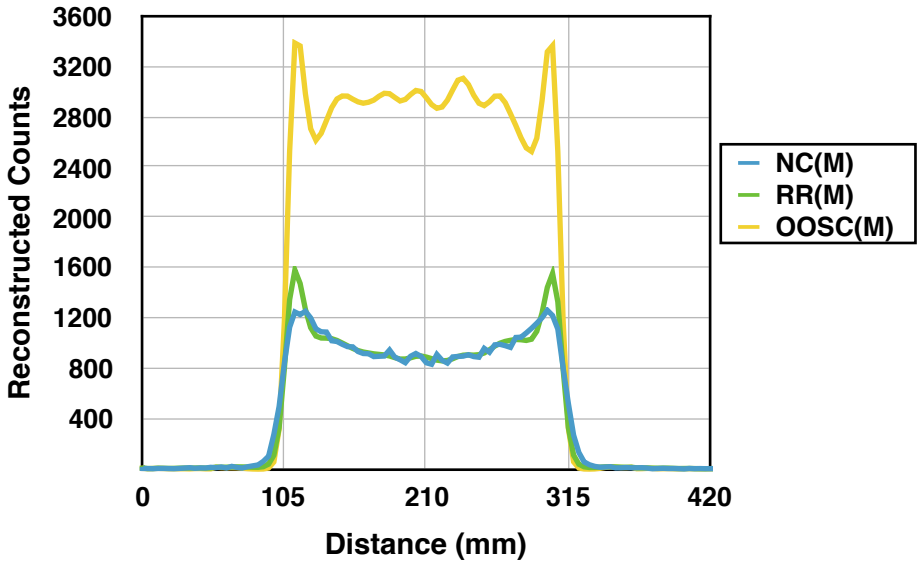

Figure 4.15: Line profiles of Siemens MELP data which compares the absolute reconstructed counts for the NC(M), RR(M) and OOSC(M) correction schemes
Line profiles for reconstructions with No Corrections (NC), Resolution Recovery (RR) and Object Only Scatter Correction (OOSC) are shown.

The quantitative Residual Sum of Squares (RSS) error confirms the qualitative assessment of line profiles (Figure 4.16).

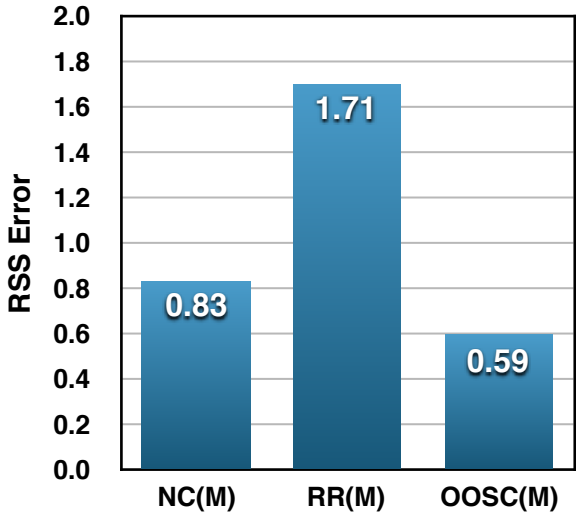

Figure 4.16: The Residual Sum of Squares (RSS) error for reconstructions of Siemens MELP data

The RR(M) reconstruction has a higher RSS error than NC(M) reconstruction due to the presence of ringing artefacts. The OOSC(M) reconstruction, which includes attenuation and scatter correction, demonstrates a flattening of the concave NC(M) and RR(M) reconstructions. This flattening of the profile results in the lowest RSS error.

Comparing the reconstructed data of both the Siemens LEHR and MELP collimators, the NC(L) and RR(L) had the lowest RSS error of 0.08 and 0.13 respectively. However, this is an artefactual finding which only applies for an object of cylindrical phantom's size and shape. It is a coincidence that the effects of attenuation and scatter cancel each other out.

The RSS error for the TEW(L) reconstruction is comparable with the OOSC(M) reconstruction (0.54 and 0.59 respectively) indicating equivalent uniformity. This finding suggests that TEW, which is the standard method used in the literature for correction of ^{123}I SPECT with LEHR collimators, provides a suitable correction for the high-energy emissions of ^{123}I.

The CDRM(L) reconstruction has a lower RSS error (0.34) than both the OOSC(M) and TEW(L) reconstructions, suggesting this novel correction is the optimum method for ^{123}I SPECT uniformity. CDRM(L) did not have the lowest COV result (Figure 4.3). However, the VOI used for COV analysis did not incorporate edge effects, such as the ringing artefacts prominent on the OOSC(M) reconstruction.

4.3.2.3 Residual Sum of Squares for the Philips Forte VXHR

The line profiles of NC(L) and RR(L) of the Philips VXHR collimator data show an intuitive concave profile (Figure 4.17). This appearance was not present for the flatter Siemens LEHR data (Figure 4.5).

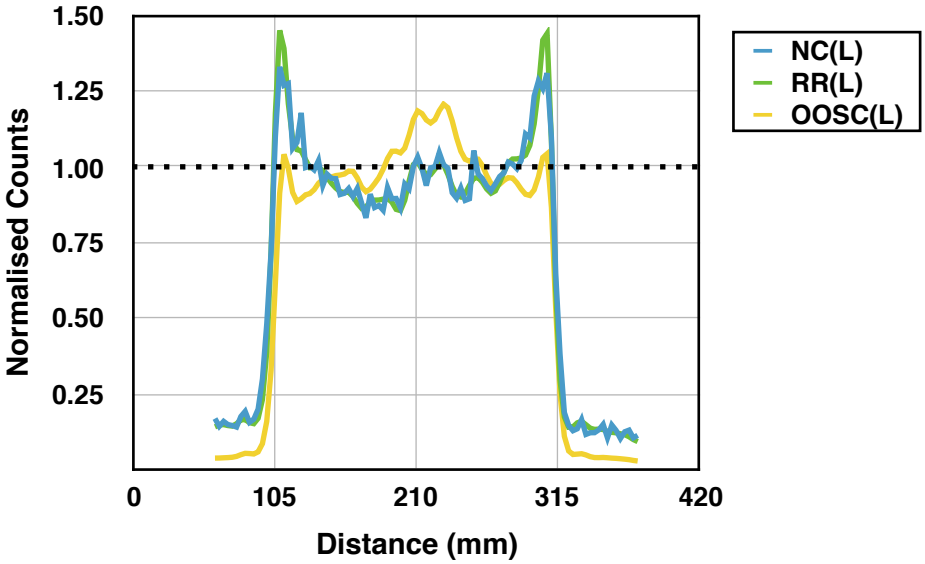

Figure 4.17: Line profiles of Philips VXHR data
Data reconstructed with No Corrections (NC(L)), depth-dependent Resolution Recovery (RR(L)) and Object Only Scatter Correction (OOSC(L)) applied are shown. Line profiles are normalised to the mean count value within the phantom boundary

The OOSC(L) reconstruction has a pronounced overcorrection in the centre. This appearance may demonstrate that, although the VXHR collimator is less susceptible to high-energy septal penetration than the Siemens LEHR collimator, there is still an influence from high-energy emissions. However, all VXHR reconstructions exhibit increased counts in the same central region. Macey [16] noted a similar central artefact specific to low-energy collimator acquisitions of ^{123}I (Figure 4.18). The presence of this artefact may be particular to the size of the phantom, dimensions of the collimator and Radius of Rotation (ROR) of the acquisition.

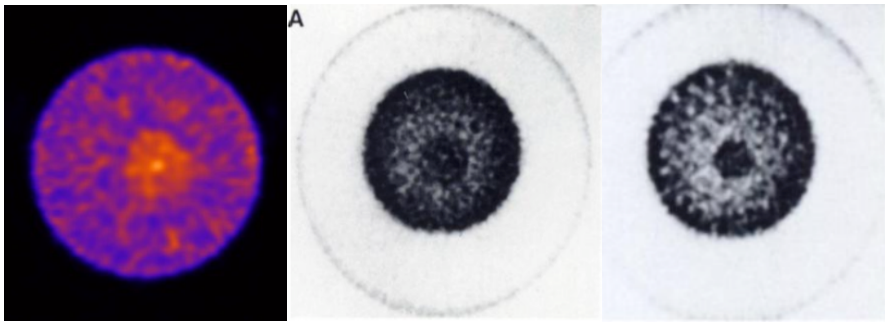

Figure 4.18: Central artefact demonstrated in the current and Macey's investigation [16]
Current investigation Philips VXHR data reconstructed with OOSC(L) (left) and the uniform (middle) and pie section (right) of a Jaszczak phantom, acquired with low-energy collimators by Macey

Figure 4.19 shows the RSS error for the line profiles of the VXHR reconstructions.

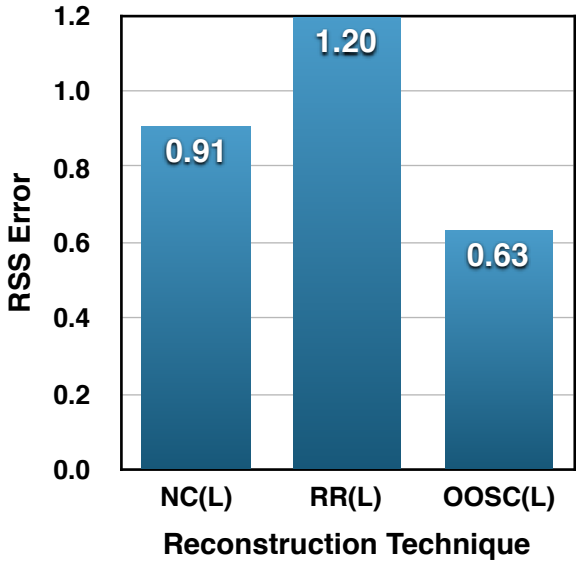

Figure 4.19: The Residual Sum of Squares (RSS) error for Philips VXHR data reconstructed with NC(L), RR(L) and OOSC(L)

The OOSC(L) reconstruction has the lowest RSS error (0.63), which is less than the equivalent Siemens OOSC(L) reconstruction (1.01) and is comparable with the Siemens OOSC(M) reconstruction (0.59). This finding suggests the dimensions of the Philips VXHR collimators are more suitable for reducing septal penetration than the Siemens LEHR collimators.

4.4 Spatial Uniformity Discussion

In this Chapter, assessment of the spatial uniformity of a cylindrical phantom has been used to evaluate the accuracy of attenuation and scatter correction. As such, one of the aims of this Chapter was to investigate novel reconstruction correction schemes to minimise known global non-uniformity for ^{123}I SPECT. This work showed that Monte Carlo Collimator and Detector Response Modelling (CDRM) resulted in the lowest Residual Sum of Squares (RSS) error compared to alternative schemes which also included attenuation and scatter correction.

There are few quantitative assessments of ^{123}I SPECT spatial uniformity in the literature. For example, Macey [16] chose to assess uniformity qualitatively in an investigation of preferred collimators for ^{123}I SPECT. However, Dickson [125] describes an acceptance criterion of COV <20% for gamma camera enrolment in a multi-centre trial of relative quantification for ^{123}I-DaTSCAN™ studies. All of the acquisition and reconstruction methods in the current study adhere to this criteria, except for the Philips VXHR data with No Corrections (NC) applied to the reconstruction.

In this study, the OOSC(M) reconstruction demonstrated the lowest COV of the correction schemes which included attenuation and scatter correction (6.0%). Gilland [33] measured a COV of 20.7% using data similarly acquired with medium-energy collimators and reconstructed with attenuation and scatter correction. The difference in COV reported by Gilland and the 6.0% found in this investigation may be mainly due to the different count densities. This assumption is supported by Leong [161] who demonstrated the relationship of reducing COV with increasing count density in an evaluation of ^{99m}Tc SPECT spatial uniformity.

The relatively high count density used in the current investigation was chosen to produce low noise data that would highlight any subtle differences between the novel correction schemes. However, the correction schemes which demonstrated greater accuracy in this study should hold for clinical data. This assumption will be assessed in subsequent Chapters which evaluate image performance measures with clinical count densities.

With regard to the qualitative assessment of line profiles, ^{123}I SPECT data acquired with Siemens LEHR collimators and reconstructed with No Corrections (NC) demonstrated a relatively flat profile. However, this is an artefactual finding resulting from the high-energy photon emissions of ^{123}I. These high-energy emissions have a lower probability than low-energy photons of being absorbed and, in this instance, compensated for absorbed low-energy photons. However, this compensation is coincidental, the effect of which is dependent on the collimator and phantom dimensions, and the Radius of Rotation (ROR) of the detector. The same compensation will not apply to different objects, such as patients. The flattening of the phantom profile has also been observed by Macey [16] who described low-energy collimators as “obliterating” the effect of attenuation without correction for high-energy emission.

Both the TEW(L) and CDRM(L) reconstructions attempt to correct for low and high-energy scatter and septal penetration. This characteristic was demonstrated by flattening of the line profile and reduced RSS error compared to OOSC(L). The CDRM(L) reconstruction demonstrated the lowest COV and RSS error for the Siemens LEHR collimators. The TEW(L) results are worse than the CDRM(L) method due to the subtraction of a significant proportion of the detected counts from projection data before SPECT reconstruction.

The OOSC(L) reconstruction results in a convex line profile. This appearance reduces SPECT spatial uniformity and results in inaccurate quantification. Overestimation of activity concentration in central regions of the FOV may be particularly important for

quantitative studies such as ^{123}I-DaTSCAN™ imaging where the object of interest lies centrally within the patient. Furthermore, a typical approach to quantifying ^{123}I-DaTSCAN™ studies involves determining the ratio of a central region to a peripheral 'background' region [31]. The convex non-uniformity demonstrated with OOSC(L) reconstruction will adversely increase the ratio of a central to a peripheral region.

An aim of this Chapter was to compare the SPECT spatial uniformity of the Siemens LEHR collimator with acquisition schemes less susceptible to septal penetration. With respect to this aim, the Siemens MELP NC(M) reconstruction and the Philips VXHR NC(L) reconstruction demonstrated a concave appearance, more typical of imaging in the absence of high-energy septal penetration. The thicker septa of the MELP and longer bores of the VXHR collimators reduce septal penetration compared with the Siemens LEHR data.

Although not previously used to evaluate ^{123}I SPECT spatial uniformity, quantifying the RSS error of line profiles provided a useful metric for uniformity. The RSS error quantified edge effects introduced by the RR algorithm which the COV did not. The Gibbs ringing edge artefact was demonstrated with Siemens MELP reconstructions. However, these artefacts have also been reported with RR applied to low-energy collimator acquisitions in an investigation by Maebatake [169] using an anthropomorphic brain phantom. As the CDRM algorithm investigated extensively in this thesis requires RR, the introduction of ringing artefacts at high contrast boundaries may be unavoidable for phantom studies. However, the line profile in Figure 4.9 indicates the CDRM algorithm does not demonstrate gross ringing artefacts.

4.5 Spatial Uniformity Conclusions

This work has shown, for the first time, that the novel CDRM correction scheme improves the global spatial uniformity of ^{123}I SPECT imaging. Therefore, based on analysis of SPECT uniformity, it is recommended that CDRM should be used where available for ^{123}I SPECT acquisitions with low-energy collimators. It is not recommended to use OOSC as this method of reconstruction can overestimate activity concentration in central regions of the FOV. If CDRM is not available, TEW correction should be used for studies requiring accurate quantification.

Hardware options for reducing high-energy septal penetration, such as Siemens MELP collimators, should be used to optimise SPECT spatial uniformity for accurate quantification where optimal spatial resolution is not necessary.

Subsequent Chapters will assess if these findings hold for other measures of SPECT performance.

Chapter 5: SPECT Spatial Resolution

5.1 Introduction

Spatial resolution is related to quantitative accuracy. Both Kojima [102] and Müller [95] suggest that a minimum spatial resolution of approximately 0.4 times the object diameter is necessary to allow accurate estimation of object size and activity. Therefore, spatial resolution is a key metric in the evaluation of accurate quantification. The aim of this Chapter is to assess system spatial resolution using iterative reconstruction for ^{123}I SPECT. Three measurement techniques will be evaluated.

Traditional methods of SPECT spatial resolution measurement involve imaging point or line sources in air and measuring the Full Width at Half Maximum (FWHM) of the reconstructed Point Spread Function (PSF) or Line Spread Function (LSF). Data are reconstructed with Filtered Back-projection (FBP) and no smoothing filter [142-144]. This approach is suitable for system characterisation. However, this traditional method does not represent the clinical imaging scenario using iterative reconstruction.

Spatial resolution improves with increasing iterations until convergence is achieved [170]. The rate of convergence is dependent on the spatial frequency content in the Field of View (FOV). Low frequency components converge more rapidly than high frequency components, and a combination of frequencies takes longer to converge. Therefore, to assess SPECT system spatial resolution in the clinical setting, this chapter will investigate the use of a method which uses a test object containing multiple spatial frequencies. The aim of this investigation is to characterise the convergence of advanced iterative reconstruction algorithms, as related to spatial resolution. A comparison of measurement methods will be used to determine a recommended approach to routine assessment of SPECT system resolution with iterative reconstruction.

LEHR collimators are often recommended for ^{123}I SPECT acquisition, as described in Section 2.1. However, low-energy collimators allow a relatively large proportion of high-energy septal penetration. An alternative option would be to use medium-energy collimators to reduce the level of septal penetration. However, spatial resolution and planar sensitivity are reduced with medium-energy collimators (see Section 3.3 and Section 3.5 respectively) which affects quantitative accuracy [102]. This chapter will assess the spatial resolution of both collimators for ^{123}I, with an aim being to inform clinical reconstruction protocols.

Depth-dependent Resolution Recovery (RR) reconstruction techniques attempt to improve SPECT spatial resolution. RR models the point spread function of an object with distance from a parallel hole collimator. As well as improving SPECT spatial resolution, depth-dependent RR may reduce radial elongation of the FWHM, which is typical in SPECT imaging [5, 100]. This chapter will assess the effect of incorporating RR into the reconstruction algorithm on ^{123}I SPECT spatial resolution. Furthermore, the effect on the FWHM of combined correction schemes which incorporate CT attenuation correction and advanced Monte Carlo scatter correction methods will be evaluated.

Increased computing power has allowed novel scatter correction to be performed by the reconstruction algorithm in a clinically relevant computational time [58, 158]. However, the addition of Collimator and Detector Response Modelling (CDRM) has not been assessed. Applying this complex correction to the iterative reconstruction algorithm increases the computational complexity of the task. Therefore, to ensure the CDRM algorithm performs image reconstruction in an acceptable time for routine clinical practice, the reconstruction time of this method was compared with standard iterative reconstruction methods.

In summary, the aims of this Chapter are to:

- characterise ^{123}I SPECT system resolution
- describe the convergence of advanced reconstruction algorithms
- assess non-traditional methods for measuring SPECT spatial resolution
- evaluate the reconstruction time of advanced reconstruction algorithms

5.2 Method and Materials

The introductory section of this chapter outlined the traditional method to characterise SPECT spatial resolution by measuring point sources in air. Alternative “Perturbation Methods” have been developed to measure the spatial resolution of images reconstructed with modern iterative reconstruction algorithms. The general approach is to reconstruct

acquisition data which contains multiple spatial frequencies. A typical setup is to surround a point or line source with a uniformly filled object. The surrounding object is subtracted from the reconstructed data leaving only the point or line source for measurement of spatial resolution.

Perturbation methods are suited to the assessment of spatial resolution when using iterative reconstruction due to the non-linear properties of the algorithm across the FOV, which depend on the image content [170, 171]. To date, perturbation methods have involved the addition of simulated data before reconstruction or the summation of two separate acquisitions. A fully practical implementation has yet to be published. In this investigation, a simple and a complex perturbation method will be compared with the traditional point source in air method of measuring spatial resolution.

The three methods of measurement which were assessed for the characterisation of SPECT system spatial resolution were:

1. Traditional method: a point source phantom in air
2. Two perturbation methods which include background activity:
    2.a. A ‘simple’ method with hot line sources in uniform background activity
    2.b. A ‘complex’ method with hot line sources only, following subtraction of uniform background activity

5.2.1 SPECT Spatial Resolution Phantoms

5.2.1.1 Traditional Point Source Phantom

The point source phantom was prepared with ^{123}I. Following guidance from the National Electrical Manufacturers Association (NEMA) [143], the point source phantom consisted of two point sources, with each source measuring ≤2mm in all dimensions (Figure 5.1). Sources were suspended in air. One source was positioned centrally on the system axis of rotation and the other source positioned approximately 75mm radially. Sources were positioned 50mm apart in the axial direction [143].

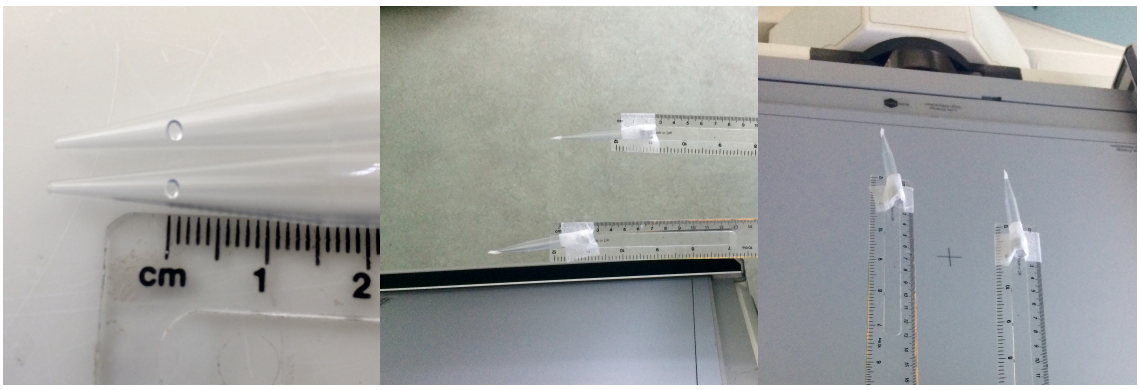

Figure 5.1: Point source size and setup

The point source phantom was prepared and acquired three times to give an indication of measurement error. The concentration of ^{123}I was either 74MBq/ml or 34MBq/ml depending on the concentration supplied by the manufacturer.

5.2.1.2 Perturbation Phantoms

Perturbation methods described in the literature involve simulation of projection data or the post processing of projection data to create composite data sets [61, 63, 170, 171]. This chapter proposes a 'simple' and 'complex' practical approach to measuring system spatial resolution using a line source phantom.

Simplistic Perturbation Method

The proposed 'simplistic' method involves the acquisition of a line source phantom containing uniform background activity. Both the simple and complex perturbation methods used the NEMA 1994 PET Image Quality phantom, which is a 20cm diameter cylindrical phantom with two line sources running the length of the phantom (Figure 5.2). The line sources are fixed in position and are filled independently of the background via an access hole. The line sources have an internal diameter less than 1mm.

Figure 5.2: The NEMA 1994 PET Image Quality phantom

As with the point source phantom, one line source was positioned centrally within the cylinder and the second source was positioned 75mm radially, which is also in keeping with the guidelines of NEMA [143] and the American Association of Physicists in Medicine (AAPM) [12]. Both NEMA and AAPM refer to hot line sources surrounded by cold scatter material (water). However, in this investigation the background compartment was filled with ^{123}I to simulate uniform uptake and, thus, additional frequencies in the FOV. This approach also allowed assessment of high-energy septal penetration from the surrounding activity.

Preliminary empirical investigation in this study determined that a line source to background activity concentration ratio of at least 500:1 was required to obtain image data of sufficient Signal to Noise Ratio (SNR) to enable accurate approximation of point spread functions.

The phantom was prepared from 74MBq of ^{123}I in a 2ml solution (37MBq/ml). The desired activity concentration ratio was achieved by dispersing 1.5ml of ^{123}I into the 5600ml phantom background compartment and 0.3ml of the solution, diluted up to 2ml, to fill the line sources. This resulted in a line source to background concentration ratio of 5550kBq/ml:9.9kBq/ml, or ~560:1. Each 20cm line source contains ~0.3ml.

Based on the volume of a voxel and the volume of line source contained within a voxel, the voxel-to-voxel activity concentration ratio was ~110:1.

Complex Perturbation Method

The ‘complex’ perturbation method involves acquiring two SPECT data sets sequentially: one with only uniform background activity and one with uniform background activity and two higher activity concentration line sources. Following reconstruction of the two sequential data sets, the uniform SPECT study is subtracted from the study containing uniform activity and line sources (Figure 5.3). The resultant images can be analysed to assess spatial resolution.

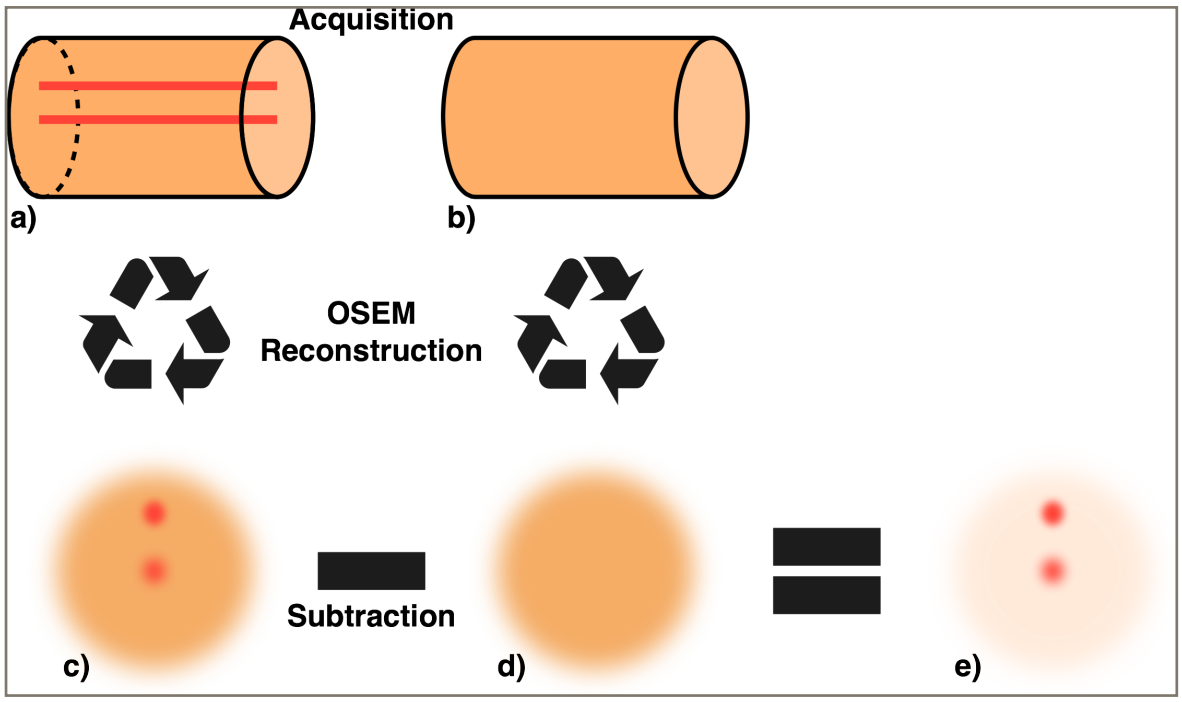

Figure 5.3: Flow diagram describing the complex practical method used to measure SPECT spatial resolution with line sources in a uniform background
Two data sets are acquired: a uniformly filled cylindrical phantom (b) and a uniform background with hot lines sources (a). Both data sets are reconstructed, with the resultant uniform phantom images (d) subtracted from the hot line source images (c). The FWHM of line sources in the subtraction (e) is measured.

The complex perturbation method was performed using the same NEMA 1994 PET Image Quality phantom used for the simple perturbation method. The background was prepared and acquired with a uniform activity concentration, and then reacquired in the same position with higher concentration line sources present. The two SPECT data sets are, therefore, spatially registered for subtraction following reconstruction.

Comparison of both perturbation methods was made. If both methods are equivalent, the simpler of the two can be used as a convenient method for routine assessment of SPECT spatial resolution. This measure can then be used to inform reconstruction parameter optimisation.

5.2.2 Phantom Acquisition

All phantom data were acquired using the Siemens Symbia T2 gamma camera, which was described in Section 3.2. The Triple Energy Window (TEW) acquisition scheme, outlined in Section 3.3.1.2, was applied to all SPECT acquisitions. The spatial resolution phantoms were acquired using LEHR and MELP collimators.

5.2.2.1 Traditional Point Source Phantom Acquisition

The NEMA protocol for acquisition suggests that data should be acquired with ~14,000 counts in the first projection. In this investigation, adherence to this criteria would result in a substantial acquisition time due to the relatively low activity concentration of the ^{123}I point sources. Therefore, in this study, data were acquired with 2,000 counts in total in the first projection. This count density was deemed sufficient as the advanced reconstruction correction schemes employed in this investigation improve Signal to Noise Ratio (SNR) (particularly depth-dependent RR) compared with the traditional method.

An acquisition zoom of 2 was applied, resulting in a pixel size of 2.4mm. This pixel size was chosen to allow comparison of results with the perturbation methods. Larger acquisition zooms would have increased the likelihood of truncating the 20cm diameter cylindrical phantom used for the perturbation methods. Table 5.1 describes the tolerance around the cylindrical phantom and the extent of line sources in the FOV for the available acquisition zooms.

Acquisition Zoom	Pixel Size (mm)	Tolerance surrounding phantom (cm)	Z-axis Extent of Line Sources (cm)
1.00	4.8	20.7	13.8
1.23	3.9	15.0	13.8
1.45	3.3	11.2	13.8
1.78	2.7	7.2	11.9
2.00	2.4	5.3	10.0
2.30	2.1	3.4	8.1
2.67	1.8	1.5	6.1
3.20	1.5	-0.4	4.2

Table 5.1: Available acquisition zooms on the Siemens Symbia T2
The 2.00 zoom was chosen as the acquisition zoom of the spatial resolution phantoms. This choice adheres with the NEMA protocol (pixel width <2.5mm) and ensured there was no truncation of the cylindrical phantom used for the perturbation methods

The 2.4mm pixel size chosen is less than 2.5mm, which is the pixel width described by the NEMA protocol [143]. Although a pixel size of 2.1mm could be achieved with an acquisition zoom of 2.3, there would be a higher probability of truncation from phantom positioning errors compared to a zoom of 2.0. Additionally, the extent of the line source in the FOV would be shortened from 10cm to 8.1cm, which would reduce the available area to sample the FWHM in the z-axis.

The Radius of Rotation (ROR) was set to 20cm, which is in accordance with AAPM [12]. Acquisition was performed using the parameters described in Table 5.2.

Parameter	Value
Matrix	128x128
Zoom	2
Pixel Size	2.4mm
Projections	128
Counts in the First Projection	2000
Radius of Rotation	20cm
Orbit	Circular
Photopeak	159keV±10%
Scatter Windows	Lower: 138±4keV Upper: 178±4keV

Table 5.2: SPECT acquisition parameters

5.2.2.2 Perturbation Phantom Acquisitions

The parameters for the line source phantom acquisition for both the simple and complex perturbation methods were the same as those used for the traditional point source phantom (Section 5.2.2.1). However, the data were acquired to the same acquisition time as the point source phantom rather than to counts in the first projection. This adaption to acquisition parameters was made as counts in the first projection for the cylindrical phantom, which contains line sources and activity in the background, were not comparable to the point source set up.

The complex perturbation phantom was initially acquired with uniform activity concentration. Following the uniform phantom acquisition, a 25cm needle was used to fill the line sources with higher activity concentration. The phantom remained in the same orientation and location. The second acquisition used the same parameters with the acquisition time adjusted to account for decay between imaging.

5.2.2.3 CT Acquisition

A sequential CT was acquired following SPECT acquisitions, using the parameters described in Table 5.3.

Parameter	Value
CT mA	35mA
CT kVp	130kVp
CT Reconstruction Slice Width	2.4mm

Table 5.3: Parameters of the sequentially acquired CT

The CT component provides a detailed map of attenuation coefficients. The attenuation map was used for attenuation correction and Monte Carlo simulation of scattered photons in the object of interest. No streaking artefacts, as a result of the metal line sources, were observed on the CT acquisition of the phantom (Figure 5.4).

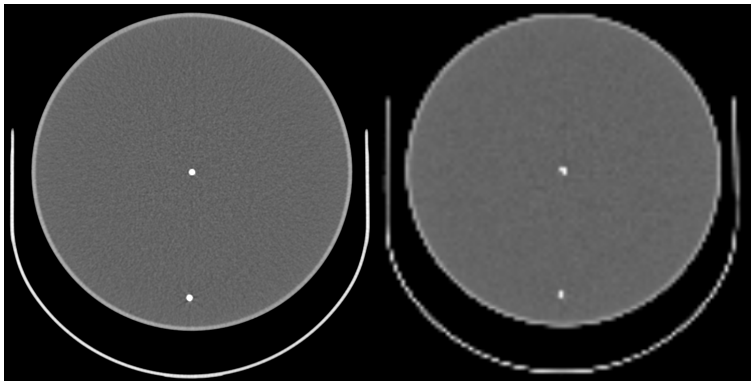

Figure 5.4: Transverse slice of CT reconstruction
The transverse slice has no significant streaking artefacts on either the original 512x512 matrix slice (left) or the re-binned 128x128 attenuation correction map (right)

5.2.3 Phantom Reconstruction

Phantom acquisitions were reconstructed using the correction schemes and parameters described in Section 4.2.2 which are reproduced here for reference in Table 5.4 for LEHR data and Table 5.5 for MELP data.

Correction Scheme Name	Resolution Recovery	Attenuation Correction	Scatter Correction
NC(L)	No Corrections (NC)		
RR(L)	✔	–	–
OOSC(L)	✔	CT	OOSC
TEW(L)	✔	CT	TEW
CDRM(L)	✔	CT	CDRM

Table 5.4: Reconstruction correction schemes applied to data acquired with low-energy collimators
Correction schemes include, where indicated, Resolution Recovery (RR), Object Only Scatter Correction (OOSC), Triple Energy Window (TEW) scatter correction and Collimator and Detector Response Modelling (CDRM). Low-energy collimator data is indicated with (L).

Correction Scheme Name	Resolution Recovery	Attenuation Correction	Scatter Correction
NC(M)	No Corrections (NC)		
RR(M)	✔	—	—
OOSC(M)	✔	CT	OOSC

Table 5.5: Reconstruction correction schemes applied to data acquired with medium-energy collimators
Correction schemes include, where indicated, Resolution Recovery (RR) and Object Only Scatter Correction (OOSC). The reconstruction of data acquired with medium-energy collimators is indicated with (M)

Reconstructions were performed using 2 to 160 equivalent iterations. The range was chosen following recommendations from work by Dickson [30] which suggests convergence at 100 iterations for relative quantification of ^{123}I-DaTSCAN™ studies when depth-independent RR is applied. Details of the OSEM iteration and subset combinations used in the current study are given in Table 5.6. Following recommendations outlined in Section 2.2.3, subsets contained a minimum of 8 projections.

Equivalent Iterations	Iterations	Subsets	Projections per Subset
2	2	1	128
4	2	2	64
8	2	4	32
12	3	4	32
16	4	4	32
20	5	4	32
24	6	4	32
48	6	8	16
96	6	16	8
128	8	16	8
160	10	16	8

Table 5.6: OSEM algorithm iteration and subset combinations used in the current investigation

All SPECT data were reconstructed without post-filtering.

5.2.3.1 Reconstruction Time

The reconstruction time was measured for each correction scheme and for each iteration value used for phantom reconstructions (2, 3, 4, 5, 6, 8 and 10). The reconstruction time was also measured for three subset options (4, 8 and 16) with the same number of iterations (6).

Reconstructions were carried out on a Hermes Applications Server. The server has an Intel® Xeon® E5-260v2 CPU and a NVIDIA® Quadro® K4000 GPU. All measurements were made when there was no additional burden on the applications server running the reconstructions.

5.2.4 Phantom Analysis: Measuring the FWHM

Spatial resolution can be measured using the PSF, LSF, edge response or Modulation Transfer Function of the imaging system [101]. Of these, the FWHM of the LSF has been described to be representative of human perception of spatial resolution [101]. The LSF can be determined either by a profile across a line source or from a wide profile integrating counts across a point source [101]. Therefore, to enable comparison of point and line source measurements the LSF was used as the method of measurement throughout this investigation.

The NEMA convention is for three FWHM spatial resolution values to be reported [143]. These include one value for the source positioned at the centre of rotation, which is the mean value in the x and y direction, and two FWHM values for the peripheral source (one for the radial direction and one for the tangential direction). These conventional measurements are illustrated in Figure 5.5 and will be used in the description of spatial resolution for the remainder of this Chapter.

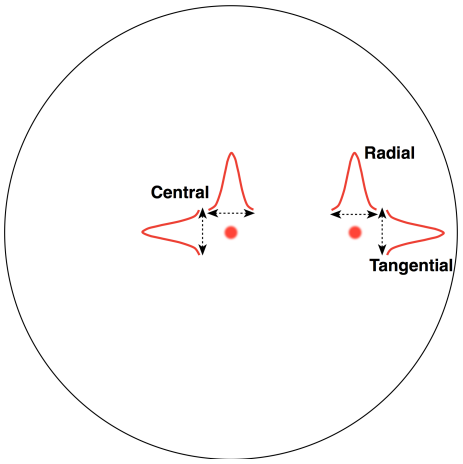

Figure 5.5: Transverse section which describes the direction of FWHM measurement The outer circle describes the orbit of the detector.

5.2.4.1 Traditional Point Source Phantom Analysis

The LSF was determined by fitting a Gaussian curve to a 10 pixel wide profile (24mm) taken over each point source. The FHWM was calculated from the equation of the Gaussian fit. The central FWHM was determined as the mean of six measurements (three acquisitions in both the x and y direction). The radial and tangential FWHM was determined as the mean of three measurements.

5.2.4.2 Perturbation Phantom Analysis

Similar to the point source phantom, the FWHM was determined by a Gaussian fit to profiles of the line sources. Profiles were automatically drawn in the same location on ten consecutive transverse slices to obtain a mean measure of FWHM. The central FWHM was calculated as the mean of the FWHM in the x and y direction. The radial and tangential FWHM was measured with profiles of the peripheral line source in the appropriate direction.

5.2.5 Statistical Analysis

The measurement error of results is described using two Standard Error (SE) of the mean value. Errors are not indicated on results when twice the SE was less than 0.5mm.

Due to the sample size being lower than thirty, normality of data could not be assumed [172]. Therefore non-parametric methods of statistical analysis have been employed in this chapter.

The non-parametric tests used in this chapter to determine statistical significance are [173]:

- *Mann-Whitney-U test:* used for comparison of two non-paired data sets, for example comparing the same reconstruction method for LEHR and MELP acquisition data sets.
- *Wilcoxon test:* used for comparison of two paired data sets. For example, a Wilcoxon test was used to assess whether a statistically significant difference exists between two paired reconstruction methods. This includes two methods of reconstruction of the same acquired data set.
- *Friedman test:* used for comparison of multiple paired data sets. Due to the consideration of paired data, the Friedman test has greater statistical strength and higher probability of detecting a difference in paired data than an unpaired Kruskal-Wallis test. The Friedman test was used to compare multiple reconstruction methods from the same acquisition data set. However, the Friedman test lacks a suitable post hoc

method to determine between which data sets the statistical difference exists. Therefore, Friedman test results which indicate statistically significant difference were followed by a Kruskal-Wallis analysis and a Dunn's post hoc test:

- *Kruskal-Wallis followed by a Dunn's post hoc test:* the Kruskal-Wallis test is used for comparison of multiple unpaired data sets. If the test suggests statistically significant differences, then a post hoc Dunn's test can be used to perform multiple comparisons allowing the two (or more) differing methods to be identified. The limitation of this method is in cases where the Friedman analysis suggests statistical significance and the following Kruskal-Wallis test does not.

If the same data set undergoes a Friedman and Kruskal-Wallis test of paired data and the Friedman test does not demonstrate statistically significant difference then neither will the Kruskal-Wallis test. Therefore, a Kruskal-Wallis with Dunn's post hoc test was only performed where the Friedman test showed statistical significance.

FWHM results were deemed to have converged where there was no statistically significant difference with the FWHM as measured at 160 iterations.

RStudio version 1.0.136 (RStudio, Inc), a graphical user interface running R version 3.3.1 (The R Foundation for Statistical Computing), was used for all statistical tests. A difference was deemed to be statistically significant for p-values of less than 0.05.

5.3 SPECT Spatial Resolution Results

For accurate quantification, the system spatial resolution (FWHM) should ideally be as small as possible. Measuring point sources in air is the traditional method of characterising system spatial resolution, with regard to FBP reconstruction. This Section will present the FWHM of iterative reconstruction algorithms using the traditional method. These results will allow comparison with the more advanced perturbation methods, which are intended for the characterisation of systems which utilise iterative reconstruction.

5.3.1 System Spatial Resolution for ^{123}I Point Sources in Air

The smallest FWHM result of the point sources in air for all reconstruction methods was obtained from the tangential measure. The RR(L) correction scheme demonstrated the smallest FWHM of 3.4±0.2mm at 160 iterations. Figure 5.6 illustrates that reconstructions which include depth-dependent RR improved the spatial resolution (FWHM) of point sources in air for both collimators compared with standard OSEM with No Corrections (NC).

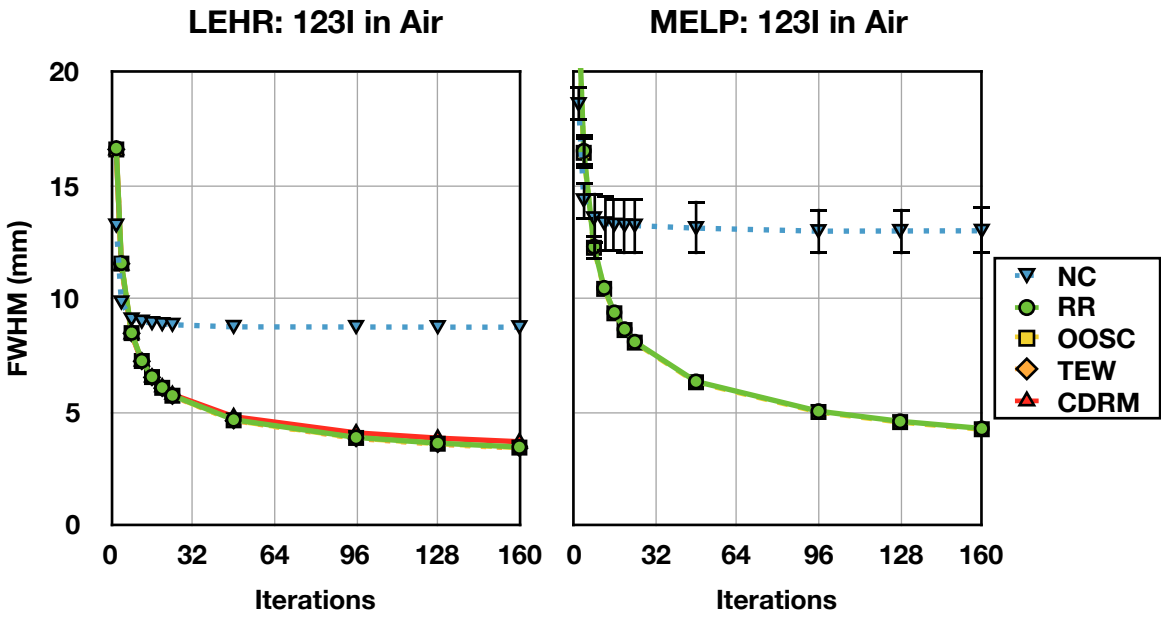

Figure 5.6: FWHM of point sources in air acquired with LEHR collimators (left) and MELP collimators (right)

The results presented are of tangential FWHM measurements from images reconstructed with the No Corrections (NC), Resolution Recovery (RR), Object Only Scatter Correction (OOSC), Triple Energy Window (TEW) and Collimator and Detector Response Modelling (CDRM) correction schemes. MELP data were not reconstructed with TEW and CDRM. Estimated measurement errors of ≤0.5mm are not shown.

The inclusion of CT attenuation correction and scatter correction in the reconstruction algorithm should not affect the LSF at the level of the FWHM and would be expected to be more effective in suppression of the extended tails of the LSF [17]. As anticipated, in this study the addition of these corrections does not alter the spatial resolution measurement compared with RR alone (Figure 5.6).

A comparison of the scatter correction techniques as applied to LEHR data demonstrated that all three (OOSC, TEW and CDRM) have a similar FWHM and rate of convergence. This finding shows that advanced correction schemes are not detrimental to spatial resolution. There was no statistically significant difference between the RR(L), OOSC(L), TEW(L) and CDRM(L) correction schemes at 160 iterations (p=0.240).

As was demonstrated with the LEHR data, the addition of attenuation and scatter correction to MELP data does not alter the spatial resolution when compared with RR alone. There was no statistically significant difference between the RR(M) and OOSC(M) correction schemes at 160 iterations (p=0.883, Confidence Interval (CI):0.0±0.1).

Table 5.7 summarises the tangential FWHM measured at 160 iterations, which was the smallest recorded for each correction scheme.

Correction Scheme	Collimator	
	LEHR: FWHM (mm)	MELP: FWHM (mm)
NC	8.7±0.8	13.0±1.0
RR	3.5±0.2	4.3±0.1
OOSC	3.4±0.2	4.2±0.1
TEW	3.4±0.2	—
CDRM	3.7±0.1	—

Table 5.7: Tangential FWHM at 160 iterations

The OOSC and CDRM Monte Carlo scatter correction algorithms require a CT attenuation correction map to simulate photons. The dimension of the point source compared to the pixel size is small and has a relatively low attenuation coefficient. Therefore, any effect of incorporating CT attenuation correction and scatter correction on FWHM will be more apparent in the results of the perturbation phantom investigations (see Section 5.3.2). However, as stated previously, scatter correction would be expected to be more effective in suppressing the extended tails of the LSF [17] rather than at the level of the FWHM.

In order to accurately measure the FWHM, the Gaussian approximation requires at least three samples in the LSF [174]. An example of the smallest FWHM measurement of a point source in air is shown in Figure 5.7.

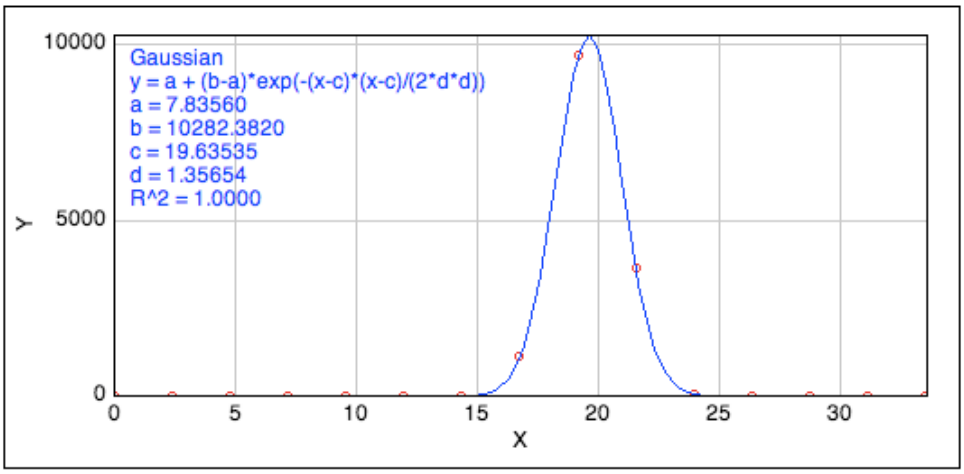

Figure 5.7: Line Spread Function profile of a point source in air reconstructed with RR(L) The LSF has a FWHM of 3.2mm based on a Gaussian curve fit of the data (red circles = data points, blue line = curve fit, x-axis = mm, y-axis = counts)

The smallest FWHM measured (3.4±0.2mm at 160 iterations with the RR(L) correction scheme) is approaching the measurable limit for the reconstructed pixel size of 2.4mm.

5.3.2 System Spatial Resolution for ^{123}I with Perturbation Methods

5.3.2.1 Comparison of Perturbation Methods

Comparison of Perturbation Methods: LEHR Data

A representative transverse slice through the phantom, reconstructed with CDRM(L) and 96 iterations shows the line sources in uniform activity used for the simple method of measurement, the uniform concentration used for subtraction and the subtraction result used for the complex method of measurement (Figure 5.8).

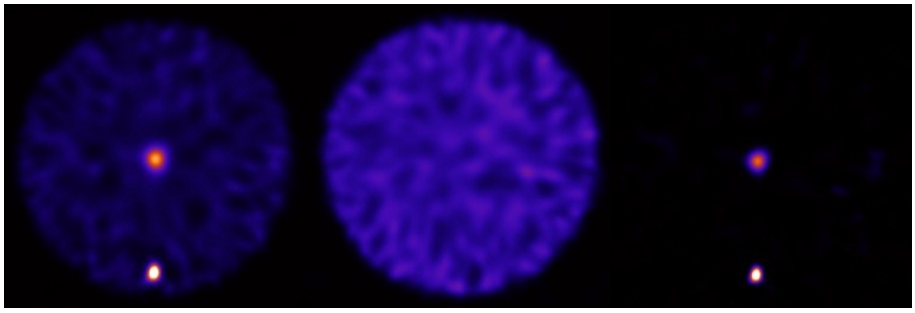

Figure 5.8: Reconstruction of line source phantom with (left) and without (centre) hot line sources, and the subtraction result (right)

As with the traditional measurement of point sources in air, the smallest FWHM result for all reconstruction methods was obtained from the peripheral line source measured tangentially. Figure 5.9 shows the tangential FWHM using the simple and complex perturbation methods.

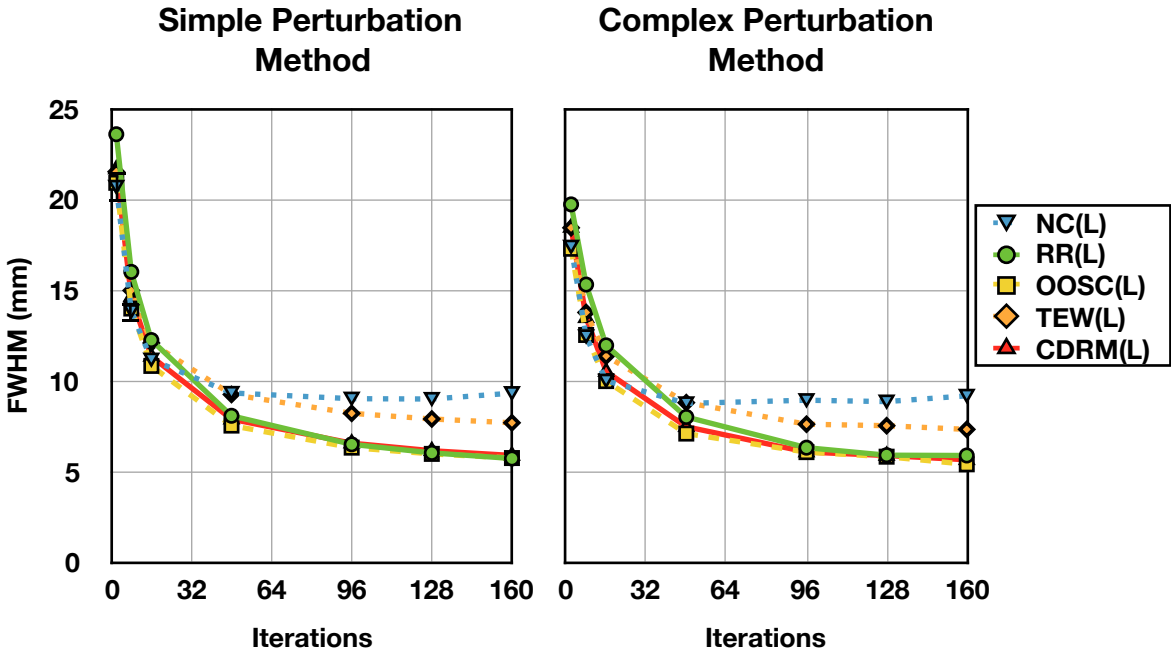

Figure 5.9: Tangential FWHM for the peripheral line source acquired with LEHR collimators and measured using the simple (left) and complex (right) perturbation methods Estimated errors of ≤0.05mm are not shown.

The smallest FWHM measured for the simple and complex methods was 5.7±0.1mm (RR(L)) and 5.4±0.1mm (OOSC(L)) respectively. Both minimum FWHM were measured at 160 iterations.

Of the perturbation methods investigated, the complex approach will, in theory, most accurately approximate SPECT system spatial resolution in the clinical setting. This is because the complex perturbation method simulates multiple spatial frequencies in the FOV and surrounds the source with background activity. However, for line sources acquired with LEHR collimators, the simple method was shown to suitably approximate the complex perturbation method results with no statistically significant difference for iterations greater than or equal to 48 (Table 5.8).

Correction Scheme	p-value	Confidence Interval
NC(L)	0.196	0.7±0.8
RR(L)	0.233	0.2±0.4
OOSC(L)	0.441	0.1±0.2
TEW(L)	0.621	0.1±0.3
CDRM(L)	0.108	0.1±0.2

Table 5.8: Wilcoxon paired test between FWHM as measured with the simple and complex perturbation method
Statistical test of tangential, radial and central FWHM for reconstructions with iterations greater than or equal to 48. Red font indicates no statistically significant difference (p-value > 0.05).

This suitable approximation is due to the relatively large activity concentration ratio, which reduces the influence of background activity on the measurement, as described by Figure 5.10.

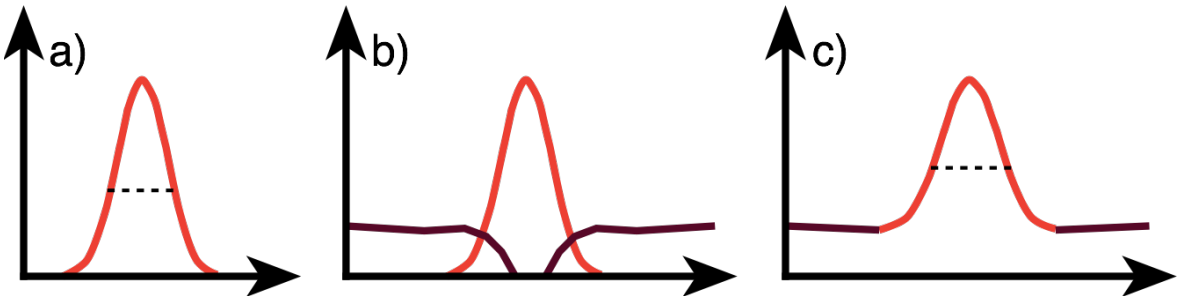

Figure 5.10: Pictorial comparison of perturbation measurement methods
The complex perturbation method measures the FWHM of the LSF which has been decoupled from surrounding activity (a). The LSF of the simple perturbation method includes a contribution from surrounding activity (b). Therefore, the FWHM measured using the simple method (c) overestimates the FWHM of the complex method. However, as the source to background concentration ratio increases, the difference between a) and c) decreases.

Therefore, for future evaluations of system spatial resolution, the simple perturbation method would be appropriate.

The reconstructions which incorporate attenuation correction and Monte Carlo scatter correction (OOSC and CDRM) demonstrate comparable FWHM values and a similar rate of convergence as the RR(L) reconstruction (Figure 5.9). However, the reconstructions which incorporate TEW scatter correction have a larger FWHM for iterations greater than 8. This is likely due to the TEW method subtracting a large proportion of counts from the photopeak prior to reconstruction. Increasing iterations further amplifies noise which, in this instance, widens the FWHM of the point spread function. These spatial resolution results, taken in isolation, suggest that the TEW correction scheme may be less accurate for quantifying small objects compared to the RR, OOSC and CDRM schemes.

Comparison of Perturbation Methods: MELP Data

As with the results for the LEHR data, the smallest FHWM of the MELP data was measured tangentially. The MELP spatial resolution tangential results, comparing reconstruction methods with increasing iterations, are shown in Figure 5.11.

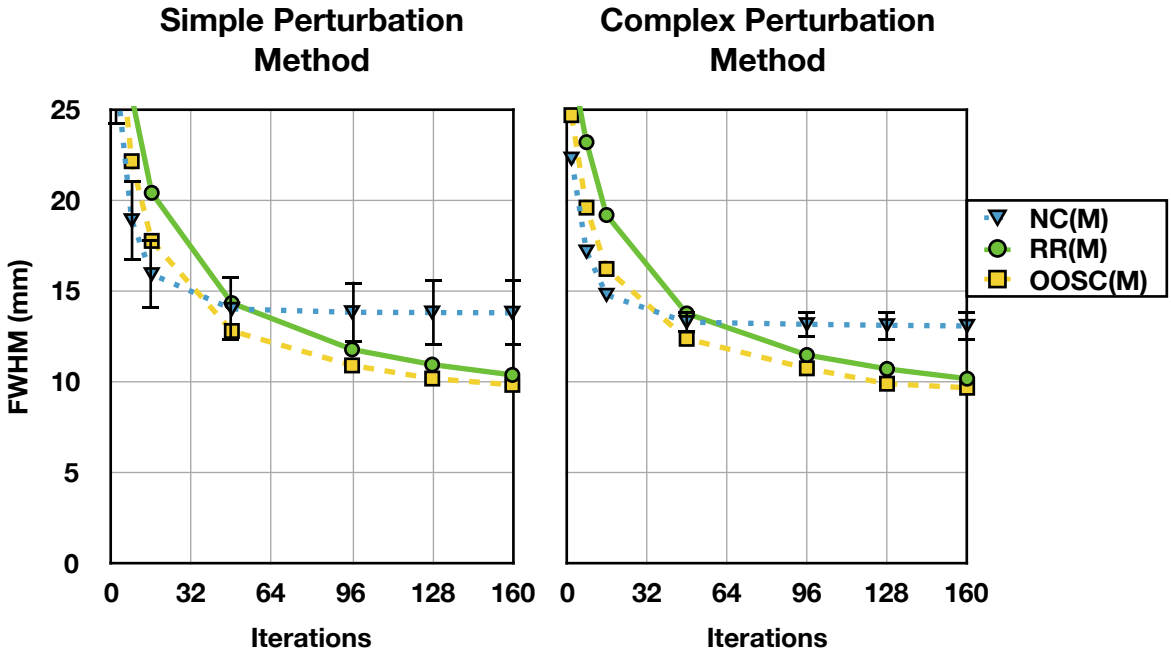

Figure 5.11: Tangential FWHM for the peripheral line source acquired with MELP collimators and measured using the simple (left) and complex (right) perturbation methods

The mean FWHM for the NC(M) measured using the complex method is lower and less variable than with the simple method. However, there is no statistically significant difference between the simple and complex perturbation method for iterations greater than or equal to 48 (Table 5.9). The simple method, therefore, suitably approximates the complex method for line sources acquired with MELP collimators.

Correction Scheme	p-value	Confidence Interval
NC(M)	0.897	0.1±1.1
RR(M)	0.178	0.2±0.4
OOSC(M)	0.120	0.1±0.2

Table 5.9: Wilcoxon paired test between FWHM as measured with the simple and complex perturbation method
Statistical test of tangential, radial and central FWHM for reconstructions with iterations greater than or equal to 48. Red font indicates no statistically significant difference (p-value ≥0.05).

This Section has shown that the simple perturbation method suitably approximates the complex perturbation method for measurement of ^{123}I SPECT spatial resolution and can, therefore, be used for future evaluations of system spatial resolution.

However, as both perturbation methods have been performed for all reconstructed data, subsequent results in this Chapter refer to the complex method of FWHM measurement, which is, theoretically, the more accurate method.

5.3.2.2 Comparison of LEHR and MELP Measurements

Table 5.10 shows the results for the tangential, radial and central FWHM for both LEHR and MELP collimators. The results refer to data reconstructed with the OOSC, which is an advanced correction scheme applied to both collimators, and measured using the complex perturbation method.

	96 Iteration FWHM (mm)			160 Iteration FWHM (mm)		
	Tangential	**Radial**	**Central**	**Tangential**	**Radial**	**Central**
LEHR data	6.1±0.1	7.9±0.1	10.6±0.2	5.4±0.1	6.9±0.1	9.6±0.3
MELP data	10.8±0.1	12.3±0.1	19.0±0.3	9.7±0.1	11.3±0.1	17.6±0.4

Table 5.10: Range of FWHM from tangential to central sources for LEHR (L) and MELP (M) Data reconstructed with OOSC and measured using the complex perturbation method.

As anticipated, the comparison indicates that the FWHM measured for the LEHR collimators is less than the equivalent measurements with MELP data.

Madsen [45] suggests the FWHM for neurology SPECT should ideally be 8-9mm. This requirement could be met with LEHR collimators and a smaller Radius of Rotation (ROR), which would reduce the FWHM further than those presented in Table 5.10.

Dickson [125] suggests a FWHM of ≤15mm is suitable of ^{123}I neurology SPECT and, further, recommends ~100 iterations for accurate quantification. With regard to MELP data, the FWHM of the central line source is 19.0±0.3mm at 96 iterations. Although the FWHM of the central line source would reduce with a smaller ROR, the evidence in this Section suggests that the MELP collimator should not be used for neurology applications.

5.3.2.3 Assessment of Convergence

For the complex perturbation method, the FWHM of the NC(L) and NC(M) reconstructions converge at 48 iterations with no statistically significant difference with the 160 iteration FWHM. The RR(L) and CDRM(L) correction schemes converge at 128 iterations (Table 5.11).

Correction Scheme	p-value	Confidence Interval
NC(L)*	0.432	0.3±0.7
RR(L)	0.644	0.3±0.7
OOSC(L)	<0.001	0.4±0.1
TEW(L)	<0.001	0.3±0.1
CDRM(L)	0.239	0.1±0.3
NC(M)*	0.191	1.9±2.2
RR(M)	<0.001	0.5±0.1
OOSC(M)	<0.001	0.5±0.1

Table 5.11: Wilcoxon paired test of FWHM convergence, measured using the complex perturbation method

Statistical test of tangential, radial and central FWHM between reconstructions with 128 and 160 iterations ((*) test between 48 and 160 iterations). Green font indicates statistically significant difference (p-value <0.05). Red font indicates no statistically significant difference (p-value ≥0.05).

The OOSC(L), TEW(L), RR(M) and OOSC(M) correction schemes demonstrate a statistically significant difference between 128 and 160 iterations. The iterative nature of advanced correction schemes may make an expectation of full convergence unreasonable within a suitable number of iterations. For example, Kappadath [175] has shown that, for advanced reconstruction of ^{99m}Tc point sources in uniform activity, the FWHM continues to narrow up to the maximum 2700 iterations tested. Therefore, in this study, the relatively small rate of change in FWHM between 128 and 160 iterations (mean difference in all correction schemes ≤0.5mm) suggests 160 can be taken as representative of a fully converged value.

5.3.2.4 Spatial Resolution Location Dependence

As spatial resolution is related to quantitative accuracy, it is important to consider the extent to which resolution varies with location in the FOV. Variability of the FWHM of the line source with location is shown for LEHR and MELP data in Figure 5.12. The representative data shown is from reconstructions using the OOSC correction scheme and measured with the complex perturbation method.

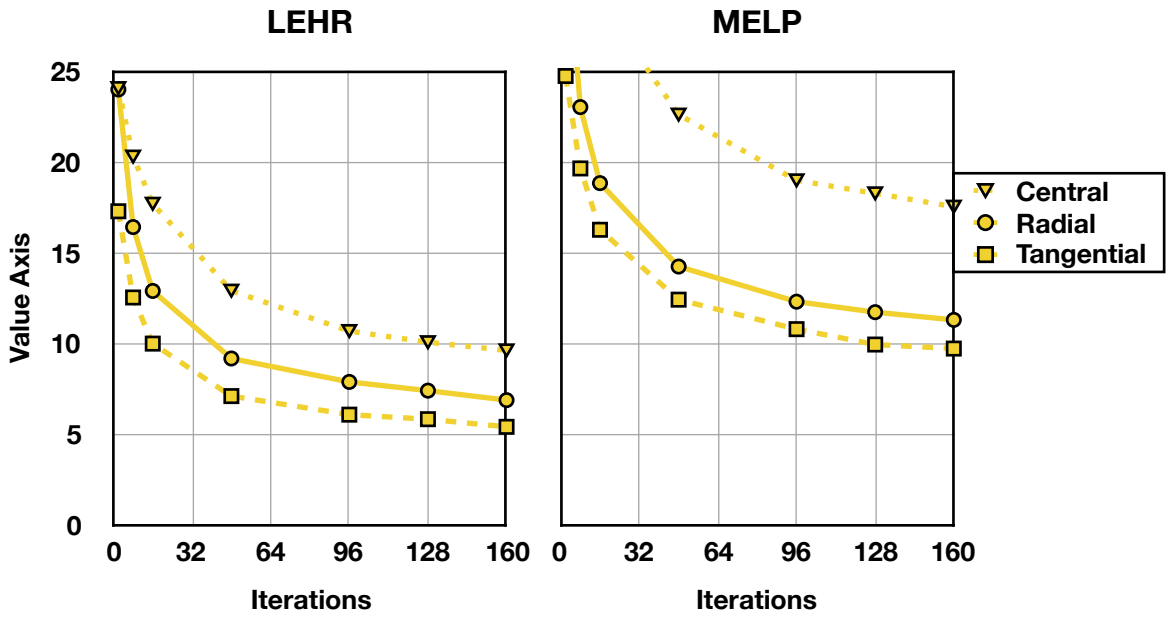

Figure 5.12: Location dependence of the FWHM
Example shown is of LEHR (left) and MELP (right) data reconstructed with the OOSC correction scheme and measured using the complex perturbation method

The difference between the central and tangential FWHM is 4.2mm and 7.8mm for the OOSC(L) and OOSC(M) correction schemes respectively. Using the complex perturbation method, the FWHM of the central source is greater than the tangential result by a factor of ~1.75 for both the OOSC(L) and OOSC(M) data. This finding is consistent with the line source elongation reported by Knoll [106] for ^{99m}Tc reconstructed with depth-dependent RR.

The difference in these measurements can be attributed to varying rates of convergence in the FOV. Kappadath [175] demonstrated that the FWHM of ^{99m}Tc point sources in uniform activity, reconstructed with depth-dependent RR, took more iterations to converge for sources closest to the isocenter. Furthermore, as also shown in the current study, Kappadath showed the radial FWHM takes higher iterations to converge compared to the tangential FWHM. This difference in FWHM can be seen visually, in Figure 5.13, for a 96 iteration reconstruction with the OOSC(L) correction scheme.

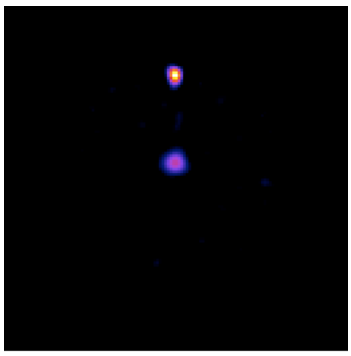

Figure 5.13: Example transverse slice of the line sources with 96 iterations of the OOSC(L) correction scheme

5.3.3 Comparison of Traditional and Perturbation Method

A comparison of FWHM for the traditional and the complex perturbation method of measurement is shown in Table 5.12.

Correction Scheme	Radial/Tangential FWHM (mm)		Central FWHM (mm)	
	Traditional	Perturbation	Traditional	Perturbation
NC(L)	11.4/8.8	11.7/8.8	11.8	11.1
NC(M)	17.7/13.1	17.3/13.1	18.7	17.3
OOSC(L)	3.8/3.4	6.9/5.4	3.5	9.7
OOSC(M)	4.6/4.2	11.3/9.7	4.4	17.7

Table 5.12: Minimum FWHM measured using the traditional and perturbation method of measurement
The estimated error for all OOSC and NC reconstructions is <0.5mm and <2.0mm respectively.

The traditional method of measuring the FWHM of point sources in air underestimated the FWHM compared with perturbation methods. This underestimation of FWHM will overestimate the SPECT system resolution performance in clinical practice. The perturbation methods will more closely represent system spatial resolution for advanced reconstruction algorithms.

The central, radial and tangential FWHM were shown to be comparable for point sources in air when reconstructed with OOSC, which includes depth-dependent RR. This finding can be attributed to faster convergence of all three measures due to limited spatial frequencies in the FOV. However, the perturbation methods demonstrated variability of FWHM with location in the FOV, which suggests that clinical quantitative accuracy will also be location dependent.

The perturbation method, with additional spatial frequencies in the FOV compared with the traditional method, has demonstrated the content dependent nature of iterative reconstruction correction schemes. The perturbation method is more representative of the clinical imaging scenario when compared with the traditional method and, consequently, is more appropriate to inform recommendations for clinical imaging protocols.

Therefore, the FWHM results as measured using the perturbation method will be used, in conjunction with the results of Chapters 4, 6, 7 and 8, to determine a recommended set of reconstruction parameters.

5.3.4 Reconstruction Time

The reconstruction time for each correction scheme versus true iterations is shown in Figure 5.14. All reconstructions incorporating CT attenuation correction perform an initial Filtered Back-projection reconstruction to confirm the spatial registration of CT and SPECT data. This step adds a fixed time overhead of 10 seconds to reconstructions.

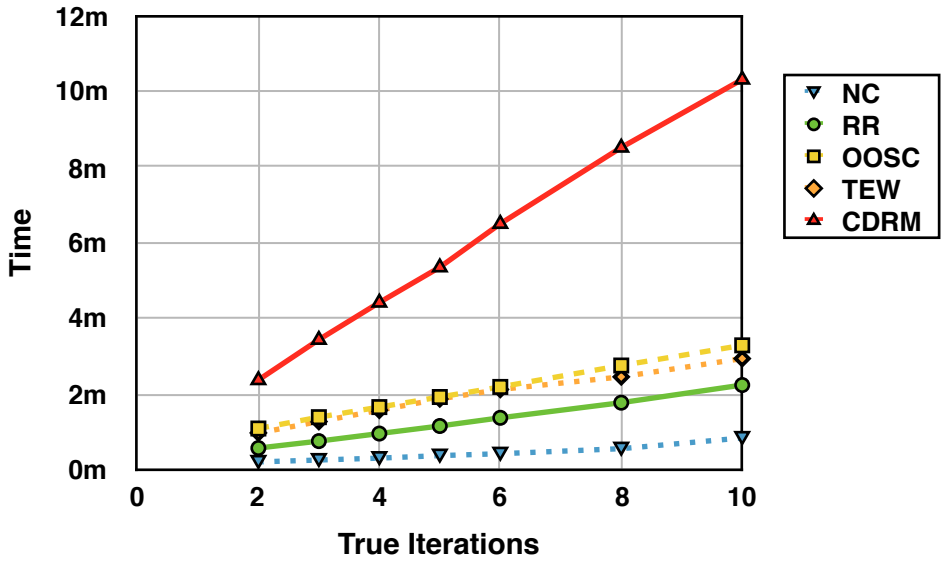

Figure 5.14: Reconstruction time versus iterations for correction schemes considered The 'true iterations' indicate the iterations described in Table 5.6. Therefore, the true iterations map to equivalent iterations in brackets as follows: 2 (2, 4 and 8 iterations), 3 (12 iterations), 4 (16 iterations), 5 (20 iterations), 6 (24, 48 and 96 iterations), 8 (128 iterations), 10 (160 iterations)

All correction schemes demonstrated a linear increase in reconstruction time with true iterations. The reconstruction time for all correction schemes, except for the CDRM method, is less than four minutes irrespective of true iterations. However, the CDRM correction scheme takes longer than 4 minutes to reconstruct for true iterations greater than 3. Furthermore, the CDRM takes over 10 minutes to reconstruct data when set to 10 true iterations.

Although using the CDRM method results in a greater reconstruction time than alternative correction schemes, it is still performed within a clinically relevant time. Therefore, reconstruction time is not a limiting factor when considering optimisation of reconstruction parameters.

For the same true iterations (6), altering the number of subsets (4, 8 and 16) made no difference to the reconstruction time.

5.4 Discussion

An aim of this Chapter was to characterise ^{123}I SPECT system resolution with regard to advanced iterative reconstruction algorithms. The traditional method of point sources in air was shown to underestimate the FWHM compared with perturbation methods. This underestimation of FWHM will overestimate the spatial resolution performance of the system in the clinical setting. Therefore, the spatial resolution figures presented in this section refer to the FWHM as measured using the complex perturbation method.

In this study, the addition of depth-dependent RR to the reconstruction algorithm was shown to have the greatest effect on measured FWHM. For example, the tangential results for LEHR data have shown that the application of RR can reduce the FWHM from 8.7±0.2mm to 5.9±0.1mm (a 38% difference). For the MELP data, the tangential FWHM reduced from 13.1±0.8mm to 10.2±0.1 when RR was employed (a 25% difference).

The addition of attenuation and scatter correction demonstrated no additional benefit over the RR reconstructions for all methods of acquisition. This is in keeping with Lawson's [5] description: "The effect of scatter on [spatial] resolution is small and so scatter … can usually be ignored." Importantly, novel reconstruction techniques were not shown to be detrimental to the FWHM.

Madsen [45] suggests a FWHM in the range of 8-9mm is preferable for ^{123}I neurology SPECT studies, while Dickson [125] suggests 15mm is a suitable maximum for central, radial and tangential FWHM. The minimum FWHM for LEHR data was 5.4±0.1mm and 9.6±0.3mm for tangential and central source measurements respectively. As spatial resolution has shown to vary with location in the FOV, the central line source measure represents the largest FWHM in a 20cm diameter cylindrical phantom with a 20cm ROR. Neurology SPECT patient studies typically have a smaller ROR as patient anatomy is less than 20cm in diameter. This smaller ROR will narrow the FWHM further and, therefore, the

complex perturbation measurements suggest LEHR collimators with RR applied is a suitable approach for clinical neurology ^{123}I SPECT studies.

However, the minimum FWHM for MELP data was 17.6±0.4mm for the central line source measurement. Although this FWHM will narrow with a smaller ROR, the evidence in this chapter suggests that, with regard to spatial resolution, MELP collimators are not suitable for clinical neurology SPECT applications.

Table 5.13 compares FWHM values quoted in the literature for ^{123}I SPECT with optimised values from this study. Figures are not directly comparable due to differences in methodology. For example, the study by Macey [16] acquired data with a 96x96 pixel matrix resulting in a pixel size of 4.5mm and the study by Rault [47] involved simulated data, a 256x256 pixel acquisition matrix, an estimated pixel width of 2.1mm and a 15.9mm ROR. Nonetheless, it is important to note Rault's simulation study quotes the lowest FWHM for LEHR and MELP collimators to date. Considering the tangential FWHM of the peripheral line source in the current study, Table 5.13 demonstrates an improvement in FWHM of 32% over the findings by Rault for the LEHR collimator, which will largely be due to the inclusion of depth-dependent RR in the current study.

Reference	Method	LEHR FWHM (mm)	MELP FWHM (mm)
Macey, 1986	96 matrix, 4.5mm pixel, 20cm ROR, FBP	~12	~17
Soret, 2006	128 matrix, 2.1mm pixel, 15.9cm ROR, OSEM	11	—
Rault, 2007	**In air:** simulation, 256 matrix, 2.1mm pixel, 100 iterations and scatter correction, OSEM	10.6	12
	In phantom: simulation, 256 matrix, 2.1mm pixel, 100 iterations and scatter correction, OSEM	7.9	13.4
Dickson, 2012	128 matrix, 2-3mm pixel, 15cm ROR, OSEM, TEW scatter correction	6-12	—
Tangential FWHM from this investigation using the complex perturbation method: 128 matrix, 20cm ROR, 2.4mm pixel OSEM		5.4	9.7

Table 5.13: Reference and FWHM of ^{123}I SPECT spatial resolution

Dickson's study [125] evaluated the ^{123}I SPECT spatial resolution of 24 gamma cameras from four manufacturers with LEHR and LEUHR parallel, and fan beam collimators. The investigation reports a minimum tangential FWHM of ~6mm. However, it is unclear from which gamma camera and collimator combination this minimum was measured.

With regard to convergence, in this investigation the LEHR and MELP data reconstructed with NC was shown to converge at 48 iterations. Correction schemes which incorporate depth-dependent RR did not converge at 160 iterations. This finding is in agreement with Kappadath [175] who demonstrated that ^{99m}Tc SPECT spatial resolution will continue to converge up to 2700 iterations. However, the rate of convergence is low between 128 and 160 iterations and, therefore, the FWHM at 160 iterations can be taken as suitably representative of the fully converged value.

As was also shown by Knoll [106] with regard to ^{99m}Tc SPECT, the current study demonstrated an elongation of line sources, which was dependent on the location of the source in the FOV. Kappadath [175] demonstrated that, for ^{99m}Tc SPECT with RR applied, this elongation was due to variable convergence rates of the iterative reconstruction algorithm. Kappadath showed that the FWHM of sources closer to the isocentre required higher iterations to converge. As spatial resolution is related to quantitative accuracy, the variable FWHM across the FOV may similarly lead to variability in quantitative accuracy.

In this investigation, the FWHM measured using perturbation methods is specific to the phantom used and acquisition parameters, such as the ROR. The same perturbation technique could be applied to anthropomorphic phantoms to more closely mimic specific imaging scenarios to measure clinical SPECT spatial resolution. Such studies have been performed by Erlandsson [171] and Badger [170] who used a method of summed data from independently acquired line source and surrounding phantom data. These authors investigated ^{99m}Tc cardiac and neurology SPECT applications respectively. However, the investigation in this thesis is both the first known practical implementation of the complex perturbation method using the same phantom for both acquisitions and the first to measure ^{123}I SPECT spatial resolution with a perturbation method.

The maximum reconstruction time measured in this investigation was 10min 19sec for the CDRM(L) correction scheme. This time can be considered acceptable for routine clinical use. Furthermore, it is less than 11.2min, which was described by Sohlberg [58] as being a significant reduction in reconstruction time in an advanced iterative algorithm acceleration study. Therefore, reconstruction time is not a limiting factor in the use of the advanced algorithms investigated in this thesis.

5.5 Conclusions

The ^{123}I SPECT system spatial resolution of data acquired with LEHR collimators and reconstructed with depth-dependent RR is suitable for neurology SPECT. However, the

spatial resolution of data acquired with MELP collimators and similarly reconstructed with RR are less suitable for neurology applications.

Advanced iterative reconstruction correction schemes failed to converge SPECT spatial resolution up to 160 iterations. However, the rate of convergence for relatively high iterations (≥96 iterations) is adequately low for LEHR data to be representative of the final converged value.

The simple perturbation method was shown to suitably approximate the complex perturbation method and is, therefore, recommended for future assessment of SPECT spatial resolution. Point source measurements in air are not suitable for characterising SPECT spatial resolution for advanced iterative reconstruction algorithms.

Finally, reconstruction time is not a limiting factor in the use of the advanced algorithms investigated in this thesis.

Chapter 6: Contrast Recovery

6.1 Introduction

Contrast Recovery (CR) describes how accurately a reconstructed image represents a known uptake to background activity concentration ratio. Improved image contrast results in enhanced detection and delineation of structures [3]. Therefore, image contrast is a critical component of the visual assessment process. Recovery of image contrast is also necessary to allow accurate quantification as greater CR increases the distinction between regions of specific and non-specific uptake. Optimisation of CR is, therefore, crucial for accurate quantification.

CR for small objects improves with spatial resolution performance due to a reduction in partial volume effect. Chapter 5 demonstrated that Siemens LEHR collimators have superior spatial resolution performance compared with MELP collimators. Therefore, LEHR collimators would seem the obvious choice to optimise the CR of small objects.

However, ^{123}I high-energy emissions result in septal penetration of low-energy collimators. As a consequence of this septal penetration, low-energy collimators have been shown to have poorer CR for ^{123}I SPECT compared with medium-energy collimators [44, 47]. The balance of spatial resolution and CR characteristics must be considered when selecting a collimator to use clinically. Historically, medium-energy collimators have been preferred to low-energy collimators where accurate quantification is required [17, 43]. Whereas LEHR collimators are preferred to achieve higher resolution images when imaging small structures [27, 44, 48, 49].

Recent advances in iterative reconstruction techniques may improve CR. In particular, Collimator and Detector Response Modelling (CDRM) of high-energy interactions may improve the CR of LEHR data. However, the number of iterations required to achieve convergence of CR for this advanced correction scheme is unknown.

An aim of the work in this Chapter was to compare the CR of ^{123}I SPECT for advanced reconstruction correction schemes. A further aim was to evaluate the convergence of CR measurements for these correction schemes. The objective of the study was to characterise CR and use these findings to support a recommendation for clinical reconstruction. This investigation included an assessment of data acquired with both LEHR and MELP collimators.

6.2 Methods and Materials

CR may refer to either Hot CR (HCR) or Cold CR (CCR). HCR measures how accurately a known uptake ratio between a region of uptake and a region of non-specific "background" activity is reproduced. CCR measures the accuracy of image contrast in photopenic regions in an image.

For clinical investigations performed locally using ^{123}I, HCR analysis is more relevant. For example, images from ^{123}I-mIBG oncology studies are assessed for the avidity of uptake in lesions and images from ^{123}I-DaTSCAN™ studies are evaluated for DaT receptor uptake compared to non-specific uptake.

While CCR is less relevant to work performed locally, it has been included for completeness.

6.2.1 Torso Phantom Description

The NEMA IEC Body phantom (manufactured by Data Spectrum Corporation, USA), used extensively in this investigation, will be referred to as the "torso" phantom. The torso shaped phantom includes six internal spheres (10mm, 13mm, 17mm, 22mm, 28mm and 37mm in diameter), a central cylindrical lung density insert and a ~9700ml background compartment (Figure 6.1).

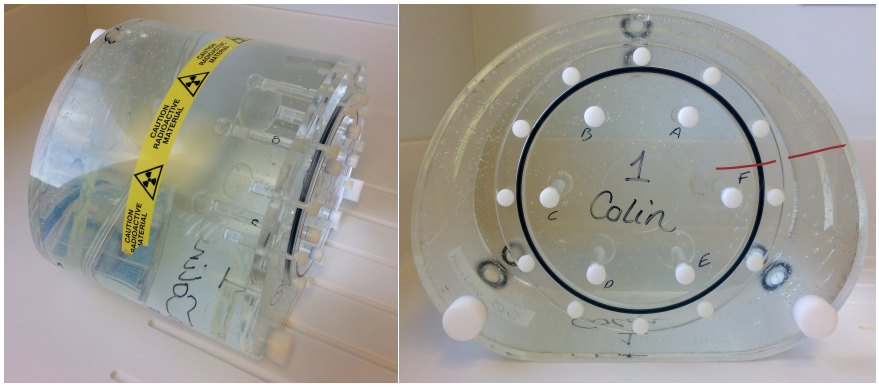

Figure 6.1: Torso shaped NEMA IEC Body phantom
NEMA IEC Body phantom, referred to in this thesis as the "torso" phantom, contains six spheres and a cylindrical lung insert (not shown)

Previous studies have measured CR using the torso phantom when assessing ^{99m}Tc SPECT [98, 106-108] and ^{131}I SPECT [111]. However, the author is not aware of any published assessment using the torso phantom for ^{123}I SPECT CR assessment. As such, the use of the phantom in itself is a novel aspect of the current investigation.

Previous investigations by Knoll [106], Armstrong [98, 176] and Brown [177] have demonstrated that ^{99m}Tc SPECT CR measurements can be affected by the orientation of spheres within the phantom. This observation is likely due to the variable convergence of spatial resolution across the FOV, as demonstrated in Section 5.3.2.4. Therefore, the sphere orientation was altered between acquisitions, to allow an average CR to be determined.

6.2.1.1 Hot Contrast Recovery (HCR) Torso Phantom Preparation

Clinical ^{123}I-mIBG studies have a broad range of uptake ratios up to 10:1 [178]. In this investigation, a sphere to background contrast ratio of 4:1 was chosen to provide a representative clinical uptake ratio. This ratio was also used by Knoll [106] and Grootjans [107] for the assessment of ^{99m}Tc SPECT CR.

The 4:1 sphere to background ratio was obtained by initially filling approximately one-quarter of the phantom background compartment with water. Following the method of Grootjans [107], ~74MBq of ^{123}I was added and, once dispersed, used to fill all six spheres. The background compartment was subsequently filled, resulting in a sphere to background activity concentration ratio of approximately 4:1. An accurate assessment of the true concentration ratio was measured from samples taken from the sphere solution and background region. The samples were counted using an auto-gamma counter. The phantom was prepared and acquired ten times to provide an indication of setup and measurement error.

6.2.1.2 Cold Contrast Recovery (CCR) Torso Phantom Preparation

The torso phantom background compartment was uniformly filled with ~74MBq of ^{123}I to match the HCR phantom setup. The six spheres were filled with water to simulate cold regions with tissue density. The phantom was prepared and acquired three times to provide an indication of setup and measurement error.

6.2.2 Torso Phantom Acquisition

A Siemens Symbia T2, previously described in Section 3.2, was used for all HCR and CCR SPECT acquisitions using LEHR and MELP collimators.

A clinically relevant count density was used to determine the phantom acquisition time. Initially, the count density in non-specific regions of 20 consecutive ^{123}I-mIBG patient studies was measured. Following this, the torso phantom was prepared with uniform activity concentration and acquired with a range of acquisition times. The acquisition of the phantom which matched the mean background count density in patient studies was used to guide the time for further phantom acquisitions. The value of total counts in the first projection of the matched phantom acquisition was used for subsequent phantom acquisitions. SPECT acquisition parameters can be seen in Table 6.1.

Parameter	LEHR	MELP
Matrix	128x128	
Zoom	1.45	
Pixel Size	3.3mm	
Projections	128	
Counts in the First Projection	57k	35k
Radius of Rotation (mean / min / max)	~19cm / ~13cm / ~25cm	
Orbit	Contoured	
Photopeak	159keV±10%	
Scatter Windows*	Lower: 138±4keV Upper: 178±4keV	

Table 6.1: Parameters for SPECT acquisition of the torso phantom
(*) Scatter windows were acquired in seven of the ten acquisitions for Triple Energy Window (TEW) correction

In this investigation, the MELP collimator was found to have 38.6% fewer total counts for the same acquisition time compared with the LEHR collimators. This finding is in agreement with the planar investigation in Section 3.5 which demonstrated that acquisitions with LEHR collimators have a greater relative sensitivity than with MELP collimators.

A sequential CT was acquired after each SPECT acquisition, with the acquisition parameters described in Table 6.2. The spatially registered CT was used as a map of attenuation coefficients for attenuation correction and Monte Carlo scatter correction.

Parameter	Value
CT mA	35mA
CT kVp	130kVp
CT Reconstruction Slice Width	3.3mm

Table 6.2: Parameters of the sequentially acquired CT

6.2.3 Torso Phantom Reconstruction

Torso phantom acquisitions were reconstructed with the correction schemes and parameters described in Table 5.4 and Table 5.5. The range of iterations investigated is outlined in Section 5.2.3. Triple Energy Window (TEW) correction was applied to seven of the ten acquisitions where appropriate energy windows were acquired.

6.2.4 Analysis of Torso Phantom Data

6.2.4.1 Determining HCR

Spherical VOIs, the same diameter as each of the six spheres in the phantom, were positioned on the CT which was spatially registered with the SPECT data. The VOIs were subsequently copied to all SPECT reconstructions. A spherical VOI, 5cm in diameter, was placed in an area of uniform background activity, centred on a transverse slice distant from the spheres. HCR was calculated using Equation 6.1:

$$HCR = \frac{\left(\frac{C_{sphere}}{C_{BG}}\right) - 1}{\left(\frac{T_{sphere}}{T_{BG}}\right) - 1}$$

Equation 6.1

where C_{sphere} was the counts in the uptake regions, C_{BG} was the counts in the background region, and T_{sphere} / T_{BG} was the true concentration ratio, determined from samples measured in an auto-gamma counter.

Using this method, HCR is the ratio of detected contrast to true contrast on a scale of 0-1, with a result of 1 indicating complete recovery of the known contrast.

6.2.4.2 Determining CCR

CCR is the ratio of counts in a cold region to counts in a background region on a scale of 0-1, with a result of 1 indicating complete recovery of a photopenic region. CCR was measured by positioning VOIs using a similar method to that used to measure HCR.

Spherical VOIs were placed on the CT. The VOIs were then copied to SPECT reconstructions. CCR was calculated using Equation 6.2:

$$CCR = 1 - (C_{sphere} / C_{BG}) \qquad \textbf{Equation 6.2}$$

6.2.4.3 Consideration of Errors

The phantom was prepared and acquired on ten occasions with a 'hot' activity concentration ratio (TEW acquisition on seven of the ten). The phantom was prepared and acquired on three occasions with 'cold' spheres. Measurements of HCR and CCR were averaged to obtain a mean value. Measurement error was estimated using twice the Standard Error (SE). The SE was determined using Equation 6.3.

$$\text{Standard Error (SE)} = SD_{CR} / \sqrt{n} \qquad \textbf{Equation 6.3}$$

where SD_{CR} is the standard deviation of the contrast measurement and n is the number of measurements. Error bars were included on results where 2*SE≥0.05.

6.2.4.4 Statistical Analysis

As with Chapter 5, the results measured in this Chapter are non-parametric in nature. Therefore, the tests described for statistical analysis in Section 5.2.5 were used in this investigation. However, the Friedman test requires a complete block of paired results. Statistical testing of HCR results which include the TEW correction scheme did not have a complete block of paired data as TEW acquisition was applied to only seven of the ten phantoms. In these instances, a Skillings-Mack test was used which is a Friedman equivalent test where missing paired data exist [179].

Convergence of the reconstruction algorithm was determined to be the number of iterations at which the CR had no statistically significant difference with the CR at 160 iterations.

As the CCR data consists of three measurements, a 95% Confidence Interval (CI) cannot be determined when performing a paired Wilcoxon tests. Therefore, for CCR results, an 80% CI is reported.

6.3 Contrast Recovery Results

6.3.1 Hot Contrast Recovery (HCR)

6.3.1.1 Initial Findings of Variability in HCR

An HCR score of 1 indicates complete recovery of the true sphere to background concentration ratio. Preliminary analysis of the torso phantom reconstructed with Collimator and Detector Response Modelling (CDRM) demonstrated a considerable variation in measurement compared with other reconstruction techniques. This variability is illustrated by the wide error bars in Figure 6.2 (left).

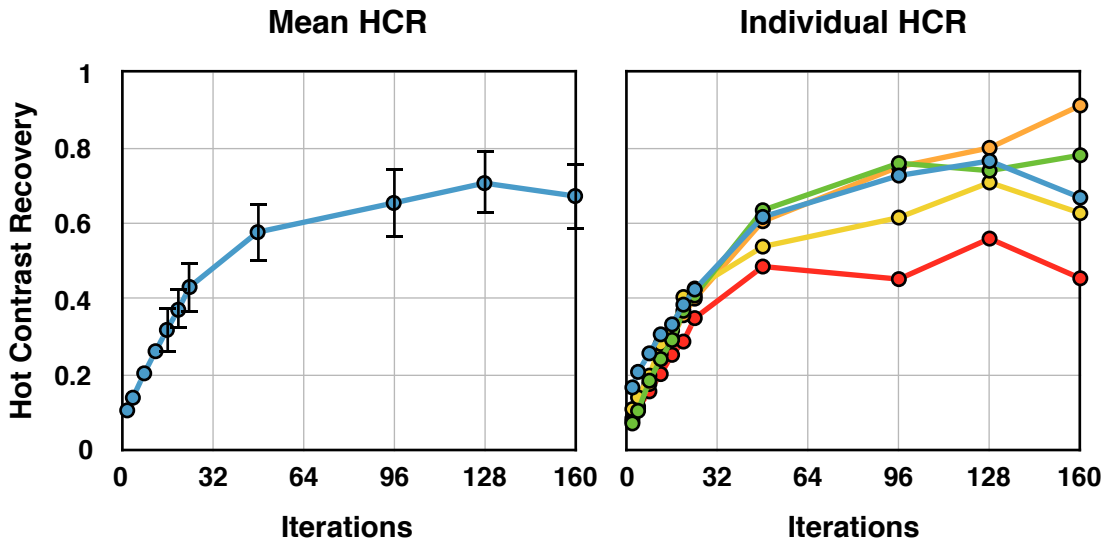

Figure 6.2: Mean HCR for 28mm sphere (left) and individual HCR measurements of the 28mm sphere (right)
All data were reconstructed with the CDRM(L) correction scheme.

The curve shown in Figure 6.2 (left) presents the mean HCR for CDRM reconstruction, which consists of 10 independent phantom acquisitions. By looking at a subset of these measurements individually (Figure 6.2, right), the HCR of the CDRM reconstruction method can be seen to be unpredictable. Increasing iterations was shown to result in both a decrease and an increase in HCR. This effect is not typical for convergence of contrast measures of an iterative algorithm [30].

The results of this initial assessment were reported to the software developer (Hermes Medical Solutions) for further investigation. On review of their CDRM algorithm, it was thought that the measurement variability was due to a limited number of photons simulated in the collimator model. Consequently, the scatter map used for correction had a noisy distribution with photon starved regions which resulted in an artefactual correction being applied. Hermes Medical Solutions revised the reconstruction algorithm with an increase in simulated photons in the collimator model by an order of magnitude [180].

The same torso phantom data was reconstructed with the updated algorithm, and individual phantom reconstructions demonstrated a more typical pattern of convergence (Figure 6.3).

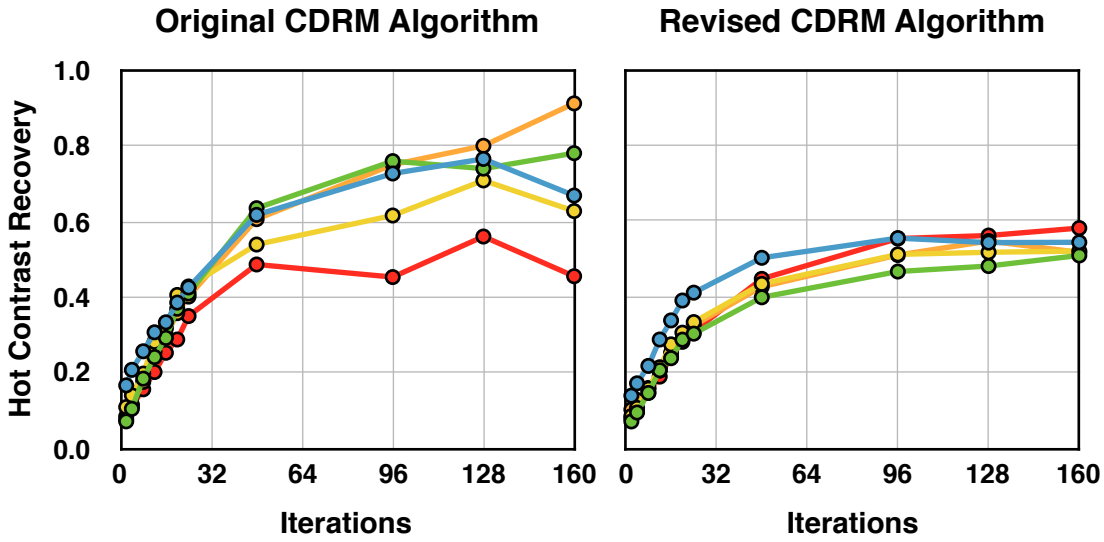

Figure 6.3: Comparison of individual HCR measurements of the 28mm sphere
Data reconstructed with the original CDRM algorithm (left) and matched reconstructions using the revised CDRM algorithm (right)

Figure 6.4 compares the mean HCR values and error from the ten phantom acquisitions reconstructed with the original algorithm and following revision to the CDRM algorithm.

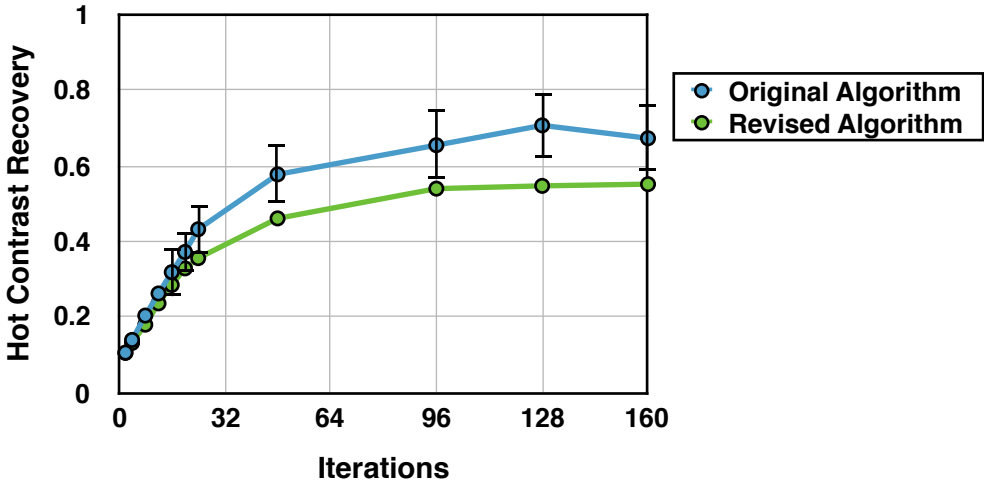

Figure 6.4: Mean HCR for 28mm sphere
Data reconstructed with original and revised CDRM algorithm. Estimated error of <0.05 not shown.

Results in Figures 6.3 and 6.4 demonstrate less variability and a more anticipated pattern of convergence when the CDRM algorithm had been revised. However, the mean HCR is lower with the revised algorithm than with the original algorithm. The original algorithm was deemed to be simulating too few photons to model high-energy septal penetration accurately. The modelled correction may then have artefactually increased HCR in regions

of noise, which would then be amplified with an increase in iterations. By increasing the number of photons, the revised CDRM algorithm is less susceptible to random fluctuations in the correction model resulting in a consistent HCR measure.

6.3.1.2 HCR: The 37mm Diameter Sphere

Of the six spheres in the phantom, the 37mm diameter sphere is least susceptible to partial volume effect. Therefore, for this investigation, the HCR results for the 37mm sphere represent the “best case scenario”. The HCR results for both the LEHR and MELP collimators for the 37mm sphere are shown in Figure 6.5.

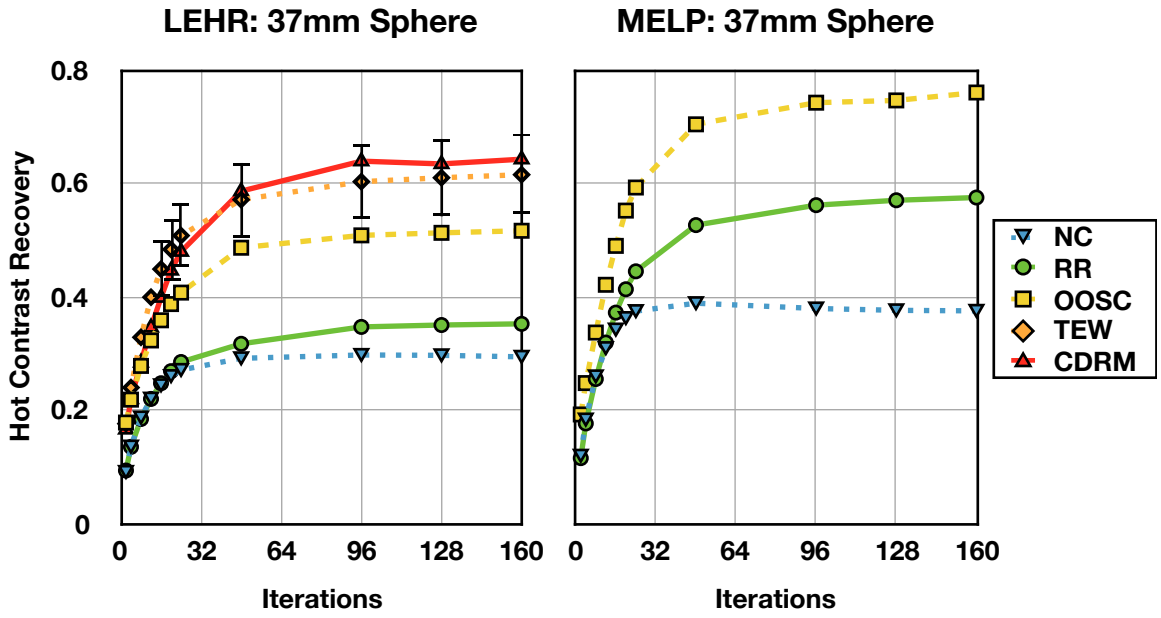

Figure 6.5: 37mm sphere HCR for LEHR acquisitions (left) and MELP acquisitions (right) TEW and CDRM not performed for MELP data. Estimated error of <0.05 is not shown.

The results demonstrate that correction schemes which include attenuation and scatter correction (OOSC, TEW and CDRM) have a higher HCR than those without (NC and RR). The results for the 37mm sphere also demonstrate that for the same reconstruction correction scheme the HCR measured with MELP data is higher than for the LEHR data (Table 6.3).

Reconstruction Scheme	LEHR		MELP	
	HCR	Iterations	HCR	Iterations
NC	0.30	96	0.39	48
RR	0.35	96	0.58	160
OOSC	0.52	160	0.76	160
TEW	0.62	160	—	—
CDRM	0.64	96	—	—

Table 6.3: Highest mean HCR value from ten acquisitions for the 37mm sphere acquired with LEHR and MELP collimators

The maximum HCR measured for the MELP acquisition data was 0.76±0.03, obtained from the reconstruction including OOSC at 160 iterations. The highest HCR measured for the LEHR data was 0.64±0.04 obtained from the reconstruction including CDRM at 96 iterations. There is a statistically significant difference between these measurements (p=0.012, CI:0.12±0.08).

For both collimators, convergence was reached at 24 iterations for the NC reconstruction as there was no statistically significant difference between the HCR at 24 iterations and 160 iterations (for NC(L) p=0.251; CI:0.02±0.04, and for NC(M) p=0.825; CI:0.00±0.04). All other reconstruction correction schemes investigated demonstrate convergence at 96 iterations, similarly having no statistically significant difference to the HCR measured at 96 and 160 iterations.

Figure 6.6 shows a box plot comparing the HCR of the 37mm sphere at 96 iterations for all correction schemes that include attenuation and scatter correction (OOSC, TEW and CDRM).

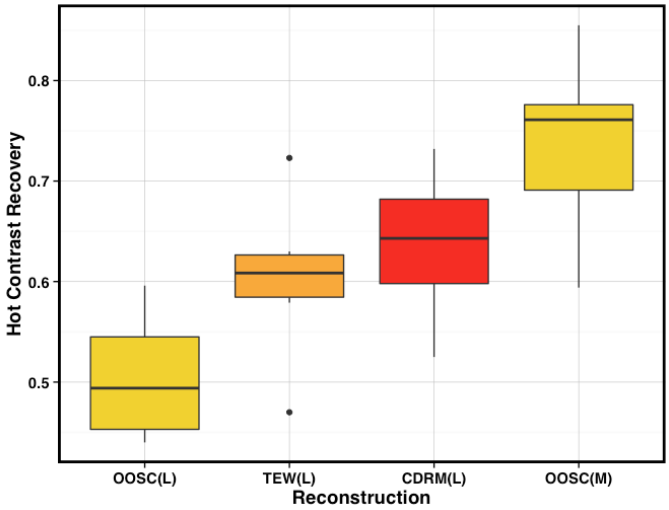

Figure 6.6: Box plot of the HCR for the 37mm sphere at convergence of the reconstruction algorithm (96 iterations) for correction schemes which include attenuation and scatter correction

At 96 iterations (convergence) there is a statistically significant difference between the LEHR and the MELP data with the OOSC reconstruction scheme ($p<0.001$, CI:0.23±0.08). This finding highlights the detrimental effect of high-energy septal penetration on the quantitative accuracy of the LEHR collimator data. Furthermore, the 96 iteration MELP reconstruction has a statistically significant difference compared with the 96 iteration LEHR TEW ($p=0.013$, CI:0.14±0.10) and CDRM ($p=0.019$, CI:0.10±0.07) methods, which both correct for high-energy septal penetration. This finding suggests that, even with relatively poor spatial resolution, the MELP collimator more accurately recovers image contrast in the 37mm sphere compared to the LEHR data with software correction for high-energy interactions.

There is no statistically significant difference between the 96 iteration LEHR TEW and CDRM methods ($p=0.463$, CI:0.04±0.08).

Neither LEHR or MELP reconstructions fully recovered image contrast (HCR=1). A study by Kojima [102] demonstrated that objects larger than 2.5 times the spatial resolution (FWHM) of the gamma camera can be accurately quantified. In the current study, the spatial resolution of the gamma camera would have to be less than 14.8mm to accurately recover the contrast ratio of 4:1 in the 37mm sphere. The lowest FWHM of SPECT spatial resolution measurements, using the perturbation method, was 5.4mm with LEHR collimators and 9.7mm with MELP collimators (Section 5.3.2). Therefore, spatial resolution is sufficient to accurately quantify image contrast at the centre of the 37mm sphere. However, each VOI used for HCR measurement is comprised of a series of ROIs, one on each transverse slice. Therefore, the individual ROIs will have a smaller diameter than

37mm towards the superior and inferior edges of the VOI than at the centre (Table 6.4). Consequently, the measurements for both collimators will suffer from partial volume effect. This effect is one reason why the maximum HCR results are not 1.

ROIs	Voxels	Diameter (mm)
1 and 11	21	16.7
2 and 10	46	25.9
3 and 9	69	31.3
4 and 8	89	34.6
5 and 7	96	36.4
6	98	37

Table 6.4: Dimensions of constituent circular ROIs which make up a 37mm diameter spherical VOI

The LEHR acquisitions with TEW corrections are the only results with an error estimate greater than or equal to 0.05, as indicated by the error bars in Figure 6.5. The additional variability compared with other correction schemes can be explained by the measurement of fewer phantoms (seven versus ten) resulting in a larger SE.

6.3.1.3 HCR: The 28mm Diameter Sphere

The sphere with a diameter of 28mm has a volume of 11.5ml. This volume corresponds to that of a typical striatum (11.2ml) [31]. Although a different shape and thus susceptible to different partial volume effect, the 28mm sphere can be considered a good indicator of a typical region of uptake in a normal clinical ^{123}I-DaTSCAN™ study. The HCR results for the 28mm sphere acquired with both LEHR and MELP collimators can be seen in Figure 6.7.

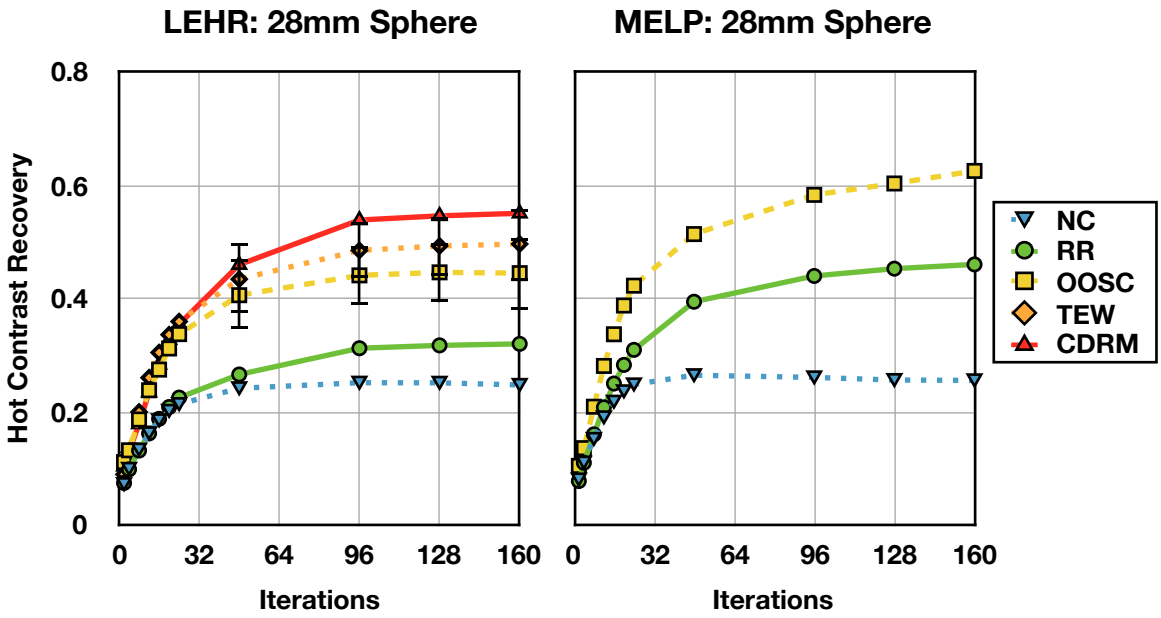

Figure 6.7: 28mm sphere HCR for LEHR acquisitions (left) and MELP acquisitions (right) TEW and CDRM not performed for MELP data. Estimated errors <0.05 are not shown.

The HCR measurements of the 28mm diameter sphere are smaller than that for the 37mm sphere due to increasing partial volume effect. Again, correction schemes which include attenuation and scatter (OOSC, TEW and CDRM) have a higher HCR than those without (NC and RR). As with the 37mm sphere, a “like-for-like” comparison between LEHR and MELP reconstructions shows the MELP has higher HCR (Table 6.5).

Reconstruction Scheme	LEHR		MELP	
	HCR	Iterations	HCR	Iterations
NC	0.25	96	0.27	48
RR	0.32	160	0.46	160
OOSC	0.45	128	0.63	160
TEW	0.50	160	—	—
CDRM	0.55	160	—	—

Table 6.5: Highest HCR value for the 28mm sphere acquired with LEHR and MELP collimators

The largest HCR recorded for the MELP collimator (0.63±0.03 at 160 iterations with the OOSC correction scheme) has a statistically significant difference (p=0.038; CI:0.10±0.08) compared to the largest HCR recorded for the LEHR collimator (HCR of 0.55±0.05 at 128 iterations with the CDRM correction scheme).

Again, convergence was determined based on a test of statistically significant difference with 160 iterations for each correction scheme. The LEHR NC reconstruction converged at 48 iterations (p=0.314; CI:0.01±0.01). The MELP NC reconstruction converged at 24 iterations (p=0.260; CI:0.01±0.02). The LEHR HCR converges at 96 iterations for all other reconstruction correction schemes. However, the HCR does not converge for the MELP RR and OOSC correction schemes. These reconstructions continue to increase with significant difference in measurements between the 128 and 160 iterations for RR (p=0.008; CI:0.01±0.00) and for OOSC (p=0.046; CI:0.02±0.02) reconstructions.

This finding was also demonstrated by Grootjans [107] when investigating HCR using the torso phantom for ^{99m}Tc SPECT with LEHR collimators. Grootjans noted the 37mm sphere converged at 96 iterations using both Hermes Medical Solutions and Siemens reconstruction algorithms, whereas the HCR of the 22mm and 28mm sphere continued to increase to the 160 and 288 iterations tested for Hermes Medical Solutions and Siemens algorithms respectively.

Figure 6.8 shows a box plot which compares reconstructions which include attenuation and scatter correction for the LEHR collimator at 96 iterations (converged) and the MELP at 160 iterations.

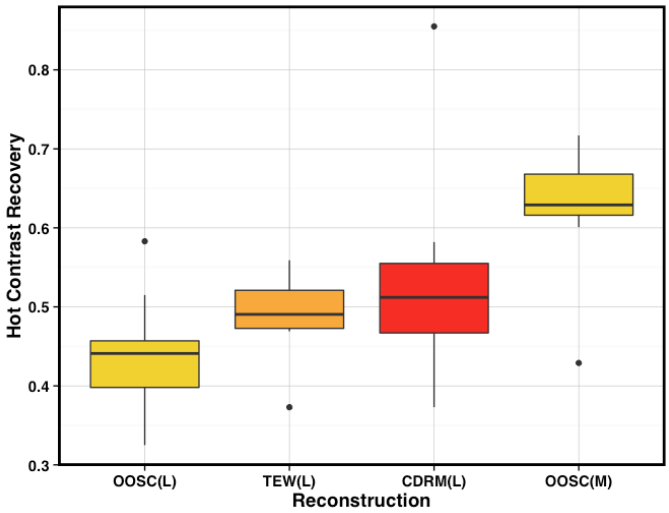

Figure 6.8: Box plot of the HCR for the 28mm sphere for correction schemes which include attenuation and scatter correction
OOSC(L), TEW(L) and CDRM(L) are at convergence of the reconstruction algorithm (96 iterations). OOSC(M) is at 160 iterations.

As with the 37mm sphere, there was no statistically significant difference between the HCR of the TEW(L) and CDRM(L) reconstruction methods at 96 iterations (p=0.345 CI: 0.02±0.06).

6.3.1.4 HCR: The 17mm and 22mm Diameter Sphere

The previous section described the 28mm sphere as indicative of HCR for a normal ^{123}I-DaTSCAN™ patient study. However, abnormal clinical studies will exhibit diminished uptake in the striatum. Therefore, the 22mm and 17mm spheres can be used as indicators of the image contrast in abnormal clinical studies.

The 22mm and 17mm diameter spheres have a 50% and 77% reduction in volume respectively compared with the 28mm sphere. The HCR results for the 22mm sphere acquired with LEHR and MELP collimators are shown in Figure 6.9.

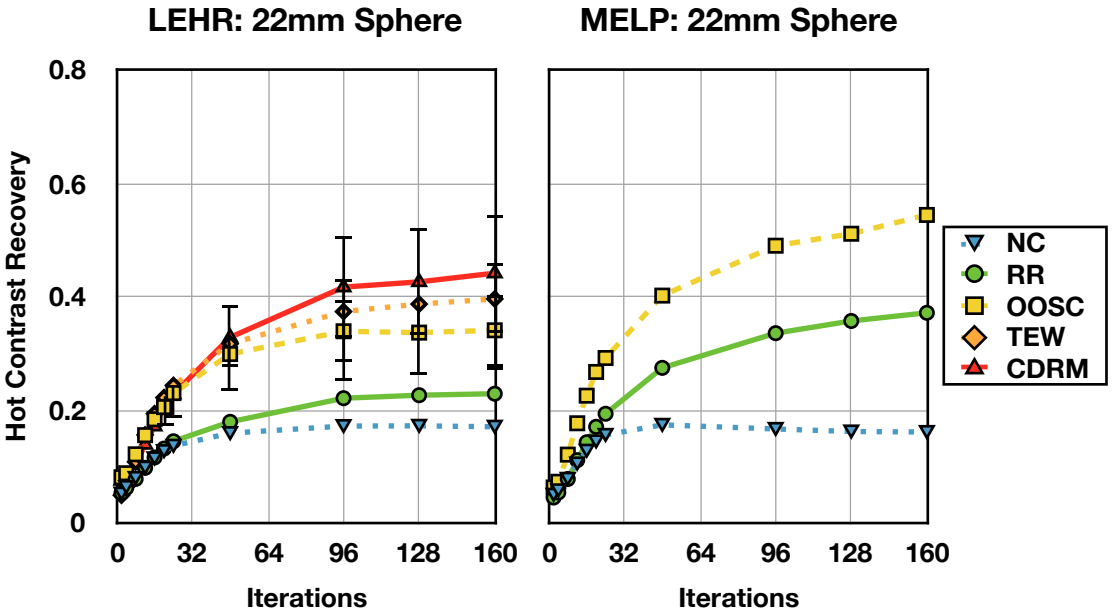

Figure 6.9: 22mm sphere HCR for LEHR acquisitions (left) and MELP acquisitions (right) TEW and CDRM not performed for MELP data. Estimated errors <0.05 are not shown.

Partial volume effect reduces the HCR measurement for the 22mm diameter sphere compared with the 37mm and 28mm spheres.

The highest HCR was 0.54±0.04, from data acquired with MELP collimators and reconstructed with OOSC. The highest HCR measured from LEHR data was 0.44±0.10 reconstructed with the CDRM method. There is no statistically significant difference at 160 iterations between the highest HCR of the CDRM(L) and the TEW(L) (p=0.600; CI: 0.04±0.23), or the OOSC(M) (p=0.133; CI:0.11±0.13).

Regarding convergence, the pattern of results for the 22mm diameter sphere is similar to that demonstrated with the 28mm sphere results. Again, the reconstruction of MELP data with RR and OOSC show continued increase in HCR up to 160 iterations, with a

statistically significant difference in HCR between 128 and 160 iterations (p=0.028; CI: 0.03±0.03).

For the 22mm, 28mm and 37mm spheres, reconstruction of LEHR data with correction schemes which include attenuation and scatter correction showed no significant difference between the CDRM and TEW method (Table 6.6).

Comparison		Sphere Diameter		
		22mm	28mm	37mm
OOSC	TEW	0.463	0.028	0.028
OOSC	CDRM	0.012	0.011	0.008
CDRM	TEW	0.463	0.345	0.463

Table 6.6: p-values for tests of statistically significant difference at 96 iterations between correction schemes employed to LEHR data
Green font indicates statistically significant difference (p-value <0.05). Red font indicates no statistically significant difference (p-value ≥0.05).

However, there was a statistically significant difference between the OOSC(L) and CDRM(L) for all three of the largest spheres in the torso phantom, and between OOSC(L) and TEW(L) for the two largest.

The HCR results for the 17mm sphere acquired with LEHR and MELP collimators are shown in Figure 6.10.

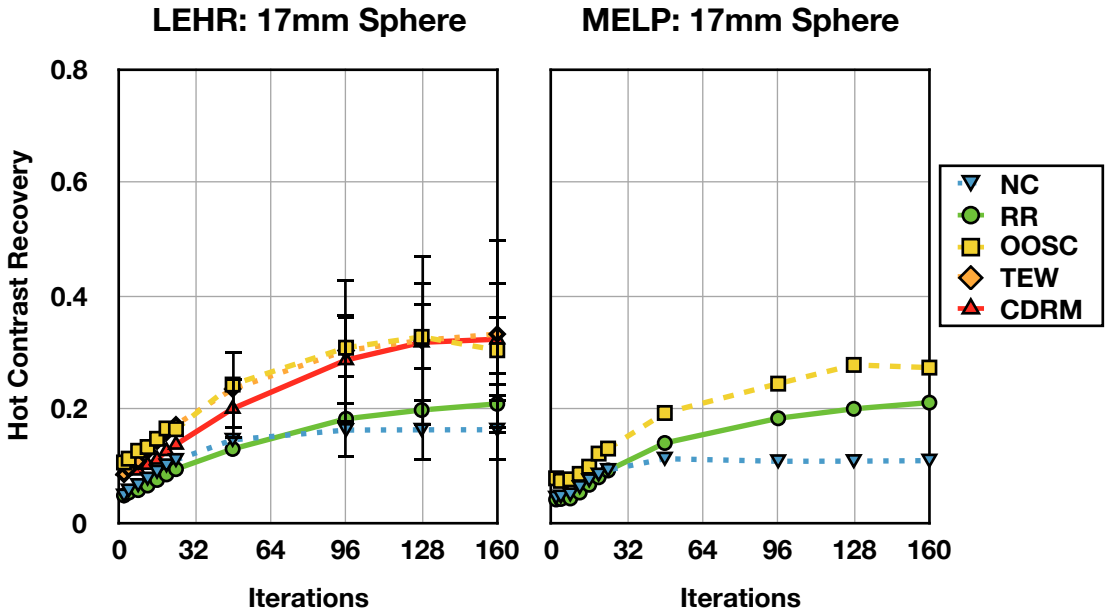

Figure 6.10: 17mm sphere HCR for LEHR acquisitions (left) and MELP acquisitions (right) TEW and CDRM not performed for MELP data. Estimated errors <0.05 are not shown.

The highest HCR for the 17mm diameter sphere was 0.32±0.11 from data acquired using the LEHR collimators and reconstructed with the CDRM method. The highest HCR recorded using the MELP collimators was 0.28±0.05, reconstructed using OOSC. However, there is no statistically significant difference with the highest LEHR and MELP measurement (p=0.402; CI:0.06±0.16).

For larger spheres, the MELP data demonstrated a higher HCR, with statistically significant difference, compared with LEHR reconstructions. However, for the 17mm sphere, there is no statistically significant difference. This finding is due to the relatively poorer spatial resolution of the MELP collimator data relative the LEHR collimator data, which results in greater partial volume effect.

6.3.1.5 HCR: The 10mm and 13mm Diameter Sphere

The HCR of the 13mm and 10mm spheres are further reduced for both collimators due to partial volume effect. There is no statistically significant difference between the maximum HCR for any of the reconstruction methods due to the relatively large variability in measurement for these smallest two spheres. Therefore, again, there is no statistically significant difference between the highest HCR measured for the LEHR and MELP collimator data for the 13mm (p=0.627; CI:0.05±0.17) or 10mm diameter spheres (p=0.354; CI:0.12±0.26) (Table 6.7).

	LEHR: CDRM		MELP: OOSC		Statistical Difference	
Sphere	**Max HCR**	**Iterations**	**Max HCR**	**Iterations**	**p=**	**CI**
37mm	0.64	96	0.76	160	0.012	0.12±0.08
28mm	0.55	128	0.63	160	0.038	0.10±0.08
22mm	0.44	160	0.54	160	0.133	0.11±0.13
17mm	0.32	128	0.28	128	0.566	0.05±0.15
13mm	0.25	128	0.27	128	0.627	0.05±0.17
10mm	0.21	160	0.12	160	0.354	0.12±0.26

Table 6.7: Maximum HCR measured for the six spheres acquired with LEHR and MELP collimators
Green font indicates statistically significant difference (p-value <0.05). Red font indicates no statistically significant difference (p-value ≥0.05).

The diameter of the 13mm sphere is less than 2.5 times the FWHM spatial resolution of the gamma camera requirement suggested by Kojima [102] for accurate SPECT quantification. The minimum FWHM measured for the LEHR and MELP collimators was 5.4mm and 9.7mm respectively (Section 5.3.2). Therefore, it is unsurprising that relatively

low HCR, with large errors due to low signal to noise ratio, was measured for the 13mm and the 10mm sphere.

An example transverse slice of the torso phantom reconstructed with 96 iterations for each correction scheme is shown in Figure 6.11.

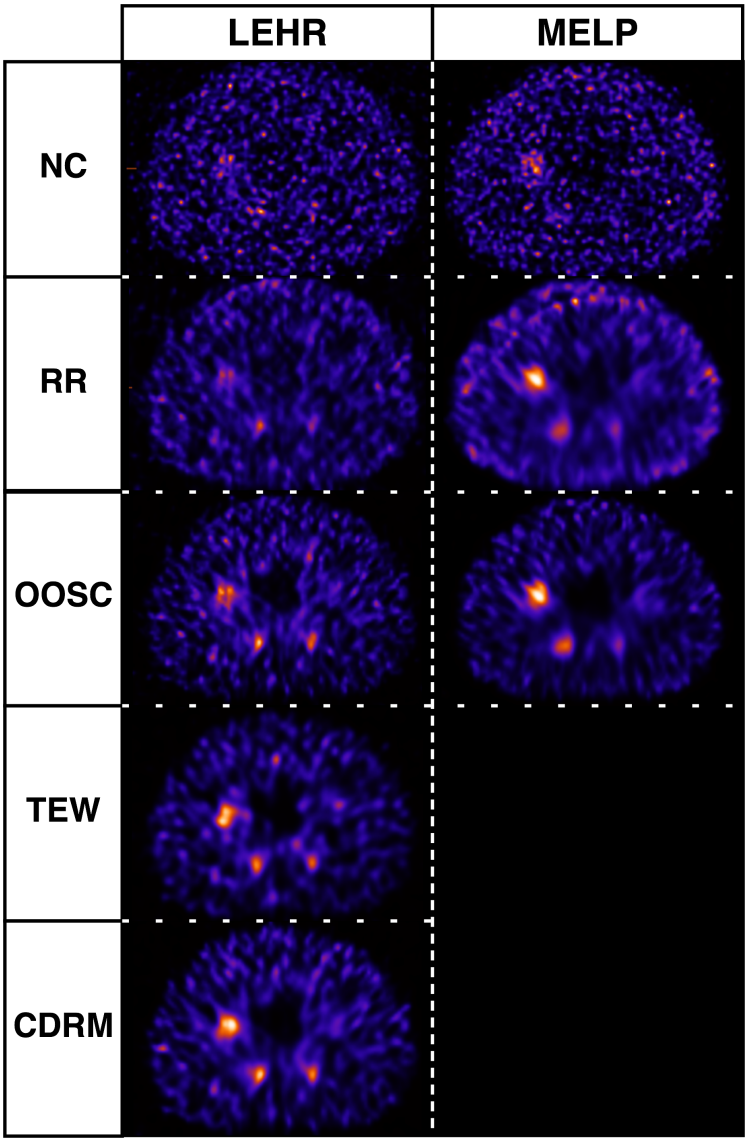

Figure 6.11: Transverse slice for each correction scheme at ninety-six iterations

Subjective visual assessment of the images in Figure 6.11 suggests that the 17mm sphere was most apparent for the CDRM(L) correction scheme. This appearance confirms the results which indicate that the HCR of the 28mm and 37mm diameter spheres is higher for the OOSC(M) scheme while the HCR of the 17mm sphere is higher for the CDRM(L) scheme. One explanation for this observation may be due to the superior spatial resolution of the CDRM(L) scheme relative to the OOSC(M) scheme.

6.3.2 Cold Contrast Recovery (CCR)

6.3.2.1 CCR: The 37mm Sphere

As was found for HCR, the CCR for the 37mm sphere is larger for data acquired with MELP collimators than LEHR collimators (Figure 6.12).

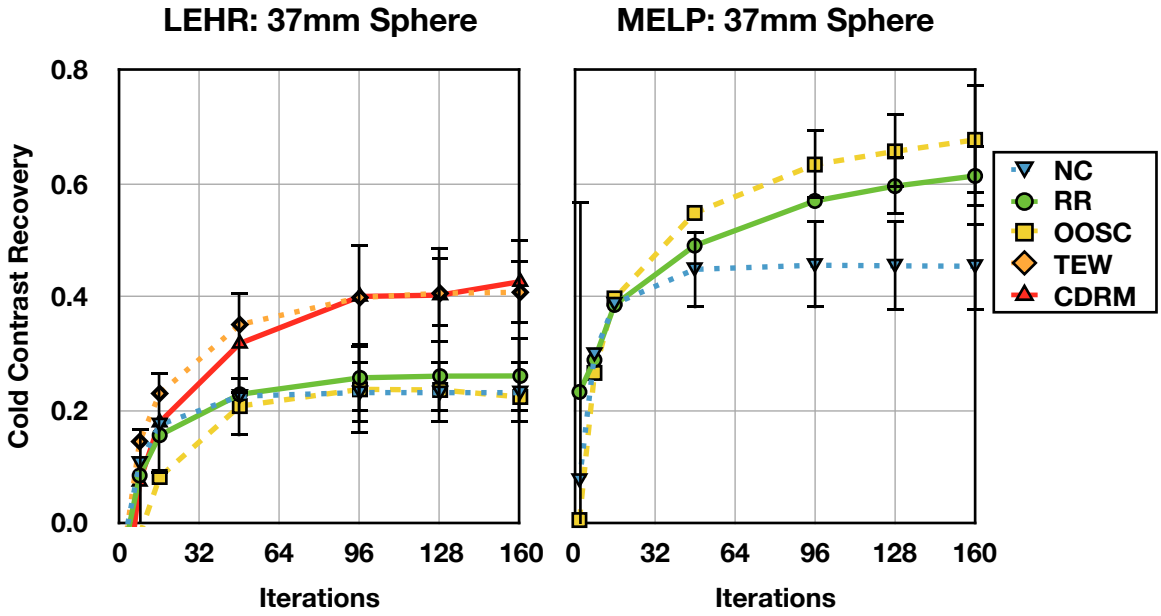

Figure 6.12: 37mm sphere CCR for LEHR acquisitions (left) and MELP acquisitions (right)

For the LEHR data reconstructed with attenuation and scatter correction, the CCR of the correction schemes which include correction for septal penetration (TEW and CDRM) is higher than the scheme without (OOSC). This finding demonstrates that the septal penetration corrections are relatively successful at the removal of counts from regions where no activity is present.

There is no statistically significant difference between the largest CCR of the CDRM(L) and TEW(L) reconstruction (p=0.827; CI:0.04±0.07). However, both have a statistically significant difference from the largest CCR of the OOSC(L) reconstruction (0.24±0.08) (p=0.050; CI:0.21±0.06 and p=0.050; CI:0.19±0.06 respectively).

At 160 iterations the CCR of MELP acquisitions with OOSC is 0.68±0.10, which has a statistically significant difference compared to the largest CCR of the LEHR acquisitions reconstructed with CDRM (0.43±0.06) and TEW (0.41±0.07) (p=0.050; CI:0.24±0.11 and p=0.050; CI:0.28±0.10 respectively). The wider error bars for the CCR measurements compared with the HCR measurements are due to increased measurement error. Three measures of CCR were made compared with ten measures of HCR.

With regard to convergence, there is no statistically significant difference between the CCR of the MELP reconstruction with OOSC at 128 and 160 iterations (p=0.593; CI: 0.03±0.04). However, the large error due to small sample size means that it is more difficult to demonstrate a statistically significant difference. This observation holds for statistical testing of all the CCR results.

6.3.2.2 CCR: The 28mm Sphere

As with the 37mm sphere, the largest CCR measured for the 28mm sphere was using the MELP with OOSC at 160 iterations (0.51±0.07) (Figure 6.13).

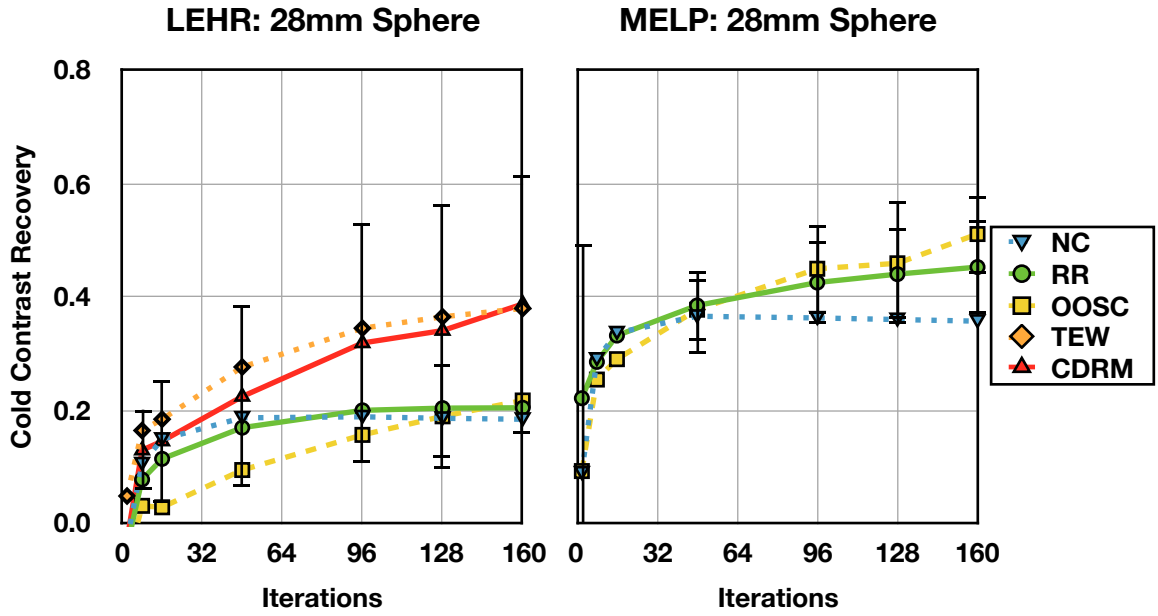

Figure 6.13: 28mm sphere CCR for LEHR acquisitions (left) and MELP acquisitions (right)

The CCR for the OOSC(M) correction scheme was higher, with a statistically significant difference, than the CDRM(L) scheme at 160 iterations (p=0.050; CI:0.10±0.09). There is no statistically significant difference between the CDRM and TEW CCR measurements at 160 iterations (p=1.00; CI:0.06±0.23).

The OOSC(L) correction scheme had a lower CCR than the TEW(L) and CDRM(L) which, similar to the 37mm sphere, demonstrates that the septal penetration corrections are relatively successful at the removal of counts from regions where no activity is present.

6.3.2.3 CCR: The 22mm Sphere

Although CCR for the 22mm diameter sphere appears larger than for the 28mm sphere for the LEHR reconstructions, the variability of the measurement for all methods is also larger (Figure 6.14). The variability reflects the increasing influence of partial volume effect as the sphere size reduces. Partial volume effect causes photons that have originated

from the background compartment of the phantom to appear as counts that have spilled into cold regions. These are then amplified by attenuation correction and included in the spherical measurement VOI.

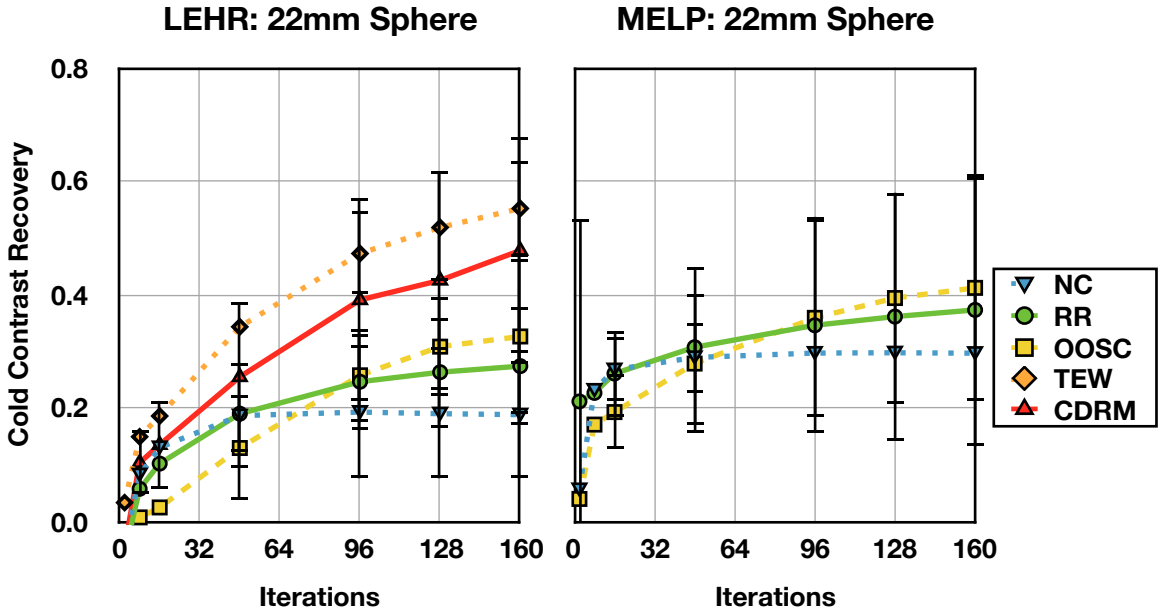

Figure 6.14: 22mm sphere CCR for LEHR acquisitions (left) and MELP acquisitions (right)

For sphere sizes smaller than 22mm the variability dominates all acquisition/ reconstruction combinations. The measures, therefore, become unreliable and are not presented here.

6.4 Contrast Recovery Discussion

An aim of this investigation was to use the torso phantom to optimise contrast recovery for ^{123}I SPECT advanced reconstruction correction schemes. A key finding of the study is that, for LEHR and MELP collimator acquisitions, HCR can be improved with correction schemes which include attenuation and scatter correction (OOSC, TEW and CDRM).

The highest HCR for the 28mm and 37mm sphere was obtained with the OOSC(M) correction scheme, which demonstrated a higher HCR than all methods of LEHR reconstruction with a statistically significant difference. Although the HCR for the 10mm and 17mm sphere was highest for the CDRM(L) reconstruction, there was no statistically significant difference with the OOSC(M) reconstruction. Therefore, these findings suggest that MELP collimators are the preferred option for clinical applications where image contrast is the primary requirement.

Considering the correction schemes employed for LEHR data, the OOSC reconstruction had a lower HCR than the TEW and CDRM with a statistically significant difference for the

22mm, 28mm and 37mm sized spheres at 96 iterations (Table 6.6). The HCR results suggest the OOSC method is not the optimum method for reconstructing LEHR data. This finding is unsurprising as OOSC does not correct for high-energy emissions, whereas CDRM and TEW do. Therefore, for LEHR data, either CDRM or TEW should be used to maximise image contrast.

One of the aims of this Chapter was to recommend the number of iterations to be used clinically for reconstruction of ^{123}I SPECT based on contrast recovery. For the LEHR collimator acquisitions, HCR was found to converge at 96 iterations for larger spheres in the phantom (28mm and 37mm in diameter) for all reconstruction methods. This observation is in agreement with findings from Dickson [30] who used a striatal phantom with uptake regions of the same volume as the 28mm sphere and concluded that 100 iterations were suitable for convergence.

While the OOSC(L) reconstruction continued to demonstrate convergence at 96 iterations for the 17mm and 22mm spheres, the CDRM(L) and TEW(L) reconstructions converged at 128 iterations. This finding shows that converging HCR takes longer for the CDRM and TEW algorithms to achieve for relatively small spheres which are more susceptible to partial volume effect.

For the 17mm and 22mm diameter spheres, there was a statistically significant difference between the HCR at 96 and 160 iterations for the CDRM(L) and TEW(L) correction schemes. However, the actual increase in HCR from 96 to 160 iterations was relatively minor (0.01 and 0.01 respectively for the 22mm sphere, and 0.03 and 0.02 respectively for the 17mm sphere). These are not clinically significant differences and, therefore, the HCR at 96 iterations can be assumed to be sufficiently converged.

Detectability is influenced by contrast and noise. As noise increases with iterations, which will be investigated in Chapter 7, it is, therefore, recommended that a 96 iteration reconstruction is used clinically for LEHR acquisitions of ^{123}I SPECT.

Similarly, for the MELP collimator data, largest sphere (37mm in diameter) converged at 96 iterations. Smaller spheres failed to converge within 160 iterations. A statistically significant difference was demonstrated between 128 and 160 iterations for the 22mm and 28mm diameter spheres. However, again, the difference in HCR was relatively small and not of a clinically significant difference (0.03 and 0.02 respectively for the OOSC

reconstruction scheme). Therefore, a 96 iteration reconstruction is also recommended clinically for MELP acquisitions of ^{123}I SPECT.

In this investigation, HCR was determined from VOIs with the same diameter as the spheres being analysed. However, an alternative method of analysis could have been used to evaluate contrast ratios. For example, Tossici-Bolt used The Southampton Method (outlined in Section 2.6.1.2) to measure uptake ratios [31]. The method reduces partial volume effect by using a relatively large VOI and subtracting a mean background value from each pixel. Reducing partial volume effect may have more clearly demonstrated convergence of small spheres in this study. However, Dickson, using the Southampton Method, is in agreement with the findings of this investigation, in that ^{123}I SPECT reconstruction suitably converges contrast ratio at ~100 OSEM iterations.

Crespo [24] measured a contrast ratio of 0.68 when applying the OOSC reconstruction technique to a Monte Carlo simulation of striatal phantoms. The study simulated phantoms with an ^{123}I uptake to background concentration ratio of between 1:1 and 7:1 which were acquired with low-energy collimators. This compares to the HCR of the 28mm diameter sphere of 0.45±0.05 for the LEHR acquisitions reconstructed with OOSC. However, a number of factors should be considered when comparing these measurements. The low-energy Siemens E.Cam collimator simulated by Crespo had a greater hole diameter (1.28mm) than the Siemens Symbia LEHR collimator (1.11mm) used in this study. The Crespo study also simulated an acquisition with a smaller ROR (15cm versus contoured), larger pixels (3.9mm versus 3.3mm) and narrower photopeak energy window (15% versus 20%). Most significantly, Crespo increased ROIs sizes to reduce partial volume effect from the measurement and performed a 256 iteration reconstruction. Therefore, comparison should only be considered as indicative of the contrast recovery of ^{123}I SPECT with LEHR collimators. The optimum result in this practical study (0.71±0.08), achieved when incorporating CDRM in LEHR reconstructions, compares favourably with Crespo's simulation study with OOSC (0.68).

The CCR results reflected the findings of the HCR results in that the CCR of MELP reconstructions is higher than those of LEHR. As with HCR, correction schemes which include attenuation and scatter correction improve CCR compared to those schemes without. However, an exception is the CCR of the OOSC correction of LEHR data which was less than that of TEW(L) and CDRM(L), and no different to RR(L), which does not correct for attenuation and scatter. This finding is due to an absence of correction for high-

energy septal penetration by the OOSC algorithm which, in this case, has increased counts in phantom compartments which contain no activity.

6.5 Contrast Recovery Conclusions

This Chapter aimed to investigate the CR of ^{123}I SPECT in order to inform recommendations for clinical reconstruction. The OOSC(M) acquisition and reconstruction scheme was shown to have a higher HCR for large spheres in the phantom (>22mm) than alternative methods, with a statistically significant difference. The CCR was also higher for the two largest spheres. Therefore, the OOSC(M) method should be used clinically where CR is the primary objective.

Evaluation of the HCR of ^{123}I SPECT data acquired with LEHR collimators demonstrated that the CDRM scheme most accurately recovered image contrast. The HCR of CDRM(L) reconstructions was not significantly different from OOSC(M) method for spheres ≤22mm in diameter.

CCR measurements using LEHR and MELP collimators demonstrated no significant differences between any reconstruction methods for spheres of diameter ≤22mm, in part due to the large variability in the measure.

A further aim of this Chapter was to determine the number of iterations suitable for clinical reconstruction, with regard to CR. For both collimators, reconstructions including corrections for attenuation and scatter converge at 96 iterations for spheres ≥28mm. However, these methods fail to converge for smaller spheres up to the maximum number of iterations investigated (160 iterations).

The HCR of iterations higher than 96, although demonstrating a statistically significant difference, resulted in a relatively small improvement in HCR. This minor increase in HCR would incur a penalty of increased noise, which will be discussed fully in Chapter 7.

In this study, the use of the torso phantom to assess ^{123}I SPECT CR was, in itself, a novel approach. The investigation has shown the torso phantom to be a useful tool in characterising the CR of ^{123}I SPECT.

In summary, MELP acquisition with the OOSC reconstruction scheme demonstrated the highest HCR and CCR. For LEHR acquisitions, CDRM demonstrated the highest HCR

and CCR. Ninety-six iterations was shown to suitably convergence CR for all reconstruction methods for spheres ≥28mm in diameter.

Chapter 7: Noise

7.1 Introduction

Noise is random variation in pixel intensity, which affects the precision of quantification [40]. Noise in nuclear medicine planar imaging is a result of the Poisson nature of the radioactive decay process. The noise level can be measured as the ratio of the standard deviation of counts detected to the counts detected (the standard deviation is $\sqrt{N}$ where N is the counts detected). This Poisson statistical relationship holds true for planar imaging. However, as SPECT reconstruction algorithms perform complex mathematical computations, this relationship cannot be assumed. Nonetheless, image count density will determine the noise level in the image.

The effect of count density on noise has been assessed by Bailey [112] for ^{99m}Tc SPECT FBP reconstructions. Bailey determined that the noise level varied with approximately $\sqrt{N_{recon}}$, where N_{recon} was the total counts in the FBP reconstructed volume. However, Schmidtlein [113] determined that this Poisson relationship did not hold for iterative reconstruction in PET imaging due to nonlinearity of the algorithm. An evaluation of the Poisson relationship has not been performed for ^{123}I SPECT in general, or with regard to novel iterative reconstruction algorithms. Therefore, to assess noise, it is necessary to investigate the effect of count density for ^{123}I SPECT reconstruction algorithms with and without advanced corrections.

Noise level is often described using Image Roughness (IR), which is a measure of how noise varies from voxel-to-voxel in a reconstructed volume (see Section 2.5.3). Background Variability (BV), which relates to how noise varies from region-to-region within an image, can also be used to describe noise properties. Schmidtlein [113] has demonstrated that noise in iterative reconstructions is position dependent. Therefore, in the following investigation, an evaluation of noise was performed by measuring both the IR and the BV within a torso phantom.

OSEM/MLEM reconstruction algorithms performed with a high number of iterations converges the estimated distribution towards the true activity distribution. However, a known limitation of these algorithms is amplification of noise with an increase in the number of iterations. Although Chapter 6 demonstrated that contrast improved with an increase in the number of iterations, observer detection is influenced by a combination of both contrast and noise [3]. Therefore, an appreciation of noise must be included in any assessment of reconstruction parameters. The following work included an evaluation of the relationship between noise and iterations for ^{123}I SPECT with advanced reconstruction correction schemes.

The aim of this Chapter is to characterise noise in ^{123}I SPECT with respect to advanced reconstruction algorithms. To achieve this aim, noise in ^{123}I SPECT iterative reconstruction was characterised by an investigation of:

- the Poisson relationship between acquired counts and Image Roughness (IR)
- the Background Variability (BV) within a torso phantom
- the amplification of IR with iterations

Additionally, as observer detection is influenced by both contrast and noise, Contrast Recovery (CR) results from Chapter 6 were combined with the findings of this Chapter. The aim of the latter investigation was to characterise the Contrast to Noise Ratio (CNR) for advanced reconstruction correction schemes.

The assessment of noise in this Chapter will be used in conjunction with the results from Chapters 4, 5, 6 and 8 to inform the reconstruction parameters used for quantification in subsequent Chapters.

7.2 Methods and Materials

7.2.1 Image Roughness versus Acquired Count Density Method

7.2.1.1 Torso Phantom Acquisition

The assessment of whether a Poisson relationship with acquired count density holds for ^{123}I SPECT iterative reconstruction was investigated by gating SPECT acquisitions with an Electrocardiography (ECG) simulator. This technique allows data to be rebinned into reduced acquisition time data sets [112, 113, 181, 182] and, thus, a range of count densities.

An ECG simulator was connected to a Siemens Symbia T2 to generate a regular trigger during data acquisition. The ECG simulator was set to generate a normal QRS wave each second (60 beats per minute). Each second of SPECT data acquisition was divided into 8 frames (Figure 7.1). Each frame is an independent acquisition with true counting statistical noise (i.e. is not a simulated reduced count frame).

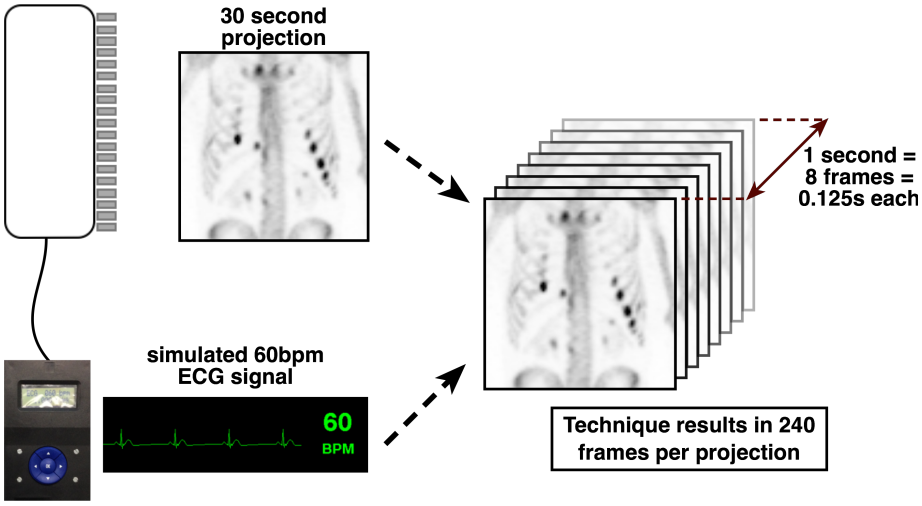

Figure 7.1: Example of ECG gating technique
In this example, the gamma camera uses a 30 second per projection acquisition time. The ECG simulator outputs a QRS trigger at 1 second intervals. Each second of data was divided into 8 frames.

For the IR versus count density investigation, the background compartment of the torso phantom (previously detailed in Section 6.2.1) was uniformly filled with ~70MBq of ^{123}I (in keeping with the activity concentration used in Chapter 6 for Contrast Recovery assessment). The phantom was acquired on three occasions with LEHR and MELP collimators.

In this investigation, the phantom acquisition time was determined by an audit of the counts acquired in ten consecutive ^{123}I-mIBG patient studies. The mean counts in these patient studies guided the counts acquired for the phantom study. Furthermore, the counts acquired for the phantom study were chosen to extend above and below the range of the audited patient studies. The torso phantom is 200mm in length. In comparison, typical ^{123}I-mIBG patient studies extend the full length of the 380mm FOV in the z-axis. Therefore, for the same total counts acquired, a phantom study will have a higher count density than a patient ^{123}I-mIBG study in areas of uniform non-specific uptake. As such, the counts acquired for the phantom study were normalised to a 380mm extent (Table 7.1).

	Extent of Data in the y-axis	Mean Total (Mcounts)	Counts Normalised to 380mm FOV	
			Min	Max
^{123}I-mIBG Patient Studies	380mm	7.6±2.0M	3.9M	10.1M
Gated LEHR Phantom Data	200mm	7.3±0.8M	1.7M	13.9M

Table 7.1: Summary of the total counts acquired in an audit of ten ^{123}I-mIBG patient studies and torso phantom acquisitions normalised to a 380mm FOV

Patient studies are acquired with LEHR collimators. Therefore, the acquired counts determined from the audit of patient studies were applied to LEHR phantom data. The full FOV sensitivity of the MELP collimator is relatively less than for LEHR data (as shown in Section 3.5). Therefore, rather than acquiring to counts, the acquisition time for LEHR collimator data was applied to acquisition of data with MELP collimators. Further details of SPECT acquisition parameters are shown in Table 7.2. A sequential CT was acquired for attenuation and Monte Carlo scatter correction.

	Value	
Parameter	**LEHR**	**MELP**
Matrix	128x128	
Zoom	1.45	
Pixel Size	3.3mm	
Projections	128	
Counts in the first projection	65k	37k
Radius of Rotation (mean / min / max)	~19cm / ~13cm / ~25cm	
Orbit	Contoured	
Photopeak	159keV±10%	
Scatter Windows*	Lower: 138±4keV Upper: 178±4keV	
CT mA	35mA	
CT kVp	130kVp	
CT Reconstruction Slice Width	3.3mm	

Table 7.2: SPECT and sequential CT acquisition parameters
(*) One of the three acquisitions included an upper and lower energy window to allow TEW correction

7.2.1.2 Post-processing and Reconstruction of Gated SPECT Data

The gated SPECT data were rebinned into 8 acquisitions of increasing count density (e.g. 1/8th, 2/8th … 8/8th of the total acquisition). Each rebinned data set was reconstructed using OSEM iterative reconstruction and the correction schemes and parameters detailed in Section 4.2.2, which are reproduced here for reference in Table 7.3 for LEHR data and Table 7.4 for MELP data.

Correction Scheme Name	Resolution Recovery	Attenuation Correction	Scatter Correction	Iterations
NC(L)	No Corrections (NC)			24
RR(L)	✔	—	—	96
OOSC(L)	✔	CT	OOSC	96
TEW(L)	✔	CT	TEW	96
CDRM(L)	✔	CT	CDRM	96

Table 7.3: Reconstruction correction schemes applied to data acquired with low-energy collimators
Correction schemes include, where indicated, Resolution Recovery (RR), Object Only Scatter Correction (OOSC), Triple Energy Window (TEW) scatter correction and Collimator and Detector Response Modelling (CDRM). The reconstruction of data acquired with low-energy collimators is indicated with (L)

Correction Scheme Name	Resolution Recovery	Attenuation Correction	Scatter Correction	Iterations
NC(M)	No Corrections (NC)			24
RR(M)	✔	—	—	96
OOSC(M)	✔	CT	OOSC	96

Table 7.4: Reconstruction correction schemes applied to data acquired with medium-energy collimators
Correction schemes include, where indicated, Resolution Recovery (RR) and Object Only Scatter Correction (OOSC). The reconstruction of data acquired with medium-energy collimators is indicated with (M)

Twenty-four iterations demonstrated suitable convergence of spatial resolution and contrast recovery with No Corrections (NC) applied (see Sections 5.3.2.3 and 6.3.1 respectively). Therefore, as additional iterations will amplify noise with no incremental improvement in spatial resolution or contrast, 24 iterations was used for NC reconstructions in the investigation of noise versus count density.

Similarly, reconstruction schemes which incorporate corrections for attenuation, scatter and depth-dependent spatial resolution demonstrated suitable convergence at 96 iterations. Furthermore, Dickson [30] recommends ~100 iterations be used for

optimisation of ^{123}I-DaTSCAN™ SPECT semi-quantification. Therefore, in this investigation, 96 iterations was used for all other correction schemes considered.

7.2.1.3 Noise Analysis

A typical approach to measuring Image Roughness (IR) in the torso phantom is described by NEMA for the evaluation of noise in PET imaging [183]. The same method has also been used to measure noise in ^{99m}Tc SPECT by Knoll [106] and Grootjans [107]. The method describes the placement of 12 circular ROIs on the transverse slice which is centred on the six spheres. The ROIs are then copied to the two transverse slices superior and inferior to this slice, resulting in a total of 60 ROIs. The IR is calculated as the average Coefficient of Variation (COV) from the 60 ROIs. These same ROIs can also be used for the assessment of Background Variability (BV).

Van Gils [111] adapted the method for assessment of IR in ^{131}I SPECT by using a singular large VOI in the uniform background section of the torso phantom. This single VOI method provides a global measure of IR. However, it does not provide a simultaneous assessment of BV. Van Gils ensured the extent of the VOI was at least 20mm from all phantom edges and spheres. This approach avoids the incorporation of partial volume effect into the measurement VOI as SPECT typically has poorer spatial resolution when compared to PET, for which the NEMA method is intended.

A compromise between the NEMA and the van Gils analysis method was used in this study to allow simultaneously measurement of both IR and Background Variability (BV). Eight spherical VOIs, 50mm in diameter, were positioned on the spatially registered sequential CT in the uniform background compartment of the phantom. VOIs were placed to ensure at least a 20mm gap existed from the VOI to phantom edges and the spheres. The VOIs were also placed ensuring no overlap with each other. Figure 7.2 shows a transverse and a coronal view of the VOI placement on the CT showing the distance from the phantom edges and spheres.

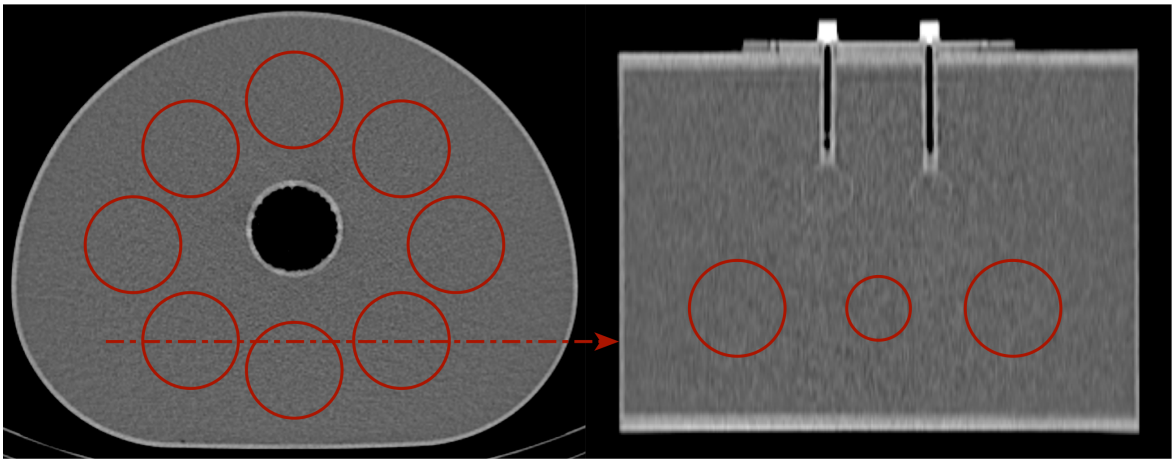

Figure 7.2: Spherical VOI placement in uniform background region of the torso phantom

The VOIs were copied to the same location on the SPECT reconstructions and IR was calculated using Equation 7.1.

$$IR = \sum_{i}^{8} COV_i \Big/ 8 \qquad \textbf{Equation 7.1}$$

where COV_i is the Coefficient of Variation for each of the 8 VOIs.

To investigate whether a Poisson relationship existed between counts acquired and the noise level of reconstructed data, trendlines were fitted to the IR results for each reconstruction correction scheme using an inverse power model (Equation 7.2).

$$IR = k.\left(C_{acq}\right)^{-P} \qquad \textbf{Equation 7.2}$$

where C_{acq} is the total counts acquired, and k and P are unknown constants. As P approaches 0.5 the equation describes a $1/\sqrt{N}$ (Poisson) relationship. This method of analysis was performed by Bailey when investigating noise with count density for FBP SPECT [112].

As the TEW scatter correction method is applied as a pre-processing step, this disturbs the Poisson nature of the acquired data and, therefore, is not expected to have a value of P suggestive of a $1/\sqrt{N}$ relationship.

The coefficient of determination (R^2), which ranges from 0 to 1, is a measure of how well the observed values fit a model, with a higher value indicating good agreement. The R^2

value of the trendlines was used to indicate how well the IR values fit the Equation 7.2 model.

7.2.2 Background Variability Method

7.2.2.1 Torso Phantom Acquisition and Reconstruction

The three torso phantom acquisitions described in Section 7.2.1.1 were used to assess noise with respect to location in the image (BV). The three gated acquisition data sets were rebinned to have comparable total counts in the study. This ranged from 6.4M to 6.8M counts for the three LEHR acquisitions and 3.6M and 3.7M for the three MELP acquisitions.

Acquisition data were reconstructed with the parameters and correction schemes described in Section 7.2.1.2.

7.2.2.2 Analysis

Background Variability (BV) assesses how noise varies from region-to-region within an image. BV can be quantified by measuring the COV of the mean counts in a series of regions. There is currently no established approach to measuring BV in SPECT data. Therefore, analysis of BV in this investigation was made using both ROIs and VOIs for comparison. The mean counts in each of the 8 spherical VOIs, positioned as described in Section 7.2.1.3, were used for VOI analysis using Equation 7.3.

$$BV = SD_{COV_i} / Mean_{COV_i} \qquad \textbf{Equation 7.3}$$

For ROI analysis, eight 50mm diameter circular regions were drawn using CT for placement at least 20mm from phantom edges and spheres. The eight ROIs were copied to the two transverse slices on either side of the central ROI, resulting in 40 circular ROIs. BV was calculated using Equation 7.3.

Additionally, the COV of each spherical VOI was plotted with respect to location within the phantom to provide a visual indication of noise versus location.

7.2.3 Image Roughness versus Iterations Method

7.2.3.1 Torso Phantom Acquisition, Reconstruction and Analysis

Ten torso phantom acquisitions, previously described for evaluation of HCR in Chapter 6, were used to assess IR with increasing reconstruction iterations. The torso phantom acquisitions contained a clinical count density, as described in Section 6.2.2.

The LEHR and MELP acquisition data were reconstructed with the same parameters outlined in Section 6.2.3. Analysis of the reconstructed data was performed according to the method described in Section 7.2.1.3, which was used for characterisation of IR with respect to count density.

7.2.4 Contrast-to-Noise Ratio Analysis

Contrast to Noise Ratio (CNR) analysis was performed using the phantom data previously described in Section 6.2 and Section 7.2.3.1 to measure HCR and IR respectively. Therefore, CNR analysis was performed with respect to increasing iterations.

The CNR was determined following the method of van Gils [111]. VOIs were placed according to the description in Section 6.2.4. CNR was calculated for each of the six spheres using Equation 7.4.

$$CNR = \frac{C_{sphere} - C_{BG}}{SD_{BG}} \qquad \textbf{Equation 7.4}$$

where C_{sphere} was the counts in the sphere VOI, C_{BG} was the counts in the background VOI and SD_{BG} was the standard deviation of counts in the background VOI. The CNR for the six spheres was then combined to provide an average CNR for a given reconstruction, as described by van Gils [111]. The validity of representing the CNR response of each correction scheme as the average CNR of the spheres was confirmed by examining the individual spheres to ensure the pattern of CNR response was the same for all six.

7.2.5 Consideration of Errors

Each section of the noise investigation varied in the number of acquisitions and analysis method. The error for each Section was estimated as follows:

- Image Roughness versus count density study: the goodness of fit to a model equation, as indicated by the coefficient of determination (R^2), was used to estimate error from three acquisitions, each rebinned into 8 data sets (24 in total)

- Background Variability (BV) study: error was estimated as twice the standard error of the three BV measurements for each reconstruction
- Image Roughness versus iterations study: error was estimated by determining twice the standard error of the COV results from ten separate phantom acquisitions
- The CNR investigation: again, error was estimated from ten acquisitions. As the CNR was averaged for the six spheres in the phantom, the error was estimated as being the Root Mean Squared (RMS) of the error in CNR for each of the six spheres.

7.3 Noise Analysis Results

7.3.1 Image Roughness versus Acquired Count Density Results

7.3.1.1 LEHR: IR versus Acquired Count Density

Image Roughness (IR) was used to assess whether the Poisson relationship holds for ^{123}I SPECT iterative reconstruction. The IR versus count density for the LEHR collimator data is shown in Figure 7.3.

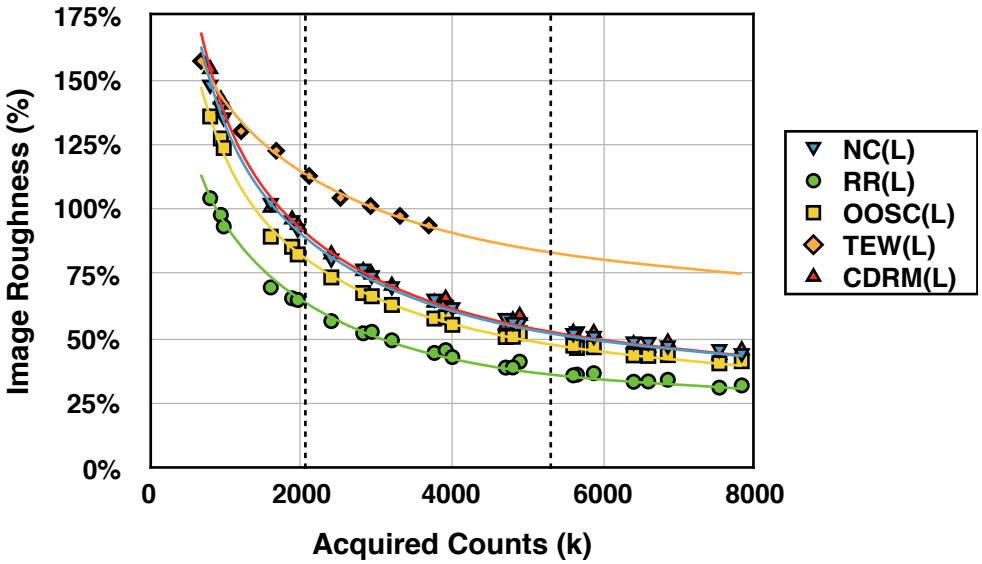

Figure 7.3: Image Roughness (IR) versus count density for LEHR data
The vertical dotted lines indicate the range of clinical count densities in an audit of 10 consecutive ^{123}I-mIBG patient studies.

The RR(L) correction scheme demonstrated a consistently lower IR than alternative schemes. This finding is a result of the inherent smoothing that RR introduces [25, 30].

The trendlines in Figure 7.3 were fitted using the model Equation 7.2. The constants from the equation of the trendline for each correction scheme, and equivalent R^2 values, are shown in Table 7.5.

Correction Scheme	Equation Constants		
	k	***P***	**R^2**
NC(L)	54.9	-0.54	0.999
RR(L)	36.3	-0.53	0.996
OOSC(L)	48.3	-0.54	0.997
TEW(L)	11.3	-0.30	0.995
CDRM(L)	60.9	-0.55	0.996

Table 7.5: Image Roughness (IR) count density model constants and R^2 for LEHR data

The R^2 values for all reconstruction methods show good agreement between IR measurements and the trendline equation. The *P* for NC(L), RR(L), OOSC(L) and CDRM(L) methods of reconstruction demonstrate an almost $1/\sqrt{N}$ (Poisson) relationship. This finding is in agreement with the findings of Bailey, with regard to FBP reconstruction of SPECT data [112]. However, the finding is surprising in the context of an iterative reconstruction algorithm when considering the complex mathematical manipulations involved. The calculations performed still maintain the relative count statistics of the acquired data.

As expected, the *P* for the TEW(L) method is not suggestive of a $1/\sqrt{N}$ relationship. This finding is a result of the scatter correction method being applied as a pre-processing step, which disturbs the Poisson nature of the acquired data. The model for the TEW(L) correction scheme suggests higher count density studies reduce the IR more slowly than for the alternative reconstruction methods.

7.3.1.2 MELP: IR versus Acquired Count Density

The results for IR versus count density for the MELP collimator data are shown in Figure 7.4.

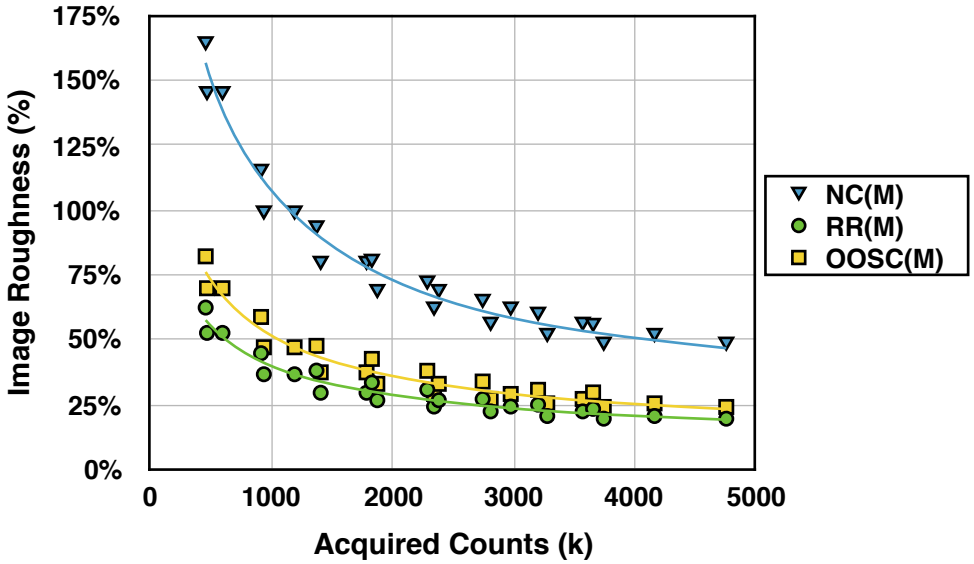

Figure 7.4: Image Roughness (IR) versus count density for MELP data

The constants from the equation of the trendline for each correction scheme and R^2 values are shown in Table 7.6.

Correction Scheme	Equation Constants		
	k	***P***	**R^2**
NC(M)	36.8	-0.52	0.969
RR(M)	10.2	-0.47	0.936
OOSC(M)	16.8	-0.51	0.937

Table 7.6: IR count density model constants and R^2 for MELP collimator

Again, the R^2 values for all correction schemes demonstrated a good agreement between IR measurements and the trendline model. All three reconstruction methods demonstrate a model suggestive of a $1/\sqrt{N}$ (Poisson) relationship between acquired counts and reconstructed IR.

7.3.2 Background Variability Results

7.3.2.1 LEHR: Background Variability

Background Variability (BV) describes how noise varies depending on location within the phantom. A low BV suggests a consistent level of noise throughout the background compartment. The BV for LEHR collimator data is shown in Figure 7.5.

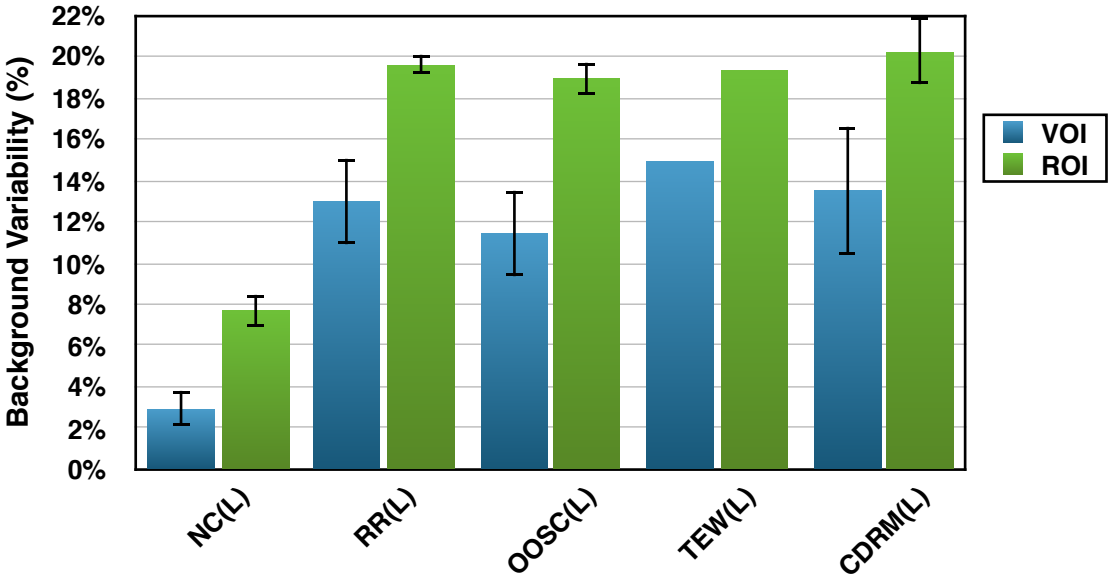

Figure 7.5: Background Variability (BV) of reconstruction correction schemes for LEHR data BV was measured using 8 VOIs, 50mm in diameter, and 24 ROIs, 50mm in diameter. The TEW(L) result does not display an error estimate as the measure was made for a single phantom acquisition.

The results demonstrate that the BV measured with VOIs is less than that measured using ROIs for the same reconstruction correction technique. This indicates that the variability in noise from ROI to ROI is higher than the variability in noise from VOI to VOI. Measuring using a VOI, which contains many more pixels than ROI analysis, averages out the effect of noise which reduces the measure of BV. Knoll [106] demonstrated a similar effect in that BV reduced with an increase in VOI diameter.

Considering the ROI method, the reconstruction with NC(L) applied shows the lowest BV of all the reconstruction methods (7.7%±0.8), which indicates a consistent noise level throughout the background region of the torso phantom. The four alternative correction schemes have a BV of between 18.9% and 20.3%. This result suggests that the inclusion of advanced corrections in the reconstruction algorithm increases the variability of noise throughout the background compartment of the phantom. This finding is likely to be a result of variable rates of convergence across the FOV, as was also demonstrated by FWHM measurements in Section 5.3.2.4.

The COV for each of the 8 VOIs plotted versus location in the phantom is shown in Figure 7.6.

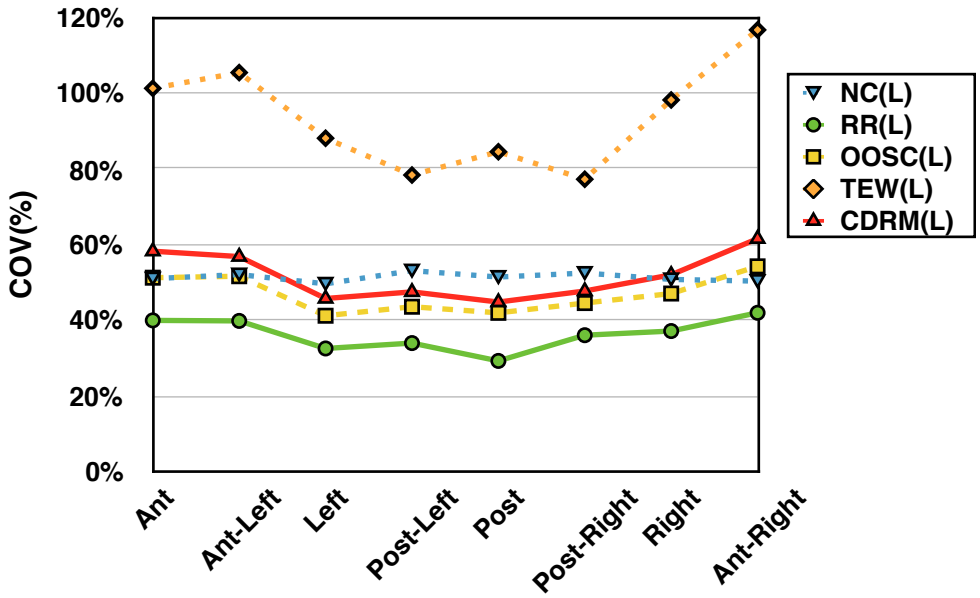

Figure 7.6: Coefficient of Variation (COV) versus location for LEHR data

The results demonstrate that the COV for the TEW(L) is reduced in the posterior aspect of the phantom relative to the anterior. The pattern is also suggested for the RR(L), OOSC(L) and CDRM(L) reconstructions, which can be illustrated more clearly with the TEW(L) results removed (Figure 7.7).

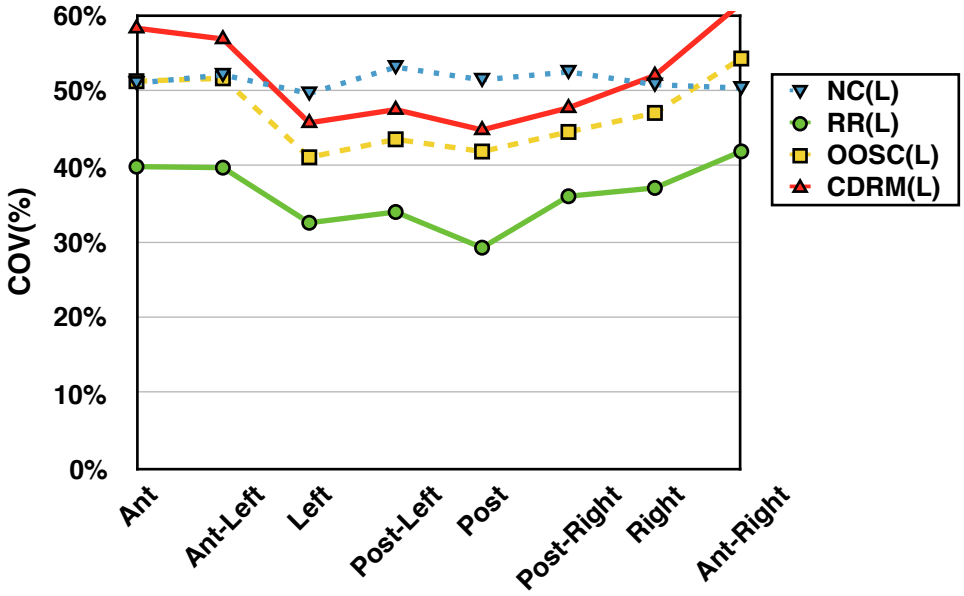

Figure 7.7: Coefficient of Variation (COV) versus location for LEHR data, with TEW(L) reconstruction removed

The noise level for the NC(L) reconstruction is consistent, as was suggested by the BV results in Figure 7.5. All of the advanced reconstruction correction schemes demonstrate a reduction in noise towards the posterior aspect of the phantom, as was also apparent for the TEW(L) reconstruction in Figure 7.6. The posterior region of the phantom is the portion

that is closest to the isocentre, due to the detector orbiting the scanning couch. An example slice of the background region of the phantom reconstructed with RR(L) is shown in Figure 7.8, demonstrating a 'smearing' look in the posterior region.

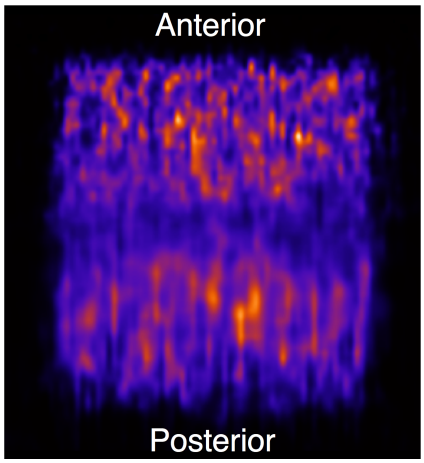

Figure 7.8: Sagittal view of the torso phantom
LEHR data reconstructed with 24 iterations and the OOSC correction scheme. The image demonstrates the noisier anterior and 'smeared' posterior portion

Larsson [184] and Dickson [30] describe RR as 'smoothing' images. However, in this study the smoothing is not consistent throughout the phantom, as highlighted by the larger BV with RR applied. This finding, therefore, is consistent with the variable rates of convergence demonstrated for FWHM measurements in Section 5.3.2.4.

7.3.2.2 MELP: Background Variability

The Background Variability (BV) for MELP collimators is shown in Figure 7.9.

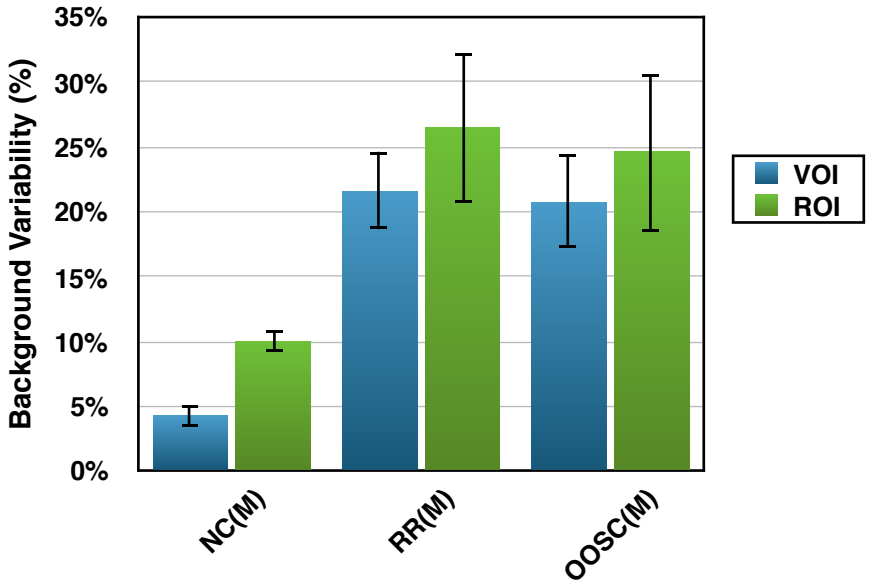

Figure 7.9: Background Variability (BV) for reconstruction correction schemes for MELP data
BV was measured using 8 VOIs, 50mm in diameter, and 24 ROIs, 50mm in diameter

As with the LEHR data, the NC(M) reconstruction has the most consistent level of noise throughout the background region of the phantom with a BV of 10.0%±0.8, as measured with ROI analysis.

The BV is larger for MELP reconstructions than for equivalent LEHR correction schemes, which have a relatively higher count density. This finding suggests that the accuracy of relative quantification, which relies upon a suitable reference region, may be poorer for MELP data.

The COV for each of the 8 VOIs is plotted versus location in the phantom in Figure 7.10.

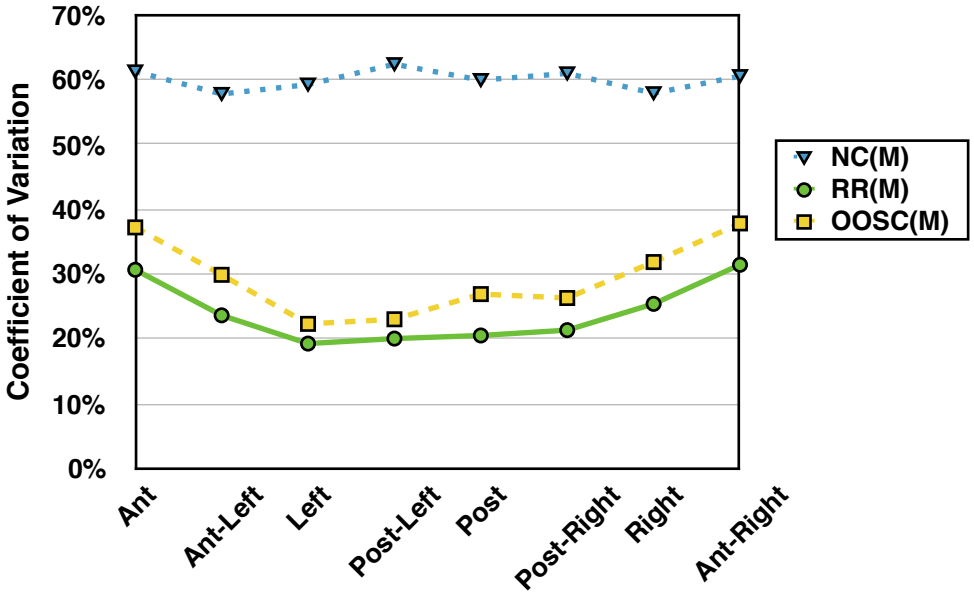

Figure 7.10: Coefficient of Variation (COV) versus location for MELP data

As was shown in the LEHR data, when advanced corrections are employed the COV for MELP data demonstrates reduced noise in the posterior region of the phantom. As was shown with the NC(L) reconstruction, the noise level for the NC(M) reconstruction is consistent throughout the background region of the phantom. A transverse slice of the background region of the phantom reconstructed with RR(M) is shown in Figure 7.11, which demonstrates the 'smearing' look of reduced noise in the posterior region, also shown with LEHR data.

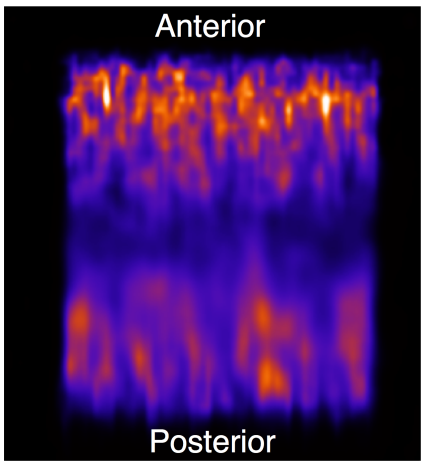

Figure 7.11: Sagittal view of the torso phantom
MELP data reconstructed with 24 iterations and the OOSC correction scheme. The image demonstrates the noisier anterior and 'smeared' posterior portion

7.3.3 Image Roughness versus Iterations Results

7.3.3.1 LEHR: IR versus Iterations

The Image Roughness (IR) for the LEHR collimator data demonstrates a non-linear curve when No Corrections (NC) are applied and a linear response to increasing iterations when corrections are applied (Figure 7.12).

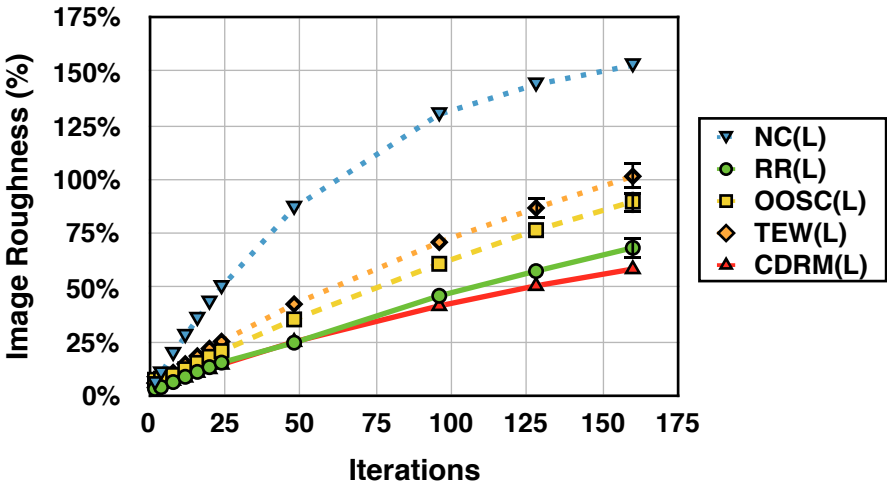

Figure 7.12: Image Roughness (IR) versus iterations for LEHR data
Estimated errors of <5% are not shown

The LEHR reconstructions which include CDRM(L) demonstrated the lowest IR at all iterations compared with all other correction schemes. The OOSC(L) correction method has a higher noise level than the CDRM(L) method due to the absence of correction for septal penetration. Noise from high-energy emissions will be present in the data and will be amplified with increasing iterations. The TEW(L) technique has the highest IR of the methods which include correction for scatter and attenuation. This finding is in agreement with the IR versus acquired count density investigation which demonstrated that, for the same count density, the TEW(L) correction technique has the highest noise level.

The IR of the NC(L) reconstruction increases linearly for the first 24 iterations. At higher iterations there is a non-linear amplification of noise. Noise characteristics can be controlled with a post-reconstruction filter (see Section 9.5). However, as both spatial resolution and HCR were shown to converge at 24 iterations with NC applied, it would be prudent not to perform NC(L) reconstructions with higher than 24 iterations. The same argument can be applied to the advanced correction schemes and, as such, should not be reconstructed for more than 96 iterations.

7.3.3.2 MELP: IR versus Iterations

The IR results for MELP data demonstrate a similar response to an increase in the number of iterations (Figure 7.13).

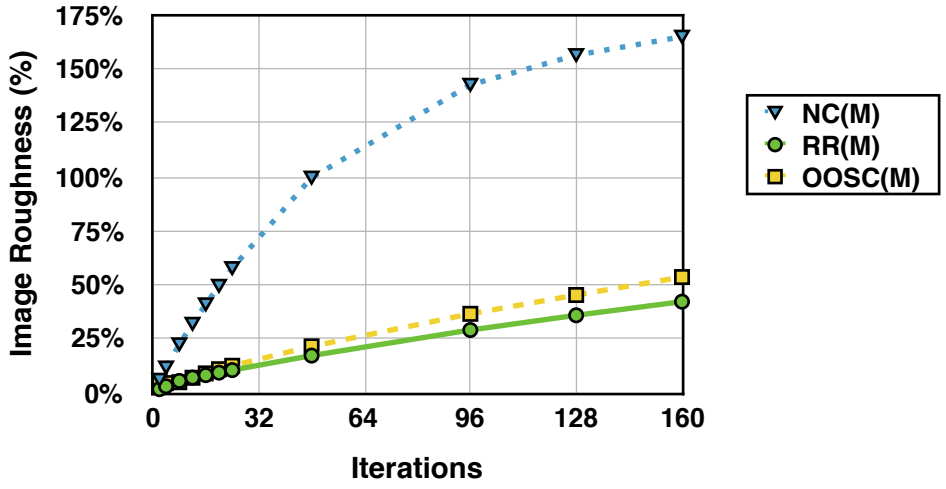

Figure 7.13: Image Roughness (IR) versus iterations for MELP data
Estimated errors of <5% are not shown

RR(M) reconstructions demonstrated the lowest IR measurements for MELP data. This finding is in contradiction with COV measurements in Section 4.3.1, Figure 4.6 where the OOSC(M) reconstruction had the lower COV. However, the cylindrical phantom acquisitions in Chapter 4 had a substantially greater count density. When attenuation and scatter correction are applied to relatively low count density data the reconstructions are noisier. This effect is due to attenuation correction amplifying areas of low count (noisy) data.

The IR of LEHR and MELP collimators at 160 iterations with NC are 153% and 165% respectively. The LEHR and MELP datasets were acquired for a comparable time per projection. However, the LEHR has an apparent higher sensitivity due to the addition of septal penetration from high-energy emissions. Therefore, for the same acquisition time, the LEHR data sets had ~7M counts whereas the MELP data had ~4M counts. This

difference in count density explains why the MELP reconstructions without corrections applied are noisier.

The MELP collimator performs better in terms of IR than the LEHR acquisitions for all of the reconstructions with corrections applied. This finding demonstrates that, although the MELP data sets have fewer counts acquired, the relatively low proportion of septal penetration in the counts detected relative to LEHR acquisitions results in a lower noise level. This finding is in agreement with the simulation study by Larsson [25] who demonstrated that reconstructions of ^{123}I SPECT data acquired with MELP data were relatively less noisy than LEHR data.

7.3.4 Contrast-to-Noise Ratio Results

Section 7.3.3 has shown that an increase in the number of reconstruction iterations increases noise, which is undesirable for image interpretation. However, Section 6.3.1 demonstrated that Hot Contrast Recovery (HCR) can be increased with an increase in iterations. Therefore, it is useful to consider both components in combination. Assessment of the reconstruction correction schemes and their effect on both contrast recovery and noise can be evaluated by determining the Contrast to Noise Ratio (CNR). The results in Figure 7.14 shows the average CNR for the six spheres in the torso phantom for each correction scheme, applied to LEHR collimator data.

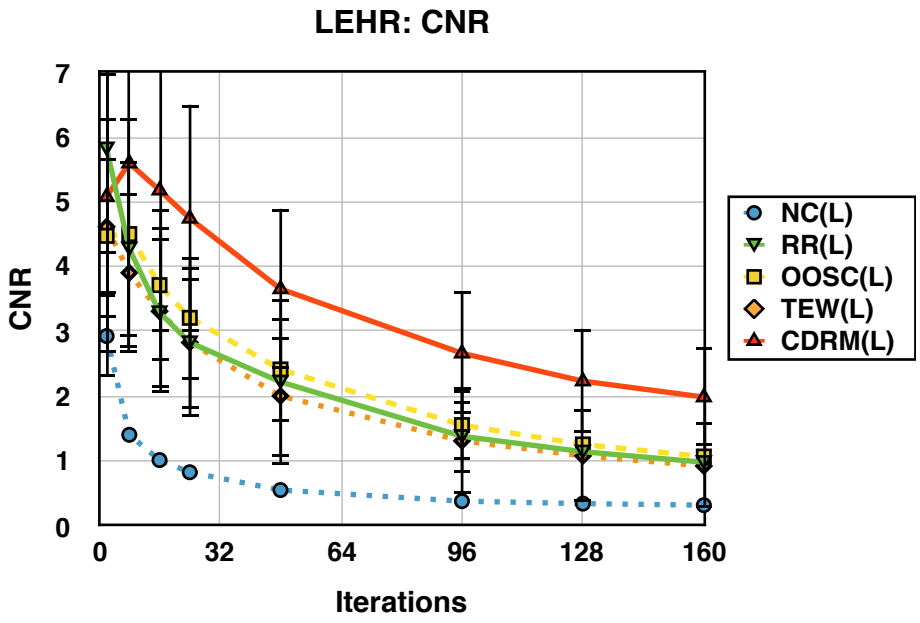

Figure 7.14: Average Contrast to Noise Ratio (CNR) for the six spheres in the torso phantom for LEHR data
Estimated error is shown for CNR >0.05

The CDRM(L) method had a higher CNR than the other methods for iterations greater than or equal to eight. This outcome is due to a combination of both higher HCR and lower IR when compared to the other correction schemes.

The wide error bars in Figure 7.14 were due to the large variability in the CNR of the smallest spheres. Although the error bars overlap, a Skillings-Mack test suggested a statistically significant difference between the advanced correction schemes ($p<0.01$). Table 7.7 shows the p-values and confidence intervals for individual paired Wilcoxon tests between the advanced correction schemes.

Correction Scheme Comparison		p-value	CI
CDRM(L)	**RR(L)**	<0.01	1.3±0.1
CDRM(L)	**OOSC(L)**	<0.01	1.1±0.1
CDRM(L)	**TEW(L)**	<0.01*	1.4±0.1
OOSC(L)	**RR(L)**	<0.01	0.2±0.1
OOSC(L)	**TEW(L)**	<0.01*	0.3±0.1
TEW(L)	**RR(L)**	0.025*	0.1±0.1

Table 7.7: p-values and Confidence Interval (CI) between advanced correction schemes The table describes paired Wilcoxon tests between advanced reconstruction correction schemes for ten phantom data sets, except where indicated by (*) for seven paired phantom data sets.

Although the TEW(L) technique had a higher HCR than both the RR(L) and OOSC(L) techniques, as the TEW(L) also had higher noise (IR), they all had a comparable CNR.

Figure 7.15 shows the results for the average CNR for the six spheres in the torso phantom for MELP data.

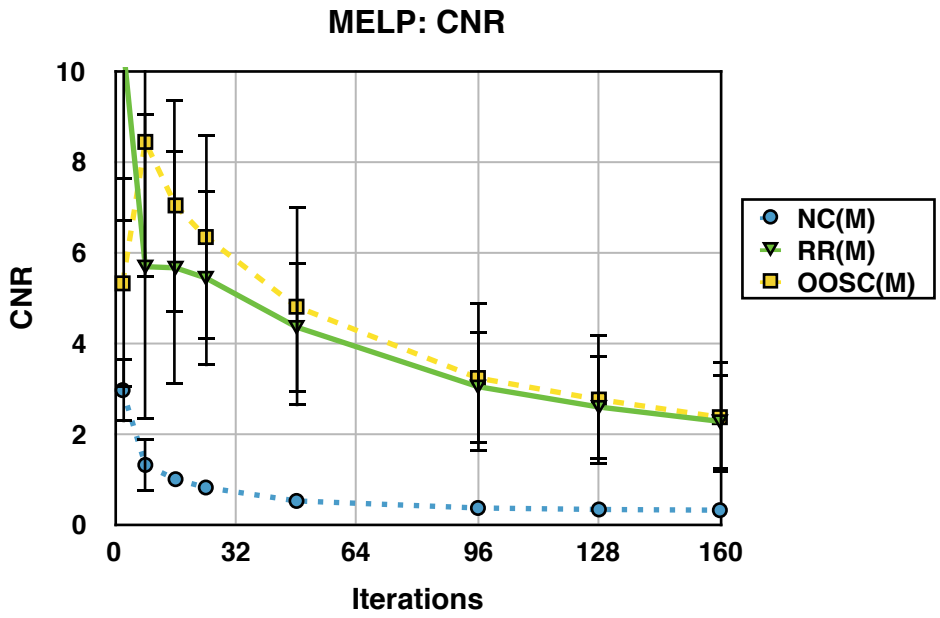

Figure 7.15: Average Contrast to Noise Ratio (CNR) for the six spheres in the torso phantom for MELP data

Estimated error shown for >0.05.

As with the LEHR data, the CNR of the RR(M) and OOSC(M) methods were comparable. There was a statistically significant difference between the RR(M) and OOSC(M) correction schemes ($p<0.01$; CI:0.4±0.1).

The highest CNR for the MELP data (OOSC(M) = 8.4) was larger than the highest for the LEHR data (CDRM(L) = 5.6) with a statistically significant difference ($p<0.01$; CI:1.0±0.2).

CNR is a useful metric for comparison of reconstruction methods. However, CNR is limited in that choosing the maximum value does not necessarily result in the optimum images, either for quantification or visual assessment. For example, in this investigation CDRM(L) and OOSC(M) were shown to maximise at 8 iterations. However, comparing images of the 8 iteration reconstruction side-by-side with the 96 iteration reconstruction demonstrates that spheres are more conspicuous in the 96 iteration images (Figure 7.16). Therefore, noise is the dominant variable in the CNR calculation.

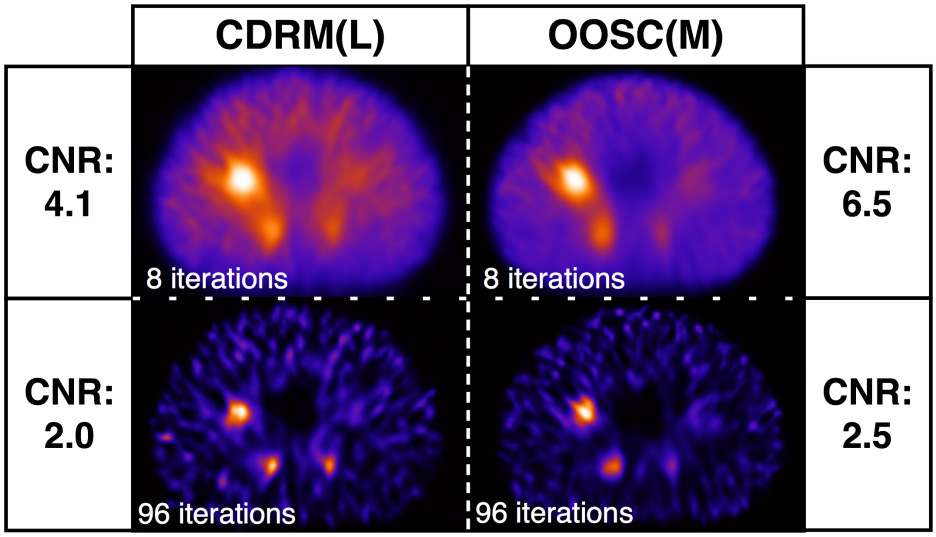

Figure 7.16: Transverse slice of CDRM(L) and OOSC(M) reconstructions Images shown include where CNR is maximised (8 iterations) and where HCR of the 37mm sphere converges (96 iterations).

CNR may be improved by using a post-reconstruction filter to reduce the relatively high standard deviation of counts in the background compartment. However, a post-reconstruction filter will also reduce contrast recovery (see Section 9.5).

7.4 Discussion

The investigation of IR versus acquired count density has demonstrated that the relationship between noise and acquired counts varies with $1/\sqrt{N}$ for iterative reconstruction techniques in ^{123}I SPECT. Although this finding is in keeping with Bailey's investigation of FBP SPECT reconstruction [112], the result remains surprising when considering the complex mathematical manipulation involved with advanced SPECT correction schemes.

A $1/\sqrt{N}$ relationship does not hold for the TEW method. This result is expected as, following energy window subtraction, the data is no longer Poisson in nature. However, the measurements do closely fit the model equation with an R^2 value of 0.995, which confirms the relationship is a negative fractional power, as also demonstrated by the other correction schemes.

The investigation of Background Variability (BV) demonstrated that applying advanced corrections to the reconstruction algorithm increased the variability of noise in the uniform background compartment of the phantom. By evaluating COV with location, this study has shown that noise in the anterior aspect of the phantom is higher than in the posterior aspect of the phantom. This finding can be explained by the variable rates of convergence

across the FOV, as also demonstrated by FWHM results in Section 5.3.2.4. The smoother posterior portion of the phantom is more central for a contoured orbit relative to the anterior aspect of the phantom. Dickson [30] also describes advanced correction schemes, and RR in particular, as leading to "… variable levels of smoothing within the data."

There is no established method for measuring the BV of SPECT reconstructions. In this investigation, the ROI method resulted in a higher value compared to the VOI method. This difference is due to the number of pixels used to measure the COV. Knoll [106] also demonstrated that larger regions reduce the measured BV. A key finding is that the method of BV measurement should be kept consistent to allow suitable comparison between systems and reconstruction algorithms. In this investigation, the VOI method was simple from a practical perspective and allowed a straightforward method to plot noise versus location within the phantom and, as such, is recommended for future assessment of BV.

With regard to IR versus iterations, as anticipated, all reconstruction correction schemes demonstrated an increase in noise with an increase in the number of iterations. There has been no similar analysis of ^{123}I SPECT performed in the literature to allow comparison. However, the results of this study are in keeping with those reported by Armstrong [98] for ^{99m}Tc SPECT. Armstrong demonstrated COV increased from ~28% to ~48% with an increase in iterations from 48 to 84. Although the count density of Armstrong's study is unclear, the ratio of increase in COV is similar to that seen for the IR results in this study between 48 and 96 iterations. For example, IR for the CDRM method increased from 25% to 42% between 48 and 96 iterations.

The noise (IR) in reconstructed data was greatest when No Corrections (NCs) were applied. Applying the depth-dependent RR algorithm resulted in a reduction in IR compared with the NC method. This noise reduction property is due to the RR algorithm, which allocates a Gaussian probability to the projection data, resulting in a smoothing of high-frequency noise in the image [25].

The CDRM correction scheme demonstrated the lowest IR of the LEHR reconstructions. This finding may be the result of the CDRM algorithm, which corrects for septal penetration, having superior spatial uniformity when compared to the OOSC algorithm (as shown in Section 4.3.2). The TEW technique had a higher IR than RR, OOSC and CDRM due to the lower count density from subtraction of counts before reconstruction.

Previous studies have shown that an increase in image noise without an improvement in contrast reduces human observer detection ability [3]. Therefore, iterating the reconstruction algorithm beyond the convergence of HCR will impair observer detection through noise amplification. Grootjans [107] compared contrast and noise for ^{99m}Tc SPECT using the torso phantom. As was found in this study for ^{123}I SPECT, Grootjans found both Siemens and Hermes Medical Solutions reconstruction demonstrated an increase in IR with no gain in HCR for the 37mm sphere for iterations greater than and equal to 96. Again, as reflected in this study, smaller spheres (22mm and 28mm diameter) showed a relatively minor increase in HCR for iterations greater than 96 while IR continued to increase linearly.

The Contrast to Noise Ratio (CNR) allowed consideration of these two metrics combined for each correction scheme. Van Gils [111] used the maximisation of CNR to determine optimum iterations for ^{131}I SPECT. However, this study has shown that optimisation of reconstruction parameters based on CNR alone would result in overly smooth images with sub-optimal contrast recovery.

In an investigation of ^{123}I SPECT, Gilland [185] measured IR of data acquired with medium-energy collimators and reconstructed with attenuation and scatter correction. A single measurement of 20.7% was recorded for a 50 iteration reconstruction. In this investigation, the IR for a 48 iteration reconstruction using a comparable correction scheme (OOSC(M)) was measured as 21.5%. Although this is a comparable figure, Gilland's study used a phantom with higher activity concentration and a medium-energy collimator with unknown dimensions. Furthermore, Gilland did not apply depth-dependent RR, which was shown in this investigation to significantly reduce IR. The comparison between the results in this investigation and Gilland's suggests that a lower count data set with RR applied has a similar noise level (IR) as a high count data set.

No post-filter has been applied to reconstructed data in this Chapter. Noise levels can be controlled with a post-reconstruction filter. However, although filtering will reduce noise, it will also reduce HCR (see Chapter 9).

7.5 Conclusions

Image Roughness (IR) varies with count density with a $1/\sqrt{N}$ (Poisson) relationship for all reconstruction correction schemes except for the TEW scheme. This exception is due to pre-processing of acquisition data.

BV increases when advanced corrections are applied. This is due to variable rates of convergence within the FOV, which results in less high-frequency noise in regions of the phantom closer to the centre of the FOV.

The noise level (IR) of ^{123}I SPECT studies acquired with LEHR or MELP collimators increased with an increase in the number of iterations. The noise level is reduced by applying RR, which also results in a linear relationship between iterations and IR.

As noise continues to increase linearly after contrast recovery has converged, all reconstructions which include advanced corrections should not run for more than 96 iterations. Similarly, reconstructions with No Corrections (NCs) applied should not run for more than 24 iterations.

Chapter 8: Scatter Suppression and Residual Error

8.1 Introduction

Scattered photons detected in the photopeak are misplaced from their origin and reduce image contrast and quantitative accuracy. ^{123}I data acquired with LEHR collimators have demonstrated a relatively high scatter fraction, largely due to high-energy septal penetration (Section 3.4). SPECT scatter correction techniques aim to either remove the influence of scatter before reconstruction, as is the case with the Triple Energy Window (TEW) measurement method, or calculate and correct for the scatter distribution during reconstruction, as is the case with Monte Carlo scatter correction algorithms.

A method for assessing the effectiveness of scatter correction techniques is to measure the level of scatter contribution to the tails of the Line Spread Function (LSF). For example, Rault [47] demonstrated that, although scatter correction had no effect on FWHM, the Full Width at Tenth Maximum (FWTM) of ^{123}I sources in scatter was improved. In this Chapter, an investigation was performed to assess scatter correction methods for ^{123}I SPECT by measuring the FWTM of LSFs.

Furthermore, the Residual Error (RE) of counts in a cold region can be used to measure the effectiveness of scatter correction. RE is used to measure the effectiveness of scatter correction as part of PET routine quality control [183, 186]. Although Van Gils [111] measured RE with reference to quantification in ^{131}I SPECT, its application in SPECT imaging is not widespread and has not been applied to ^{123}I SPECT. Therefore, an aim of this investigation was to use RE as an additional metric in the assessment of scatter correction methods for ^{123}I SPECT.

As previously outlined, the overall aim of Chapters 4-8 is to assess advanced reconstruction techniques for ^{123}I SPECT based on quantitative image quality metrics. In this Chapter, the intermediate aims are to:

- Perform an assessment of scatter suppression by evaluating the FWTM of line sources
- Perform an assessment of the effectiveness of attenuation and scatter correction by measuring the Residual Error (RE)
- Determine the more sensitive method for evaluation of the effectiveness of scatter correction algorithms

8.2 Methods and Materials

8.2.1 Scatter Suppression

Scatter suppression was assessed by measuring the FWTM of line sources acquired and reconstructed using the complex perturbation method, which was previously used for measuring SPECT spatial resolution in Chapter 5. A summary of the complex perturbation method is as follows:

- A cylindrical phantom containing uniform activity is acquired
- An additional acquisition is performed with hot line sources added to the cylindrical phantom
- Both acquisitions are reconstructed
- The uniform activity concentration data is subtracted from the phantom with hot line sources

Data were acquired with LEHR and MELP collimators and reconstructed using 2-160 iterations. Details of the phantom preparation, and acquisition and reconstruction parameters are given in Sections 5.2.

8.2.1.1 Scatter Suppression Analysis

Line profiles were generated across the line sources (as detailed in Chapter 5 to measure FWHM). The FWTM was calculated by fitting a Gaussian to the data points. Chapter 5 demonstrated that the FWHM varied with location in the Field of View (FOV). In this Chapter, the primary focus was to compare the scatter suppression of advanced reconstruction algorithms. Therefore, variability with location was not assessed. As such, the tangential FWTM of the peripheral line source was used to assess scatter suppression. This source was chosen as the FWHM of this peripheral source was shown in Chapter 5 to converge more quickly relative to the central source. Error bars are presented on data where twice the Standard Error was ≥1.0mm.

8.2.2 Residual Error

Residual Error (RE) was measured by evaluating counts in a low-density region. The torso phantom (described in Section 6.2.1) was used in this investigation. The torso phantom contains a central cylindrical region known as the 'lung insert'. No photons originate from this region and the low-density material means there will be a low probability of photon scatter. Consequently, following reconstruction, counts in the lung insert should tend towards zero. Measuring the counts in this region, therefore, indicates the effectiveness of attenuation and scatter correction.

Details of the preparation, acquisition and reconstruction of the torso phantom are given in Section 6.2. In summary, the phantom contained ~74MBq, with a ~4:1 sphere to background activity concentration ratio and was acquired with both LEHR and MELP collimators. The phantom was filled and acquired on ten occasions to give an assessment of measurement error. Of these ten acquisitions, seven included an energy window acquisition scheme suitable for TEW correction.

The torso phantom data was reconstructed with the correction schemes shown in Table 8.1 for LEHR data and Table 8.2 for MELP data.

Correction Scheme Name	Resolution Recovery	Attenuation Correction	Scatter Correction
NC(L)	No Corrections (NC)		
RR(L)	✔	—	—
OOSC(L)	✔	CT	OOSC
TEW(L)	✔	CT	TEW
CDRM(L)	✔	CT	CDRM

Table 8.1: Reconstruction correction schemes applied to data acquired with low-energy collimators

Correction schemes include, where indicated, Resolution Recovery (RR), Object Only Scatter Correction (OOSC), Triple Energy Window (TEW) scatter correction and Collimator and Detector Response Modelling (CDRM). The reconstruction of data acquired with low-energy collimators is indicated with (L)

Correction Scheme Name	Resolution Recovery	Attenuation Correction	Scatter Correction
NC(M)	No Corrections (NC)		
RR(M)	✔	—	—
OOSC(M)	✔	CT	OOSC

Table 8.2: Reconstruction correction schemes applied to data acquired with medium-energy collimators
Correction schemes include, where indicated, Resolution Recovery (RR) and Object Only Scatter Correction (OOSC). The reconstruction of data acquired with medium-energy collimators is indicated with (M)

Data were reconstructed using 2-160 iterations.

8.2.2.1 Residual Error Analysis

The cylindrical lung insert in the phantom has a 51mm diameter. Therefore, to minimise partial volume effect on the measurement, a 30mm diameter spherical VOI was positioned in the centre of the lung insert region. The VOI was positioned using the spatially registered CT and copied to the SPECT reconstructions.

This size of VOI was also used by van Gils [111] to measure RE in a torso phantom filled with ^{131}I acquired with high-energy collimators. Therefore, van Gils study will have greater partial volume effect due to the lower spatial resolution of high-energy collimators than the data acquired in this study.

An example of VOI placement in the lung insert is shown in Figure 8.1.

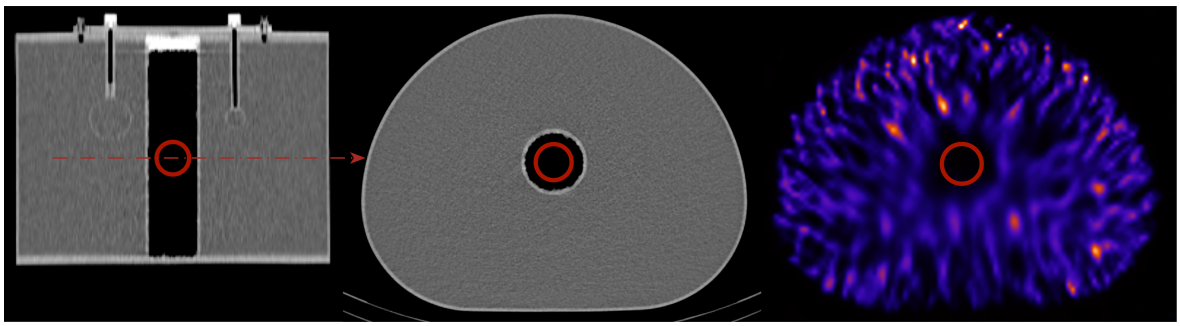

Figure 8.1: VOI placement on CT and SPECT for Residual Error (RE) measurement
Coronal CT (left) and transverse CT (middle) and SPECT (right) images demonstrate placement of a 30mm diameter spherical VOI. The SPECT transverse slice is of the OOSC(M) data with 96 iterations.

The counts in the background compartment of the phantom were measured using a 50mm spherical VOI placed in a uniform region using the CT. The RE was calculated using Equation 8.1.

$$RE(\%) = 100x\frac{C_{lung}}{C_{bgnd}} \qquad \textbf{Equation 8.1}$$

where C_{lung} is the count density in the lung compartment VOI and C_{bgnd} is the count density in the background compartment VOI. The lung region should have no counts and, therefore, RE should tend towards zero to indicate minimal error in this compartment.

Measurement of RE from each phantom acquisition was averaged for all acquisitions to obtain a mean value. Measurement error was estimated as twice the Standard Error (SE), (as described in Section 3.3.1.3). The SE was determined using Equation 8.2.

$$\text{Standard Error (SE)} = SD_{RE}/\sqrt{n} \qquad \textbf{Equation 8.2}$$

where SD_{RE} is the standard deviation of the RE measurements and n is the number of measurements. Error bars were included on results where 2*SE≥5%.

Due to the small sample size, the normality of results in this Chapter cannot be proven and are, therefore, assumed to be non-parametric in nature. Consequently, the statistical analysis of results was performed using the approach described in Section 5.2.5. However, as highlighted in Section 6.2.4.6, analysis of results which include the TEW method require a Skillings-Mack test (for data with missing pairs), as only seven of the ten acquisitions included the energy windows necessary for TEW correction.

8.3 Scatter Suppression and Residual Error Results

8.3.1 Scatter Suppression Results

8.3.1.1 Scatter Suppression (FWTM) of LEHR Data

The FWTM results for a tangential measurement of the peripheral line source in the cylindrical phantom can be seen in Figure 8.2.

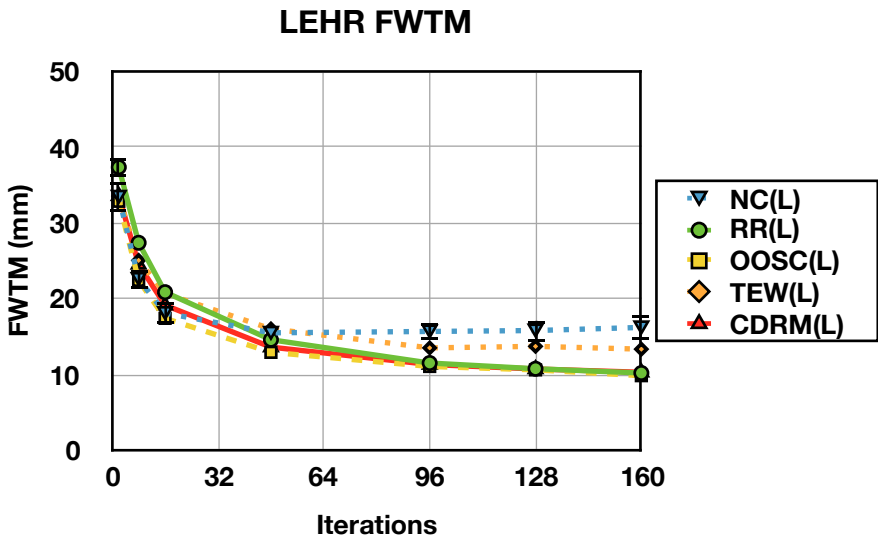

Figure 8.2: FWTM of peripheral line source acquired with LEHR collimators

The results show a similar rate of convergence for all methods of reconstruction. The RR(L), OOSC(L) and CDRM(L) have a lower FWTM than the reconstruction with TEW(L) and NC(L) at 96-160 iterations. There is no statistically significant difference between the RR(L), OOSC(L) and CDRM(L) methods. However, there is a statistically significant difference between these three methods and the TEW(L) and NC(L) methods. The results for these statistical tests are summarised in Table 8.3.

Statistical Test		Iterations 96	128	160
Friedman test	**All data**	<0.001	<0.001	<0.001
Dunn's test	**CDRM v RR**	0.360	0.473	0.412
	CDRM v OOSC	0.272	0.374	0.187
	RR v OOSC	0.119	0.349	0.240
	CDRM v TEW	<0.001	<0.001	<0.001
	CDRM v NC	<0.001	<0.001	<0.001
	TEW v NC	0.277	0.260	0.169

Table 8.3: Test for significant difference between reconstruction methods based on FWTM results of LEHR data
Friedman test for any significance differences in the dataset, followed by Dunn's test for individual p-values. The font colour indicates significance (green) or no significance (red).

A boxplot comparing the measurements of each reconstruction method at 160 iterations is shown in Figure 8.3.

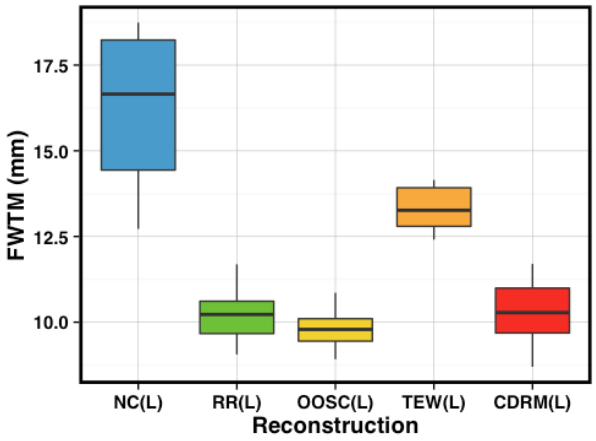

Figure 8.3: FWTM of correction schemes at 160 iterations for data acquired with LEHR collimators

These results show that reconstructions which include Resolution Recovery (RR) demonstrate a lower FWTM than the reconstruction with No Corrections (NC). This finding is due to the RR algorithm improving Signal to Noise Ratio (SNR) by increasing the signal relative to the tails of the LSF. Of the methods which include RR, the TEW(L) correction scheme will have the lowest SNR due to the subtraction of counts prior to reconstruction. Therefore, as expected, the TEW(L) has the largest FWTM of those reconstructions which included depth-dependent RR.

Although the evaluation of the FWTM of line sources was intended to assess the effectiveness of scatter suppression, comparison of the RR(L), OOSC(L) and CDRM(L) reconstruction results does not allow differentiation of these correction schemes. A visual inspection of the LSFs (Figure 8.4) illustrates that, in this instance, the FWTM is not a reliable indicator of effective scatter suppression as the tenth maximum is too high on the LSF.

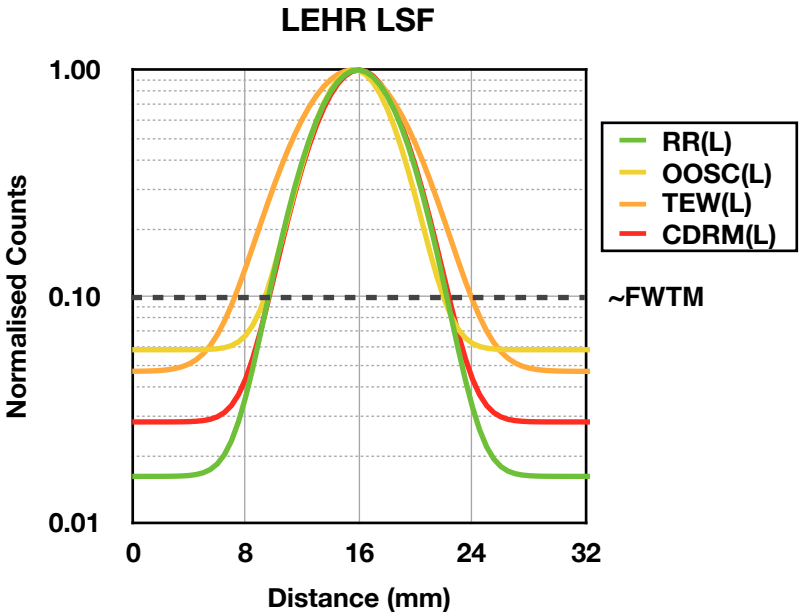

Figure 8.4: Gaussian fit of the tangential Line Spread Function (LSF) measurement at ninety-six iterations

Although Figure 8.4 shows that the LSF of the RR(L) correction scheme (without attenuation and scatter correction) demonstrates the lowest baseline, this has also been shown by El Fakhri [187] for ^{99m}Tc SPECT.

The LSF of the CDRM(L) algorithm demonstrates a lower baseline than the OOSC(L) and TEW(L) methods (which incorporate scatter correction). This finding suggests that CDRM(L) is the preferred correction scheme evaluated for scatter suppression of ^{123}I SPECT with LEHR collimators.

Of interest, the TEW(L) LSF has a lower baseline in Figure 8.4 compared with the OOSC(L), which suggests TEW is a more effective method of ^{123}I scatter correction. This finding contradicts the conclusion that would be drawn based on the FWTM measurement alone (Figures 8.2 and 8.3). This observation provides further evidence that the FWTM is not a sensitive metric for the assessment of scatter suppression by advanced iterative reconstruction algorithms.

8.3.1.2 Scatter Suppression (FWTM) of MELP Data

The FWTM results for a tangential measurement of the peripheral line source in the cylindrical phantom can be seen in Figure 8.5.

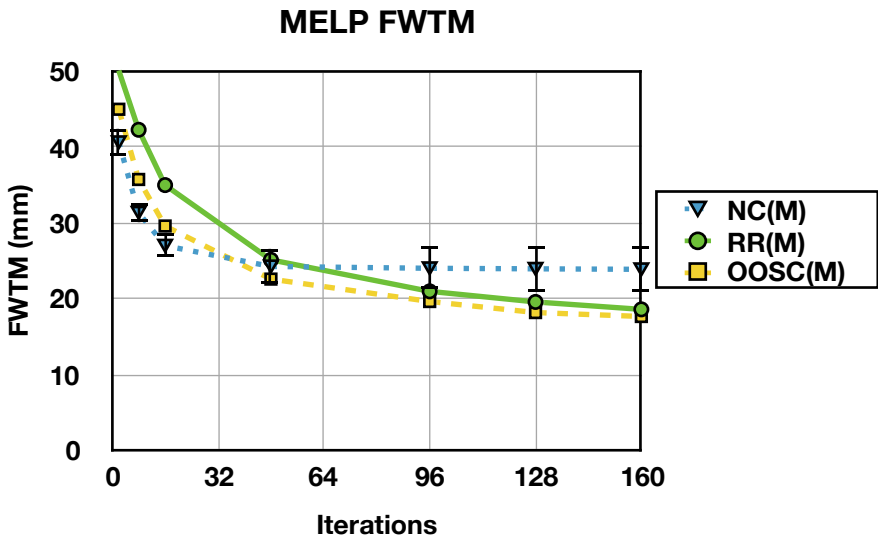

Figure 8.5: FWTM of peripheral line source acquired with MELP collimators

As expected, the FWTM of the MELP data is larger than the equivalent LEHR data reconstructions. For example, at 160 iterations the LEHR and MELP FWTM for the OOSC reconstruction are 9.8±0.4mm and 17.7±0.4mm respectively. However, similar to the LEHR FWTM results, the MELP reconstructions which include depth-dependent RR have a smaller FWTM than the reconstruction with NC at 96-160 iterations. A summary of tests for significant differences are shown in Table 8.4.

Statistical Test		Iterations 96	128	160
Friedman test	**All data**	<0.001	<0.001	<0.001
Dunn's test	**NC v RR**	0.180	0.008	0.004
	NC v OOSC	<0.001	<0.001	<0.001
	RR v OOSC	<0.001	0.004	0.017

Table 8.4: Test for significant difference between reconstruction methods based on FWTM results for MELP data
Friedman test for any significance differences in the dataset, followed by Dunn's test for individual p-values. The font colour indicates significance (green) or no significance (red).

Although there is a statistically significant differences between the FWTM of the RR(M) and OOSC(M) methods at 96-160 iterations, the actual difference is relatively small and not of clinical significance. For example, at 96 iterations, the OOSC(M) FWTM is 19.6±0.3mm while the RR(M) FWTM is 20.9±0.1mm.

8.3.2 Residual Error Results

Effective attenuation and scatter correction is indicated by the Residual Error (RE) approaching 0%. The percentage error indicates the potential error in activity

concentration measurement made in photopenic regions and, therefore, should be kept suitably low. An RE of 100% suggests that the central lung insert of the phantom contains the same mean count value as the surrounding uniform activity. The results for the error in the lung insert for LEHR and MELP acquisitions are shown in Figure 8.6.

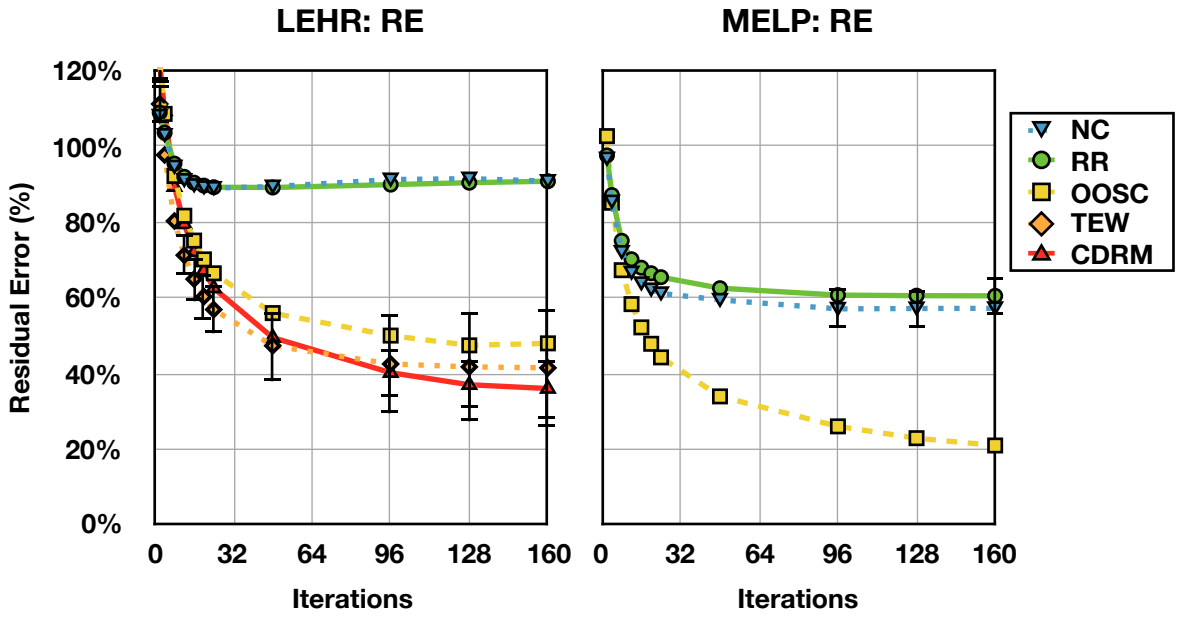

Figure 8.6: Residual Error (RE) in the torso phantom lung region
Comparison of correction schemes for LEHR data (left) and MELP data (right). Estimated error of 2xSE<5% is not shown.

Considering the LEHR reconstructions, the methods which incorporate attenuation and scatter correction (OOSC, TEW and CDRM) have a lower RE than the NC or RR reconstructions. There is a statistically significant difference between the methods with attenuation and scatter correction, and those without, for iterations greater than or equal to 12 (Table 8.5).

	OOSC(L)	TEW(L)	CDRM(L)
NC(L)	0.006	<0.001	0.001
RR(L)	0.003	<0.001	<0.001

Table 8.5: Test for statistically significant difference in RE between LEHR correction schemes
The p-values demonstrate significant difference (p<0.05) for all comparisons of 12 iteration reconstructions of LEHR data with and without attenuation and scatter correction.

There are statistically significant differences in RE between some of the reconstructions with attenuation and scatter correction, for example between the CDRM(L) and OOSC(L) methods for iterations greater than or equal to 48 (p=0.010; CI:6.7%±2.8). This difference may be of clinical significance in detection of, for example, the subtle uptake of a thyroid cancer lung metastasis.

Although the CDRM(L) reconstruction has a lower RE than the TEW(L) method at 128 and 160 iterations, there is no statistically significant difference (p=0.724; CI:5.5%±18.9 and p=0.637; CI:6.5%±20.3 respectively). The CDRM(L) reconstruction demonstrates the lowest RE of all the methods at 160 iterations, with RE lower by 11.3%±6.7 (p=0.011) compared with the OOSC(L) reconstruction and by 54.1%±7.0 (p=0.001) compared with the RR(L) reconstruction.

Regarding reconstruction of MELP data, the OOSC(M) method has a lower RE than the NC(M) or RR(M) reconstructions with a statistically significant difference for iterations greater than or equal to 8 (p=0.011; CI:4.6%±2.3 and p=0.011; CI:6.9%±2.6 respectively at 8 iterations). At 160 iterations the OOSC(M) method reduces RE by 39.6%±2.8 compared with the RR(M) reconstruction.

The results for both LEHR and MELP data show that the addition of attenuation and scatter correction provides a significant reduction in RE. Comparing like-for-like reconstructions, the RE results for the MELP collimator are lower compared to the LEHR collimator. There are two reasons for this: firstly, as was demonstrated by the lower Image Roughness (IR) results in Section 7.3.3, the MELP acquisition has a higher proportion of primary counts compared with the LEHR acquisitions. Secondly, the relatively large septal penetration present in the LEHR acquisition from the surrounding activity creates a uniform increase in counts in a region where no activity is present. The reconstruction algorithm fails to completely remove these counts in cold regions, even with corrections designed to solve this problem.

The coronal slices of the torso phantom shown in Figure 8.7 were chosen to illustrate the appearance of counts in the central lung insert. The images have no post reconstruction filter applied and are, therefore, not intended for overall comparison of image quality.

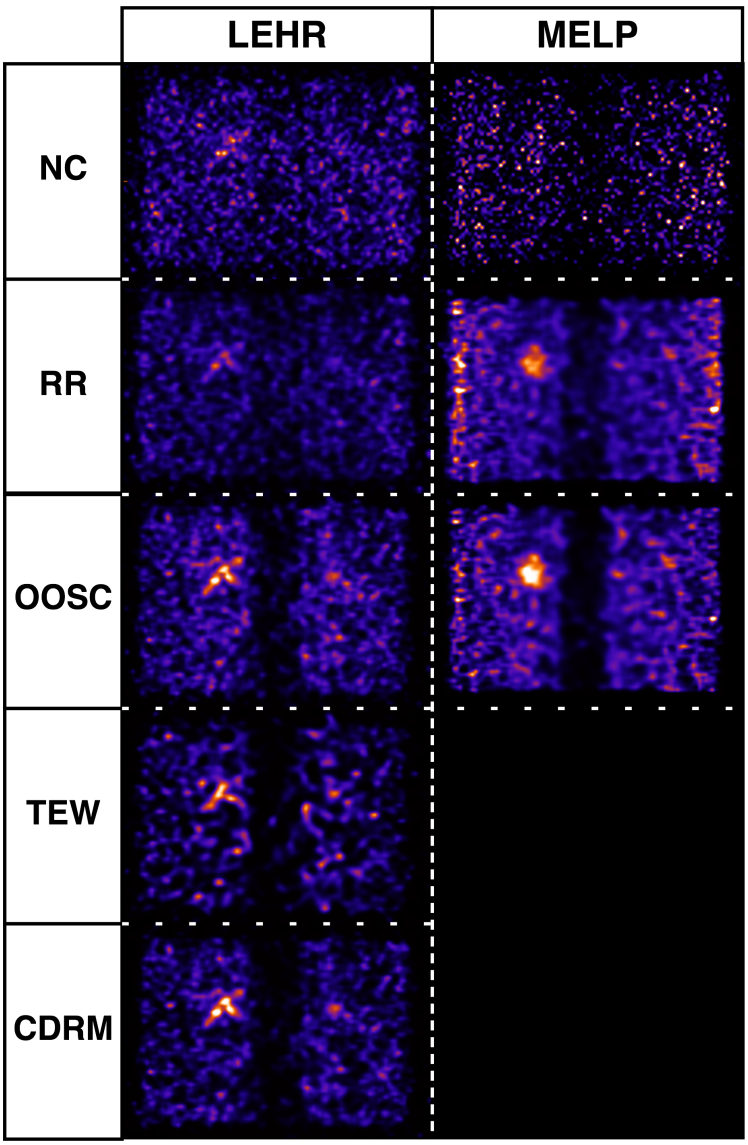

Figure 8.7: Coronal slice of the torso phantom which compares correction schemes at 96 iterations

8.4 Discussion

An aim of this Chapter was to investigate the effectiveness of combined attenuation and scatter correction methods for ^{123}I SPECT. A challenge for the scatter correction algorithm is to correct for high-energy septal penetration. These photons are detected across the full FOV in relatively high proportions when LEHR collimators are employed, as was shown by planar relative sensitivity results in Section 3.5.2.

Regarding FWTM measures, Rault [47] reported an improvement in FWTM of 29.3mm to 25.3mm for MELP acquisitions of ^{123}I when scatter correction was applied. However, the work in this thesis showed an almost negligible difference (18.6mm and 17.7mm respectively at 160 iterations). Similarly, the FWTM of the LEHR data demonstrated a negligible difference with and without CDRM(L) scatter correction of 10.2mm and 10.3mm

respectively at 160 iterations. The main differentiator between the study methods is that Rault did not apply RR which has been shown here to be a primary contributor in the reduction of the FWTM.

In this investigation, the FWTM did not differentiate advanced methods of scatter correction for LEHR data. Rather, a closer inspection of the LSF demonstrated that the FWTM was too high on the profile to discriminate between methods. Evaluation of the LSF showed that the CDRM technique had the lowest extended tails of the reconstruction methods which include attenuation and scatter correction.

The Residual Error (RE) investigation of this Chapter assessed counts in the lung insert of a torso phantom (a low-density structure with a relatively low probability of scatter). However, a proportion of high-energy septal penetration will appear as having originated from this region. For accurate quantification of photopenic low-density regions, the RE should be as low as possible.

As the lung insert is in the centre of the torso phantom, attenuation correction applies a large amplification to any photons which appear to have originated from there. Consequently, it was anticipated the OOSC(L) method would not appropriately subtract high-energy septal penetration in this region. This expectation was demonstrated by the OOSC(L) method having the highest RE of all the reconstruction methods which incorporate attenuation and scatter correction. Theoretically, the TEW(L) and CDRM(L) methods should correct for high-energy septal penetration. However, the lowest RE demonstrated by the CDRM(L) method (36.0% at 160 iterations) is 14.0%±9.0 larger than the OOSC(M) method ($p=0.004$). This result suggests that both Monte Carlo simulation and measured estimates of septal penetration are not optimal corrections.

The NC(M) demonstrated a 32.4%±7.1 improvement in RE over the NC(L) at 160 iterations. This comparison shows the improvement in RE using a hardware correction for septal penetration without software corrections. A comparable improvement of 27.0%±8.5 is also shown between the OOSC(M) and OOSC(L) schemes at 160 iterations. Published measurement of the RE in SPECT has been limited to date. It has not been used to characterise the effectiveness of attenuation and scatter correction in ^{123}I SPECT. However, van Gils applied the measure to ^{131}I SPECT and found RE was lowered from ~52% to ~28% with the addition of TEW scatter correction, and to ~23% with CDRM.

The lowest RE achieved by the OOSC(M) method in this study was 20.9%±3.6. This result suggests that, even with a hardware correction for septal penetration and an advanced software correction for scatter, there is a lower limit on RE. This limit will be based on both the relatively low proportion of septal penetration still experienced with the MELP collimators and noise amplification with relatively high iterations. In support of this conclusion, the lowest RE measured by van Gils [111] for ^{131}I SPECT was ~23% with a CDRM correction scheme. Van Gil's data consisted of initially low noise images from high activity concentration acquisitions and were reconstructed for 400 iterations. This idealised assessment provides further evidence of a lower limit on RE with increasing iterations.

8.5 Conclusions

Residual Error (RE) was shown to be a more sensitive measure for the evaluation of the effectiveness of attenuation and scatter correction than the FWTM of the Line Spread Function (LSF). Therefore, RE is recommended as an approach in future assessments of SPECT reconstruction algorithms.

OOSC(M) was shown to minimise RE of ^{123}I SPECT. Additionally, as anticipated, CDRM(L) and TEW(L) are more effective at reducing RE than OOSC(L) for LEHR acquisitions.

Chapter 9: Recommended Reconstruction Parameters and Post Reconstruction Filters

The aim of this Chapter is to consider, in combination, the results of quantitative image quality assessments performed in Chapters 4-8. The conclusions of these Chapters will be summarised with a recommended set of iterative reconstruction parameters.

Additionally, as the evaluations in Chapters 4-8 were performed without post-reconstruction filtering, this Chapter will introduce filter options and will investigate the impact of post-reconstruction filtering on the recommended reconstruction parameters.

9.1 Recommended Parameters for Iterative Reconstruction of ^{123}I SPECT

Chapters 4-8 have investigated quantitative image quality measures to assess advanced reconstruction correction algorithms applied to ^{123}I SPECT. The aim of this Section is to combine the results of these Chapters to summarise the optimal reconstruction parameters for routine use.

9.1.1 Summary of Practical Investigations

9.1.1.1 Reconstruction of Data Acquired with LEHR Collimators

In Chapter 4, spatial uniformity was assessed using a high count density cylindrical phantom. The reconstruction with No Corrections (NC) resulted in images with a uniform profile. This artefactual appearance is a result of high-energy septal penetration compensating for absorbed low-energy photons. Consequently, the OOSC scheme (which corrects for attenuation and scatter, but not septal penetration) demonstrated the poorest spatial uniformity, with an overestimation of counts towards the centre of the phantom. Both the CDRM and TEW schemes include correction for septal penetration. Of these, the CDRM option demonstrated superior spatial uniformity. Therefore, based on this measure, CDRM was recommended for reconstruction of LEHR data.

In Chapter 5, the application of depth-dependent Resolution Recovery (RR) was shown to significantly improve SPECT spatial resolution. Of the correction schemes which included RR, attenuation and scatter correction, only the TEW scheme was shown to be detrimental to the FWHM. Spatial resolution performance reached sufficient convergence for all correction schemes at greater than or equal to 96 iterations.

In the contrast recovery investigation of Chapter 6, the CDRM correction scheme demonstrated the highest Hot Contrast Ratio (HCR) in spheres ≥22mm in diameter when compared to the other correction schemes (with a statistically significant difference). However, there was no significant difference between schemes for spheres <22mm in diameter. For these smaller spheres, contrast recovery is poor for all methods of reconstruction as a consequence of partial volume effect, due to the limited spatial resolution of the imaging system. As with spatial resolution performance, contrast recovery reached sufficient convergence for all correction schemes at greater than or equal to 96 iterations.

As anticipated, noise (as measured by Image Roughness (IR)) was shown to increase with an increase in the number of iterations for all correction schemes. The CDRM algorithm outperformed alternative correction schemes by demonstrating the lowest IR and the lowest Background Variability (BV) of those schemes which included both attenuation and scatter correction. Furthermore, Contrast to Noise Ratio (CNR) was shown to be highest for the CDRM algorithm, with a statistically significant difference for iterations greater than or equal to 8 when compared to all other correction schemes.

In Chapter 8, in a demonstration of effective scatter correction, the CDRM algorithm was shown to have the lowest Residual Error (RE) in the lung insert of a torso phantom. However, there was no statistically significant difference when compared with the TEW method. RE suitably converged at greater than or equal to 96 iterations.

In summary, the CDRM correction scheme has been shown as the optimal method for reconstruction of ^{123}I SPECT data acquired with LEHR collimators. This conclusion is evidenced by the algorithm's superior spatial uniformity, contrast recovery, noise characteristics and scatter suppression when compared with alternative correction schemes evaluated in this thesis. Where the CDRM algorithm is not available, the TEW correction scheme, which includes correction for high-energy septal penetration, should be used.

With regard to convergence of the quantitative measures summarised here, clinical ^{123}I SPECT studies, reconstructed using the CDRM or TEW correction schemes, should use 96 iterations. Further iterations will continue to increase noise with no clinically significant improvement in spatial resolution, contrast recovery or scatter suppression.

9.1.1.2 Reconstruction of Data Acquired with MELP Collimators

Data acquired with MELP collimators and reconstructed with the OOSC correction scheme demonstrated superior spatial uniformity, contrast recovery, noise characteristics and scatter suppression when compared with alternative reconstruction methods evaluated. Therefore, the OOSC algorithm should be used for reconstruction of MELP data.

Furthermore, the use of the OOSC algorithm to reconstruct MELP data outperformed the CDRM reconstruction of LEHR data in terms of spatial uniformity, contrast recovery, noise and scatter suppression. This outcome suggests that quantitative accuracy may be improved with SPECT data acquired using MELP collimators. However, the spatial resolution of MELP data is poorer than that of LEHR data and is, therefore, not recommended for neurology applications.

As with the LEHR findings, MELP reconstructions demonstrated reasonable convergence for iterations greater than or equal to 96. Therefore, 96 iterations should be used for clinical ^{123}I SPECT studies acquired with MELP collimators.

9.1.2 Recommended Reconstruction Parameters

LEHR collimators should be used to acquire SPECT data where spatial resolution is of primary importance, such as for neurology applications. MELP collimators should be used for other clinical applications if accurate quantification is required and spatial resolution is secondary. Table 9.1 presents recommended parameters for reconstruction of ^{123}I SPECT based on the findings of Chapters 4-8.

	Collimator	
	LEHR	**MELP**
Iterations	96 (6 iterations, 16 subsets)	
Resolution Recovery	Yes	
Attenuation Correction	CT	
Scatter Correction	CDRM*	OOSC
Reconstruction Time	~6min 30sec	~2min 11sec

Table 9.1: Recommended reconstruction parameters for ^{123}I SPECT
(*) TEW to be used where CDRM is unavailable

9.2 Introduction to Post Reconstruction Filters

The reconstruction parameters recommended in Section 9.1 are with regard to optimisation of quantitative image quality metrics. However, the number of reconstruction iterations required to optimise these measures results in images that are too noisy for visual interpretation by human observers [188]. These noisy images affect not only the ability of the observer to confidently diagnose a patient study but will also impair manual placement of ROIs/VOIs. Therefore, post-reconstruction filters are often applied to suit an observer's preference for noise level and to make images more visually appealing. Performing fewer iterations will also reduce noise, as was shown in Section 7.3.3. However, reducing iterations will result in poorer spatial resolution and contrast recovery.

Consequently, the use of a post-reconstruction filter to regulate the noise in data optimised for quantification is currently routine practice in SPECT imaging [132]. For example, similar to the approach presented in this thesis, recent work by Dickson [30], which investigated optimisation of ^{123}I-DaTSCAN™ SPECT reconstruction parameters for relative quantification, was performed with no post-reconstruction filter applied. This approach allows assessment of the convergence of advanced reconstruction algorithms without the compounding effects of a filter.

The findings from Dickson's study were used to inform the European Association of Nuclear Medicine (EANM) Research Ltd (EARL) approach to standardisation of reconstruction parameters for ^{123}I-DaTSCAN™ relative quantification. However, the reconstruction parameters have been adopted by EARL with the addition of a Butterworth low-pass post-filter [29, 51, 117, 123, 125, 126]. This approach has been recommended in EANM guidelines for ^{123}I SPECT neurotransmitter imaging [27]. Therefore, this Chapter will review commonly used filter options for ^{123}I SPECT.

As previously suggested, post-reconstruction filters have an effect on image quality metrics. For example, Lyra [188] showed that post-filtered ^{99m}Tc-DMSA SPECT images had improved kidney to background contrast compared to unfiltered data. However, typical low-pass smoothing filters reduce spatial resolution [188] and increase partial volume effect [2]. With regard to quantification, Dewaraja [2] demonstrated that a low-pass post-filter reduced the effects of noise in the object of interest, which resulted in a near constant activity measurement within the object.

Consideration of all potential filter options would be a substantial undertaking. The full effect of these options on quantification has yet to be assessed [189] and is beyond the scope of this thesis. However, as patient data will be post-filtered for visual interpretation, the effect of post-filters on image quality metrics should be included. In the current work, the most relevant candidates for ^{123}I SPECT will be assessed.

Therefore, the aim of this Section is to review recommendations for post-reconstruction filters and investigate the effect of these filters on image quality metrics. Following this evaluation, a preferred approach to post-reconstruction filtering for quantitative ^{123}I SPECT imaging will be made.

9.3 Review of Filter Options

The Hermes Medical Solutions Hybrid Recon™ application used in this thesis has the option of two post-reconstruction filter types: a Butterworth and a Gaussian. The Butterworth filter is defined by a frequency cutoff in units of cm^{-1} and a filter order which, combined, control the rolloff of the filter. The Gaussian filter is defined by the Full Width at Half Maximum (FWHM) of a Gaussian profile.

Dickson [30] performed a study to optimise ^{123}I SPECT reconstruction parameters based on convergence of relative uptake ratios. These parameters have subsequently been used clinically and in multi-centre trials, with an additional post-filter applied [29, 51, 117, 123, 125, 126]. In each of these studies, a 10th order Butterworth filter with a $0.5cm^{-1}$ cutoff was used. Dickson [190] described these filter parameters as being chosen to provide a good visual balance between resolution and noise. Further work by Dickson [191] suggested that for a wide range of filter cutoffs examined there was no clinically significant difference in relative uptake ratios.

In published work to date [29, 51, 117, 123, 125, 126], the 10th order Butterworth filter with $0.5cm^{-1}$ cutoff has been applied to data acquired with a Siemens Symbia gamma camera

and reconstructed with Triple Energy Window (TEW) scatter correction. The Butterworth filter parameters were, therefore, chosen to suitably reduce the noise in a TEW corrected reconstruction. However, in Chapter 7 of this thesis it was demonstrated that TEW reconstructions have a greater noise level (Image Roughness) than alternative reconstructions with Monte Carlo scatter correction. Therefore, the same filter may overly smooth advanced reconstruction techniques which features less noise and superior spatial resolution performance (see Section 5.3.2).

The order and cutoff of the commonly used Butterworth filter results in a sharp filter rolloff, which can introduce ringing artefacts. However, the rolloff can be controlled by reducing the order of the filter. An alternative approach is to use a Gaussian filter with a suitable FWHM. The latter approach has been adopted by Hermes Medical Solutions in their recommended parameters for reconstruction of ^{123}I SPECT data intended for relative quantification [192, 193]. Furthermore, Lyra [188] showed that Gaussian filters have maintained suitably high contrast and Signal to Noise Ratio in reconstructed images.

Hermes Medical Solutions recommend a Gaussian post-reconstruction filter with a FWHM of 7mm. A similar Gaussian filter, with a FWHM of 8mm, was used by Winz [194] to limit noise in background reference regions of ^{123}I SPECT data reconstructed without scatter correction. As Hermes Medical Solutions reconstruction parameters for relative quantification include advanced scatter correction, their suggested filter with a FWHM of 7mm may have been chosen to maintain image quality metrics without over smoothing, compared with Winz. Figure 9.1 compares the filter profiles of the commonly used Butterworth and the recommended Gaussian filter.

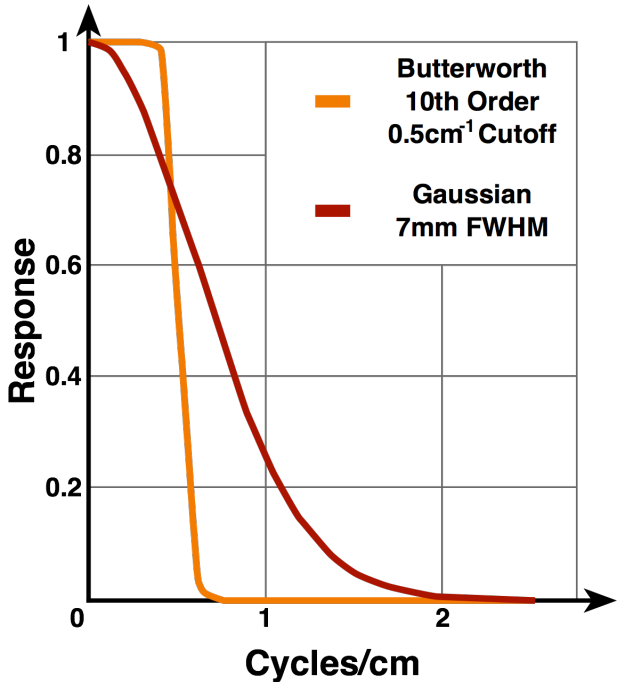

Figure 9.1: Response of the commonly used Butterworth and Hermes Medical Solutions recommended Gaussian filters
The Butterworth filter (10th order, 0.5cm^{-1} cutoff) is commonly used in the literature and the Gaussian filter (7mm FWHM) is recommended by Hermes Medical Solutions

Figure 9.2 compares images filtered with a Gaussian (7mm FWHM) and a Butterworth (10th order, 0.5cm^{-1} cutoff) filter, with ringing demonstrated in the latter image.

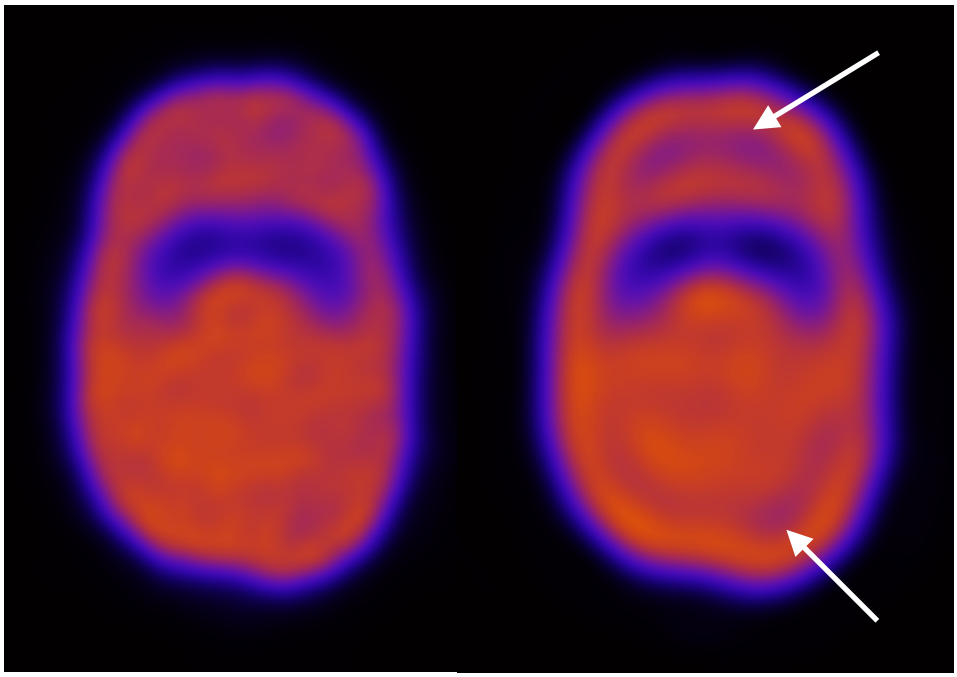

Figure 9.2: Post-filtering of a striatal phantom with a uniformly filled background compartment
Reconstructions are post-filtered with Hermes Medical Solutions recommended Gaussian (7mm FWHM) filter (left) and the commonly used Butterworth (10th order, 0.5cm^{-1} cutoff) filter (right), which demonstrates ringing artefacts.

Post-reconstruction filters are used to reduce high frequency noise. However, using a post-reconstruction filter can influence image quality metrics such as spatial resolution and contrast. For example, the use of a low-pass filter to suppress high frequency noise will result in poorer spatial resolution. Given this trade-off, it is important to investigate how significant these effects are. Therefore, an investigation was performed which compared the unfiltered image data from Chapters 5-8, with images post-filtered with the Butterworth and Gaussian filter options outlined in this Section. Specifically, the metrics evaluated were:

- Image Roughness (IR)
- Hot Contrast Recovery (HCR)
- Residual Error (RE)
- Spatial resolution

Furthermore, an evaluation of Hermes Medical Solutions recommended Gaussian filter width was performed by comparing a range of filter widths.

9.4 Methods and Materials

9.4.1 Post Reconstruction Filters

Two post-reconstruction filters were evaluated in this study:

1. A 10th order Butterworth filter with a cutoff frequency of 0.5cm^{-1} (as commonly used for ^{123}I SPECT reconstruction [29, 51, 117, 123, 125, 126]).
2. A Gaussian filter with a FWHM of 7mm (as recommended by Hermes Medical Solutions for ^{123}I SPECT reconstruction including advanced corrections [192, 193]).

Furthermore, the Gaussian filter width was varied from 2mm to 20mm to assess Hermes Medical Solutions choice of filter width.

9.4.2 Effect of a Post-filter on Contrast, Noise and Residual Error

Hot Contrast Recovery (HCR), Image Roughness (IR) and Residual Error (RE) were described with reference to a torso phantom in Sections 6.2, 7.2 and 8.2 respectively. In summary, the torso phantom was prepared with a sphere to background concentration ratio of ~4:1 and was acquired with LEHR and MELP collimators. The phantom was acquired with the parameters outlined in Section 6.2.2.

The data assessed in Chapters 6-8 were unfiltered. In this Chapter, the same torso phantom reconstructions had the two previously described post-reconstruction filters

applied. HCR, IR and RE were then remeasured for comparison with the unfiltered results. In this Chapter, data were reconstructed with the set of recommended parameters described in Table 9.1.

9.4.3 Effect of a Post-filter on Spatial Resolution

In Chapter 5, the Full Width at Half Maximum (FWHM) was used to measure spatial resolution. A perturbation method with line sources in surrounding activity was used to estimate system spatial resolution with advanced reconstruction correction schemes. The same data was used in this Chapter to assess the influence that a post-filter had on the spatial resolution.

In summary, the data were acquired using both the LEHR and MELP collimators. The acquisitions were performed using the complex perturbation method and parameters outlined in Section 5.2.2.2. The spatial resolution phantom data was reconstructed using the set of recommended parameters described in Table 9.1. Spatial resolution was measured by fitting a Gaussian curve to the Line Spread Function (LSF) of sources, as described in Section 5.2.4.

9.4.4 Analysis of Post Filtered Data

Image quality metrics for reconstructions with a post-filter applied were compared with the same metrics for unfiltered data and a percentage bias calculated to evaluate the effect of the filter. For example, Image Roughness (IR), as measured in the torso phantom, was used to quantify the reduction of noise due to a post-reconstruction filter.

The percentage bias in HCR was measured for the three largest spheres in the torso phantom. The percentage bias for HCR of the three smallest spheres was not measured due to both the small HCR values and significant measurement variation. These factors make the HCR of the smallest spheres susceptible to a large bias when having undergone a relatively minor change in value.

9.5 Post Reconstruction Filter Results

9.5.1 Bias Introduced by Post Reconstruction Filters

The percentage bias of post-reconstruction filtered image data compared to unfiltered data is shown in Table 9.2. A reduction in Image Roughness (IR) is desirable. However, a reduction in Hot Contrast Recovery (HCR) indicates a worsening of image contrast. An

increase in Residual Error (RE) indicates counts have been smoothed into what should be a cold region, and an increase in FWHM indicates a worsening of spatial resolution.

	CDRM(L)		TEW(L)		OOSC(M)	
	Butterworth	**Gaussian**	**Butterworth**	**Gaussian**	**Butterworth**	**Gaussian**
Noise (IR)	-33.6%	-32.9%	-47.4%	-35.2%	-34.1%	-30.2%
HCR 37mm	-0.4%	-4.8%	-4.8%	-5.3%	10.3%	-3.4%
HCR 28mm	3.4%	-4.4%	3.8%	-5.3%	5.3%	-6.7%
HCR 22mm	4.1%	-3.0%	-8.8%	-12.4%	4.6%	-9.2%
RE	1.4%	3.4%	-1.3%	5.1%	-2.3%	2.3%
FWHM	74.2%	22.6%	53.8%	27.5%	22.8%	8.1%

Table 9.2: The effect of two post-reconstruction filters on image quality measures Commonly used 10th order Butterworth with a 0.5cm^{-1} cutoff, and a Gaussian with a 7mm FWHM. Acronyms: Collimator and Detector Response Modelling (CDRM), Triple Energy Window (TEW), Image Roughness (IR), Hot Contrast Recovery (HCR), Residual Error (RE)

The primary aim of a post-reconstruction filter is to reduce noise. The TEW reconstruction with the commonly used Butterworth post-filter demonstrates the largest negative bias in IR (-47.4%). Assuming noise reduction is the primary objective, this result supports Dickson's [125] proposal for use of the filter as part of a standardised approach to ^{123}I SPECT reconstruction. The post-filtering of all other datasets demonstrate comparable values for noise reduction (-30.2% to -35.2%).

A positive bias is shown in some HCR results with a Butterworth filter applied, in particular the OOSC(M) 22mm, 28mm and 37mm, and CDRM(L) 22mm and 28mm sphere results. This positive bias supports the suggestion that a 10th order Butterworth filter may introduce ringing artefacts.

With regard to the CDRM(L) and OOSC(M) reconstructions, the Gaussian 7mm FWHM filter has a comparable reduction in noise level to the Butterworth. Importantly, the Gaussian filter demonstrates less degradation of spatial resolution (FWHM) compared with the Butterworth filter. This finding, in conjunction with a concern over the recommended Butterworth filter parameters which may introduce ringing artefacts, suggests that, of the two filter profiles investigated in this Section, the Gaussian filter should be used for quantitative reconstructions.

9.5.2 Evaluation of Hermes Medical Solutions Choice of Gaussian Filter Width

A Gaussian post-reconstruction filter, ranging in filter width from 2mm to 20mm, was applied to the torso phantom data. The percentage bias in noise (IR) between the post-filtered and unfiltered data is shown in Figure 9.3.

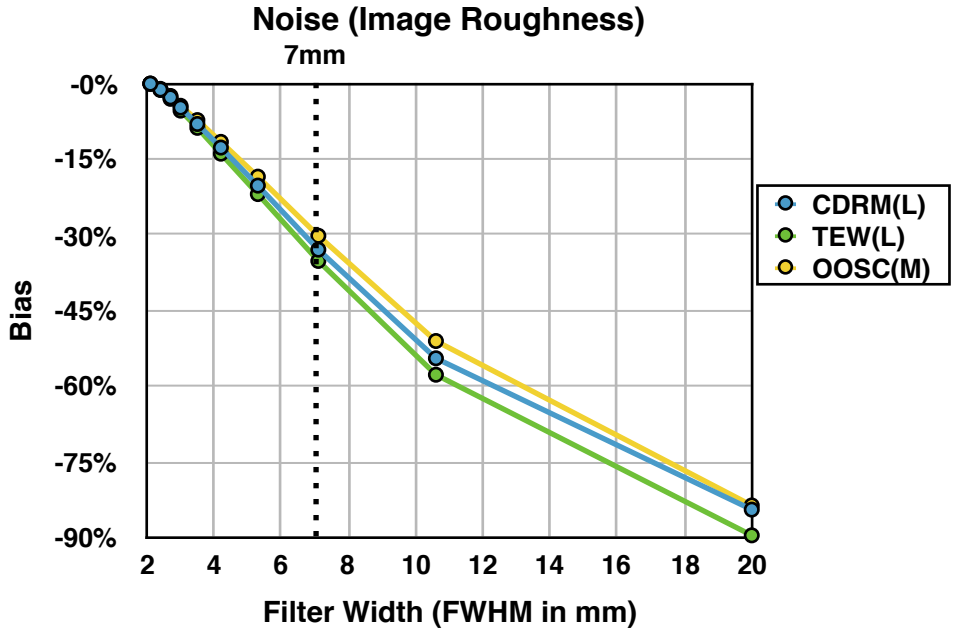

Figure 9.3: Percentage bias in noise (Image Roughness) between unfiltered and post-filtered data
A negative bias indicates a reduction in noise, which is a primary goal of the post-reconstruction filter

With regard to image noise, a comparable response to post-filtering was demonstrated for all three reconstruction schemes. With reference to Hermes Medical Solutions recommended filter width of 7mm, a reduction of >30% is achieved for all three methods. A wider filter profile could be chosen given that the aim of a post-filter is to reduce noise. For example, a filter width >10mm would reduce noise by >50% for all three methods. However, this approach would negatively affect other image quality metrics.

The percentage bias in HCR for the three largest spheres in the torso phantom is shown in Figure 9.4.

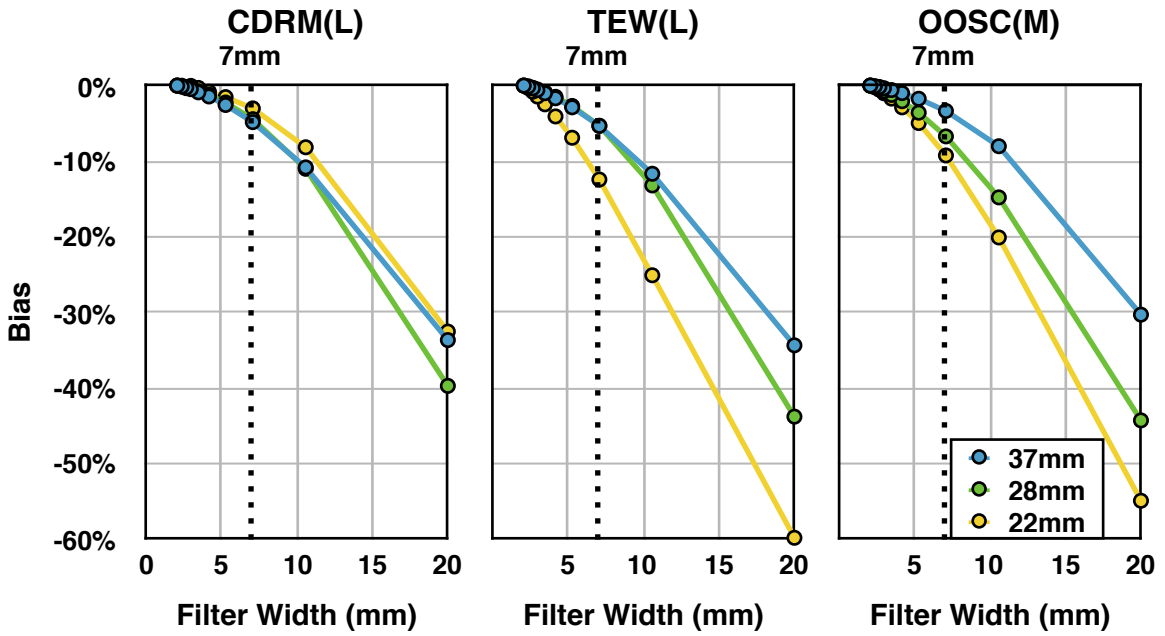

Figure 9.4: HCR curves for the three largest spheres in the torso phantom Reconstructed with CDRM(L) (left), TEW(L) (middle) and OOSC(M) (right), post-filtered with a Gaussian filter ranging in FWHM from 2mm to 20mm

All spheres demonstrate a reduction in HCR for all filter widths and with all three reconstruction schemes. Considering Hermes Medical Solutions recommended filter width of 7mm, the HCR negative bias of the three spheres is:

- less than 15% for the TEW(L) correction scheme
- less than 10% for the OOSC(M) reconstruction, and
- less than 5% for the CDRM(L) reconstruction scheme

These reductions in HCR compared with unfiltered images can be considered an acceptable compromise to achieve a reduction in noise (IR) of >30%. As suggested previously, increasing the filter width to >10mm would further reduce noise but would also double the reduction in HCR.

The bias in Residual Error for post-reconstruction filtered data compared with unfiltered images is shown in Figure 9.5.

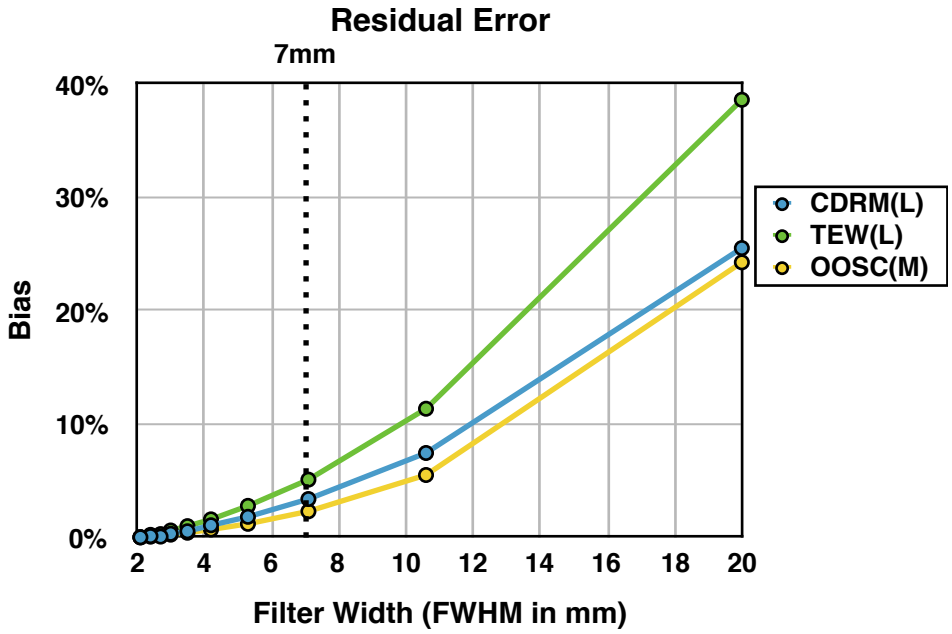

Figure 9.5: Bias in Residual Error (RE) for the lung insert of the torso phantom Post-filtered with a Gaussian filter which ranged in width from a FWHM of 2mm to 20mm

All three reconstruction correction schemes demonstrate a positive bias in RE, which increased with an increasing filter width. As RE should tend towards zero, a positive bias indicates a worsening of the metric. The RE increases as counts from surrounding uniform regions are smoothed into the cold lung insert in the centre of the phantom.

The increase in RE is less than 5% for all reconstruction schemes using Hermes Medical Solutions recommended 7mm filter width. This result is an acceptably low bias in order to achieve the reduction in noise (IR) which the filter fulfils (>30% reduction in IR).

9.6 Discussion

The Butterworth filter, used in the literature for iterative ^{123}I SPECT data, resulted in a positive bias in HCR. This finding may be as a result of a Gibb's ringing artefacts from the 10th order relatively sharp rolloff (see Figure 9.1). A study by O'Mahoney [88] demonstrated that even a Butterworth post-filter with a shallower 5th order, used for ^{99m}Tc SPECT data, still resulted in Gibb's ringing artefacts in small sources (2-3cm). However, the shallower rolloff of the Gaussian filter profile recommended by Hermes Medical Solutions appears to reduce the likelihood of ringing artefacts.

Evaluation of the Gaussian filter width demonstrated the trade-offs inherent in parameter optimisation. In this investigation, the 7mm filter width was shown to reduce noise (IR) by 30.2-35.2%. Noise analysis results from Section 7.3.3 suggest a similar reduction in IR could be achieved by a reduction in the reconstruction iterations from 96 to 48. However,

this would also reduce HCR. For example, lowering the number of iterations from 96 to 48 reduces HCR by 31% and 21% for the 17mm and 22mm sphere respectively for CDRM(L) reconstructions. That compares with a 12% and 3% reduction in HCR of the 17mm and 22mm spheres with 96 iterations and a 7mm wide Gaussian filter. Therefore, the post-filter approach provides a more effective means of reducing noise whilst maintaining HCR.

In clinical terms, Winz [194] reported noise levels (IR) in ^{123}I-DaTSCAN™ patient studies as 17.6% with 96 iterations and a Gaussian post-filter with an 8mm FWHM. Patient studies had a higher count density than the torso phantom used in this investigation and, therefore, IR is not directly comparable. However, it is important to note Winz chose the filter width to achieve a low noise reference region for relative uptake measurements and, therefore, a wider filter FWHM was preferable. With regard to absolute quantification, prioritising optimal HCR is more important and so the Gaussian filter with a FWHM of 7mm used in the current study would be more appropriate.

Although the application of a post-filter was shown to preserve contrast compared with a reduction in the number of iterations, the effect on spatial resolution is comparable. The ^{123}I SPECT spatial resolution results in Section 5.3.2 indicate that reducing iterations from 96 to 48 would increase FWHM by 21.0%, whereas post-filtering resulted in a 22.6% increase.

The current study is not a comprehensive assessment of the full range of filter options and parameters available, which is beyond the scope of this thesis. However, this phantom evaluation has demonstrated that the use of a Gaussian filter with a FWHM of 7mm is a good compromise between noise reduction and any deterioration in image quality metrics.

9.7 Conclusions

The filter commonly used in the literature for ^{123}I SPECT reconstruction (a 10th order Butterworth with a 0.5cm^{-1} cutoff) has a profile with a sharp rolloff which may introduce ringing artefacts.

Use of the Gaussian filter with a 7mm FWHM, as recommended by Hermes Medical Solutions, sufficiently suppresses noise whilst suitably maintaining other quantitative image quality metrics. Therefore, for subsequent work in this thesis, iterative reconstruction of ^{123}I SPECT data will be post-filtered using a Gaussian filter with a 7mm FWHM.

Chapter 10: Relative Quantification of ^{123}I SPECT

10.1 Introduction

Quantification of activity concentration can be a useful tool to assist with the interpretation of clinical studies. Standard approaches to quantification are outlined in Section 2.6. The two most common methods used in SPECT imaging are relative and absolute quantification. Relative quantification is a measure of uptake in relation to another disease-free region, whereas absolute quantification refers to a direct measure of activity concentration [9]. This Chapter will focus on relative quantification and the relationship between measured and true uptake ratios for advanced reconstruction correction schemes applied to ^{123}I SPECT data. Chapter 11 will be dedicated to absolute quantification.

To date, relative quantification has been the most common method of analysis in nuclear medicine imaging. In particular, assessment of ^{123}I-DaTSCAN™ studies using automated packages such as Hermes Medical Solutions BRASS™ [29], open source Bas-Gan [123] and GE Healthcare's DaTQUANT [124] have become routine clinical practice in many centres. These software packages spatially register SPECT data to a template, which allows regions to be automatically applied for analysis. The ratio between an area of specific and non-specific uptake is measured and compared with either a local normal range or an international normal database. The Bas-Gan and BRASS™ packages use the European Association of Nuclear Medicine (EANM) Research Ltd (EARL) ENC-DAT database [117], while DaTQUANT uses the Parkinson's Progression Markers Initiative database [124]. An international normal database is important for standardisation across multiple centres and is particularly useful for multi-centre clinical trials [125].

The EANM published guidelines for the determination of a gamma camera Calibration Coefficient (CC) for inclusion in ^{123}I-DaTSCAN™ multi-centre trials [51]. The purpose of

the guidance was to characterise and harmonise imaging equipment from the various institutions involved in the generation of the European ENC-DAT database. The method described uses the linear regression of measured to true uptake ratios in a striatal phantom to determine the CC. The CC is the gradient of a linear slope, which describes the relationship between measured and true uptake ratios in a striatal phantom. Therefore, a CC allows conversion of a measured uptake ratio to the true uptake ratio. The preliminary setup for using BRASS™ analysis software, to allow comparison of clinical studies with the integrated ENC-DAT normal database, follows the EANM guideline to determine a camera and reconstruction specific CC.

The Triple Energy Window (TEW) scatter correction technique [82], combined with uniform attenuation correction, has been the most widely used reconstruction protocol by centres participating in the ENC-DAT normal database project [29-31, 51, 123, 125]. However, since integration of the ENC-DAT data into their BRASS™ application, Hermes Medical Solutions have retro-reconstructed the data using Object Only Scatter Correction (OOSC) rather than TEW. The reconstruction scheme uses a uniform map of attenuation coefficients for attenuation correction and OOSC. Uniform attenuation correction was used as the patient studies did not have CT and, furthermore, many centres do not routinely acquire a sequential CT.

There is no published data on whether the OOSC algorithm maintains a linear relationship between measured and true uptake ratios. Similarly, there has been no assessment of the Collimator and Detector Response Modelling (CDRM) correction scheme. Therefore, in this chapter an investigation was performed to evaluate the linearity of relative uptake measurements for data reconstructed with OOSC and CDRM, including CT attenuation correction. In this investigation, CCs were determined for a Siemens Symbia T2 gamma camera using Hermes Medical Solutions recommended reconstruction protocol and the advanced reconstruction correction schemes which include CT attenuation correction and Monte Carlo scatter correction. The primary aim of this chapter was to assess the linearity of the measured to true uptake ratio curves of these advanced correction schemes.

The EANM guideline for the determination of a CC describes the use of a striatal phantom containing ~27MBq with an acquisition Radius of Rotation (ROR) of 15cm [51]. As such, the relationship between measured and true uptake ratio with higher activity concentrations has not been assessed. This thesis has shown that the planar count rate response to a focal source of ^{123}I at a distance of 15cm is non-linear when activities exceed 40MBq (Section 3.6). Therefore, using this calibration method, as activity

concentration in the striatal phantom increases the apparent sensitivity of the detector may lower. Although the striatal phantom contains a more diffuse activity concentration than the focal sources used to characterise count rate response in Section 3.6, a further aim of this investigation was to assess the effect of higher activity concentrations on the linearity of the CC curve.

10.2 Methods and Materials

Determination of CCs was performed using a striatal phantom. A striatal phantom consists of a brain shell containing five fillable compartments: a left and right caudate and putamen of the basal ganglia, and a background region. Each section can be filled independently to simulate various striatal to background uptake ratios. The volume of the caudate and putamen sections are 5.4ml and 6.0ml respectively, which is typical of normal volumes [31]. The background region has a volume of ~1260ml. A skull section surrounds the brain shell. The skull section simulates bony attenuation surrounding the brain and includes the sinuses and nasal cavity. The striatal phantom from Radiology Support Devices is shown in Figure 10.1.

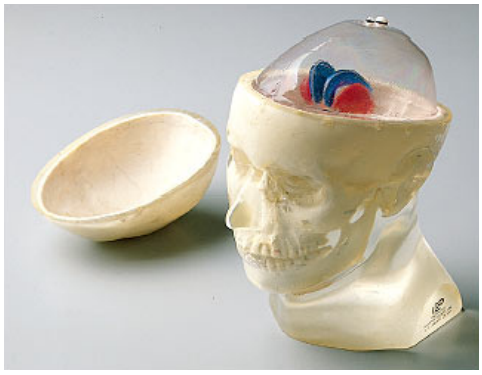

Figure 10.1: Radiology Support Devices striatal phantom with skull

10.2.1 Striatal Phantom Preparation

The guidelines from the ENC-DAT project [51] were followed. Three separate phantoms were used: a high, a medium and a matched activity concentration to that used in the guidelines. The matched activity concentration simulated typical count rates in clinical ^{123}I-DaTSCAN™ studies. In keeping with the guidelines, the right and left caudate and putamen sections initially contained 8 and 10 times the activity concentration of the background compartment respectively. The activity concentration in the background compartment was doubled twice to achieve a range of uptake ratios from approximately 2 to 10. True Uptake Ratios (TURs) in the phantom were determined by counting aliquot samples of the activity concentrations in a gamma counter and using Equation 10.1 [51].

$$TUR = \left(\frac{U}{BG} \right) - 1 \qquad \textbf{Equation 10.1}$$

where *U* is activity concentration in the right or left striatum, and *BG* is the activity concentration in the background region. Table 10.1 shows the range of TURs and activity concentrations used for each of the three phantom setups.

	Calibration Guidelines	Matched Activity Concentration	Medium Activity Concentration	High Activity Concentration
Left Striatal Concentration	50kBq/ml	44kBq/ml	85kBq/ml	169kBq/ml
Right Striatal Concentration	40kBq/ml	36kBq/ml	68kBq/ml	135kBq/ml
Background Concentrations	5kBq/ml 10kBq/ml 20kBq/ml	4.4kBq/ml 8.8kBq/ml 17.6kBq/ml	7.7kBq/ml 15.4kBq/ml 30.8kBq/ml	15.4kBq/ml 30.8kBq/ml 61.6kBq/ml
Activity in the FOV	7.5-27.0MBq	6.7-23.8MBq	12.0-42.0MBq	24.0-84.0MBq
Range of TURs	1-9	0.8-8.5	1.2-9.3	0.9-8.3

Table 10.1: Comparison of activity concentration ratios and range of True Uptake Ratios (TURs) for striatal phantom setups

10.2.2 Striatal Phantom Acquisition

Data were acquired using a Siemens Symbia T2 gamma camera with LEHR collimators. The guidelines recommend that the images should include ~3M counts [51]. To achieve this count density, a preliminary audit of 25 consecutive ^{123}I-DaTSCAN™ patient studies with ~3M counts demonstrated an average of ~25kcts in the first projection. Therefore, all phantom acquisitions were acquired based on 25kcts in the first projection. This methodology ensured that the count rate was the only difference between acquisitions. Table 10.2 shows the total counts in each study.

	Count Rate (kcts/s)	Total Counts (M)
Matched activity concentration	2	3.4
Medium activity concentration	3.5	2.9
High activity concentration	6.8	2.7

Table 10.2: Count rate and total counts in the study for striatal phantom acquisition

Table 10.3 shows additional SPECT acquisition parameters.

Parameter	Value
Matrix	128x128
Zoom	1.45
Pixel Size	3.3mm
Projections	128
Orbit	Circular
Radius of Rotation	15cm
Photopeak	159keV±10%
Scatter windows	Lower: 138±4keV Upper: 178±4keV

Table 10.3: SPECT acquisition parameters for ENC-DAT calibration

Acquisition of a sequential CT, acquired with the parameters in Table 10.4, was used for attenuation and Monte Carlo scatter correction.

Parameter	Value
CT mA	35mA
CT kVp	130kVp
CT Reconstruction Slice Width	2.4mm

Table 10.4: Parameters of the sequentially acquired CT

10.2.3 Striatal Phantom Data Reconstruction

The method of reconstruction recommended by Hermes Medical Solutions for use with BRASS™ includes depth-dependent Resolution Recovery (RR), uniform attenuation correction and OOSC. In addition to this correction scheme, data were reconstructed with the TEW(L) and CDRM(L) advanced correction schemes, as recommended in Section 9.1. Furthermore, the OOSC(L) correction scheme was applied to allow comparison of reconstruction with CT and uniform attenuation correction, and comparison of reconstructions with and without correction for septal penetration. These reconstructions used 96 OSEM iterations (6 iterations, 16 subsets) as recommended in Section 9.1 and by Dickson [30] for accurate relative quantification of ^{123}I-DaTSCAN™ studies. The reconstruction correction schemes applied to the data acquired for CC determination are summarised in Table 10.5.

Name	Hermes Method	Alternative methods		
	OOSC(Uniform)	OOSC(CT)	TEW(CT)	CDRM(CT)
Iterations	64	96	96	96
RR	✔	✔	✔	✔
Attenuation Correction	Uniform: Attenuation Coefficient = 0.146cm^{-1} Outline Threshold = 30% Outline Filter FWHM = 2.5cm	CT	CT	CT
Scatter Correction	OOSC	OOSC	TEW	CDRM

Table 10.5: Reconstruction correction schemes

10.2.4 Image Analysis

Hermes Medical Solutions BRASS™ application is a method of analysis which allows automated relative quantification of ^{123}I-DaTSCAN™ studies. BRASS™ registers and compares patient data to three-dimensional reference templates, created from images of normal patients. The process of registration follows a rigid method which applies translation and rotational shifts. Predefined anatomical VOIs (the size and shape of a normal caudate and putamen) are automatically applied to measure relative uptake between specific striatal and non-specific occipital regions (Figure 10.2).

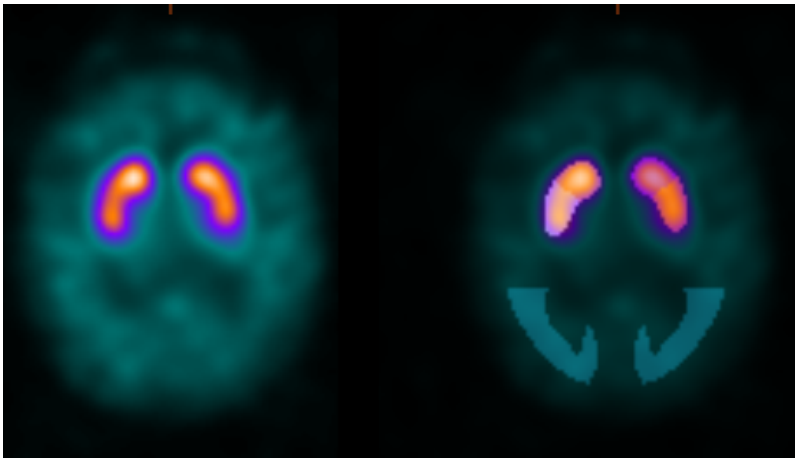

Figure 10.2: Transverse slice of a patient ^{123}I-DaTSCAN™ study (left) and VOIs automatically positioned using the BRASS™ application (right)

The reconstructed volumes in this investigation were automatically quantified using BRASS™ to determine a Measured Uptake Ratio (MUR). MURs are determined using the same calculation for TURs (Equation 10.1) where U is the counts in the uptake region and BG is the counts in the occipital region.

MURs were compared with TURs to assess the linearity of the relationship. It was anticipated that CCs would be lower than 1 due to partial volume effect as the VOIs defined by BRASS™ match the true size of the anatomical structures under investigation.

The coefficient of determination (R^2) was used to assess goodness of fit to a linear model. In this investigation, the CC is equivalent to the gradient of the linear response between MURs and TURs of the gamma camera.

10.3 Results

10.3.1 Linearity of Uptake Ratio Measurements for Reconstruction Methods

Figure 10.3 shows the relationship between the MUR and the TUR for each of the reconstruction methods evaluated.

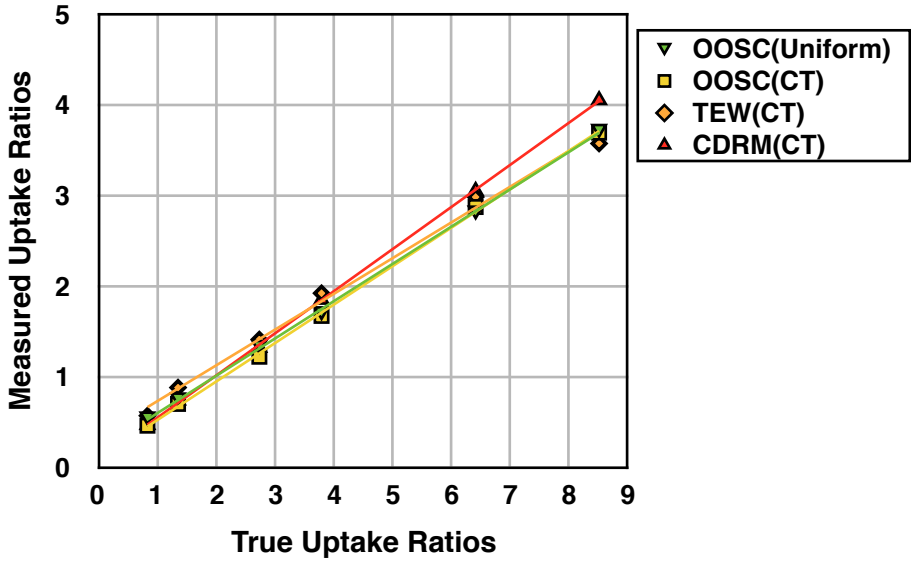

Figure 10.3: Data and linear trendlines of the four reconstruction schemes for the matched concentration acquisition

The OOSC(Uniform) and OOSC(CT) reconstructions have comparable linear gradients of 0.443 and 0.440 respectively (Table 10.6). The CDRM(CT) reconstruction has a slightly higher gradient of 0.478. This finding is in keeping with the greater HCR of the CDRM method when compared with OOSC, as demonstrated in Section 6.3.1.

	CC	R^2
OOSC(Uniform)	0.443	0.991
OOSC(CT)	0.440	0.997
TEW(CT)	0.451	0.962
CDRM(CT)	0.478	0.998

Table 10.6: Calibration Coefficients (CC) which are equivalent to the gradient of the linear relationship between measured and true uptake ratios

The TEW reconstruction has the lowest R^2 (0.962) suggesting greater variability in measurement. This finding is likely due to lower count density in background regions which will have higher noise level, as demonstrated in Section 7.3.3.

The predefined VOIs used by BRASS™ to measure uptake ratios are representative of the size of normal caudate and putamen structures and, therefore, there is substantial partial volume effect. This effect results in a linear gradient between measured and true uptake ratio which is much lower than 1.

10.3.2 Linearity of Uptake Ratio Measurements with Activity Concentration

All three activity concentrations demonstrated a linear relationship. The trendlines shown in Figure 10.4 are obtained using the CDRM(CT) correction scheme and are representative of the alternative reconstructions.

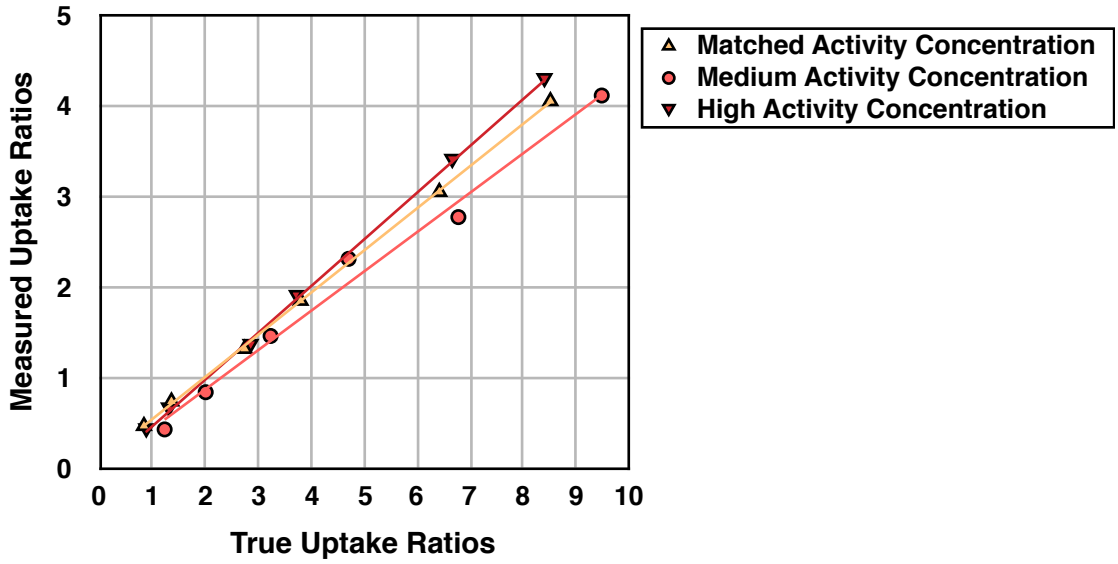

Figure 10.4: Linear relationships for three activity concentrations reconstructed with the CDRM(CT) correction scheme

The trendline with the matched activity concentration lies between the medium and high activity concentrations, suggesting that the curves are independent of activity in the FOV. The results for the CDRM(CT) reconstruction are representative of the alternative reconstruction schemes evaluated. The linear relationships provide confidence that a reconstruction specific CC is suitable for patient studies regardless of activity concentration in the FOV.

The range in CC is larger between the three activity concentration acquisitions than the range of CCs between reconstruction methods in a single acquisition (Table 10.7). This finding demonstrates the dependence of the calibration method on a single variable

parameter. A potentially more robust method of calibration would be to calculate a mean value of CC from multiple acquisitions.

	Matched Concentration		Medium Concentration		High Concentration		
	CC	**R^2**	**CC**	**R^2**	**CC**	**R^2**	**Range:**
OOSC(Uniform)	0.443	0.991	0.398	0.994	0.449	0.994	**0.05**
OOSC(CT)	0.440	0.997	0.413	0.988	0.472	0.997	**0.06**
TEW(CT)	0.451	0.962	0.419	0.976	0.477	0.988	**0.06**
CDRM(CT)	0.478	0.998	0.434	0.987	0.506	0.999	**0.07**
Range:	**0.04**		**0.04**		**0.06**		

Table 10.7: Calibration Coefficients (CC) and coefficient of determination (R^2) for the four reconstruction techniques and three activity concentrations

The CDRM(CT) reconstructions had the highest mean R^2 value of the three acquisitions (0.995) which indicates that the CDRM correction scheme most closely fits a linear response model for a range of true activity concentrations. This finding is due to a combination of improved HCR and reduced noise when compared with the alternative correction schemes.

10.4 Discussion

The results for calibration of the gamma camera for BRASS™ relative quantification demonstrated a linear relationship between measured and true uptake ratios for all four reconstruction schemes. Similarly, an increase in the activity concentration in the FOV did not affect the linear response or gradient of the curves. This linearity is an important finding as a study by Jarritt [195] of 115 reconstruction algorithms suggested 14% of systems did not demonstrate a linear response to changes in input count density.

The CDRM(CT) reconstruction scheme demonstrated the highest linear gradient between measured and true uptake ratios, in keeping with the higher HCR results of Section 6.3.1.

Koch [196] performed a calibration of Siemens ECAM and Multispect 3 systems with LEHR collimators using BRASS™ analysis. The linear gradients were 0.356 and 0.375 respectively. The CCs determined by Koch are smaller than those found in this investigation. However, Koch's calibration used an FBP reconstruction with uniform attenuation correction. Furthermore, no scatter correction or RR was applied. Results published by Dickson [125] suggest a gradient of ~0.400 with iterative reconstruction, TEW scatter correction and uniform attenuation correction, but no depth-dependent RR

applied. Therefore, the gradients reported by Koch and Dickson would be expected to be lower than those found in the current investigation.

A study by Varrone [29] compares the uptake ratios measured using BRASS™ and the Southampton Method (which removes partial volume effect) in normal patient studies. Varrone's results show that striatal uptake ratios measured using the former method are lower by a factor of ~0.4 compared with the Southampton Method, which has been shown by Tossici-Bolt [51] to result in a CC of ~1. Therefore, Varrone's evidence confirms that the relatively lower CC demonstrated in the current study, and that of Koch [196] and Dickson [125], is due to partial volume effect.

Although this investigation provides confidence in the linear nature of the calibration curve under varying conditions, there are more general problems with ENC-DAT relative uptake approach. For example, Du [197] describes overestimation of activity in background regions when correction for septal penetration is not applied. Therefore, as the reconstruction scheme recommended by Hermes Medical Solutions for BRASS™ does not include correction for septal penetration, this will affect the accuracy of relative measurements. However, as all patient studies are analysed using a standard template, the error will be a consistent systematic difference, which makes comparison with the similarly analysed normal patient studies justifiable.

Although the ENC-DAT calibration guidelines suggest the use of TEW scatter correction, issues with the reliance on a suitable background region remain. The guideline authors identify this reliance on a potentially noisy reference region as a source of error [126]. In this thesis, TEW scatter correction has proven to be relatively noisy (see Section 7.3.3). Therefore, CDRM, which demonstrated the lowest Image Roughness (IR), would reduce the noise in reference regions and, thus, be more suitable in relative quantification tasks.

A disadvantage of employing the BRASS™ method is the assumption that the ENC-DAT normal database is representative of a local normal patient cohort. Centres may choose to develop a local normal database. However, this approach requires ethical approval for imaging normal volunteers or relying on the discrimination of normal patients by visual interpretation from a population referred due to clinical symptoms. The benefit of a multi-centre normal database is that the subjects are often volunteers with no underlying symptoms.

The reconstruction parameters recommended by Hermes Medical Solutions (OOSC(Uniform)) are a requirement for using BRASS™ as they were also applied to the normal patient studies in the ENC-DAT database. Any development in reconstruction protocols would require either two reconstructions to be performed (one for BRASS™ and one for visual assessment) or for Hermes Medical Solutions to retro-reconstruct the normal database with the new parameters. However, as a CC is used to normalise data acquisition between gamma camera systems, a suitable CC may also allow normalisation for alternative reconstruction schemes. The advantage would be to make analysis with BRASS™ reconstruction independent, which would enable centres to develop their own locally optimised parameters. This study has shown novel correction schemes maintain a linear response. However, a study comparing the output of BRASS™ using matched and individualised reconstruction parameters for a range of patient studies would be required to validate this approach. Such a study is beyond the scope of this thesis. Alternatively, absolute quantification would allow site-specific optimisation with no dependence on a potentially noisy reference region.

10.5 Conclusions

Advanced reconstruction correction schemes, including Monte Carlo scatter correction, were shown to have a linear response between measured and true uptake ratios over a range of uptake ratios. A linear response was also maintained for a range of activity concentrations in the FOV.

The CDRM correction scheme may improve the accuracy of relative quantification due to reduced noise in the reference region and superior contrast recovery compared to alternative schemes. However, for use of the BRASS™ analysis application using the ENC-DAT normal database, Hermes Medical Solutions recommended reconstruction scheme, with uniform attenuation correction and OOSC, should be maintained.

Chapter 11: Absolute Quantification of ^{123}I SPECT

The aim of this Chapter is to determine a best practice approach to enable absolute quantification of clinical ^{123}I SPECT data.

11.1 Introduction

Quantification of activity concentration can be a useful tool to assist with the interpretation of clinical studies. Standard approaches to quantification are outlined in Section 2.6. The two most common methods of quantification used in SPECT imaging are relative quantification and absolute quantification. Of these, absolute quantification refers to a direct measure of activity concentration, which requires correction for degrading factors such as scatter, attenuation and resolution loss [9].

Absolute quantification requires calibration of the gamma camera by determining a Calibration Factor (CF). The CF converts counts measured in a reconstructed image to activity concentration, typically stated in kBq/ml. Therefore, a CF differs from a Calibration Coefficient (CC), introduced in Chapter 10, in that a CC converts a measured to a true uptake ratio whereas a CF converts counts in a region to kBq/ml.

Bailey [127] noted that calibration should be applicable to different geometries in the clinical setting which vary in attenuation, scatter and have heterogeneous radionuclide distribution. However, a typical approach to determine a CF for SPECT quantification involves the acquisition of a uniform cylindrical phantom with a 15cm Radius of Rotation (ROR) [10, 13, 14, 98, 132, 143, 198]. ^{99m}Tc studies have constant sensitivity with distance from a parallel hole collimator and so this single calibration acquisition may be used for all clinical scenarios.

The planar sensitivity of LEHR acquisitions to ^{123}I is dependent on the source to detector distance, as demonstrated in Section 3.5. Consequently, CFs may also be distance-

dependent. Section 3.6 demonstrated that the count rate response of the detector to ^{123}I was non-linear when imaging focal sources greater than 40MBq in the FOV relatively close to the detector. This response is due to a relatively large proportion of high-energy septal penetration. Therefore, the CFs of low-energy collimators may also depend on the activity concentration and the object geometry used for calibration.

Additionally, SPECT reconstruction algorithms must keep counts per pixel in the reconstruction linear with acquisition zoom [127]. Consequently, the first Section of this Chapter aims to establish ^{123}I CFs for:

- a range of RORs
- a range of activity in the FOV
- three phantoms: a cylindrical, a striatal and a torso phantom
- two acquisition zooms

The second Section will assess the accuracy of activity concentration measurements for a variety of potential clinical applications. The aim of this investigation was to recommend absolute quantification of ^{123}I SPECT for particular clinical scenarios.

11.2 Determination of Calibration Factor for Absolute Quantification

11.2.1 Introduction

Activity concentration measurements are dependent on the sensitivity of the gamma camera, the accuracy of the calibrator used to measure the radionuclide and synchronised timing of the camera and calibrator. Furthermore, accurate measurement requires reconstruction with corrections for attenuation, scatter and distance-dependent spatial resolution. A gamma camera and reconstruction specific Calibration Factor (CF), which converts reconstructed counts into units of kBq/ml, must be determined to enable absolute quantification. This Section describes the calibration process with regard to a Siemens Symbia T2 gamma camera.

Determination of a CF requires measurement of the SPECT sensitivity of the gamma camera. A common approach to this calibration is to acquire a cylindrical phantom containing a known concentration of radionuclide with a 15cm ROR [10, 13, 14, 98, 132, 143, 198].

The distance-dependent sensitivity of ^{123}I SPECT is particularly appreciable when imaging with low-energy collimators (see planar sensitivity measurements in Section 3.5).

However, data reconstructed with Collimator and Detector Response Modelling (CDRM) or Triple Energy Window (TEW) scatter correction, which correct for septal penetration, may reduce distance-dependent sensitivity and result in a constant CF. Similarly, as the sensitivity of medium-energy collimator acquisitions is less dependent on distance, a single CF may be applicable. Furthermore, calibration may be affected by additional variables such as the object geometry used for calibration and the activity concentration in the FOV. This potential variability is especially applicable for ^{123}I SPECT where the extent of septal penetration is object-dependent. The reconstruction algorithm must also maintain linearity of counts per pixel with acquisition zoom. Therefore, the aim of this work is to establish the variability of CF for ^{123}I SPECT with respect to:

- a range of RORs
- a range of activity in the FOV
- three phantoms: a cylindrical, a striatal and a torso phantom
- two acquisition zooms

As referred to previously, a common method of performing a calibration acquisition is to use a fixed 15cm ROR. In this investigation, the distance from the collimator was varied for a cylindrical and a striatal phantom. A torso phantom was acquired with a contoured orbit to mimic the method of acquiring body section data and a 25cm circular orbit, 25cm being the minimum ROR which also avoids collision with the patient couch. The activity in the FOV was varied using a cylindrical phantom.

A cylindrical and a torso phantom were used to calibrate the gamma camera with low and medium-energy collimators. A striatal phantom was used to perform calibration with low-energy collimators. A calibration with the striatal phantom and medium-energy collimators was not performed as medium-energy collimators are not recommended for neurology applications due to poorer spatial resolution (see Section 5.3.2.2). CFs were evaluated for acquisition zooms used for neurology and torso acquisitions. The aim of the investigation was to identify a CF applicable to a range of clinical scenarios.

The investigation also assessed the consistency of CFs by repeating the calibration procedure over the course of a year. The aim of this work was to inform the frequency with which quality control checks should be performed.

11.2.2 Calibration Factor Determination Method

11.2.2.1 Cylindrical Phantom Calibration Acquisition Method

Calibration with a cylindrical phantom is a method used commonly in the literature [10, 13, 14, 98, 132, 143, 198]. Following this approach, a cylindrical phantom, 20.9cm in diameter and 18.2cm in length (6244ml volume), was uniformly filled with ^{123}I. Previous publications have used cylindrical phantoms filled with as much as ~430MBq of ^{99m}Tc [132]. However, Section 3.6 of this thesis demonstrated that ^{123}I count rate response reduces substantially with activities of ~400MBq in the FOV. Therefore, in this study, the cylindrical phantom was filled with 106.1MBq of ^{123}I. This is also in keeping with the method of Kangasmaa [13] and that recommended by Hermes Medical Solutions [199].

Variability of Calibration Factor with Distance

Acquisitions of the cylindrical phantom used a circular orbit. Published methods use a ROR of 15cm. However, for this investigation, the ROR was varied from 15-30cm in 5cm increments. This method was chosen to evaluate ^{123}I SPECT sensitivity as the planar sensitivity of ^{123}I is known to vary with distance.

The time per angle was selected so that each calibration scan would have an equivalent relative acquisition time. However, as sensitivity varies with distance, particularly for the LEHR collimator, the total acquired counts described in Table 11.1 are not equivalent. The cylindrical phantom was acquired with LEHR and MELP collimators.

	LEHR Acquisitions				**MELP Acquisitions**			
ROR (cm):	**15**	**20**	**25**	**30**	**15**	**20**	**25**	**30**
Activity Concentration (kBq/ml)	12.0	14.6	16.3	17.0	11.4	10.9	10.4	9.8
Activity in the FOV (MBq)	74.9	91.2	101.8	106.1	71.2	68.1	64.9	61.2
Acquisition Time per Angle (s)	42	35	31	30	44	47	49	52
Total Acquired Counts (M)	34.6	32.1	29.1	27.3	20.0	19.9	19.5	19.4

Table 11.1: Activity concentration in the cylindrical phantom at time of acquisition

The Hermes Medical Solutions reconstruction algorithm decay corrects the counts in each projection to the acquisition start time. Therefore, the activity concentrations quoted in Table 11.1 relate to the concentrations at the start of each acquisition.

Variability of Calibration Factor with Activity Concentration

To assess variation of CF with activity concentration, the cylindrical phantom was acquired six times with a 15cm ROR as activity in the phantom decayed. For these acquisitions, the

activity concentration in the phantom ranged from 2.5-12.6kBq/ml. Therefore, the phantom contained 15.5-78.1MBq at acquisition time. The range was chosen to evaluate the consistency of CF with lower activity concentrations or, equivalently, shorter acquisition time. The data with reduced activity concentration was acquired using LEHR collimators for 30s per angle.

Variability of Calibration Factor with Pixel Size

The cylindrical phantom was acquired with two camera zooms applied. These zooms were representative of pixel sizes used clinically for ^{123}I neurology studies (3.3mm) and torso studies (4.8mm). These studies were acquired sequentially with LEHR collimators and a 15cm ROR.

Table 11.2 shows the SPECT and sequential CT acquisition parameters.

Parameter	Value	
Matrix	128x128	
Zoom	1.0	1.45
Pixel Size	4.8mm	3.3mm
Projections	128	
Orbit	Circular	
Photopeak	159keV±10%	
Scatter Windows	Lower: 138±4keV Upper: 178±4keV	
CT mA	35mA	
CT kVp	130kVp	
CT Reconstruction Slice Width	3.3mm	

Table 11.2: Cylindrical phantom acquisition parameters for gamma camera calibration

The sequential CT was acquired after each SPECT acquisition for attenuation and Monte Carlo scatter correction.

Cylindrical Phantom Calibration Factor Consistency Method

The cylindrical phantom was acquired a further four times in a one-year period to assess the consistency of CFs. The repeat cylindrical phantom acquisitions were prepared with 68.3MBq, 57.5MBq, 60.8MBq and 72.5MBq of ^{123}I respectively to match the typical activity concentration of the original calibration acquisitions. The four consistency setups were acquired with LEHR collimators, a circular 15cm ROR, a zoom of 1.45 and otherwise the

parameters shown in Table 11.2. Three of the four consistency setups were acquired with MELP collimators.

11.2.2.2 Torso Phantom Calibration Acquisition Method

Clinical acquisitions of body sections use a contoured orbit to minimise the source to detector distance. In this investigation, the NEMA IEC Body phantom, or “torso” phantom (previously described in Section 6.2.1), was used to determine a CF based on this acquisition method. With the sphere and lung inserts removed, the remaining 9.7l torso shaped compartment was uniformly filled with 73.0MBq of ^{123}I to match that of the cylindrical phantom described in Section 11.2.2.1.

The torso phantom was acquired with a contoured orbit that ranged in ROR from 14.8cm to 24.4cm with a mean radius of 19.0cm. For comparison, the phantom was also acquired with a circular 25cm ROR, which is the minimum fixed ROR achievable due to the patient table. The phantom was otherwise acquired with the acquisition parameters listed in Table 11.2.

Torso Phantom Calibration Factor Consistency Method

The CF of the torso phantom was evaluated six months after the initial calibration to assess long-term consistency. The phantom was uniformly filled with 75.7MBq of ^{123}I and acquired using the same parameters as the original calibration scan.

11.2.2.3 Striatal Phantom Calibration Acquisition

An anthropomorphic striatal phantom with hard brain shell (previously described in Section 10.2) was used to determine CFs with varying circular ROR. To determine CFs, the striatal phantom was uniformly filled with ^{123}I, including the caudate and putamen compartments. 73.2MBq of ^{123}I was used to match the cylindrical and torso phantom calibration setup. The striatal phantom was acquired with a pixel size of 3.3mm, which is the pixel size used locally for clinical neurology studies, such as ^{123}I-DaTSCAN™. The phantom was acquired with a circular orbit and a ROR that was varied from 15-30cm in 5cm increments. Determination of CF was made using LEHR collimators only as MELP collimators are not recommended for neurology SPECT due to poorer spatial resolution.

Striatal Phantom Calibration Factor Consistency Method

The CF of the striatal phantom was evaluated six months after the original calibration to assess long-term consistency. The phantom was uniformly filled with 69.5MBq of ^{123}I and acquired using the same parameters as the initial calibration.

11.2.2.4 Reconstruction of Calibration Acquisitions

Cylindrical, torso and striatal phantom calibration data were reconstructed with 96 iterations (6 iterations, 16 subsets). This value was chosen on the basis of the quantitative image quality evaluation, summarised in Section 9.1, and recommendations by Dickson for ^{123}I-DaTSCAN™ relative quantification optimisation [30]. Reconstruction schemes evaluated included CDRM(L), TEW(L) and OOSC(M), as recommended in Section 9.1. Additionally, data were reconstructed with OOSC(L) to include a scheme without explicit correction for septal penetration for comparison. Table 11.3 describes the reconstruction schemes.

	LEHR Reconstruction			**MELP Reconstruction**
Name:	**OOSC(L)**	**TEW(L)**	**CDRM(L)**	**OOSC(M)**
Iterations	96	96	96	96
RR	✔	✔	✔	✔
AC	CT	CT	CT	CT
SC	OOSC	TEW	CDRM	OOSC

Table 11.3: Reconstruction parameters for gamma camera calibration acquisitions Depth-dependent Resolution Recovery (RR) and CT Attenuation Correction (AC) were used for all reconstruction correction schemes. Methods of Scatter Correction (SC) included Triple Energy Window (TEW) subtraction, and Monte Carlo Object Only Scatter Correction (OOSC) and Collimator and Detector Response Modelling (CDRM)

Tables 4.5 and 4.6 describe the parameters used for depth-dependent RR and scatter correction.

11.2.2.5 Calibration Factor Determination Method

The CFs were determined by the mean counts in a large VOI for each reconstruction. For the cylindrical phantom data, the mean counts were measured in a cylindrical VOI in the centre of the phantom. The dimensions of the VOI were 70% that of the phantom, chosen based on guidelines from Hermes Medical Solutions [199]. Therefore, the VOI for the cylindrical phantom had a diameter of 14.7cm and length 12.6cm (Figure 11.1).

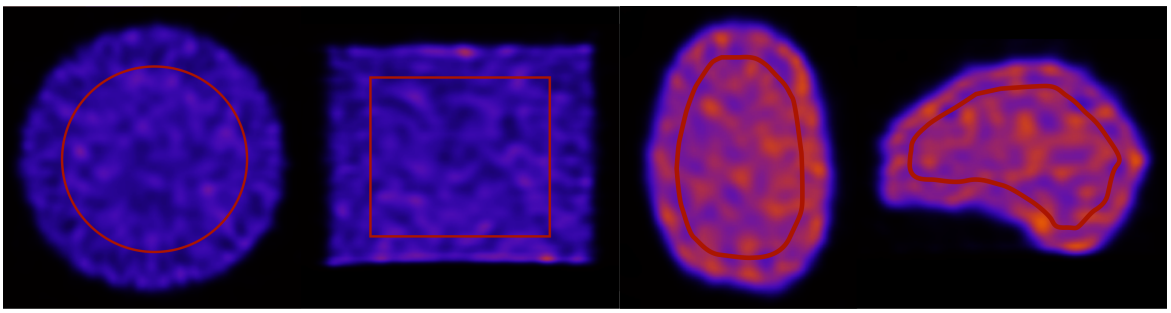

Figure 11.1: VOI used to determine Calibration Factors for the cylindrical (left) and striatal (right) phantom

For the striatal phantom, ROIs were manually drawn on 25 consecutive slices due to the irregular shape of the phantom. They were drawn with a relative separation from the edge similar to that with the cylindrical phantom (Figure 11.2). The ROIs were then grouped into a single VOI. The VOIs for the cylindrical and striatal phantom were positioned on a single reconstruction and copied to the same position on all other reconstructions.

A CF can be determined from the sensitivity of the gamma camera to a volume of uniform known activity concentration. To determine sensitivity the mean counts in an analysis VOI must first be converted to a count rate in cts/s using Equation 11.1.

$$CountRate_{VOI} = Counts_{VOI} / Time \qquad \textbf{Equation 11.1}$$

where *Time* is the time per projection angle in seconds. $CountRate_{VOI}$ is the count rate per voxel and can be converted to count rate per ml (cts/s/ml) using Equation 11.2.

$$CountRate_{ml} = CountRate_{VOI} / Voxel^3 \qquad \textbf{Equation 11.2}$$

where *Voxel* is the voxel dimension in cm. The CF was calculated using Equation 11.3:

$$CF(kBq / cts / s) = \frac{ActCon}{CountRate_{ml}} \qquad \textbf{Equation 11.3}$$

where *ActCon* is the known activity concentration in kBq/ml at the start time of acquisition. Zeintl [132], Ritt [10] and NEMA guidelines [143] describe a similar equation which additionally includes a correction for radionuclide decay to the mid-point of data acquisition. However, Hermes Medical Solutions Hybrid Recon™ reconstruction application decay corrects the counts in each projection to the start time of the acquisition. Therefore, an additional correction is not required.

To compare methods, the percentage difference was calculated between CFs that were determined with different object, acquisition and reconstruction schemes. Similarly, the percentage difference was calculated between the original calibration and subsequent consistency tests. Finally, a Coefficient of Variation (COV) was determined by dividing the standard deviation by the mean of the CFs measured five times over the course of a year.

11.2.3 Calibration Results

This Section will present the results for the variability of CF for ^{123}I SPECT with respect to distance from the detector, the activity in the FOV, the geometry of the test object and for two different pixel sizes.

11.2.3.1 Calibration Results with the Cylindrical Phantom

Cylindrical Phantom CF versus Distance

The CF increases with distance from the collimator for all acquisitions and reconstructions of the cylindrical phantom (Figure 11.2). This finding is in keeping with the Siemens Symbia's known distance-dependent planar sensitivity to ^{123}I (Section 3.5).

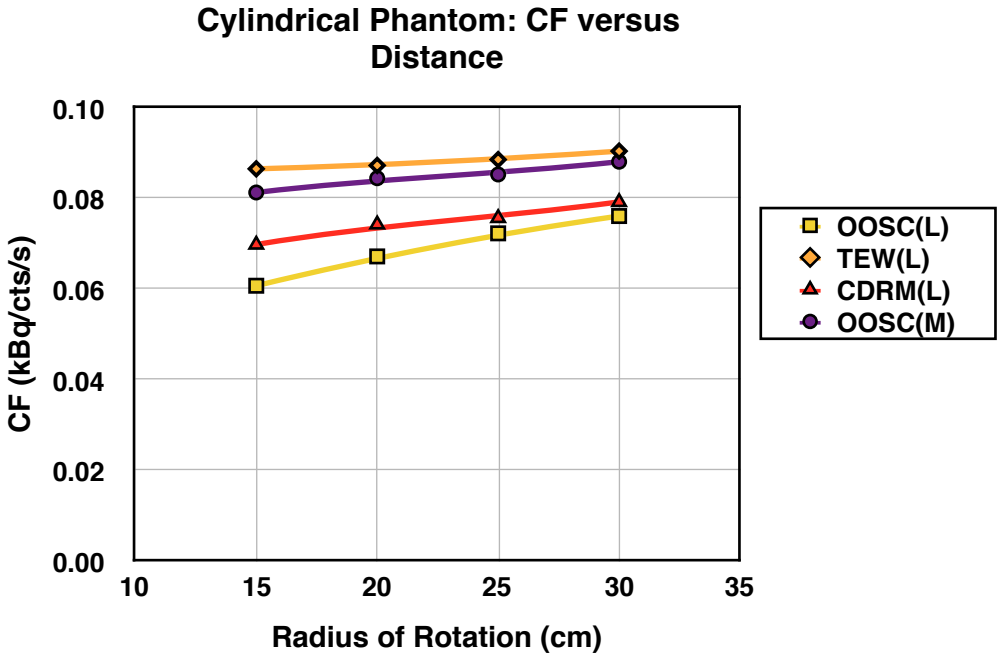

Figure 11.2: Calibration Factors (CFs) for the cylindrical phantom versus distance from LEHR (L) and MELP (M) collimators

The OOSC(M) and TEW(L) reconstructions have larger CFs than the other reconstructions, which indicates lower sensitivity. This outcome is anticipated due to poorer relative sensitivity of MELP collimators compared with the LEHR acquisition. Similarly, the TEW reconstruction has lower relative sensitivity due to the subtraction of counts from the LEHR acquisition data before reconstruction.

The OOSC(L) reconstruction demonstrates the greatest variability with distance (Table 11.4), which was anticipated as OOSC does not correct for high-energy septal penetration. The TEW(L) method of reconstruction demonstrated the smallest percentage difference in CF between 15cm and 30cm (Table 11.4).

Correction Scheme	CF Percentage Difference from 15cm to 30cm ROR
OOSC(L)	22.5%
TEW(L)	4.4%
CDRM(L)	12.6%
OOSC(M)	8.0%

Table 11.4: Percentage difference in Calibration Factor from 15cm to 30cm Radius of Rotation (ROR)

Cylindrical Phantom CF versus Activity Concentration

For the investigation of CF variability with activity concentration, data were acquired with LEHR collimators. The TEW(L) scheme was the most variable of the three correction schemes evaluated, as shown in Figure 11.3 and Table 11.5.

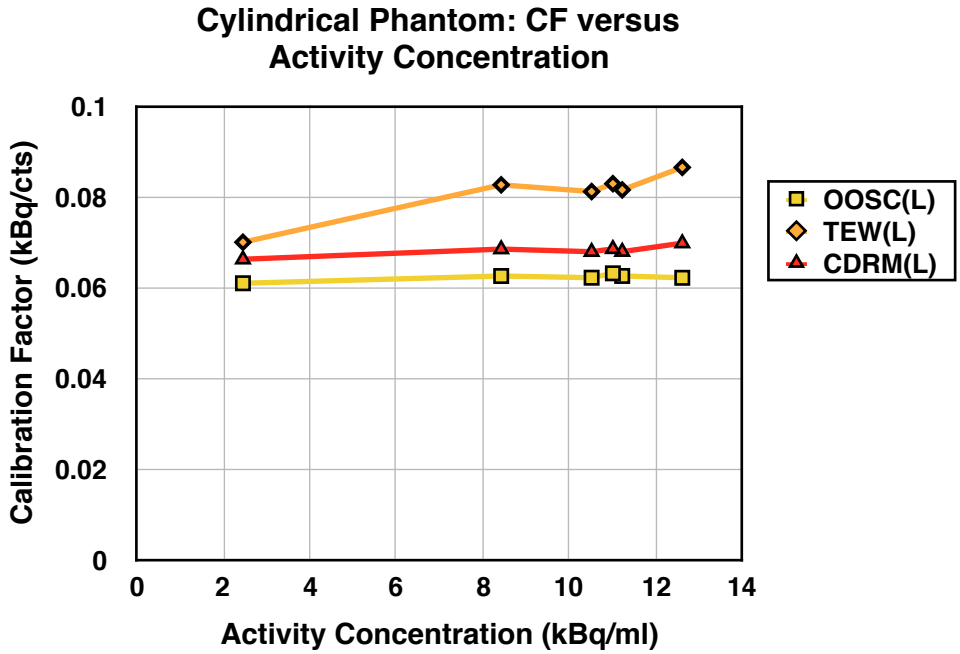

Figure 11.3: Calibration Factors for LEHR acquisition/reconstruction of the cylindrical phantom versus activity concentration

	OOSC(L)	TEW(L)	CDRM(L)
Max. Difference	3.5%	21.1%	5.2%

Table 11.5: Maximum percentage difference in Calibration Factor with activity concentration

This finding, of TEW(L) variability, can be explained by the method subtracting counts before reconstruction. Acquisitions of relatively low activity concentrations will have low count density. Further subtraction of counts will reduce the Signal to Noise Ratio (SNR) of the measurement. For the other reconstructions the variation in CF with activity was minimal for the range studied.

Cylindrical Phantom CF versus Acquisition Zoom

In a comparison of CF with pixel size, it was found that the percentage difference between CF for 3.3mm and 4.8mm pixel widths was <2% for all reconstructions.

Consistency of Cylindrical Phantom CF

The CF was measured five times in a year using the cylindrical phantom. The largest percentage difference in CF measured in subsequent acquisitions was 4.9% (Table 11.6).

Correction Scheme	Test 1	Test 2	Test 3	Test 4	Test 5	COV(%)	%Diff.
OOSC(L)	0.061	0.063	0.062	0.062	0.063	1.6	3.9
TEW(L)	0.086	0.083	0.084	0.083	0.084	1.8	4.2
CDRM(L)	0.070	0.069	0.070	0.068	0.069	1.2	2.9
OOSC(M)	0.081	—	0.078	0.077	0.077	2.3	4.9

Table 11.6: Consistency of Calibration Factors measured using the cylindrical phantom over a calendar year

Review of CFs in Table 11.6 suggests the repeat measurements of OOSC(M) CFs (“Test 3” to “Test 5”) were consistently ~5% lower than the original calibration (“Test 1”). This suggests an error in the original calibration. The error is unlikely to be drift in gamma camera performance as the LEHR CFs remained consistent over the same time period. Therefore, the discrepancy can be attributed to experimental error. This finding demonstrates the value in routine quality control of CFs. In this example, an experimental error during calibration would not be detected by simple monitoring of gamma camera sensitivity with planar measurements, as has been suggested by Dewaraja [2]. The complete method of calibration should be repeated to monitor any deviation in CF.

11.2.3.2 Calibration with the Torso Phantom

Torso Phantom CF with a Contoured and a Circular Orbit

The CFs measured using the torso phantom are shown in Table 11.7. As the mean ROR of the contoured orbit was 19.0cm, Table 11.7 compares the CFs obtained using the torso phantom with those obtained using the cylindrical phantom and a 20cm fixed ROR.

Similarly, the cylindrical phantom 25cm ROR CFs have been reproduced for comparison with the 25cm ROR circular acquisition of the torso phantom.

Phantom	Acquisition	OOSC(L)	TEW(L)	CDRM(L)	OOSC(M)
Torso Phantom	**Contoured Orbit**	0.061	0.085	0.069	0.082
	25cm ROR Circular Orbit	0.072	0.091	0.075	0.083
Cylindrical Phantom	**20cm ROR**	0.069	0.087	0.074	0.084
	25cm ROR	0.072	0.089	0.076	0.084

Table 11.7: Calibration Factors determined using a torso phantom
The torso phantom was acquired with a contoured orbit and is compared above with CFs determined with a comparable fixed orbit of the cylindrical phantom

The CFs obtained using a contoured orbit of the torso phantom are similar to those obtained with the cylindrical phantom with a 20cm ROR for the TEW(L) and OOSC(M) reconstructions. Similarly, the CFs for the torso phantom acquired with a 25cm ROR circular orbit are comparable with the equivalent cylindrical phantom acquisition. However, there is a difference of 12.3% and 7.0% for the OOSC(L) and CDRM(L) respectively when comparing the contoured orbit with the 20cm ROR cylindrical phantom CF.

This finding suggests that the TEW correction scheme appropriately corrects for the change in sensitivity with variable orbit distance, while the CDRM scheme does not. It is unsurprising that the TEW technique demonstrates this outcome as the data is corrected on a projection by projection basis before reconstruction. The discrepancy between the CDRM CFs indicates that Monte Carlo simulation of scatter and septal penetration does not appropriately model the varying sensitivity with orbit distance.

Torso Phantom CF versus Acquisition Zoom

As with the cylindrical phantom, it was found that the percentage difference between CF for 3.3mm and 4.8mm pixel widths was <2% for all reconstructions.

Consistency of Torso Phantom CF

Consistency of CF was determined by a repeat calibration procedure six months after the initial calibration. The largest percentage difference in CF measured in the repeat acquisition was 2.8% (Table 11.8).

	OOSC(L)	TEW(L)	CDRM(L)	OOSC(M)
Original Torso Phantom	0.063	0.085	0.073	0.081
Repeated Torso Phantom	0.062	0.087	0.071	0.082
Percentage Difference (%)	**1.6%**	**2.3%**	**2.8%**	**1.2%**

Table 11.8: Comparison of Calibration Factors measured six months apart

11.2.3.3 Calibration with the Striatal Phantom

Striatal Phantom CF versus Distance

As was shown with the cylindrical phantom, the striatal phantom also demonstrated an increase in CF with ROR (Figure 11.4).

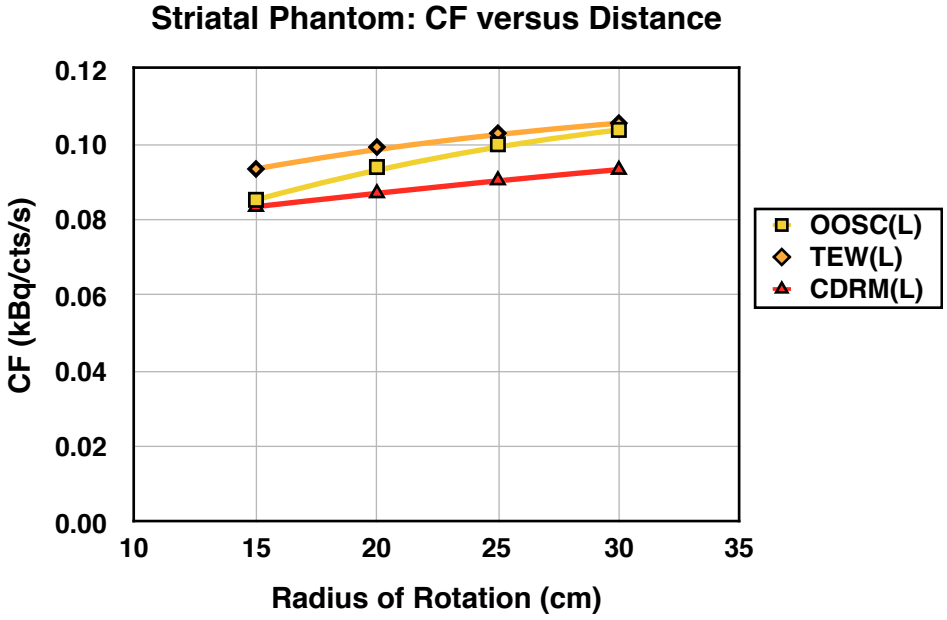

Figure 11.4: Calibration Factors for the striatal phantom versus distance from LEHR collimators

For neurology imaging, both the SNM and EANM procedural guidelines for ^{123}I transporter imaging recommend the smallest fixed ROR possible [27, 49]. The percentage difference between the 15cm and 20cm acquisition was 9.7%, 6.0% and 5.1% for the OOSC(L), TEW(L) and CDRM(L) reconstructions respectively. This difference is relatively small, particularly for the TEW(L) and CDRM(L) reconstructions. Therefore, the error in CF determination for clinical neurology studies is acceptably small.

Striatal versus Cylindrical Phantom CF with Distance

The CF response with distance for the striatal and cylindrical phantoms demonstrated a matching linear gradient. Figure 11.5 presents the CFs measured with CDRM(L) reconstruction.

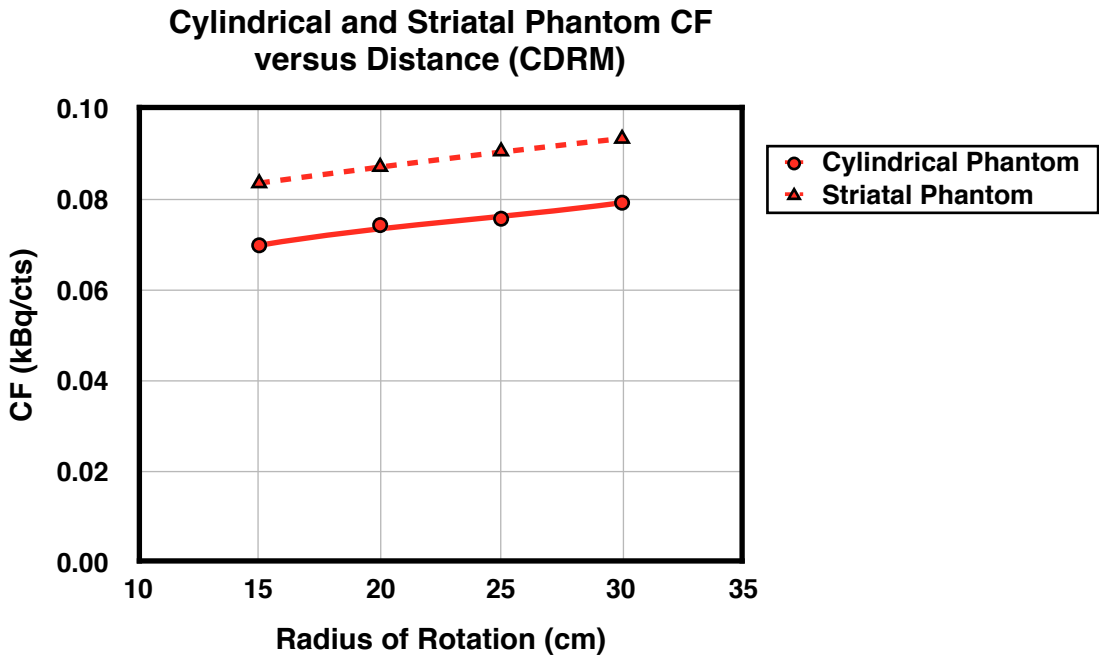

Figure 11.5: Comparison of Calibration Factors measured using the cylindrical and striatal phantoms versus distance from the LEHR collimator (CDRM(L) reconstruction)

The striatal phantom CF values are consistently higher than the cylindrical phantom CF at equivalent distances, with a percentage difference of ~17%. This finding is due to a combination of the different geometry and heterogeneity of the phantom.

The difference in CF determined using the cylindrical and striatal phantom was also demonstrated for the OOSC(L) and TEW(L) reconstructions, shown in Figure 11.6.

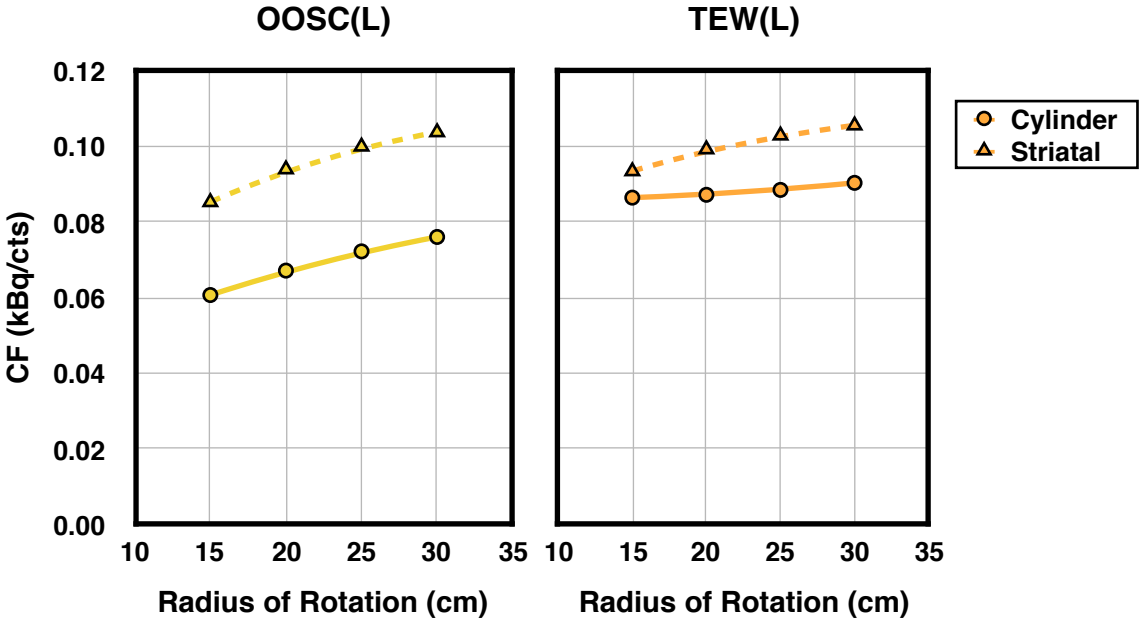

Figure 11.6: Comparison of Calibration Factors measured using the cylindrical and striatal phantoms versus distance from the LEHR collimator, OOSC(L) reconstruction (left) and TEW(L) reconstruction (right)

The CDRM(L) and OOSC(L) reconstructions demonstrated a consistent difference in CFs between the striatal and cylindrical phantoms of ~17% and ~33% respectively. However, the TEW(L) correction scheme shows a variable difference, which increased with ROR from 7.8% at 15cm to 15.5% at 30cm.

This finding suggests that the effective correction of high-energy septal penetration by the TEW method shown in the cylindrical phantom does not hold when the phantom is surrounded by a higher density material.

Consistency of Striatal Phantom CF

Reconstructions of the uniformly filled striatal phantom acquired with a 15cm ROR six months after the initial determination of CFs demonstrated a maximum difference of 2.4%, as shown in Table 11.9.

	OOSC(L)	TEW(L)	CDRM(L)
Original Striatal Phantom	0.085	0.093	0.084
Repeated Striatal Phantom	0.084	0.092	0.082
Percentage Difference (%)	**1.2%**	**1.1%**	**2.4%**

Table 11.9: Comparison of Calibration Factors measured six months apart

11.2.3.4 Summary of Calibration Factor Variation

Table 11.10 summarises the variability of CF established in this investigation.

	Maximum Percentage Differences			
	OOSC(L)	TEW(L)	CDRM(L)	OOSC(M)
Distance	22.5%	4.4%	12.6%	8.0%
Pixel Size	<2%			
Activity Concentration	4.9%	21.7%	5.5%	—
Phantom*	33.7%	15.5%	17.6%	3.6%
Long term stability	3.9%	4.2%	2.9%	4.9%

Table 11.10: The variability of CF for each reconstruction method
The maximum value is stated where a range of CFs was measured. (*) LEHR results compare striatal to cylindrical phantom, MELP results compare torso to cylindrical phantom

In Table 11.10, the percentage difference due to the phantom was determined between the cylindrical and striatal phantom for LEHR collimators. However, as the striatal phantom was not acquired with MELP collimators, the difference stated for the OOSC(M) relates to the cylindrical and torso phantom.

11.2.4 Calibration Discussion

^{123}I SPECT calibration has been performed with three phantom volumes: a cylindrical phantom, a torso phantom and a striatal phantom. The Calibration Factors obtained with the striatal and cylindrical phantoms were different. A consistent difference was noted at all distances with CDRM(L) and OOSC(L) reconstruction. The TEW(L) reconstruction demonstrated a variable difference. The differences observed between phantom geometries and with distance demonstrates an underlying limitation in the method of calibration. This has been recognised by Bailey [127] who noted calibration has to be applicable to different geometries in the clinical setting which vary in attenuation, scatter and have heterogeneous radionuclide distribution. This investigation has shown that, with respect to ^{123}I, a single CF is not appropriate for multiple clinical scenarios.

A predetermined CF may only be applicable where the clinical setup is matched to the calibration method and is accurately reproducible. With regard to clinical applications of ^{123}I SPECT, a fixed ROR is used for acquisition of projections around the head for neurology imaging. Therefore, neurology applications, such as ^{123}I-DaTSCAN, are the most obvious candidates for accurate absolute quantification of ^{123}I SPECT.

There are few publications which investigate the variability of CF with calibration setup. An evaluation by Koral [131] of calibration for quantitative ^{131}I SPECT showed a constant CF with distance (19-26cm ROR) using high-energy collimators. The investigation in this Chapter has shown that CF is not constant with distance for ^{123}I SPECT. The OOSC(L) reconstruction was found to be the most variable, as expected, given the absence of correction for high-energy emissions. Therefore, a single CF solution for LEHR data reconstructed with OOSC is not appropriate for application to quantitative ^{123}I imaging scenarios with variable distance. Considering the variability of CF with distance for the OOSC(M) data (8.0%), a CF chosen midway between 15cm and 30cm would result in an error of ±4% which would be acceptable for data acquired within this range.

In this investigation, the CF demonstrated a linear increase with distance from the collimator for all acquisition and reconstruction methods evaluated. An increase in CF is equivalent to a decrease in relative sensitivity. Therefore, the increase in CF is in keeping with a known reduction in high-energy septal penetration with distance. As expected, the OOSC(L) method demonstrated the largest percentage difference (22.5%) as it does not correct for high-energy septal penetration. Both the TEW(L) and CDRM(L) method correct for high-energy emissions. Of these, the TEW(L) method measured the lowest variation in CF with distance for the cylindrical phantom (4.4%). This finding indicates that the upper

energy window provides an accurate estimate for high-energy contamination in the photopeak window.

As the TEW(L) reconstruction demonstrated the least variation with distance, this method of reconstruction may seem the most appropriate method for auto-contoured acquisitions which have a varied ROR. However, the TEW(L) method also demonstrated the largest variation of CF with activity concentration (21.7%), with low count studies providing the lowest CF. As previously described, subtraction of the combined upper and lower scatter windows from already low count photopeak data reduces the Signal to Noise Ratio (SNR) of the acquisition data, which introduces variability in CF determination.

The CFs determined with the cylindrical and torso phantoms were comparable for circular orbits with matched ROR. However, torso phantom data acquired with a contoured orbit had a lower CF (higher sensitivity) than the cylindrical phantom with the same ROR as the mean distance of the contoured projections. This may be due to the substantial increase in sensitivity when the detector is particularly close to the phantom for a number of projections.

Bailey [127] outlines the requirement of SPECT reconstruction algorithms to alter the counts per pixel with acquisition zoom to keep counts in the reconstruction linear. Hermes Medical Solutions reconstruction algorithm demonstrates this linearity as evidenced by CFs within 2% when comparing 3.3mm and 4.8mm pixel width data.

The consistency of CF over a twelve month period (2.9%) is reassuring. The method has shown routine quality control of the CF is straightforward and can be performed relatively infrequently, for example, biannually or following major component changes to the system.

Although consistency of CF for ^{123}I SPECT has not been investigated in the literature, Kangasmaa [13] demonstrated the CF for ^{99m}Tc quantitative SPECT varies by 2.9% over 6 months at one site and 1.9% between 5 similar systems. Kangasmaa's result is comparable with the consistency demonstrated in this investigation for ^{123}I SPECT.

11.2.5 Calibration Conclusions

The method used to determine CFs for absolute quantification of ^{123}I SPECT should closely match the geometry and acquisition protocol of the intended clinical application. Therefore, neurology applications with fixed ROR acquisition of data are the most

suitable. Correction for septal penetration must be made either with software (the TEW or CDRM scatter correction techniques) or hardware (medium-energy collimators).

Quality control of CFs should be performed by repeating the calibration procedure biannually.

The following Section will provide an assessment of quantitative accuracy before a final recommendation for clinical practice will be made.

11.3 Accuracy of Absolute Quantification

11.3.1 Introduction

Quantification of ^{123}I SPECT using low-energy collimators is desirable as these collimators provide improved spatial resolution [24, 135]. Nevertheless, medium-energy collimators are often recommended for quantification [16, 17, 19, 42, 43] as they are less susceptible to septal penetration from high-energy emission and, therefore, they will also be evaluated for quantitative accuracy.

Advanced reconstruction algorithms, which are now commercially available, may improve the quantitative accuracy of low-energy collimator acquisitions. Therefore, an evaluation of the accuracy of absolute quantification was performed for both low and medium-energy collimators using advanced reconstruction techniques. The accuracy assessment used anthropomorphic test objects to simulate clinical imaging scenarios.

The primary aim of this Section is to evaluate the accuracy of ^{123}I SPECT activity concentration measurements. A further aim is to inform which clinical applications may be suitable for routine quantification.

11.3.2 Method for Assessment of Accuracy

In the clinical environment, measurement of activity concentration is typically made in the presence of heterogeneous concentrations and structures. Therefore, an assessment of quantitative accuracy with phantoms containing similarly heterogeneous activity concentrations was performed.

Accuracy was evaluated by measuring known activity concentrations in a torso phantom to model body section applications. This method has previously been used by Zeintl [132] and Armstrong [98] with regard to ^{99m}Tc SPECT, and by Koral [14] with regard to ^{131}I

SPECT. However, to the author's knowledge, the current study presents the first assessment of the accuracy of activity concentration measurements for ^{123}I SPECT using the torso phantom. In the current study, the sphere to background activity concentration ratio and pixel size were varied to investigate dependence of quantitative accuracy on these variables.

A further assessment was performed using the striatal phantom to evaluate quantitative accuracy of ^{123}I activity concentration measurements in neurology applications. The aim of the torso and striatal phantom quantitative accuracy investigations was to provide a recommended best practice approach for absolute quantification in body section and neurology applications.

11.3.2.1 Torso Phantom Accuracy: Method of Acquisition

The torso phantom, described in Section 6.2.1, was used to assess the accuracy of activity concentration measurements as they relate to clinical SPECT imaging. In particular, the accuracy assessment using the torso phantom related to body section imaging, for which data are acquired with a contoured orbit. A sphere to background concentration ratio in the torso phantom enabled assessment of heterogeneous activity distribution. In this study, two methods of investigation were used to evaluate accuracy: idealised and clinical acquisition methods. These two methods will now be outlined.

The method used to assess accuracy under idealised conditions was the acquisition of relatively high-count, low-noise datasets. A sphere to background concentration ratio of 8:1-10:1 has typically been employed by authors using a torso phantom [13, 98, 132, 200]. Therefore, a concentration ratio of 10:1 was used for the idealised investigation.

The accuracy of quantification in the clinical setting is of particular importance. Therefore, for this investigation the torso phantom was acquired with clinically relevant protocols. These protocols included a range of three sphere to background concentration ratios and two acquisition zooms used clinically.

Consequently, quantitative accuracy of activity concentration was evaluated with two methods:

1. Accuracy with idealised imaging parameters: this method involved a relatively high-count, low-noise acquisition

2. Accuracy of routine clinical acquisition: this method included three activity concentration ratios, acquired with a clinical count rate and two clinical acquisition zooms

The data for method one were acquired with both a contoured and a circular orbit. Additionally, as a sphere orientation dependence on Hot Contrast Recovery (HCR) was identified in the contrast investigation in Chapter 6, the high-count acquisition was repeated with the spheres rotated 180° about the central axis of the phantom (Figure 11.7). This method of preparation keeps two spheres (the largest 37mm diameter sphere and the 17mm diameter sphere) in relatively the same position in the phantom and, therefore, act as a point of reference.

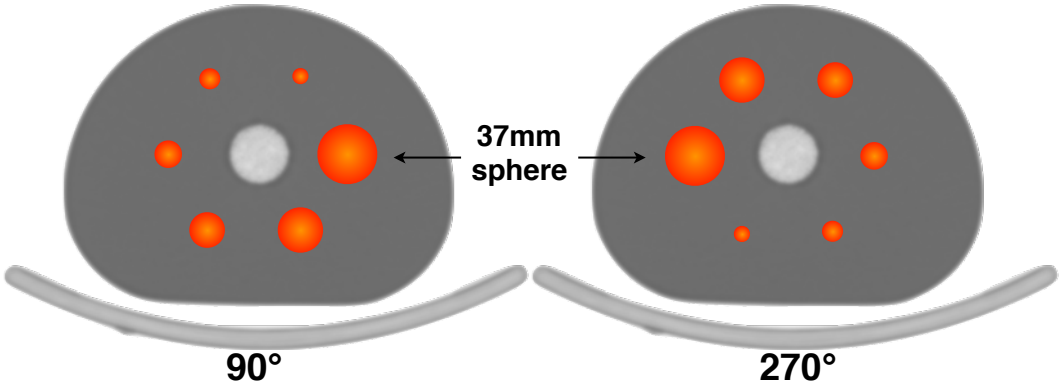

Figure 11.7: Sphere orientation for the idealised acquisitions
Orientations referred to as 90° position (left) and 270° position (right) based on the position of the 37mm sphere.

These sphere orientations will be referred to as 90° and 270° indicating the position of the largest sphere.

The data for method two were acquired with a contoured orbit to mimic an individual clinical patient data set. These data were acquired with spheres in the 90° orientation.

Accuracy with Idealised Imaging Parameters: Acquisition Method

A sphere to background concentration ratio of 8:1-10:1 has been typical for those using a torso phantom to assess quantitative accuracy [13, 98, 132, 200]. Furthermore, Bomanji [178] suggests a wide range of uptake ratios up to 10:1 for clinical ^{123}I-mIBG studies. Therefore, for the idealised imaging assessment, the maximum contrast of 10:1 was used. The phantom was filled with 78.4MBq, chosen to match previous calibration acquisitions.

Data were acquired with 2M counts in the first projection to achieve a high-count data set. However, using this method, the acquisition time of the 270° sphere orientation, which

was acquired after the 90° orientation, resulted in fewer total counts in the study. This reduction in counts is due to the longer time to acquire 2M counts in the first projection which results in further decay during acquisition. Nevertheless, total counts in all studies can be considered relatively high-count compared with routine clinical studies (Table 11.11).

Orbit:	Contoured		Circular	
Sphere Orientation:	**90°**	**270°**	**90°**	**270°**
Matrix	128x128			
Acquistion Zoom	1.45			
Pixel Size	3.3mm			
Projections	128			
ROR (cm) mean / max / min	19.0 / 11.1 / 25.8		25.0 / 25.0 / 25.0	
Counts in the First Projection	2M			
Total Counts in the Study	170M	130M	206M	145M
Photopeak	159keV±10%			
Scatter Windows	Lower: 138±4keV Upper: 178±4keV			

Table 11.11: Acquisition parameters for the torso phantom setup

Due to the substantial acquisition times involved and the 13.2h half-life of ^{123}I, equivalent acquisitions of the phantom with MELP collimators were not feasible. Therefore, data were only acquired with LEHR collimators.

Accuracy of Routine Clinical Acquisition: Acquisition Method

As mentioned previously, a sphere to background concentration ratio in the torso phantom of 10:1 has been used for assessment of quantitative accuracy. However, Bomanji [178] describes a large clinical range of uptake ratios of ^{123}I-mIBG up to ~10:1. Therefore, in this investigation, the phantom was prepared with a wider range of uptake ratios, from 5.2:1 to 9.5:1.

To evaluate the consistency of accuracy with pixel size, the phantom was acquired with two acquisition zooms. These zooms represent the pixel sizes used locally for clinical abdominal studies (4.8mm) and for neurology applications (3.3mm). The torso phantom was prepared using 51.7-65.8MBq of ^{123}I to match the typical activities used for

calibration. The phantom was acquired with LEHR and MELP collimators. The contoured orbit varied in ROR from 11.1cm to 25.8cm (mean=19.0cm).

Data were acquired with 110k counts and 62k counts in the first projection for LEHR and MELP studies respectively. This method ensured comparable total counts for all acquisitions for each collimator. The counts in the first projection were chosen based on the counts in the first projection of a typical ^{123}I-mIBG study in which the liver is included. The LEHR and MELP data were acquired for an equivalent acquisition time. The MELP collimator data had fewer counts compared with the LEHR collimator data due to the lower relative sensitivity across the full FOV, as demonstrated by planar sensitivity measurements in Section 3.5.

A summary of the acquisition parameters is given in Table 11.12.

Parameter	Value		
Activity in Phantom at First Acquisition	65.8MBq	51.7MBq	57.9MBq
Sphere to Background Concentration Ratio	5.2	8.8	9.5
Matrix	128x128		
Zoom	1.0	1.45	1.0/1.45
Pixel Size	4.8mm	3.3mm	4.8mm/3.3mm
Projections	128		
Orbit	Circular		
ROR mean/min/max (cm)	19.0 / 11.1 / 25.8		
Counts in First Projection	LEHR: 110k MELP: 62k		
Photopeak	159keV±10%		
Scatter Windows	Lower: 138±4keV Upper: 178±4keV		

Table 11.12: Acquisition parameters for the four clinical acquisitions of the torso phantom for assessment of accuracy of activity concentration measurement

A sequential CT was acquired for attenuation and Monte Carlo scatter correction of the torso phantom quantitative accuracy data. The CT acquisition parameters are shown in Table 11.13.

Parameter	Value
CT mA	35mA
CT kVp	130kVp
CT Reconstruction Slice Width	3.3mm

Table 11.13:Parameters of the sequentially acquired CT

11.3.2.2 Striatal Phantom Accuracy: Method of Acquisition

The striatal phantom was used to investigate the accuracy of activity concentration measurements for a neurological imaging setup. The striatal phantom was acquired on two occasions, with 11.5MBq and 51.4MBq of ^{123}I respectively.

The first phantom acquisition contained activity concentrations typically encountered in clinical studies, as suggested by Tossici-Bolt [51]. As the planar count rate response was shown to be non-linear for focal sources of ^{123}I greater than 40MBq (see Section 3.6), the second phantom acquisition allowed evaluation of the measured to true concentration response with higher activity concentrations. The activity concentrations in the second phantom acquisition were higher than in the torso phantom and, therefore, the highest of the accuracy evaluation.

Acquisitions of the two phantoms allowed measurement of six activity concentrations by dividing the striatal phantom into three compartments: the background, right striatum and left striatum (Table 11.14).

	First Acquisition		Second Acquisition	
Compartment	**Activity Concentration (kBq/ml)**	**True Uptake Ratio**	**Activity Concentration (kBq/ml)**	**True Uptake Ratio**
Background	7.2	—	36.5	—
Right Striatum	56.8	6.9	99.2	1.7
Left Striatum	72.2	9.0	148.8	3.1

Table 11.14: True activity concentration and uptake ratios in the two striatal phantom acquisitions

The True Uptake Ratio (TUR) in the striatal phantom was determined by counting aliquot samples of the activity concentrations in a gamma counter and using Equation 10.1.

The TURs in the two striatal phantom acquisitions ranged from 1.7:1 to 9.0:1, which is representative of the range of clinical ^{123}I-DaTSCAN™ uptake ratios [31]. The circular

15cm Radius of Rotation (ROR) acquisitions had 3.8Mcts and 12.4Mcts in each study respectively. The striatal phantom was acquired with LEHR collimators only as MELP collimators are not recommended for neurology imaging due to inadequate spatial resolution [27]. Acquisition parameters are shown in Table 11.15.

	Acquisition 1	Acquisition 2
Matrix	128x128	
Projections	128	
Zoom	1.45	
Pixel Size	3.3mm	
Orbit	Circular	
Radius of Rotation	15cm	
Time per Projection	30s	
Photopeak	159keV±10%	
Scatter Windows	Lower: 138±4keV Upper: 178±4keV	
Total Counts in Study	3.8M	12.4M

Table 11.15: Striatal phantom acquisition parameters for accuracy assessment

A sequential CT was acquired for attenuation and Monte Carlo scatter correction of the striatal phantom quantitative accuracy data. The CT acquisition parameters are shown in Table 11.13.

11.3.2.3 Reconstruction of Accuracy Data

The torso and striatal phantom data were reconstructed using the correction schemes described previously in Table 11.3. Data were converted to kBq/ml using the Calibration Factors (CFs) given in Table 11.16, which were established in Section 11.2.3.

	OOSC(L)	TEW(L)	CDRM(L)	OOSC(M)
Torso Phantom Contoured Orbit CF	0.061	0.085	0.069	0.082
Torso Phantom Circular Orbit CF	0.072	0.091	0.075	0.083
Striatal Phantom CF (15cm)	0.085	0.093	0.084	—

Table 11.16: Calibration Factors determined in Section 11.2.3 which were used for reconstruction of the cylindrical, torso and striatal phantom data

11.3.2.4 Method of Accuracy Analysis

Torso Phantom Accuracy Analysis Method

The Southampton Method of analysis, previously described in Section 2.6 and detailed in Appendix A, uses relatively large analysis regions to correct for partial volume effect due to limited spatial resolution. Therefore, this method, which has previously been used by Lagerburg [21] for torso phantom analysis, was used to measure activity concentrations without the confounding effects of partial volume.

Spherical VOIs, 60mm in diameter, were placed over the six spheres in the torso phantom, positioned using the sequentially acquired CT and copied to the SPECT volumes. A further 60mm diameter circular VOI was placed in a region of uniform activity centred in a transverse slice distant from the six spheres.

The VOI size and placement was chosen to ensure the maximum volume possible to include partial volume while ensuring no overlap between VOIs to avoid crosstalk between regions. Additionally, placement of VOIs was chosen to avoid the reduced count central region in the phantom. A transverse slice demonstrating the position of the VOIs placed over spheres is shown in Figure 11.8.

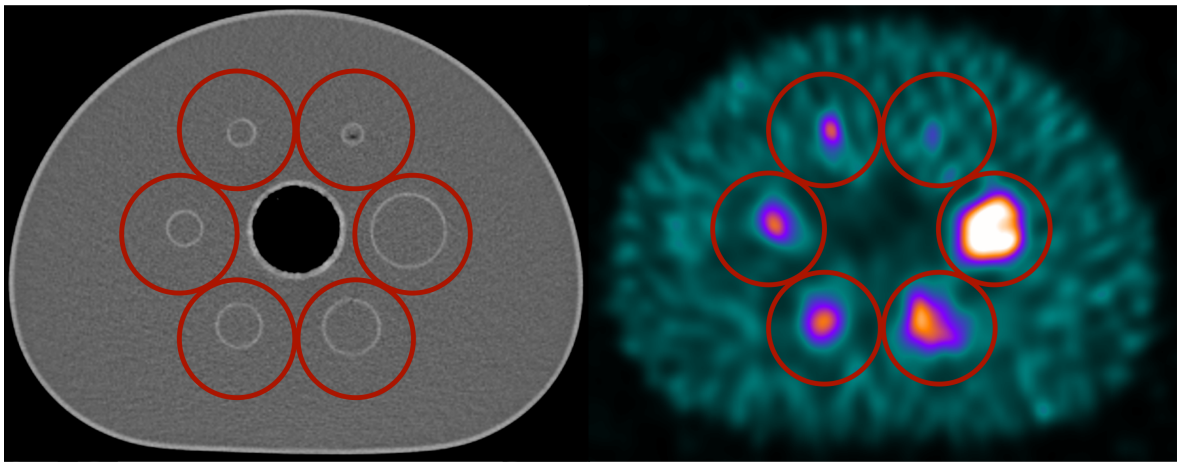

Figure 11.8: VOI placement for assessment of accuracy using the NEMA phantom

The Southampton Method was used by Fleming [121] to determine uptake ratios. Therefore, the method used in this investigation was altered such that the total concentration in the sphere volume was calculated rather than the ratio to the background reference region (see example in Appendix A). The mean activity concentration within a sphere ($ActCon_{sphere}$) in units of kBq/ml is given by Equation 11.4.

$$ActCon_{sphere} = \frac{Act_{total} - Act_{non-specific}}{Volume_{sphere}} \qquad \textbf{Equation 11.4}$$

where Act_{total} is the total activity measured in the VOI containing a sphere in kBq, $Volume_{sphere}$ is the volume of the sphere in ml, and $Act_{non\text{-}specific}$ is the activity contribution of non-specific uptake to the VOI containing the sphere. $Act_{non\text{-}specific}$ is calculated using Equation 11.5.

$$Act_{non-specific} = ActCon_{bkgd} \times (Volume_{bkgd} - Volume_{sphere} - Volume_{Perspex})$$

Equation 11.5

where $ActCon_{bkgd}$ is the mean activity concentration in the background VOI in kBq/ml and $Volume_{bkgd}$ is the volume in the background region in ml. $Volume_{Perspex}$ is the volume of Perspex making up the sphere and, therefore, contributes no counts. Hofheinz [201] identified the cold sphere walls in the phantom as a fixed source of measurement error. Therefore, $Volume_{Perspex}$ is included in Equation 11.5 to correct for this inaccuracy. The volume of Perspex was calculated based on the manufacturer's internal dimensions of the spheres and description of 2mm thick Perspex [202]. The constants used in Equations 11.4 and 11.5 are shown in Table 11.17.

	Volume (ml)	***$Volume_{Perspex}$ (ml)***
bkgd	113.10	—
37mm sphere	26.52	4.54
28mm sphere	11.49	2.64
22mm sphere	5.58	1.66
17mm sphere	2.57	1.02
13mm sphere	1.15	0.62
10mm sphere	0.52	0.38

Table 11.17: Constants used in Equations 11.4 and 11.5 for determining the mean activity concentration measured in spheres

The percentage error between true and measured activity concentration in the spheres was calculated. A Wilcoxon rank sum test for non-parametric paired data was used to determine any statistically significant difference between measured activity concentrations for the two acquisition zooms. Similarly, a Wilcoxon test was used to evaluate any statistically significant difference between contrast ratios.

Striatal Phantom Accuracy Analysis Method

Activity concentrations in the striatal phantom were measured using the Southampton Method described previously. Relatively large VOIs were manually drawn on the

sequentially acquired CT. The VOIs were then copied to the reconstructed SPECT data (Figure 11.9).

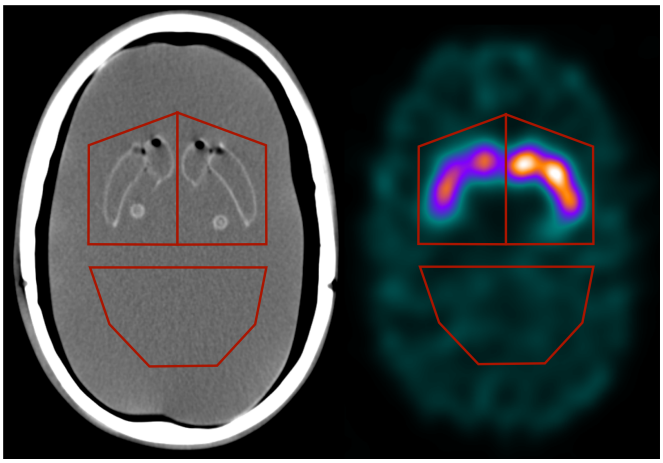

Figure 11.9: Transverse slice of striatal phantom showing VOIs on CT (left) and copied to SPECT (right)
Air bubbles in the caudate and putamen compartments, as demonstrated on the CT image, will result in an underestimation of activity concentration

The volume of the striatal VOIs was ~75ml. The volume of the background VOI was ~90ml. The volume of each striatal compartment is 11.2ml [31]. The volume of Perspex of the striatal inserts is difficult to establish as the shape is irregular and the thickness of Perspex is unknown. Therefore, no correction was made for the presence of Perspex in the uptake VOI.

Linear regression was used to compare the true and measured activity concentrations. The coefficient of determination (R^2) was used to indicate goodness of fit.

11.3.3 Results

This Section will describe the results for the accuracy of activity concentration measurements in the torso and striatal phantom.

11.3.3.1 Torso Phantom: Accuracy Results

In this Section of the accuracy investigation, two scenarios were evaluated:

1. Accuracy with idealised imaging parameters: high-count, low-noise acquisition
2. Accuracy of routine clinical acquisition: clinical count rates with three uptake ratios and two acquisition zooms applied

Torso Phantom Results: Accuracy with Idealised Imaging Parameters

Contoured Orbit

The accuracy of activity concentration was investigated with both a contoured and a circular orbit high-count acquisition, and with spheres in a 90° and 270° degree orientation. Figure 11.10 shows the error between true and measured activity concentration for a contoured orbit of both sphere orientations.

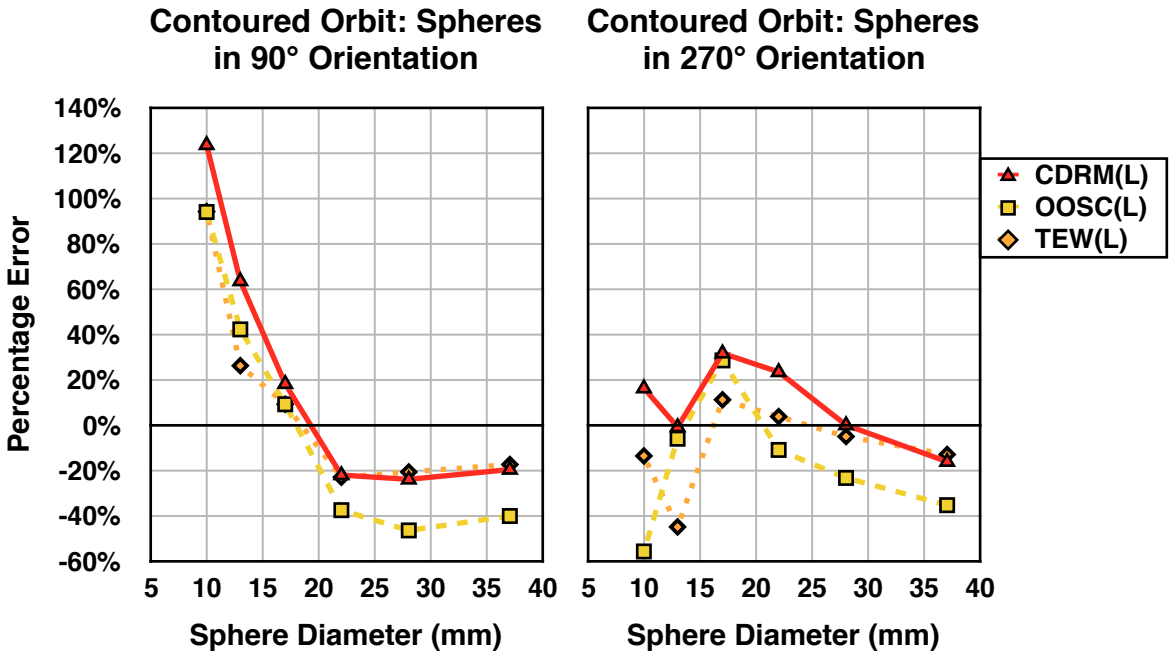

Figure 11.10: Accuracy of activity concentration measurements in the 90° (left) and 270° (right) sphere orientation, both with contoured data acquisition

The results shown in Figure 11.10 demonstrate a position dependence for all three methods of reconstruction. The position dependence can be illustrated using a single reconstruction method. Figure 11.11 shows this relationship for the CDRM(L) reconstruction.

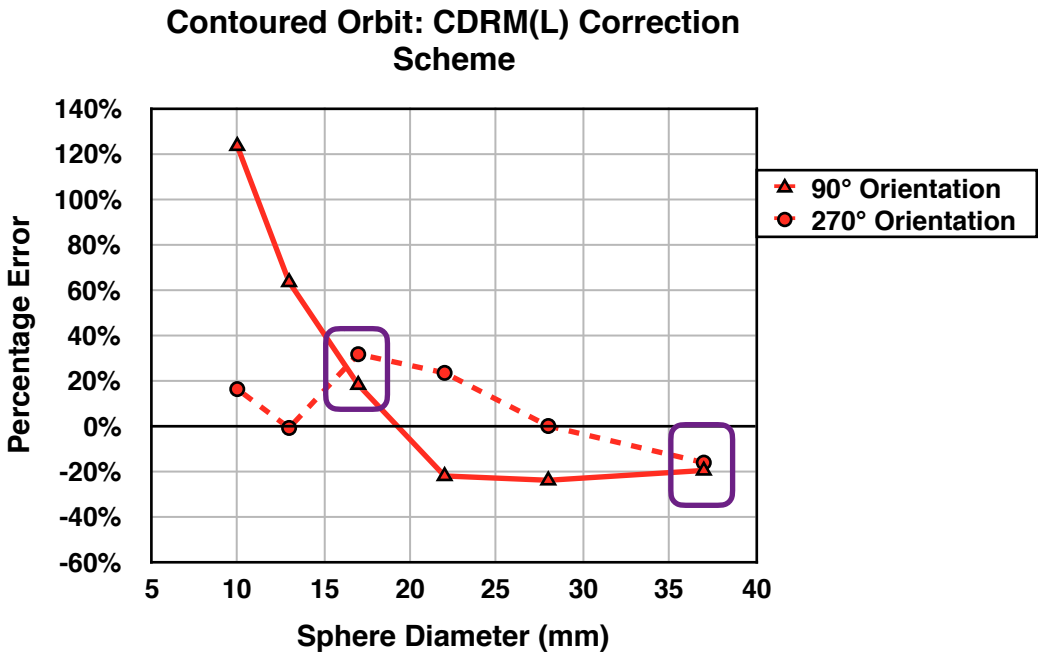

Figure 11.11: Accuracy of CDRM reconstruction comparing change in sphere orientation The purple boxes indicated spheres in relatively the same position in the phantom in both orientations

The two purple boxes in Figure 11.11 indicate the two spheres that are in relatively the same position in the phantom following rotation. These data points are the most consistent and this finding was demonstrated for all three reconstruction methods.

The position dependency suggests that spheres close to the arc of the detector are overestimated. This was more apparent in the 90° orientation with the smallest spheres in the anterior aspect of the torso phantom (as illustrated by Figure 11.6). In the 90° orientation, the smaller spheres are considerably overestimated as only a relatively small increase in reconstructed counts leads to a marked increase in estimated activity concentration. The position dependence is less severe in the 270° orientation, when the larger spheres are closer to the arc of the collimator anteriorly. In this orientation, the larger sphere VOIs would require substantially more counts to reverse an underestimation and result in an overestimation.

Figure 11.12 shows a transverse slice through the centre of the spheres in both orientations, acquired with a contoured orbit and reconstructed with CDRM(L). A ringing artefact is apparent in the larger spheres. This artefact explains the underestimation of activity concentration in larger spheres.

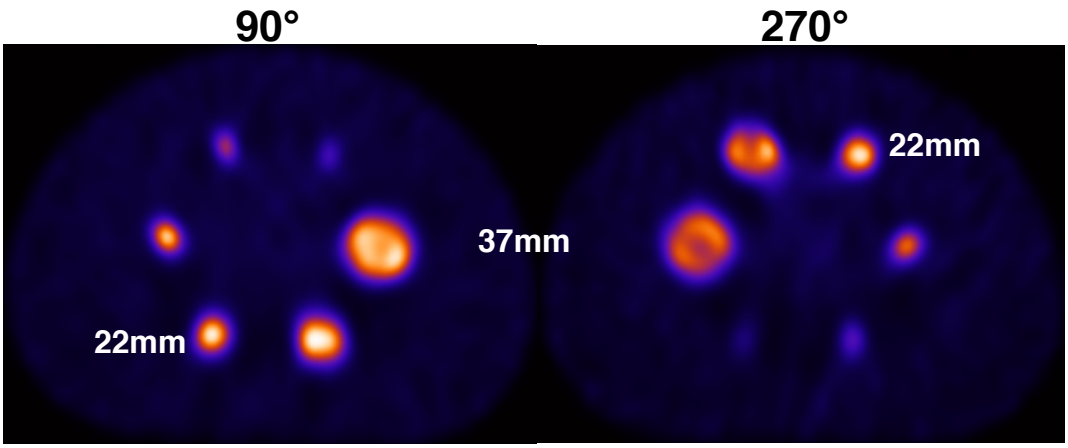

Figure 11.12: Position dependent accuracy example. Both the 90° orientation (left) and 270° (right) orientation are scaled to their own maximum.

In Figure 11.12 there is an apparent loss of counts in the 37mm sphere between the 90° and 270° orientation. In fact, the accuracy of the 37mm sphere is consistent in both reconstructions. However, the appearance can be explained by the activity concentration in the 22mm sphere which is underestimated in the 90° orientation and overestimated in the 270° orientation. The 22mm sphere in the 270° orientation raises the maximum count in the image relative to the 90° orientation.

Circular Orbit

With the phantom positioned centrally in the FOV, a circular orbit acquisition demonstrates that the sphere position dependence is less apparent (Figure 11.13).

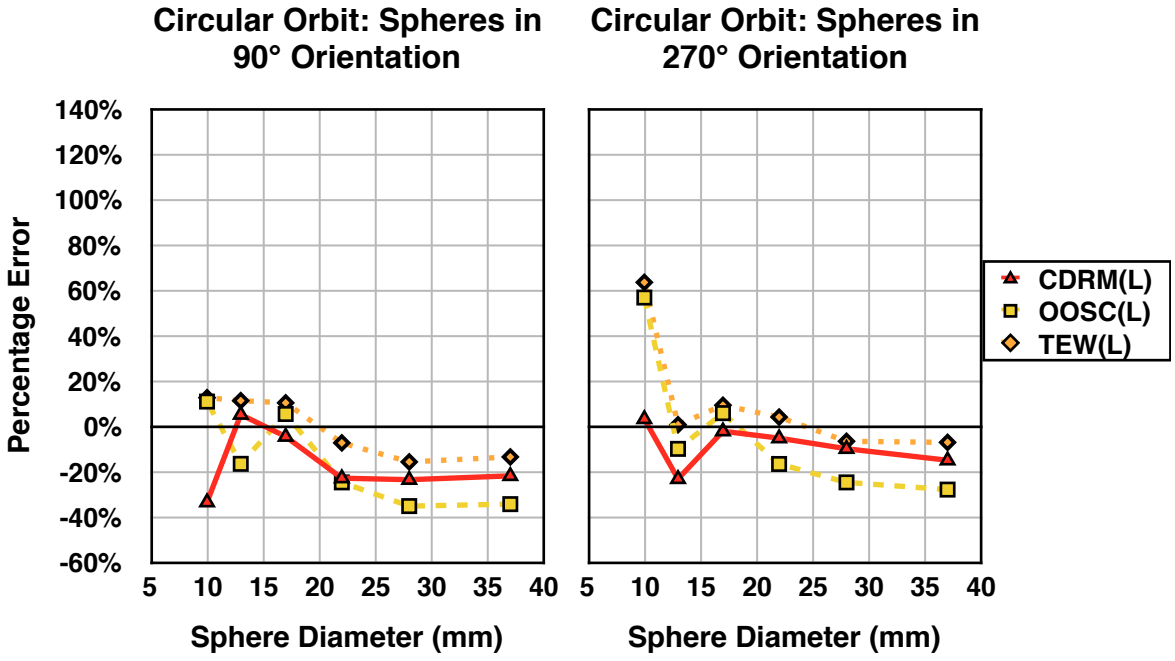

Figure 11.13: Accuracy of activity concentration measurements in the 90° (left) and 270° (right) sphere orientation, both with circular orbit data acquisition

A relatively small position dependence still exists and can be illustrated using a single reconstruction method. Figure 11.14 shows this relationship for the CDRM(L) reconstruction. Again, the two purple boxes indicate the two spheres that are in relatively the same position in the phantom following rotation.

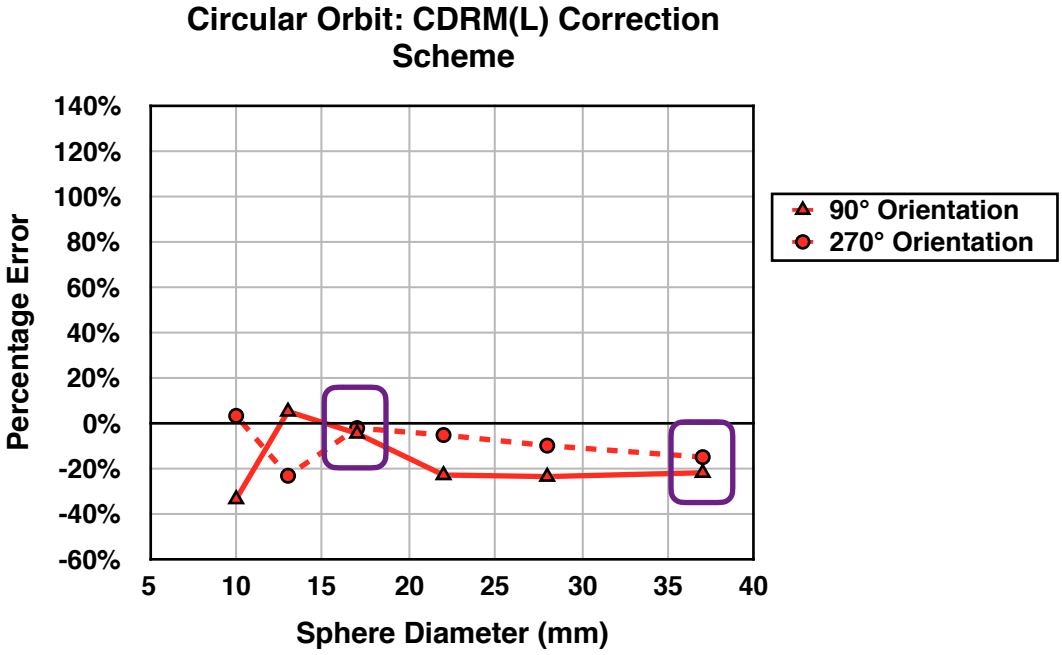

Figure 11.14: Accuracy of CDRM reconstruction comparing change in sphere orientation. The purple boxes indicated spheres in relatively the same position in the phantom in both orientations

Although a circular orbit reduces position dependent accuracy, a large fixed Radius of Rotation (ROR) would not be used clinically as spatial resolution would be impaired. Additionally, in this study, the spheres are located relatively centrally within the torso phantom. Depending on patient habitus, superficial lesions in clinical studies may be close to the arc of the detector, leading to inaccuracy of quantification. Therefore, the wide circular orbit results presented here are informative of the practical effect of a fixed detector orbit without being directly applicable to a clinical scenario.

Torso Phantom Results: Accuracy of Routine Clinical Acquisition

The accuracy of routine clinical acquisitions was assessed by evaluating the error in activity concentration measurements from four acquisitions. The four data sets included a combination of three uptake ratios and two acquisition zooms, and were acquired with LEHR and MELP collimators (described in Table 11.13). All data were acquired with a contoured orbit, as would be the case clinically, and spheres in the 90° orientation.

The mean percentage error between true activity concentration and the mean measured activity concentration in the uniform background region of four acquisitions is shown in Table 11.18.

Correction Scheme	Percentage Error
CDRM(L)	3.1%
OOSC(L)	-2.4%
TEW(L)	-3.6%
OOSC(M)	2.5%

Table 11.18: Percentage error in activity concentration measurements in a uniform region of the torso phantom
The estimated error was <0.05 for all correction schemes.

The errors in the background region for the four reconstruction schemes were all within ±5%.

There was no statistically significant difference found between the two voxel sizes of the activity concentrations measured in the six spheres (p=0.084, CI:3.4%±4.1). Furthermore, the mean difference in activity concentration between the acquisition zooms was 3.4%, which is sufficiently small to be considered of no clinical significance.

Similar to voxel size, there was no statistically significant difference found between the three contrast ratios evaluated (Table 11.19).

Concentration Ratios		p-value	CI
5.2:1	**9.5:1**	0.114	5.6%±8.0
8.8:1	**9.5:1**	0.597	5.5%±10.7
8.8:1	**5.2:1**	0.232	8.6%±11.4

Table 11.19: p-values and Confidence Intervals (CI) for Wilcoxon test of statistical significance between activity concentration ratios measured in the torso phantom

The largest mean difference in error was 8.6%, between the 5.2:1 and 8.8:1 activity concentration contrast ratios.

Statistical testing has shown no differences in accuracy of activity quantification dependent on voxel size or contrast. Therefore, measurements from all acquisitions were combined into a single mean measurement for subsequent analysis of sphere activity concentration.

The percentage error of measured activity concentration to true activity concentration in spheres is shown in Figure 11.15.

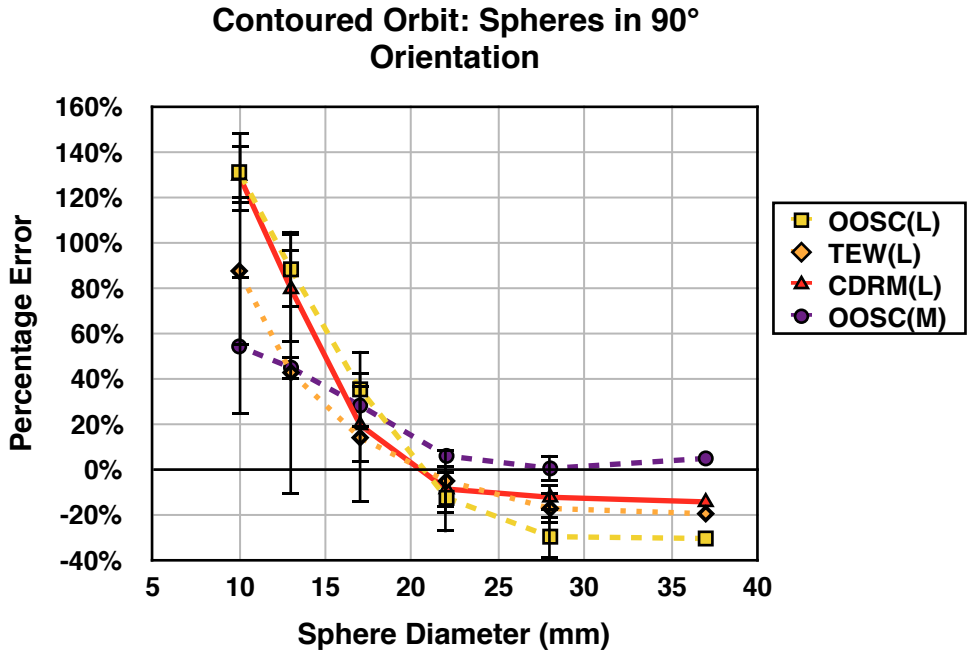

Figure 11.15: Percentage error between true and measured activity concentrations of spheres in the torso phantom

For LEHR acquisitions, the largest three spheres demonstrate underestimation of activity concentration, whereas the smallest three spheres demonstrate overestimation. The CDRM(L) and TEW(L) methods of reconstruction have a mean measurement error of ±20% for the largest four spheres. In contrast, with regard to the OOSC(L) reconstruction, only one sphere (22mm diameter) demonstrates a measured activity concentration within ±20% of true activity concentration. The quantitative accuracy of OOSC(L) will be impaired by poorer SPECT spatial uniformity compared to the alternative reconstruction methods, as was shown in Section 4.3.

The OOSC(M) data most closely represents true activity concentration in the 22mm, 28mm and 37mm spheres, to within ±6%. As the MELP collimator measurements are more accurate for these spheres compared with LEHR collimator data, this suggests the MELP data has a less pronounced ringing artefact. This finding is a result of the poorer spatial resolution of the MELP collimator which produces a shallower activity concentration gradient due to partial volume effect. Figure 11.16 shows the 37mm reconstructed using the OOSC(L) and OOSC(M) correction schemes.

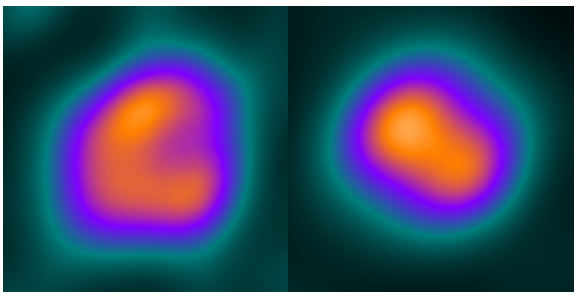

Figure 11.16: Extent of ringing artefact in the 37mm sphere for OOSC(L) (left) and OOSC(M) (right) correction schemes

The source of the gross overestimation in the smallest spheres is a result of position dependence, as described previously. A compounding source of error is localised noise in the relatively low count clinical data. Figure 11.17 shows an example of a noisy region within the measurement VOI of the 10mm sphere. This increase in counts will contribute significantly to the additional counts in the VOI compared to the true uniform background count density.

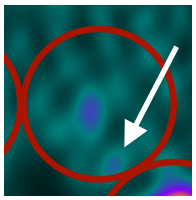

Figure 11.17: Small region of noise seen within the 10mm sphere VOI

This investigation has shown that, following careful calibration of the gamma camera, considerable errors in measured activity concentration in the torso phantom remain. In particular, the activity concentration in small spheres close to the arc of the collimator were overestimated. The activity concentration was underestimated in the larger spheres due to ringing artefacts.

Ringing should be less apparent for structures observed clinically, which may be irregular in shape and have a shallower activity concentration gradient compared with the torso phantom. However, it is also worth noting that some patients undergoing SPECT studies of the abdomen/pelvis will often have a wider diameter than the torso phantom. Therefore, the inaccuracies demonstrated in the phantom work are likely to be increased in the clinical setting.

11.3.3.2 Striatal Phantom: Accuracy Results

The accuracy of six activity concentration measurements in the striatal phantom demonstrate a linear fit close to unity between true and measured concentration (Figure 11.18).

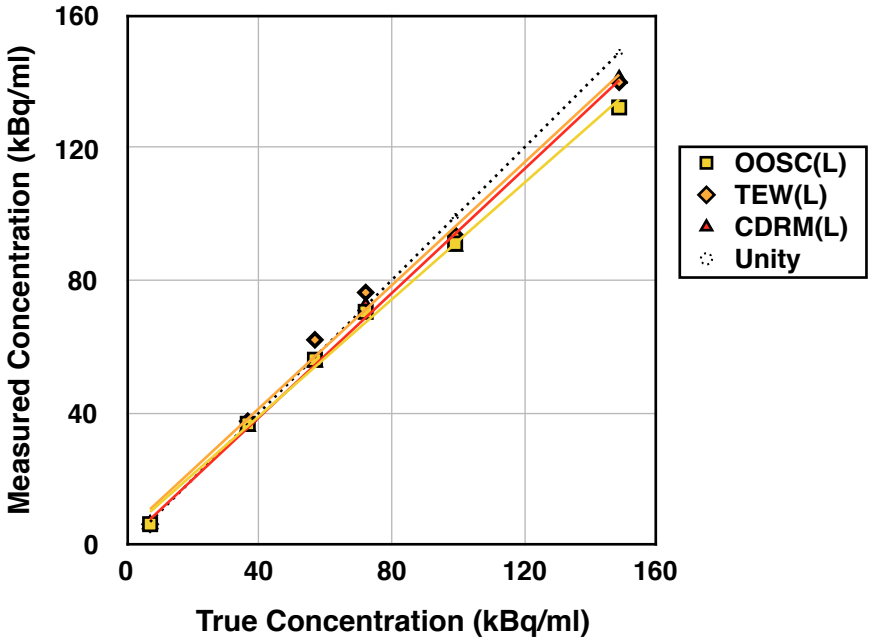

Figure 11.18: Accuracy of activity concentration measurements in the striatal phantom

There are no error bars presented in Figure 11.18 as each data point is a single measure. However, each striatum contains the same volume as the 28mm sphere in the torso phantom. Therefore, the errors demonstrated for measuring activity concentration in the 28mm sphere of the torso phantom can be assumed to be representative.

A summary of the linear gradient (m) and the coefficient of determination (R^2) are shown in Table 11.20.

	Equation Values	
	m	**R^2**
OOSC(L)	0.88	0.996
TEW(L)	0.93	0.992
CDRM(L)	0.94	0.997

Table 11.20: Gradient (m) and coefficient of determination (R^2) of the trendlines presented in Figure 11.18

No correction has been made for the volume of Perspex in the measurement VOI. Not incorporating this correction may have resulted in an underestimation of activity concentration. However, the volume of each striatal VOI is large relative to the Perspex included within the VOI. Therefore, the influence on the activity concentration measurement will be small. Filling defects (as demonstrated by air bubbles in Figure 11.9) will also lead to underestimations in measured activity concentrations.

The percentage differences between measured and true activity concentration in the striatal phantom are shown in Table 11.20.

True Activity (kBq/ml)	Percentage Difference		
	OOSC(L)	TEW(L)	CDRM(L)
7.0	-10.8%	-11.2%	-9.7%
36.5	0.3%	2.4%	-2.1%
56.8	-1.5%	8.7%	-2.9%
72.2	-2.4%	5.6%	0.1%
99.2	-8.5%	-5.8%	-9.5%
148.8	-11.8%	-6.2%	-5.4%

Table 11.20: Percentage differences between true and measured activity concentrations in the striatal phantom

The CDRM(L) reconstruction was within ±10% of the true concentration. The activity concentration measurements in the striatal phantom are within ±12% of the true activity concentration for the OOSC(L) and TEW(L) methods.

The three reconstruction methods demonstrate underestimation for the highest two activity concentrations. This finding could be a result of a non-linear count rate response at these high concentrations. However, the underestimation at the two highest concentrations is comparable with that of the smallest activity concentration and so, therefore, may simply be explained by measurement error.

11.3.4 Discussion of Quantitative Accuracy

11.3.4.1 Accuracy of Quantification in the Torso Phantom

The results of the OOSC(M) correction scheme suggest an accuracy of ±5.9% for the measurement of activity concentrations in spheres ≥22mm. For ^{123}I-mIBG SPECT quantification this range is an acceptable tolerance for intra-patient serial studies. However, the Southampton Method employed in this investigation requires the volume of the object of interest to be known. This volume could be estimated in patient studies using a registered CT but would introduce further variability to the measurement.

The high-count, low-noise acquisitions of the torso phantom demonstrated that the accuracy of all correction schemes was position dependent. This dependence was more pronounced for contoured orbits when compared with circular orbits. The finding suggests that lesions close to the arc of the collimator will be overestimated. This novel finding is

the result of varying rates of reconstruction algorithm convergence across the FOV, as described by Kappadath [175] and demonstrated by spatial resolution measurements in Section 5.3.2.

The appearance of a ringing artefact in the three largest spheres for data acquired with LEHR collimators has resulted in an underestimation of the activity concentration of these spheres. Koral [14] presented images with a similar ringing artefact in a torso phantom with ^{131}I filled spheres (Figure 11.19).

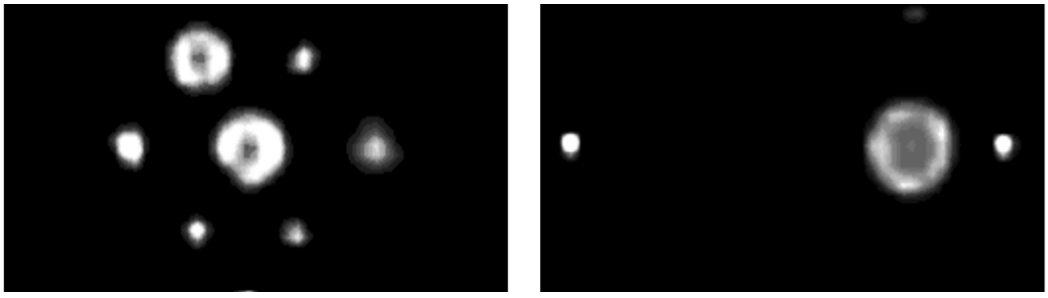

Figure 11.19: Images presented by Koral [14] of ringing artefacts in spheres filled with ^{131}I in a torso phantom with a cold background compartment

Practical phantom studies by O'Mahoney [88], Kangasmaa [13] and Armstrong [98] highlight errors in quantification introduced by ringing artefacts when RR is applied to ^{99m}Tc SPECT reconstruction. The effect is also described by Snyder [203] and Liu [204] in simulation studies. However, RR has shown to be necessary for improved FWHM (see Section 5.3.2), which should improve quantitative accuracy overall. Kangasmaa [97] has demonstrated that novel reconstruction techniques can reduce ringing artefacts. However, the method of depth-dependent RR implemented in this investigation may make ringing artefacts unavoidable. Furthermore, ringing should be less pronounced in clinical studies where structures are irregular shapes and have less severe contrast gradients than in phantom studies.

The activity concentration in uniform background regions in the clinical equivalent acquisitions of the torso phantom was measured to within 3.6% of the true activity concentration. Similarly, Du [135] demonstrated an error in activity concentration measurement of ±3.5% when including modelling of high-energy contamination for ^{123}I SPECT.

The activity concentration of the largest three spheres in the phantom is underestimated by up to 30.5% for LEHR acquisitions without correction for high-energy emissions (OOSC(L)). Similarly, a phantom study by Gilland [33] demonstrated underestimation of ^{123}I concentration using LEHR collimators. The study suggested an approximate 20-25%

underestimation in 28mm and 34mm diameter spheres. The discussion notes that this underestimation could be calibrated for and that the error could be reduced by improving resolution effects. However, an adjustment of the CF to correct for an underestimation of sphere concentration would result in an overestimation of the activity concentration in larger regions.

In the current investigation, the largest underestimation was 19.6% for the TEW(L) reconstruction and 14.4% for the CDRM(L) reconstruction. The CDRM(L) result would be in keeping with results by Iida [134] who suggested a mean underestimation of activity concentration of 12.5% between 12 gamma cameras for ^{123}I SPECT. In the current study, position dependence contributed to gross errors in the smallest spheres.

In this study, the results of activity concentration accuracy for ^{123}I are comparable with published findings for other radionuclides. For example, a summary by Shcherbinin [129] suggests errors of up to approximately 20% in a range of radionuclides. Bailey [1] has also described underestimation of ^{99m}Tc activity concentration by approximately 10-40% in the three larger spheres of the torso phantom.

Shcherbinin [129] demonstrated a 4-5% error in ^{123}I quantification of activity concentration for bottles in a torso phantom using a VOI created with a 1% threshold of maximum activity concentration. However, Shcherbinin measured activity concentration of cylindrical sources, larger in volume than the 37mm diameter sphere, and in the absence of surrounding activity.

Both Gilland [33] and Bailey [1] suggest quantification errors are dependent on spatial resolution. This is re-enforced by Zeintl [132] who measured an underestimation of ^{99m}Tc activity concentration in a 37mm diameter sphere of 8% and 35% for a 2.4mm and 4.8mm pixel size respectively. Kangasmaa [13] similarly showed deficits consistent with Zeintl for ^{99m}Tc with 4.8mm pixels. Kangasmaa suggested that sphere size in the torso phantom, while suitable for PET imaging, may not be appropriate to evaluate SPECT quantification. Similarly, Bailey [1] suggests accurate SPECT quantification may require objects to be no smaller in diameter than 40-50mm. However, in this study the implementation of the Southampton Method removed dependence on pixel size. The Southampton Method determines that all additional counts above a background reference value have come from the object of interest, thereby removing partial volume effect from the measurement. This method demonstrated no statistically significant difference in activity concentration measurements with pixel size.

An alternative approach to measurement would be to establish a Recovery Coefficient (RC) for each sphere. Although this method was used by Koral [14, 131] for ^{131}I and Zeintl [132] for ^{99m}Tc quantification, Bailey [1] suggests “such measures are cumbersome” and require accurate experiments to establish the RCs. As was discussed in Section 6.2.1, Contrast Recovery (CR) is dependent on sphere location in the phantom and would, therefore, provide an unreliable correction.

As was also shown in the current study, Gilland [33] observed no difference in the accuracy of activity concentration measurements for sphere to background ratios between 5:1 and 10:1. Contrast ratios below 5.4:1 were not evaluated in this study. Gilland and Koral [14] disagree on whether larger errors are measured for a contrast ratio of ~2.6:1, with the latter suggesting no difference compared with a contrast ratio of 10:1. Therefore, further work which investigates lower contrast ratios may be of interest.

In summary, accuracy measured using the torso phantom with a clinical acquisition protocol demonstrated an underestimation of activity concentration in the 22-37mm diameter spheres for LEHR data. Activity concentration was overestimated for the 10-17mm spheres for both LEHR and MELP data due to position dependence. Although marketed as a ‘torso’ phantom, patient studies will often have a larger widest dimension. Inter-patient variability, therefore, will introduce greater uncertainty to measured activity concentrations, which limits the utility of the absolute quantification approach for body section applications. However, the technique may prove suitable for intra-patient follow-up, based on an assumption that lesion location will be relatively consistent between studies.

11.3.4.2 Accuracy of Quantification in the Striatal Phantom

Using the Southampton Method, Crespo [24] reduced the error in activity concentration measurements for a simulated striatal phantom, reconstructed with Monte Carlo scatter correction of high-energy emissions, from 35% to ±5%. In this current investigation, the error in CDRM(L) measurements was ±10%, which is acceptable in clinical practice.

A study by Du [135] is highlighted in reviews by Shcherbinin [129] and Bailey [1] as having demonstrated an accuracy of 2% for ^{123}I SPECT. However, the figure given in the paper (2.35%) relates to the accuracy of a relatively high count acquisition which is not indicative of the clinical setting. Additionally, the reconstruction algorithm used by Du included Partial Volume Effect Compensation, which was based on a segmented MRI map and ran for 320

iterations. Therefore, the errors accepted in measurement of uniform activity concentration in this study are sufficiently comparable to Du's idealised technique.

There were no ringing artefacts observed in the reconstructed images of the striatal phantom which, although having the same volume as a 28mm sphere, are more irregular structures. This finding is in agreement with Maebatake [169] who presented striatal phantom images from data acquired with Siemens LEHR and Low-to-Medium Energy General Purpose (LMEGP) collimators. The LEHR data demonstrated no ringing artefacts while the LMEGP did. Both data sets in the study by Maebatake were reconstructed with depth-dependent RR.

Therefore, absolute quantification of activity concentration has been shown to be suitably accurate for neurology applications, which use a fixed ROR and acquire data from a consistent section of patient anatomy. However, this recommended approach also requires the implementation of a measurement method which reduces partial volume effect. The Southampton Method can be employed in this regard as the volume of a normal striatum is known to vary by only ±0.8ml in normal patients [205, 206].

11.3.5 Conclusions

Results of quantitative accuracy using the torso phantom suggest that ^{123}I SPECT data, acquired with MELP collimators and reconstructed with Object Only Scatter Correction (OOSC), provide the best approach for data acquired with a contoured orbit. As accuracy has been shown to be position dependent, the utility of inter-patient comparison of measurements is limited. However, serial studies may benefit from this approach with intra-patient comparison of lesion uptake.

Results of quantitative accuracy using the striatal phantom suggest that ^{123}I SPECT neurology studies, acquired with LEHR collimators and reconstructed using Collimator and Detector Response Modelling (CDRM), are sufficiently accurate for routine clinical use. Furthermore, the Southampton Method should be employed for measurement of activity concentration to remove partial volume effect.

Chapter 12: Quantification of Patient Data

12.1 Introduction

The previous Chapter evaluated the accuracy of absolute quantification using ^{123}I and identified neurology as a suitable clinical application. Therefore, in this Chapter, absolute quantification, via Standardised Uptake Values (SUVs), will be applied to routine clinical neurology data.

The calibration of a gamma camera for absolute quantification (performed in Section 11.2) allows measurement of activity concentration. A Standardised Uptake Value (SUV) can be determined from this measure. An SUV is the ratio of activity concentration measured in the patient to the injected activity per kilogram of the patient's body weight. SUVs are used extensively in PET imaging, particularly in the analysis of ^{18}F-FDG images of cancer patients. Bailey [1, 127] suggests the technique could find widespread use in SPECT imaging as clinicians have become familiar with absolute quantification and an SUV approach to analysis.

Currently, relative quantification of ^{123}I-DaTSCAN™ studies with reference to a European normal database (described in Section 10.1) has an established advantage as an adjunct to visual assessment [117]. However, the utility of using SUVs has yet to be examined. Furthermore, ^{123}I-DaTSCAN™ images are typically displayed relative to their maximum count value. However, studies reconstructed in units of SUV (g/ml) can be displayed with absolute values using a normalised colour table. To the author's knowledge, clinical ^{123}I-DaTSCAN™ studies have not previously been presented in units of SUV. The key difference between displaying data in relative and absolute scaling is that:

- relative scaling will display the maximum value for normal and abnormal studies with the same colour from a Look Up Table (LUT)

- absolute scaling will display the maximum value for a normal study at the top end of the LUT, whereas abnormal studies will have their maximum represented at a lower level

Additionally, the presentation of Lewy Body Dementia (DLB) in ^{123}I-DaTSCAN™ studies is described by Tatsch [26] as a global reduction in striatal uptake. This global reduction should not change the appearance of non-specific uptake when using absolute scaling. However, the current approach, which is to display these studies in a relative scale, means a global reduction of uptake in the striatum is presented as a 'raised background'. Furthermore, there is an ongoing debate surrounding the most suitable SUV method of measurement (SUV_{max}, SUV_{peak} or SUV_{mean}), as outlined in Section 2.6.2.1.

The primary aim of this Chapter is to apply absolute quantification of ^{123}I to clinical studies. However, due to the novel application of this technique, a number of secondary aims will also be addressed, which are to:

- Compare the diagnostic performance of SUV_{max}, SUV_{peak} and SUV_{mean}, with regard to ^{123}I-DaTSCAN™ imaging, by the application of a threshold to differentiate normal and abnormal studies
- Compare the diagnostic performance of SUV measures with the currently established method of relative quantification (BRASS™) for the differentiation of normal and abnormal studies
- Identify a suitable colour scale for display of ^{123}I-DaTSCAN™ studies in units of g/ml
- Assess non-specific uptake in normal and abnormal ^{123}I-DaTSCAN™ studies

To achieve these aims, this Chapter is divided into two Sections. The first Section evaluates SUV measures for diagnosis of ^{123}I-DaTSCAN™ studies and compares SUV thresholds for classification of diagnosis, which includes comparison with existing relative quantitative approaches. The second Section determines a suitable maximum SUV for an LUT for displaying ^{123}I-DaTSCAN™ studies in an absolute colour scale and will also assess regions of non-specific uptake.

12.2 Comparison of Quantitative Measures

A gamma camera, calibrated for absolute quantification, allows in vivo measurement of activity concentration. Section 11.3.5 concluded that the technique could be accurately applied to ^{123}I-DaTSCAN™ SPECT. This conclusion is a result of the reproducible acquisition setup and similar inter-patient anatomy.

As described in Section 2.6.2, absolute activity concentration measurements are of little use for inter-patient comparison or even with intra-patient follow-up scans. A simple method of normalising between patient studies is to convert activity concentration to SUVs. However, a threshold of normality has not been established for ^{123}I-DaTSCAN™ studies as SUVs are a novel technique.

An analysis of ^{123}I-DaTSCAN™ patient data was performed with an aim of determining a threshold of normality based on SUV measurements. As a preferred metric for measuring SUV is undefined, SUV_{mean}, SUV_{peak} and SUV_{max} were evaluated.

Currently, relative quantification analysis with Hermes Medical Solutions BRASS™ application, with reference to the ENC-DAT normal database, is an established adjunct to reporting [117]. Therefore, this investigation compared the diagnostic accuracy of an SUV threshold of normality with the accuracy of classification using BRASS™.

12.2.1 Methods and Materials

12.2.1.1 Patient Studies

101 patient studies were acquired in the calendar year from the start of June 2015 to the end of May 2016. Of these, 50 patients had combined SPECT and CT studies and the required demographics recorded to allow reconstruction for SUV measurement. Requirements are the:

- Height and weight of the patient
- Activity in the syringe before administration
- Time of injection
- Residual activity in the syringe following administration, and
- Time of activity measurements, including measurement of residual activity

Determination of Patient Outcomes

Definitive patient outcomes are difficult to determine in the patient population under investigation due to the often slow progression of the disease. An ideal gold standard would be histopathology at autopsy to determine loss of nigrostriatal nerve terminals, as performed by Seibyl [207]. Such a study would require long-term follow-up of patients and is, therefore, outside the scope of this thesis. In the absence of a gold standard, clinical follow-up was performed on patients one year post imaging. For the clinical follow-up, a consultant radiologist reviewed case notes.

Patients referred for an ^{123}I-DaTSCAN™ study present with a variety of clinical questions relating to neurological illness. The differential question may be Essential Tremor (ET) or Parkinson Disease (PD), or Lewy-body type versus Alzheimer dementia. A useful paper on ^{123}I-DaTSCAN™ imaging by Tatsch [26] describes the categorisation of patient outcomes into normal and abnormal imaging findings. In the present study, Table 12.1 was used for differentiation of clinical follow-up into normal and abnormal appearance, which is based on the description by Tatsch.

Normal	Abnormal
Essential Tremor (ET)	Parkinson disease (PD)
Drug induced parkinsonism	PD with dementia
Normal-pressure hydrocephalus	Multiple System Atrophy
Psychogenic Parkinson Syndrome	Progressive Supranuclear Palsy
Dopa-Responsive Dystonia	Lewy-body type dementia (DLB)
Alzheimer dementia	Vascular parkinsonism

Table 12.1: Classification of patient follow-up as having normal or abnormal ^{123}I-DaTSCAN™ image appearance based on categorisation by Tatsch [26]

To minimise bias, patient outcomes that were established based on the original imaging test alone were not included. The disease status was established for 36 of the 50 patient studies. The gender and age demographics for these 36 patients are shown in Table 12.2.

Gender	M = 20 F = 16
Age (years)	Mean = 75.8 Min = 59 Max = 89

Table 12.2: Demographics for the thirty-six patients included in the study

Clinical follow-up indicated 13 normal and 23 abnormal studies.

12.2.1.2 Acquisition of ^{123}I-DaTSCAN™ Patient Studies

Patient studies were acquired using a Siemens Symbia T2 gamma camera with LEHR collimators. The clinical acquisition parameters are shown in Table 12.3.

Parameter	Value
Time per Projection	30s
Projections	128
Photopeak	159kev±10%
Scatter Windows	Lower: 138±4keV Upper: 178±4keV
Matrix	128x128
Zoom	1.45
Pixel Size	3.3mm
Orbit	Circular
Radius of Rotation	14-19cm
CT mA	35mA
CT kVp	130kVp
CT Reconstruction Slice Width	3.3mm

Table 12.3: Acquisition parameters for ^{123}I-DaTSCAN™ patient studies

The Radius of Rotation (ROR) for patient studies is dependent on patient compliance, anatomy and symptoms. The mean, minimum and maximum RORs for the 36 patient acquisitions are shown in Table 12.4.

	ROR (cm)	Injected Activity (MBq)	Uptake Time
Mean	15.4	176.5	3h 59mins
Minimum	13.9	167.0	3h 1mins
Maximum	19.0	185.6	5h 16mins

Table 12.4: The Radius of Rotation (ROR), injected activities and uptake time for patients included in the study

12.2.1.3 Reconstruction of ^{123}I-DaTSCAN™ Patient Studies

The ^{123}I-DaTSCAN™ patient studies were reconstructed with the Collimator and Detector Response Modelling (CDRM) correction scheme. CDRM includes Monte Carlo scatter correction of low and high-energy photons in the patient and detector system. This method was shown in Section 11.3.3.2 to be the most accurate method for quantification of activity concentration. The data were reconstructed with the Calibration Factor (CF) determined with the striatal phantom and a 15cm ROR (0.084). The studies were also reconstructed using the parameters recommended by Hermes Medical Solutions for BRASS™ automated analysis (Table 12.5).

	BRASS™ Reconstruction	SUV Reconstruction
Algorithm	Iterative	
Iterations	64 (16 iterations, 4 subsets)	96 (6 iterations, 16 subsets)
Resolution Recovery	✔	
Attenuation Correction	Uniform: Attenuation Coefficient = 0.146cm^{-1} Outline threshold = 30% Outline Filter FWHM = 2.5cm	CT AC
Scatter Correction	OOSC	CDRM
Postfilter	Gaussian 6mm FWHM	
Calibration Factor	—	0.084
Scheme Name	OOSC(L)	CDRM(L)

Table 12.5: Reconstruction parameters for ^{123}I-DaTSCAN™ patient studies

Hermes Medical Solutions Hybrid Recon™ reconstruction application decay corrects the counts in each projection to the start time of the acquisition.

12.2.1.4 SUV Measurement

Activity concentration measurements were converted to SUV in units of g/ml using Equation 12.1.

$$SUV = \frac{ActCon}{(InjAct_{DC}/BM)} \qquad \textbf{Equation 12.1}$$

where *ActCon* is the activity concentration in kBq/ml within a VOI, $InjAct_{DC}$ is the injected activity in kBq decay corrected to the start time of image acquisition and *BM* is the body mass of the patient in g.

Measuring SUVmax and SUVpeak

SUV_{max} is simply the maximum voxel value in a VOI. SUV_{peak} is the mean SUV of voxels in the hottest 1cm^3 within the VOI structure [137]. SUV_{max} and SUV_{peak} were measured in the left and right striatum of each patient using a 60mm diameter spherical VOI to encompass the full striatum. SUV_{max} and SUV_{peak} for each patient will most often be found in the caudate as the putamen is a thinner structure which is more susceptible to partial volume effect. Separate measurements of SUV_{max} and SUV_{peak} in the caudate and putamen were not made as the putamen value may often be found at the boundary

defined between the caudate and putamen and is, therefore, not representative of the putamen as a whole. An example of VOI placement is shown in Figure 12.1.

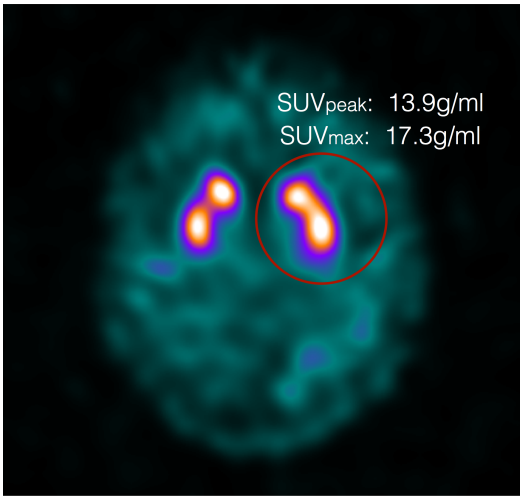

Figure 12.1: Example placement of a 60mm diameter spherical VOI used to determine SUV_{peak} and SUV_{max}

Measuring SUV_{mean}

SUV_{mean} is the mean SUV within a region or volume. For regions manually drawn to match the striatal boundary, there would be a considerable measurement error in the mean value due to substantial partial volume effect. Therefore, the Southampton Method was used to remove partial volume effect from the measurement. This method was used in Section 11.3.3.2 to establish accurate quantification of activity concentration in the striatal phantom. SUV_{mean} was measured in the left and right striatum. Furthermore, as the putamen is typically affected sooner and more severely than the caudate [26], SUV_{mean} was also measured separately in the caudate and putamen.

The Southampton Method was performed using the regularly shaped relatively large ROIs shown in Figure 12.2. The ROIs were copied to 13 slices containing the striatum and merged into a single VOI.

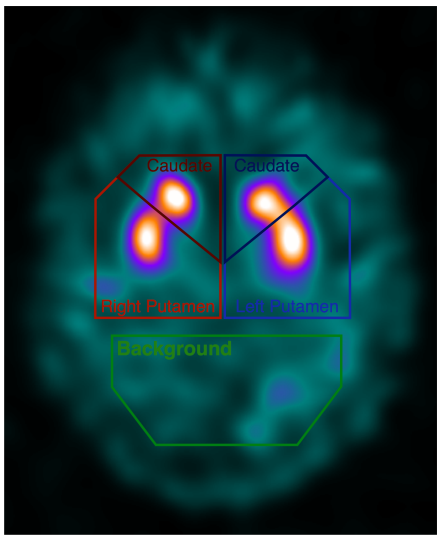

Figure 12.2: Example ROI placement on an ^{123}I-DaTSCAN™ patient study
The ROIs were copied to 13 transverse slices which contained the striatum and merged into a single VOI.

The volume of the anatomical structure is required to determine SUV_{mean} in the striatum, the caudate and the putamen. The volume of a normal striatum was assumed to be 11.2ml [31], the volume of which is known to vary by only ±0.8ml in normal patients [205, 206]. The individual volume of the caudate and putamen, required to calculate SUV_{mean} in these regions, was determined from published estimates of the ratio of putamen-to-caudate volume, which range from 1:1 [206] to 1:1.1 [31, 205]. A ratio of 1:1 was assumed and, therefore, the volume of each caudate and putamen was taken to be 5.6ml. The volume used is a scaler in the calculation of SUV_{mean} and, therefore, the exact value is not critical but should be used consistently to allow comparison between studies.

Age Correction of SUVs

In normal studies, Koch [208] showed a 9.5% loss in striatal binding ratios per decade until the age of 48, followed by a 6.4% loss per decade for ages greater than 48. Therefore, an age correction was performed on SUV measurements. The age correction is based on the 'broken stick model' developed by Koch. All of the patients in the current study were aged 55 and over. Accordingly, to normalise for age, all SUVs measured in this patient study were increased by 0.66% per year over 48, which is equivalent to a cumulative increase of 6.4% per decade.

12.2.1.5 Analysis of SUV Results

Disease progression usually reduces dopamine reuptake in one striatum relatively more than the other, typically contralateral to clinical symptoms [26]. Therefore, the lower values of SUV_{peak}, SUV_{max} and SUV_{mean} from the measurement of the left and right striatum were

used for analysis. Similarly, the lower value of SUV_{mean} from the left and right putamen was used for analysis. Box plots were used to compare SUVs for normal and abnormal studies. Thresholds for clinical application of SUV measurement were determined based on common statistical measures.

Sensitivity, specificity and diagnostic accuracy are statistical measures commonly used to measure the performance of a classification test, such as differentiating normal and abnormal studies [209-211]. Sensitivity indicates the proportion of True Positives (TP) identified. Specificity indicates the proportion of True Negatives (TN) identified. Diagnostic accuracy indicates the proportion of correctly determined TP and TN in the total population. Sensitivity, specificity and diagnostic accuracy can be determined using Equations 12.2, 12.3 and 12.4 respectively.

$$Sensitivity(\%) = \frac{TP}{TP + FN} \qquad \textbf{Equation 12.2}$$

$$Specificity(\%) = \frac{TN}{TN + FP} \qquad \textbf{Equation 12.3}$$

$$DiagnosticAccuracy(\%) = \frac{TP + TN}{TP + TN + FP + FN} \qquad \textbf{Equation 12.4}$$

where *FP* is the number of False Positives and *FN* is the number of False Negatives. The consequence of classification of the diagnostic test for the patient can indicate which statistical measure has greater importance. For example, if it is critical to ensure all positive classifications are true then a threshold to maximise sensitivity should be chosen. Conversely, if it is essential to ensure all negative classifications are true, then a threshold to maximise specificity should be selected.

12.2.1.6 BRASS™ Automated Analysis

BRASS™ registers patient studies to a reference template and compares measured uptake ratios with a database of normal uptake ratios. Patient images are quantified relative to the database on a voxel-by-voxel basis. Therefore, voxels can be assessed statistically using standard deviation from normal. The mean standard deviation from normal for each region assessed is reported to the user as a z-score. Consequently

BRASS™ suggests abnormality if the z-score is greater than two standard deviations below the normal patient mean.

In addition to automatic registration of a patient study to a template and generating VOIs, BRASS™ performs an age correction that modifies the region statistics. The age correction is based on the 'broken stick model' developed by Koch [208], which was previously described for correction of SUVs in Section 12.2.1.4.

The 36 patient studies were analysed using BRASS™. A five region model (the left and right caudate and putamen, and occipital reference region) was used. The outcome of the automated analysis was compared with clinical follow-up and used to generate a confusion matrix (Table 12.6).

		Test Method	
		Normal	**Abnormal**
Clinical Follow-up	**Normal**	TN	FP
	Abnormal	FN	TP

Table 12.6: Standard layout of a confusion matrix for assessing agreement between methods

From the confusion matrix, the sensitivity, specificity and diagnostic accuracy were determined for comparison with SUV analysis. Furthermore, a Kappa coefficient, which reduces the confusion matrix to a single value metric, was used to compare methods [212].

A Kappa coefficient is a statistical measure for assessing the agreement of a method with a reference standard, in this case, clinical patient follow-up. The Kappa coefficient is measured on a scale of 0 to 1 where 1 is perfect agreement, and 0 is what would be expected due to chance. Kappa coefficients and 95% confidence intervals for the SUV and BRASS™ methods were determined and cross-referenced using two online Kappa calculators: GraphPad [213] and VasserStats [214].

12.2.2 Results from Analysis of ^{123}I-DaTSCAN™ Patient Studies

12.2.2.1 SUV Measurements

Measurements of SUV_{peak} and SUV_{max} in patient studies are shown in Figure 12.3.

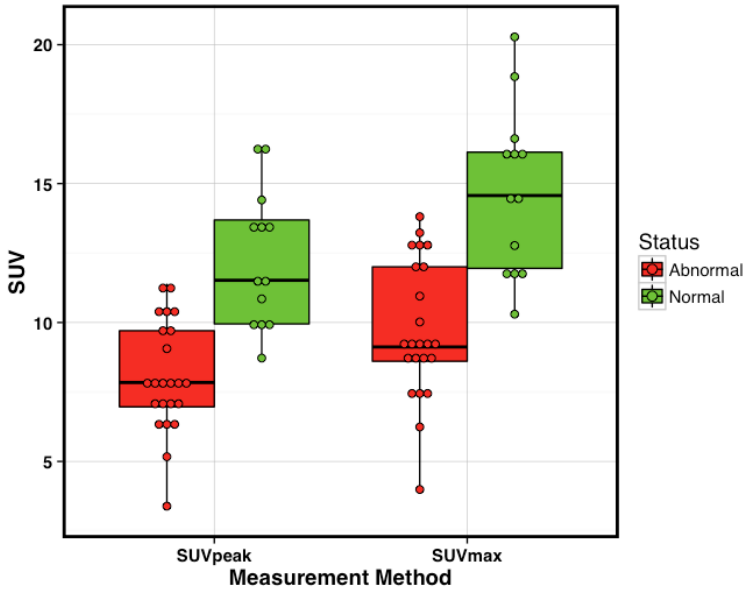

Figure 12.3: Box plot comparing the lower value of SUV_{peak} and SUV_{max} in the striatum of the thirty-six patient studies

As expected, the SUV_{max} values are, on average, larger than SUV_{peak}. There is a statistically significant difference between normal and abnormal patients for both SUV_{peak} ($p<0.001$; CI:3.23±1.41) and SUV_{max} ($p<0.001$; CI:3.83±1.81). However, the overlap between normal and abnormal measures for both methods indicates there is no distinct threshold for determination of abnormality.

Similarly, a box plot for SUV_{mean} of the whole striatum, and separated into the SUV_{mean} in the caudate and putamen (Figure 12.4), shows no distinct threshold for determination of abnormality.

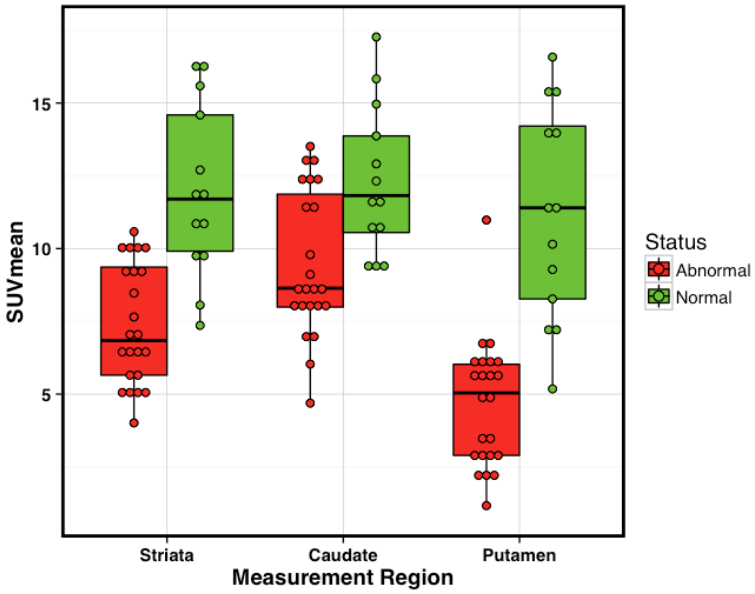

Figure 12.4: Box plot comparing the lower value of SUV_{mean} in the whole striatum, caudate and putamen in the thirty-six patient studies

Again, there is a statistically significant difference between the normal and abnormal patients in SUV_{mean} as measured in the whole striatum, the caudate and the putamen (Table 12.7).

SUV_{mean} Region	p-value	Confidence Interval
Striatum	<0.001	4.39±1.97
Caudate	0.004	2.77±1.78
Putamen	<0.001	6.56±2.44

Table 12.7: Test of significance between normal and abnormal patients for SUV_{mean} p-value and Confidence Interval for SUV_{mean} in the striatum, caudate and putamen demonstrating a statistically significant difference between normal and abnormal patient studies

12.2.2.2 SUV Threshold Determination

As all methods of SUV measurement demonstrate an overlap between the normal and abnormal studies, the choice of a threshold to aid differentiation of patient studies involves a tradeoff between FP and FN. This decision can be assisted by consideration of sensitivity, specificity and diagnostic accuracy. The box plots presented in Section 12.2.2.1 can be used to determine thresholds to maximise these parameters. Figure 12.5 demonstrates an example of this method for the SUV_{mean} of the putamen.

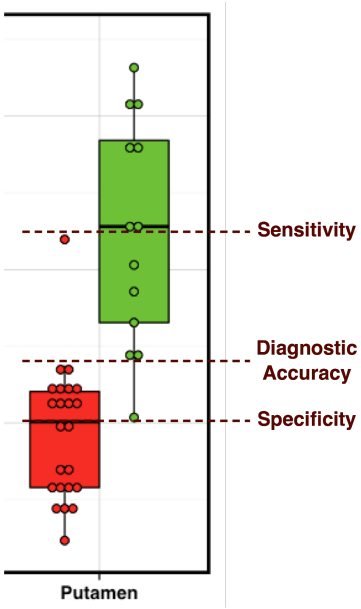

Figure 12.5: Method for determination of an SUV threshold

The SUV_{mean} for the whole striata and caudate will not feature in further analysis as these methods demonstrated greater overlap than SUV_{mean} of the putamen.

Threshold for SUV_{peak} of the Striatum

SUV_{peak} thresholds chosen to maximise sensitivity, specificity and diagnostic accuracy are shown in Table 12.8.

Aim	Threshold	Sensitivity	Specificity	Diagnostic Accuracy
Maximise Sensitivity	**11.4**	100%	61.5%	86.1%
Maximise Specificity	**8.7**	65.2%	100%	77.8%
Maximise Diagnostic Accuracy	**11.4**	100%	61.5%	86.1%

Table 12.8: SUV_{peak} thresholds chosen to maximise sensitivity, specificity and diagnostic accuracy alternately

An operator may use the thresholds suggested in Table 12.8 to conclude that all SUV_{peak} measurements below 8.7 are likely to be abnormal studies and all SUV_{peak} measurements above 11.4 are likely to be normal studies. However, there is uncertainty in outcome between these values.

Threshold for SUV_{max} of the Striatum

SUV_{max} thresholds chosen to maximise sensitivity, specificity and diagnostic accuracy are shown in Table 12.9.

Aim	Threshold	Sensitivity	Specificity	Diagnostic Accuracy
Maximise Sensitivity	**14.0**	100%	61.5%	86.1%
Maximise Specificity	**10.2**	65.2%	100%	77.8%
Maximise Diagnostic Accuracy	**14.0**	100%	61.5%	86.1%

Table 12.9: SUV_{max} thresholds selected to maximise sensitivity, specificity and diagnostic accuracy alternately

A comparison of Table 12.8 and 12.9 demonstrates the same values for all performance measures. Therefore, it is apparent that, based on these measures, the diagnostic performance of SUV_{max} thresholds is equivalent to that of SUV_{peak}.

Threshold for SUV_{mean} of the Putamen

SUV_{mean} thresholds chosen to maximise sensitivity, specificity and diagnostic accuracy are shown in Table 12.10

Aim	Threshold	Sensitivity	Specificity	Diagnostic Accuracy
Maximise Sensitivity	**11.0**	100%	53.8%	83.3%
Maximise Specificity	**5.1**	52.2%	100%	69.4%
Maximise Diagnostic Accuracy	**7.0**	95.7%	92.3%	94.4%

Table 12.10: SUV_{mean} of the putamen thresholds selected to maximise sensitivity, specificity and diagnostic accuracy alternately

The diagnostic accuracy of SUV_{mean} of the putamen is higher than that for SUV_{peak} and SUV_{max}. However, the diagnostic performance is poorer for SUV_{mean} of the putamen when thresholds are chosen to maximise either sensitivity or specificity.

In the clinical setting, reporting clinicians differentiate a high proportion of normal and abnormal studies correctly [215]. The role of quantitative software is to assist in the case of inconclusive studies. In that respect, it is important to minimise the overlap region in the measures considered. Therefore, maximisation of diagnostic accuracy was chosen as the metric to be optimised.

This analysis shows that, with regard to diagnostic accuracy, SUV_{mean} of the putamen is more accurate than SUV_{peak} and SUV_{max} of the striatum for differentiation between normal and abnormal ^{123}I-DaTSCAN™ studies. Therefore, SUV_{mean} of the putamen was used for comparison with BRASS™.

12.2.2.3 Comparison with BRASS™ Analysis

BRASS™ categorised the 36 patient studies as normal or abnormal based on a z-score threshold of negative two in either the caudate or putamen. Table 12.11 shows a confusion matrix of the resultant classification versus true outcome.

		BRASS™ Classification	
		Normal	**Abnormal**
True	**Normal**	11	2
	Abnormal	3	20

Table 12.11: Confusion matrix for BRASS™ automated relative quantification analysis

Therefore, analysis with BRASS™ resulted in a sensitivity of 87.0%, specificity of 84.6% and diagnostic accuracy of 86.1%. A z-score in the caudate was solely responsible for only one classification of abnormality. The other 21 classifications of abnormality were

based on the z-score in the putamen. Therefore, comparison with SUV_{mean} in the putamen is suitably like-for-like.

A confusion matrix for SUV_{mean} in the putamen, with a threshold of 7.0g/ml, is shown in Table 12.12.

		SUV_{mean} Classification	
		Normal	**Abnormal**
True	**Normal**	12	1
	Abnormal	1	22

Table 12.12: Confusion matrix for SUV_{mean} in the putamen with a threshold of 7.0g/ml

Comparing Tables 12.11 and 12.12 demonstrates that SUV_{mean} measures in the putamen correctly classifies more patient studies than BRASS™. Consequently, SUV_{mean} has a higher Kappa coefficient than BRASS™ (Table 12.13). However, there is not a statistically significant difference between both approaches to classification.

	Kappa coefficent	**Confidence Interval**
SUV_{mean} (putamen)	0.880	0.718-1.000
BRASS™	0.704	0.464-0.966

Table 12.13: Kappa coefficient and confidence interval for differentiation of normal and abnormal ^{123}I-DaTSCAN™ patient studies

12.2.3 Discussion

All SUV measurement methods demonstrated statistically significant differences between normal and abnormal studies. However, the overlap in measurements makes implementation of a threshold value a trade-off. As quantitative software is used to assist in the case of inconclusive studies, maximisation of diagnostic accuracy was chosen as the metric to optimise. SUV_{mean} of the putamen had the highest diagnostic accuracy and would, therefore, be recommended for routine use.

In the current investigation, SUV_{mean} of the putamen demonstrated a sensitivity, specificity and diagnostic accuracy of 95.7%, 92.3% and 94.4% respectively. A recent systematic review by Suwijn [215] reports rates of sensitivity and specificity for ^{123}I-DaTSCAN™ to be 98%. However, the analysis recognises that the studies reviewed included patients with a high suspicion of PD, rather than clinically uncertain Parkinsonism. Furthermore, the

sensitivity and specificity rates were based largely on whether the imaging reports matched for two ^{123}I-DaTSCAN™ studies acquired two years apart.

As highlighted in the methods section, final patient outcomes are difficult to determine due to the slow progression of disease in the patient population under investigation. Therefore, the reference standard of one year clinical follow-up, as used in this evaluation, is not ideal. However, the investigation has provided sufficient evidence of the utility of routinely measuring SUVs in ^{123}I-DaTSCAN™ patient studies as an aid to diagnosis.

SUV_{mean} of the putamen compared favourably with BRASS™. SUV_{mean} had a higher diagnostic accuracy than BRASS™, although there was no statistically significant difference. Furthermore, SUV_{mean} measurements are independent of population variance as they do not depend on a normal database. BRASS™ uses a European normal database, acquired on multiple gamma cameras with slightly different protocols [51]. A more robust method would be to establish a local normal database unique to the local population and gamma camera used clinically. This approach may improve diagnostic accuracy; however, it is beyond the scope of this thesis.

A recent study by Yokoyama [216] demonstrated that an uptake ratio approach allowed clear differentiation of normal and abnormal ^{123}I-DaTSCAN™ patients. However, the method was non-routine, using Statistical Parametric Mapping (SPM) of a diagnostic CT to define volumes. VOIs are, therefore, patient specific which is a novel approach to ^{123}I-DaTSCAN™ quantification. It is unclear what reference Yokoyama uses for discrimination of normal and abnormal studies, other than to describe a known limitation of the investigation as being “diagnosis by neurologists”. In the current study, use of the sequentially acquired CT to define regions would be unsuitable as the images are not of diagnostic quality.

Although Yokohama’s novel analysis demonstrated differentiation between normal and abnormal patients, a notable finding from the study was that commercially available automated semi-quantitative packages, comparable with BRASS™, did not differentiate normal and abnormal studies with 100% success. This finding was also demonstrated in the current study.

From a practical perspective, BRASS™ is dependent on a single calibration. The calibration is dependent on a number of variables with associated errors. It is hard to perform quality control on BRASS™ calibration without either a local normal database,

which is rare, or repeating the calibration process to assess consistency. Calibration for SUV measurements similarly depends on a number of variables. However, the practical setup for calibration and routine quality control is simpler than that for BRASS™. The calibration can be checked by repeat measurements of gamma camera sensitivity. This check can be performed relatively infrequently as a SPECT acquisition and more frequently via planar acquisition, as a basic method to detect drift [2].

It is worth noting that normal studies with low SUVs may be as a result of a tissued injection. SUVs could be corrected with an estimate of the tissued activity. This estimate is straightforward to achieve through a planar acquisition of the injection site, which can be quantified if the sensitivity of the gamma camera is known. Tissuing was not evaluated in this investigation as the patient subset did not have additional imaging of the injection site. However, an example of a tissued injection site image is shown in Figure 12.6.

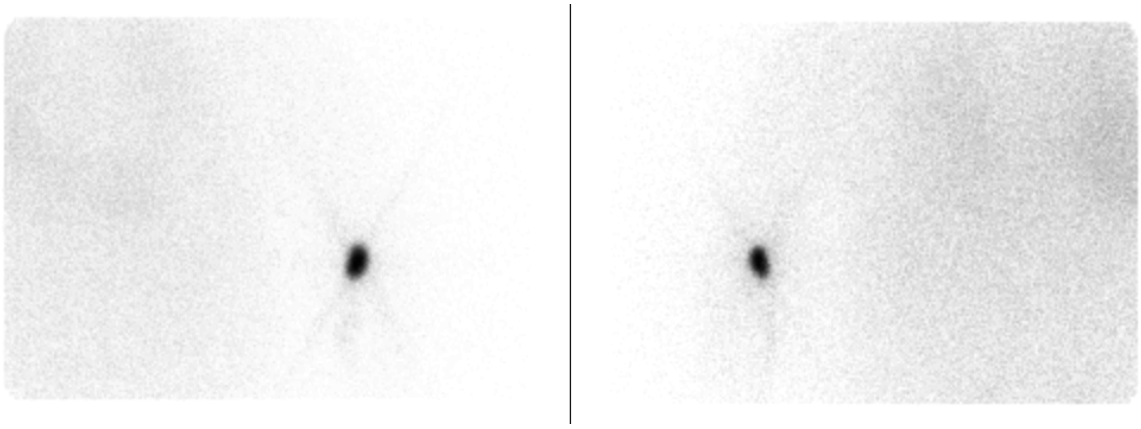

Figure 12.6: Anterior (left) and posterior (right) planar images of the injection site of an ^{123}I-DaTSCAN™ patient study

In the example presented, the patient injection site had an estimated 1% of injected activity. The SUV measurement would be reduced by a similar proportion and, therefore, in this example, would not affect the conclusions of the current work. However, minimising measurement errors, such as compensation for tissued activity, may improve differentiation between normal and abnormal patients.

12.2.4 Conclusion

SUV_{mean} of the putamen, measured using the Southampton Method, can provide a useful adjunct to visual assessment. It was shown to have the highest diagnostic accuracy of the SUV methods considered.

This investigation has demonstrated that the SUV_{mean} of the putamen can marginally outperform BRASS™, with reference to the European normal database, in differentiating

normal and abnormal studies. Furthermore, SUV_{mean} has the advantage of being independent of normal databases obtained from non-local populations.

12.3 Normalised Colour Table for SUV Display

Display of ^{123}I-DaTSCAN™ images in an SUV scale is, to the author's knowledge, a novel development. As such, a best practice approach has not been investigated for presenting images clinically. The aim of this Section is to determine the maximum SUV for the display LUT.

Additionally, as some images of ^{123}I-DaTSCAN™ patients with DLB are described as having the appearance of a 'raised background' [26], the mean SUV in background regions of normal and abnormal studies will be compared. This work was performed to confirm whether both cases have the same non-specific uptake.

12.3.1 Methods and Materials

The 36 ^{123}I-DaTSCAN™ patients categorised as normal and abnormal, as described in Section 12.2.1.1, were used to determine a maximum SUV for the display LUT and to evaluate areas of non-specific uptake. Patient studies were reconstructed using the parameters described for CDRM(L) in Table 12.5.

12.3.1.1 Maximum SUV for LUT

The SUV_{peak} of left and right striatum in 13 normal patients was measured to determine the maximum SUV for the display LUT. SUV_{peak} was measured as the mean SUV of voxels in the hottest 1cm^3 within in a 60mm diameter sphere placed over each striatum, as was shown previously in Figure 12.1. Again, SUVs were age corrected, as described in Section 12.2.1.4. The mean value of SUV_{peak} for this patient group was chosen for the maximum of the LUT.

12.3.1.2 SUV of Non-specific Uptake

The SUV_{mean} of areas of non-specific uptake in normal and abnormal patient studies was measured using a manually drawn irregular VOI in the occipital region. The VOI was composed of the ROI, shown in Figure 12.7, which was copied to 13 slices consecutive transverse slices and merged into a single VOI.

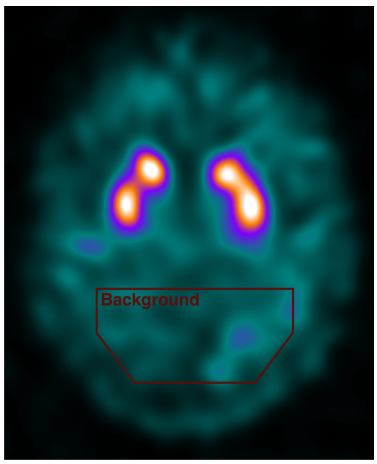

Figure 12.7: Background ROI used to measure non-specific uptake
The ROI was copied to 13 transverse slices which contained the striatum and merged into a single VOI.

The error in SUV_{mean} was calculated as twice the Standard Error (SE) of the measurements.

12.3.2 Results

12.3.2.1 Maximum SUV for LUT

The mean value of SUV_{peak} for the 26 normal striata was 12.8±1.1g/ml with a range of 8.4-17.8g/ml. Three examples of normal studies scaled to a maximum of 12.8g/ml are shown in Figure 12.8.

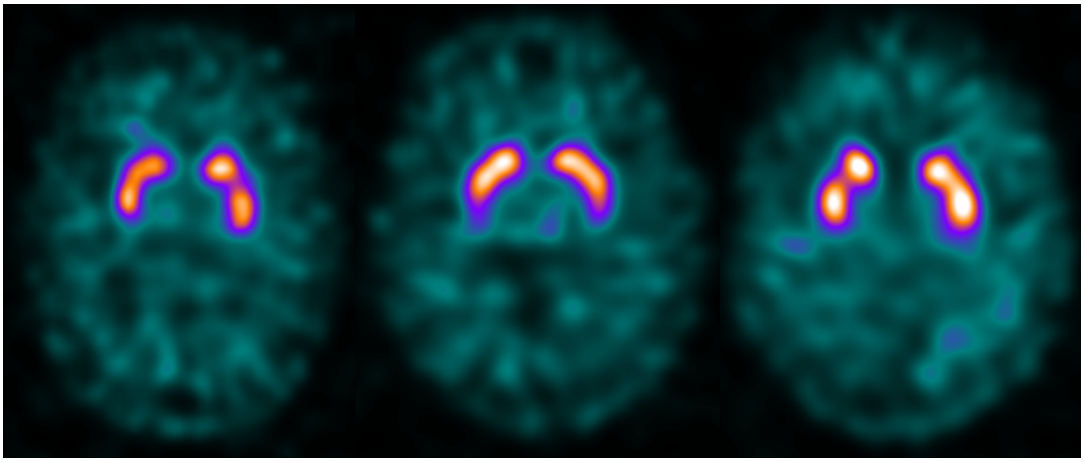

Figure 12.8: Three normal patient studies with a Look Up Table (LUT) maximum of 12.8g/ml
The three examples have an SUV_{peak} of 11.3g/ml (left), 13.0g/ml (middle) and 17.8g/ml (right)

12.3.2.2 SUV of Non-specific Uptake

The SUV_{mean} of background regions, grouped into normal and abnormal patients based on clinical follow-up, is shown in Figure 12.9.

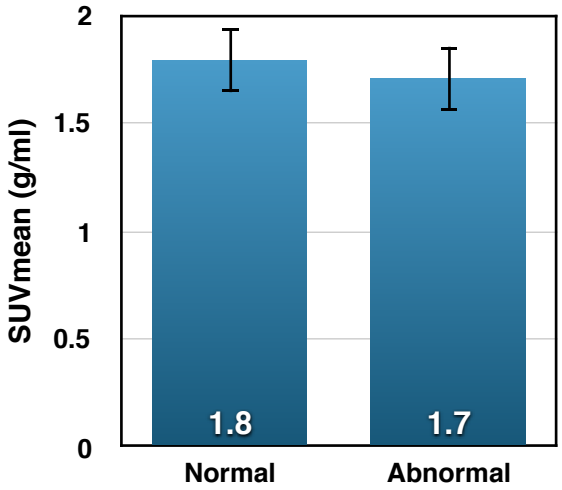

Figure 12.9: The SUV_{mean} in non-specific uptake regions of normal and abnormal patients

There was no statistically significant difference between the SUV_{mean} of background regions in normal and abnormal patients (p=0.624; CI:0.10±0.30). Therefore, absolute scaling of patient images to a normalised LUT will present background regions in the same colour tone whether normal or abnormal. This method of display allows the observer to evaluate striatal uptake without consideration of areas of non-specific uptake.

12.3.4 Discussion

Analysis of normal ^{123}I-DaTSCAN™ patients demonstrated a mean SUV_{peak} value of 12.8g/ml. The use of this value as the maximum for the LUT appears suitable for evaluation of a range of clinical studies. However, the effectiveness of this method of display will be assessed in greater detail via an observer study in Chapter 13.

As anticipated, there was no difference in the non-specific uptake of normal and abnormal patient studies. Therefore, when images are scaled to a normalised LUT, an observer can evaluate ^{123}I-DaTSCAN™ studies by the uptake in striatal regions alone. This approach may be particularly useful in DLB cases where there is a global reduction of striatal uptake. An example of three age and gender matched patient studies is shown in Figure 12.10. Each example shows the images scaled to its maximum (relative scaling) and scaled using an SUV maximum of 12.8g/ml (absolute). All three studies were referred for imaging with a clinical question querying DLB.

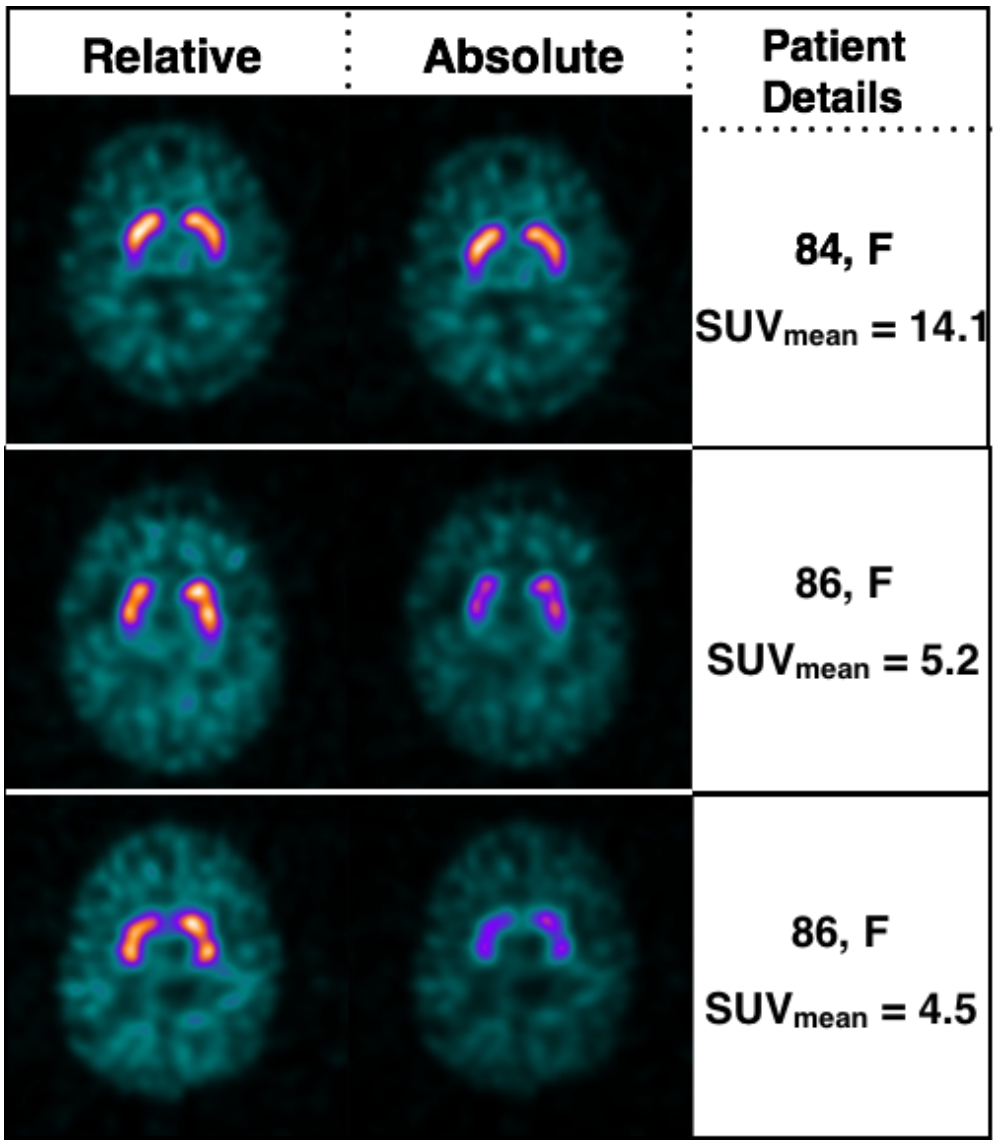

Figure 12.10: Three patient examples which compare ^{123}I-DaTSCAN™ images in relative and absolute scale

The lower two patient examples demonstrate that the background regions do not appear significantly raised with relative scaling. However, the SUV measurements and absolute scaling suggests that there is a global reduction in the striatum, typical of DLB appearances.

A further advantage to absolute scaling is when non-diagnostic areas of uptake enter the FOV. In the case of ^{123}I-DaTSCAN™ imaging, care must be taken not to include parotid glands in the SPECT reconstruction as they accumulate the radiopharmaceutical. If the parotid glands are included, and the study is relatively scaled to a maximum count value which is found in the parotids, then the appearance of the striata could be deceptive. A normal study may seem as though there is a global reduction in counts. However, if absolute scaling is used then the inclusion of the parotids in reconstruction has no bearing on the appearance of the striata.

As the evaluation includes only 13 normal patient studies, the findings of this investigation can, therefore, be considered as preliminary guidance for the display of clinical studies. Based on these initial findings, ^{123}I-DaTSCAN™ patient studies, reconstructed with units of absolute concentration, should be presented using an LUT with a maximum SUV of 12.8g/ml. However, this conclusion should be reviewed with greater patient numbers.

12.4 Conclusions

This Chapter has demonstrated the application of absolute quantification of ^{123}I to clinical studies. In doing so, SUV_{mean}, as measured in the putamen of ^{123}I-DaTSCAN™ studies using the Southampton Method, was shown to provide the highest diagnostic accuracy of SUV metrics investigated.

SUV_{mean} in the putamen was shown to outperform an established method of relative quantification (BRASS™) for differentiation of normality in the relatively small patient cohort assessed. However, there was no statistically significant difference between the two methods of analysis.

Preliminary investigation has shown that ^{123}I-DaTSCAN™ patient studies, reconstructed with units of absolute concentration, should be displayed using an LUT with a maximum SUV of 12.8g/ml. Regions of non-specific uptake were shown to have comparable SUVs in normal and abnormal studies.

Chapter 13: Qualitative Observer Assessment

13.1 Introduction

Previous chapters in this thesis evaluated optimum reconstruction parameters for ^{123}I SPECT quantification, with the outcomes summarised in Section 9.1. Chapter 12 demonstrated the use of these parameters for the objective assessment of patient data. However, a quantitative assessment is typically used as an adjunct to aid visual reporting. Therefore, assessment of qualitative image quality is essential.

Two observer studies were performed to evaluate qualitative image quality: a phantom and a patient study. The phantom study mimicked oncology applications of ^{123}I SPECT. A torso phantom was used with the aim of assessing lesion detection and overall image quality using an acquisition typical of ^{123}I-mIBG clinical studies. The patient observer study assessed qualitative image quality of ^{123}I-DaTSCAN™ patient data and accuracy of diagnosis based on clinical follow-up.

Section 9.1 described a recommended correction scheme for data acquired with LEHR collimators and a scheme for data acquired with MELP collimators. In this Chaper, these two methodologies were compared with the local clinical protocol for acquisition and reconstruction of ^{123}I neurology studies, as recommended by the radiopharmaceutical manufacturer, and the method currently recommended in the literature for optimisation of ^{123}I-DaTSCAN™ relative quantification. Therefore, this Chapter will assess four imaging methodologies. These are:

- Data acquired with LEHR collimators and reconstructed with Filtered Back-projection (FBP) using filter parameters recommended by the radiopharmaceutical manufacturer (GE Healthcare) for ^{123}I neurology SPECT
- Data acquired with LEHR collimators and reconstructed with iterative reconstruction parameters recommended by Dickson [30] for optimisation of ^{123}I-DaTSCAN™ relative uptake quantification

- Data acquired with LEHR collimators and iteratively reconstructed with the Collimator and Detector Response Modelling (CDRM) correction scheme, which was recommended in Section 9.1 for LEHR data
- Data acquired with MELP collimators and iteratively reconstructed with the Object Only Scatter Correction (OOSC), which was recommended in Section 9.1 for MELP data

MELP collimators are not used to acquire ^{123}I-DaTSCAN™ patient studies. Therefore, only the three reconstruction schemes for LEHR data were included in the patient study.

The aim of the observer studies was to assess qualitative image quality in the clinical setting of advanced reconstruction protocols for ^{123}I SPECT. This Chapter is divided into two Sections, one for each observer study.

13.2 Torso Phantom Observer Study

13.2.1 Method and Materials

13.2.1.1 Torso Phantom Preparation and Acquisition

The torso phantom, detailed in Section 6.2.1, was used for an observer assessment of lesion detection and image quality. As the torso phantom is used routinely for PET quality control, experienced observers are familiar with the typical position and orientation of the six spheres in the phantom. Therefore, a phantom insert was developed which replaced the standard lung insert and allowed random sphere placement within the phantom (Figure 13.1). The six spheres can be placed at any of 22 possible locations in the phantom background.

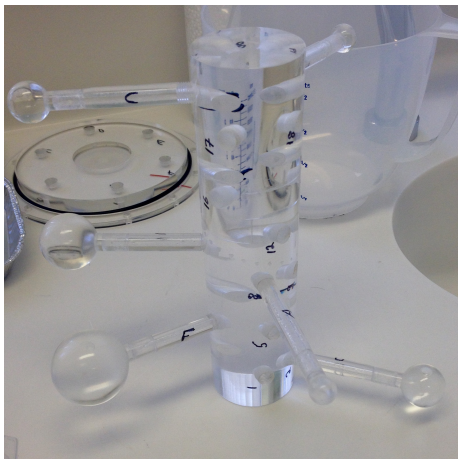

Figure 13.1: Custom central insert from the torso phantom
The insert was custom made to include 22 possible locations for the six spheres of the torso phantom. The site of spheres for each of three acquisitions was determined using a random number generator.

Sphere placement within the phantom was determined by the random allocation of spheres labelled A-F (largest to smallest) with positions 1-22. Sphere placement was randomised for three acquisitions. For each acquisition, the phantom was prepared with ~60MBq ^{123}I, typical of that used in the same phantom in Chapters 6-8. Clinical ^{123}I-mIBG studies have a broad range of uptake ratios up to 10:1 [178]. Therefore, for this phantom study, a sphere to background concentration ratio of 4:1 was chosen in order to provide a suitable challenge for observers.

The torso phantom was acquired with 57k and 35k in the first projection angle for LEHR and MELP data respectively. These values were chosen based on the count density of 20 consecutive ^{123}I-mIBG patients, as described in Section 6.2.2.

Data were acquired with the parameters shown in Table 13.1, including a sequential CT which was acquired for attenuation and Monte Carlo scatter correction.

Parameter	LEHR	MELP
Projections	128	
Zoom	1.45	
Pixel Size	3.3mm	
Projections	128	
Counts in the First Projection	57k	35k
Radius of Rotation (mean / min / max)	~19cm / ~13cm / ~26cm	
Orbit	Contoured	
Photopeak	159keV±10%	
Scatter Windows	Lower: 138±4keV Upper: 178±4keV	
CT mA	35mA	
CT kVp	130kVp	
CT Reconstruction Slice Width	3.3mm	

Table 13.1: Parameters for SPECT acquisition of the torso phantom

13.2.1.2 Phantom Reconstruction and Assessment

Each of the three acquisitions was reconstructed using four correction schemes, which resulted in 12 volumes for observer assessment. The reconstruction parameters are shown in Table 13.2.

Parameter	GE Parameters for Neurology	Dickson's Recommended Parameters	LEHR Data Recommended Parameters	MELP Data Recommended Parameters
Collimator	LEHR			MELP
Recon Method	FBP	Iterative (OSEM)		
Recon Filter	10th Order, 0.85cm^{-1} cutoff	—		
Iterations	—	96 iterations (6 iterations, 16 subsets)		
Resolution Recovery	—	Depth Dependent		
Attenuation Correction	—	CT		
Scatter Correction	—	TEW	CDRM	OOSC
Post Filter	—	Gaussian, 7mm FWHM		
Scheme Name	FBP(L)	TEW(L)	CDRM(L)	OOSC(M)

Table 13.2: Parameters for reconstruction of each torso phantom acquisition into four datasets

The recommended parameters by Dickson [30] relate to the optimisation of relative quantification of ^{123}I-DaTSCAN™ studies. The parameters for LEHR and MELP data were recommended based on quantitative image quality measures as summarised in Section 9.2 of this thesis.

Four experienced observers participated in the study. The 12 reconstructions were randomly ordered and divided into viewing sessions such that the same sphere setup did not appear twice in the same batch. Observers viewed three data sets in four sessions. The data sets were anonymised as to which imaging methodology was being viewed. Viewing sessions were at least two weeks apart to reduce familiarity. Observers could scroll through data sets in all three planes.

Observers were asked to triangulate the location of detected spheres using a transverse, coronal and sagittal coordinate system. The estimate of sphere location was compared with a true location as determined from a registered CT. Location of a sphere was deemed successful if all three coordinates were within ±3 pixels (9.9mm) of the actual location in all planes. This tolerance allows for misregistration of the CT and individual variances in the determination of the centre of spheres. False sphere localisations were also recorded.

Observer studies of CT phantoms in the literature suggest a larger radius of acceptance (up to 40mm) [217]. However, as the background of ^{123}I SPECT volumes is noisy relative to CT data, a large radius of acceptance may result in noise hotspots being accepted as

true sphere localisations. Each localisation was classified as a True Positive (TP) for successfully located spheres or False Positive (FP) for non-sphere localisation. Additionally, a confidence score from 0-100 on a continuous scale was recorded for each sphere localisation, with 100 being complete confidence. Observers were not informed how many spheres each volume contained.

Finally, participants were asked to rate overall image quality on an ordinal scale of 1 to 5 with 1 being very poor, 5 being excellent and 3 being neutral.

13.2.1.3 Statistical Analysis

Image Quality

The observers' ordinal image quality scores are non-parametric. Therefore, a Friedman test was used to assess any statistically significant difference between correction schemes based on paired image quality scores [173]. As described in Section 5.2.5, the Friedman test does not have a suitable post-hoc test for detailing significance between all pairs of data. Therefore, if significance was found using a Friedman test, an unpaired Kruskal-Wallis was performed followed by a post-hoc Dunn's test.

Lesion Detection: Receiver Operating Characteristic Curve Analysis

Receiver Operating Characteristic (ROC) curves are commonly used to compare imaging modalities [212, 218]. A ROC curve is a graphical method which demonstrates the performance of a binary operator system based on a variable threshold. With regard to medical imaging, the binary operator may be the diagnosis of normality or abnormality, or the detection of a lesion or not. The variable threshold can be an observer's confidence in classification. A typical ROC curve, shown in Figure 13.2b, has a True Positive Fraction (TPF) on the y-axis and (1-True Negative Fraction (TNF)) on the x-axis (also known as the False Positive Fraction (FPF)). The TPF is a measure of the sensitivity of a diagnostic test. The FPF is a measure of the specificity of a diagnostic test, where the lower the FPF, the more specific a test is deemed to be. The ROC curve takes on a square shape for a TPF of 1 and an FPF of 0. As TPF reduces and FPF increases the curve tends towards that shown in Figure 13.2b. A further reduction in TPF and increase in FPF results in a ROC curve that tends towards a line of unity (Figure 13.2c).

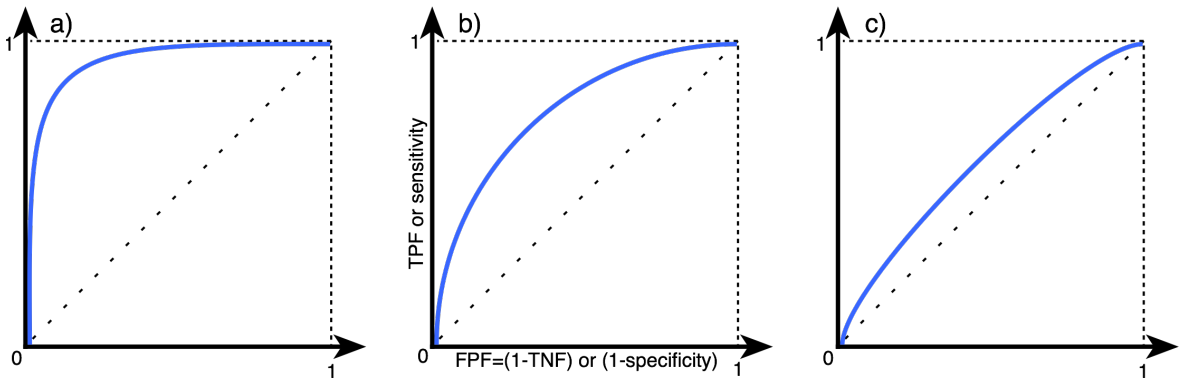

Figure 13.2: Example Receiver Operating Characteristics (ROC) curves Examples include a) an almost perfect diagnostic test, b) a typical ROC curve appearance, and c) a poor diagnostic test

A typical Figure of Merit (FOM) for comparing methods is the Area Under the Curve (AUC). In Figure 13.2a the 'best case scenario' curve will have an AUC of ≈1 meaning almost perfect differentiation between normal and abnormal studies. The 'worst case scenario' (Figure 13.2c) will have an AUC of ~0.5, which indicates a poor diagnostic test with completely random determination between normal and abnormal.

Variations on ROC Analysis

ROC curves are useful for analysis of scenarios where the outcome is known, binary and the observer's confidence in the decision is recorded. However, medical imaging has a wide variety of determination tasks, such as normal/abnormal or detected/not detected. Therefore, variations on ROC analysis have been designed to suit experimental setup. A useful differentiator between methods of ROC analysis is shown in Figure 13.3 [218].

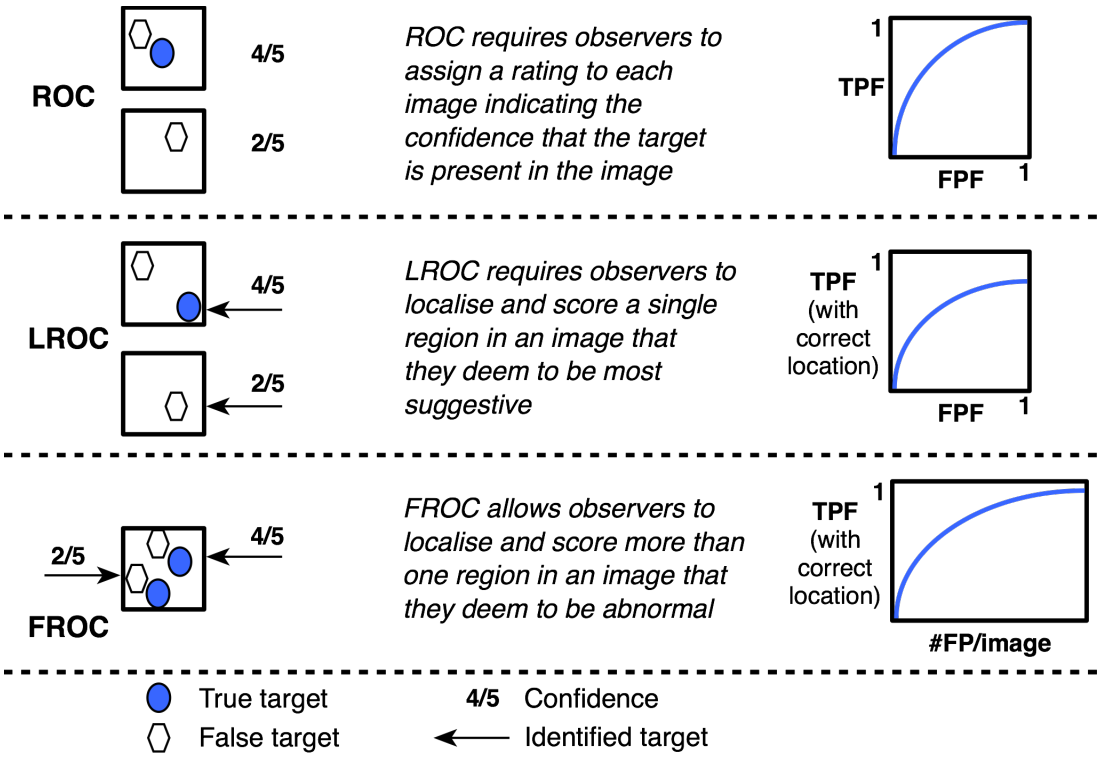

Figure 13.3: Common methods of ROC analysis, the use of which depends on the particular experimental method
Methods shown include Receiver Operating Characteristics (ROC) (top), Localisation ROC (LROC) (middle) and Free-response ROC (FROC) (bottom)

The experimental design in this Section features multiple observers (4) assessing multiple phantom acquisitions (3), each with multiple spheres (6) in variable locations. This method of observer assessment, in which each observer may indicate multiple true and false localisations with an associated confidence level, can be evaluated using a Free-response ROC (FROC) analysis [218-220].

The y-axis of an FROC curve is the Lesion Location Fraction (LLF) which is analogous to the TPF in standard ROC analysis. The x-axis of an FROC curve is the False Localisation Rate (FLR) which is analogous to FPF. The FLR is the number of False Localisations (FL) per image. The x-axis is, therefore, not bound by 0-1, as standard ROC analysis is. The AUC is unreliable for FROC curves as a perfect observer's curve would be a vertical line extending from (0,0) to (0,1), for which the AUC would be zero. Therefore, it is not recommended to use the AUC for FROC analysis [220, 221].

However, an Alternative FROC (AFROC) curve can be analysed to determine an AUC. AFROC curves plot the LLF versus the FPF where the uppermost point is connected to (1,1) by a dotted line and provides a valid AUC for comparison of methods. As AFROC curves are forced to a maximum at (1,1) via an interpolated dotted line, they are often not intuitive for reader interpretation [221]. Therefore, in this investigation, results are

presented visually using FROC curves and the AUC were determined using AFROC curves.

RStudio version 1.0.136 (RStudio, Inc), a graphical user interface running R version 3.3.1 (The R Foundation for Statistical Computing) was used for the analysis and display of ROC data. More specifically, an open source R package called “RJafroc” [222] was used, which is distributed by Chakraborty, a leading author on AFROC analysis [219-221, 223-225].

13.2.2 Results of the Torso Phantom Study

13.2.2.1 Torso Phantom Results: Overall Image Quality

Observers were asked to rate image quality on an ordinal scale. A mean value for these image quality scores would translate discrete data to a continuous scale. This approach is not recommended by Keeble [212] in a review of medical imaging statistical tests. A mean score of 3.5, for example, can confuse interpretation of fixed levels. Therefore, in this Section, image quality scores are presented in a bubble chart. A bubble chart maintains the ordinal nature of the data.

Figure 13.4 shows the image quality score for each imaging methodology, with 1 indicating very poor quality and 5 indicating excellent quality. The size of each bubble is relative to the number of instances of the image quality score. The number of instances is also detailed within each bubble.

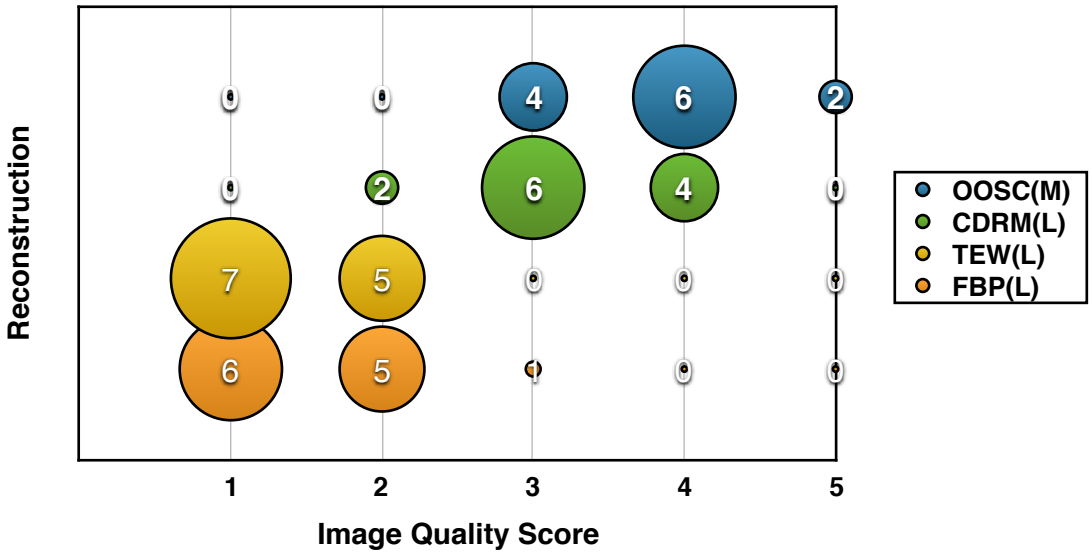

Figure 13.4: Bubble chart of image quality scores for four ^{123}I SPECT imaging methodologies

An image quality score of 1 indicates very poor quality, 3 is a neutral response and 5 indicates excellent image quality

66.7% of the OOSC(M) images were considered to have better than neutral image quality (4 or 5). This proportion compares with 33.3% for the CDRM(L) images and 0% for both the TEW(L) and FBP(L) images.

There was not a statistically significant difference between the OOSC(M) and the CDRM(L) image quality scores (p=0.124). Similarly, there was no statistically significant difference between the FBP(L) and the TEW(L) scores (p=0.359). There was a statistically significant difference between all other comparisons (p<0.05).

13.2.2.2 Torso Phantom Results: Lesion Detection Performance

The FROC curve for each of the four imaging methodologies, averaged from all four observers, is shown in Figure 13.5.

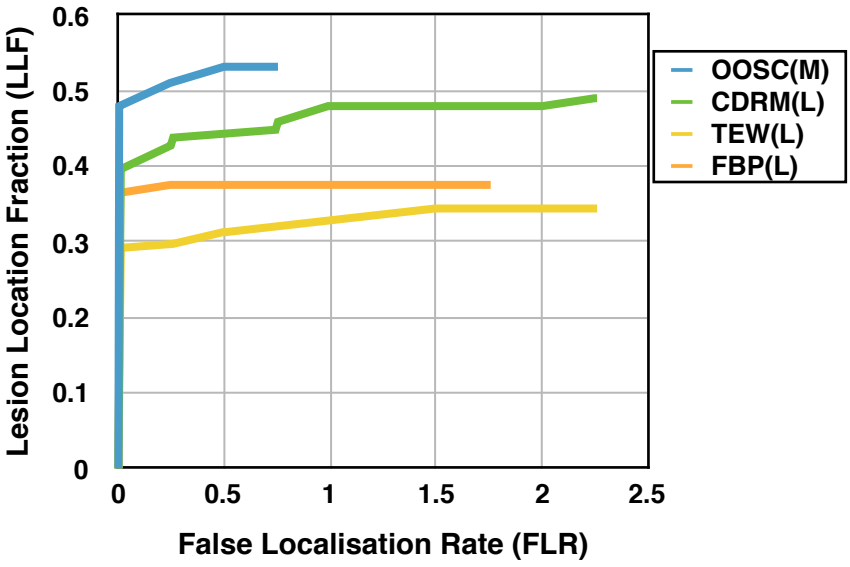

Figure 13.5: Free-response Receiver Operating Characteristic (FROC) curves for lesion detection task

The curves demonstrate that the OOSC(M) images had the highest Lesion Location Fraction (LLF) and the lowest False Localisation Rate (FLR) of the four methods. The CDRM(L) methodology had the highest LLF of the data acquired with LEHR collimators. However, the CDRM(L) had a higher FLR than the FBP(L) methodology. The square appearance of the FBP(L) curve indicates that all observers detected the same number of lesions and missed the same number of lesions in all studies. The TEW(L) methodology has a lower LLF and higher FLR than the FBP(L) reconstruction.

The Area Under the Curve (AUC), determined using an AFROC analysis from combined observer data, are shown in Table 13.3:

Method	AUC
OOSC(M)	0.686
CDRM(L)	0.583
TEW(L)	0.509
FBP(L)	0.549

Table 13.3: Area Under the Curve (AUC) Figure of Merit (FOM) for four reconstruction methods using AFROC analysis

The OOSC(M) method has the largest AUC, which suggests a better imaging test. However, there is no statistically significant difference between the OOSC(M) method and the CDRM(L) method (p=0.098). The AUC for the TEW(L) method (0.509) is close to 0.5, which indicates a poor diagnostic test. There is a statistically significant difference between the OOSC(M) and both the FBP(L) (p=0.028) and TEW(L) (p=0.004) methods. All other comparisons have no statistical significance.

13.2.3 Torso Phantom Study: Discussion

The count density in this investigation was typical of an ^{123}I-mIBG oncology study acquired 24 hours post injection of the radiopharmaceutical. This count density is relatively low when compared with other clinical ^{123}I SPECT studies, such as thyroid and cardiac imaging. Therefore, the results of this investigation are only applicable to an ^{123}I-mIBG oncology imaging situation.

The OOSC(M) imaging method, had the highest ROC Area Under the Curve (AUC). This result indicates that using MELP collimators is the superior imaging method for ^{123}I oncology SPECT. Gregory [226] describes the same finding in relation to ^{123}I-mIBG planar imaging.

It is interesting to note that the smallest sphere in the phantom was only detected in an OOSC(M) image (albeit by a single observer with a confidence score of 5 out of a possible 100) (Figure 13.6).

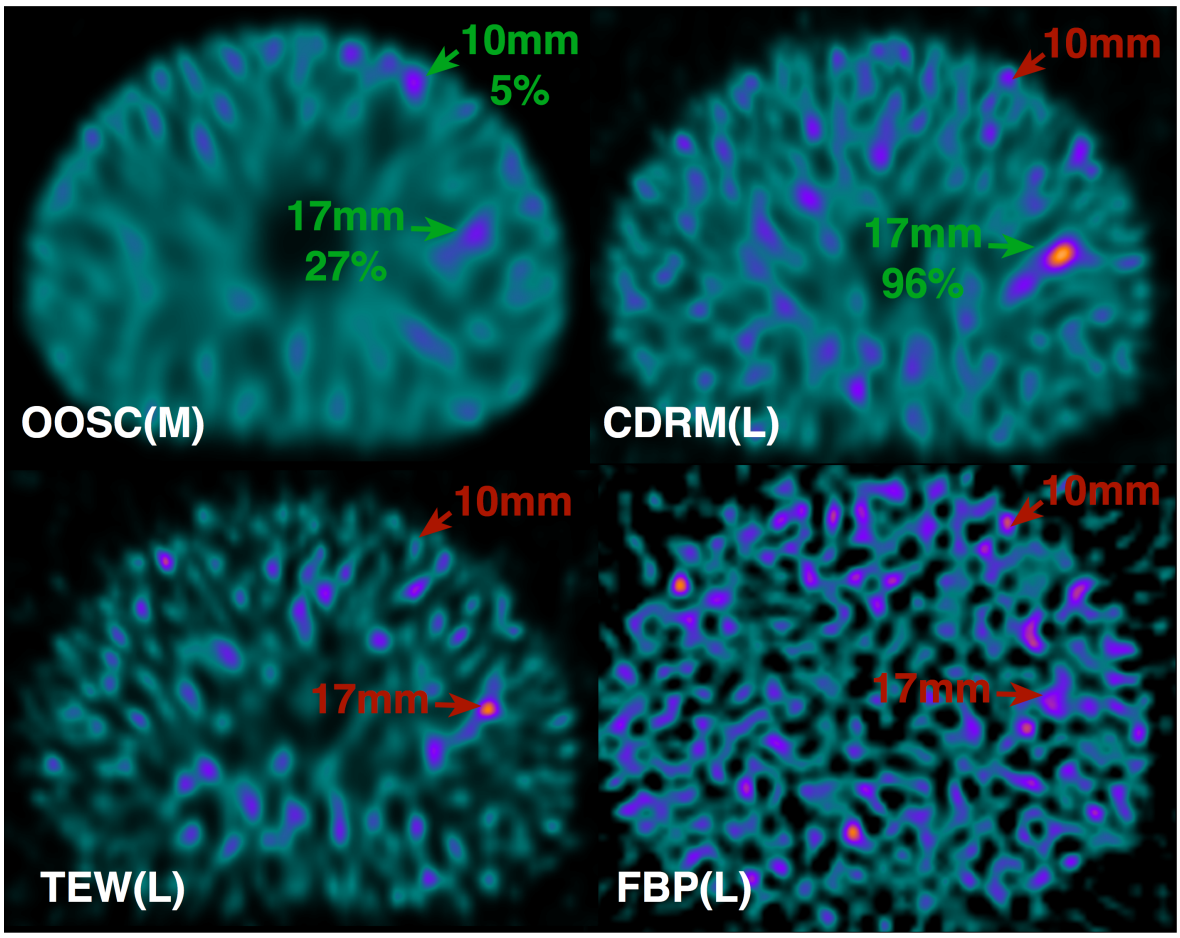

Figure 13.6: The 10mm sphere was detected by one observer on the OOSC(M) reconstruction (top left)
Green text indicates those spheres that were detected. The percentage indicates the mean confidence of those observers that detected the sphere. Red text indicates spheres that were not detected by any observer.

The detection of the 10mm sphere using the OOSC(M) method is despite the MELP collimator having poorer spatial resolution relative to the LEHR collimator. This finding may be explained by the low count density of the acquisitions in combination with the lower scatter fraction of MELP collimators compared to LEHR collimators (as shown in Section 3.4.2).

The TEW(L) imaging methodology had the lowest ROC AUC which indicates a poor diagnostic test. The relatively low count density may account for the comparatively poor performance of the TEW technique. Section 7.3.3 demonstrated higher noise level in TEW corrected images compared to CDRM reconstructions. Significant noise in background regions may be interpreted by an observer as being a lesion, which increases the False Localisation Rate (FLR). An example of a false localisation from a TEW(L) image is compared with the same slice of an OOSC(M) image in Figure 13.7.

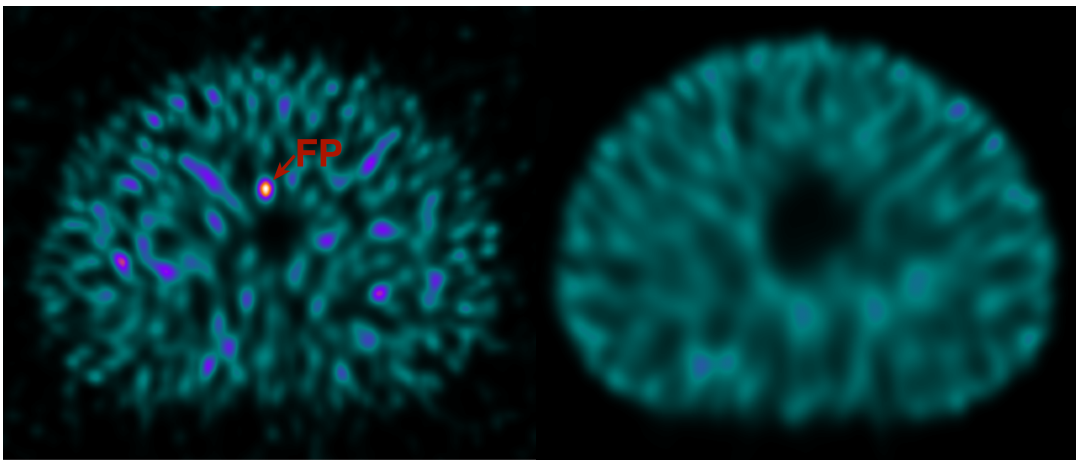

Figure 13.7: A False Localisation (FL) identified by two observers on the TEW(L) image (left), not present on the OOSC(M) image (right)

For data acquired with LEHR collimators, the CDRM(L) correction scheme had the highest image quality. This outcome confirms the conclusions of the practical investigations of quantitative image quality metrics in Chapters 4-8. However, the 10mm was not detected by any observer. An example which demonstrates the 10mm sphere relative to noise in a CDRM(L) image is shown in Figure 13.8.

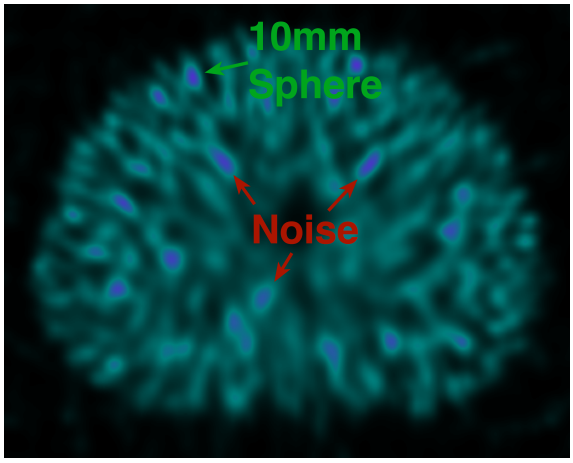

Figure 13.8: Transverse slice of CDRM(L) image which demonstrates the 10mm sphere relative to noise

Previous work on spatial resolution (Section 5.3.2.4), noise (Section 7.3.2) and absolute quantification (Section 11.3.3.1) demonstrated a dependence on location due to varying rates of convergence across the Field of View (FOV). This location dependence was further demonstrated by observer confidence in sphere detection. An example is shown in Figure 13.9 where the 22mm sphere, in the posterior aspect of the phantom, had a lower average confidence score (71.7%) than the smaller 13mm (93.8%) and 17mm (100%) spheres in the anterior aspect of the phantom.

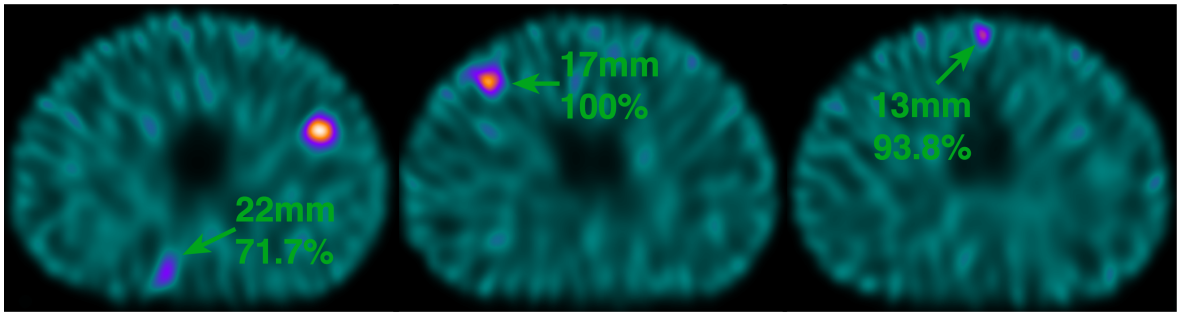

Figure 13.9: Example of the 22mm sphere detected in the posterior aspect of the torso phantom with lower mean confidence than the 17mm and 13mm sphere in the anterior aspect

The spatial resolution analysis in Section 5.3.2.4 described elongation of sources further from the centre of the FOV. This appearance of elongation was also demonstrated for spheres in the torso phantom. An example is shown in Figure 13.10.

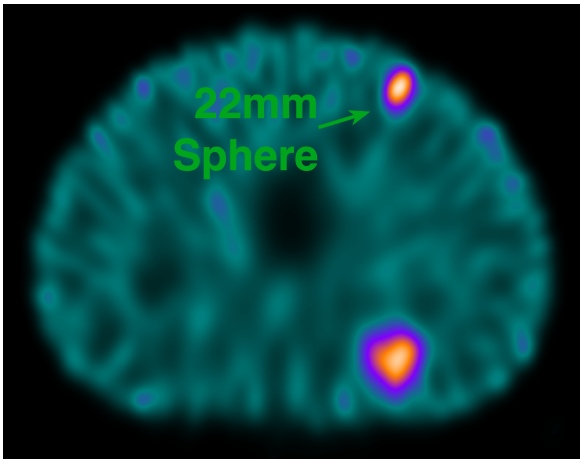

Figure 13.10: Elongation of the 22mm sphere in an MELP reconstruction

Knoll [106] also demonstrated this elongation of spherical ^{99m}Tc sources in the torso phantom, reconstructed with depth-dependent RR. Again, this appearance is the result of varying rates of convergence, as demonstrated by Kappadath [175] and the spatial resolution results in Section 5.3.2.4.

Conclusions based on the torso phantom study will be summarised in Section 13.4, in combination with findings from the patient observer study.

13.3 ^{123}I-DaTSCAN™ Patient Observer Study

A patient observer study was performed to assess the clinical validity of reconstruction parameters optimised for ^{123}I SPECT quantification. Optimised parameters were evaluated against best practice recommendations in the literature and the local clinical protocol, which was approved by the radiopharmaceutical supplier (GE Healthcare) for clinical use during site setup.

13.3.1 Methods

13.3.1.1 Patient Selection

^{123}I-DaTSCAN™ studies were chosen for the patient observer study due to their greater availability locally compared with other ^{123}I imaging studies. 101 patient studies were acquired in the calendar year from the start of June 2015 to the end of May 2016. Of these, 50 patients had combined SPECT and CT studies and the required demographics recorded to allow reconstruction in units of g/ml for display with an absolute colour scale. Requirements are the:

- Height and weight of the patient
- Activity in the syringe before administration
- Time of injection
- Residual activity in the syringe following administration, and
- Time of activity measurements, including measurement of residual activity

13.3.1.2 Acquisition of Patient Data

SPECT-CT patient studies were acquired using a Siemens Symbia T2 and the parameters shown in Table 13.4.

Parameter	Value
Collimators	LEHR
Time per Projection	30s
Projections	128
Photopeak	159kev±10%
Scatter Windows	Lower: 138±4keV Upper: 178±4keV
Matrix	128x128
Zoom	1.45
Pixel Size	3.3mm
Orbit	Circular
Radius of Rotation	14-19cm
CT mA	35mA
CT kVp	130kVp
CT Reconstruction Slice Width	3.3mm

Table 13.4: Acquisition parameters for the ^{123}I-DaTSCAN™ patient study

The Radius of Rotation (ROR) for patient studies is dependent on patient compliance, anatomy and symptoms. The mean, minimum and maximum RORs for the 50 patient acquisitions were 15cm, 14cm and 19cm respectively.

13.3.1.3 Reconstruction and Display of Patient Data

Patient data were reconstructed using the three methods detailed in Table 13.5:

	GE Approved Parameters for ^{123}I-DaTSCAN	Dickson's Recommended Parameters	LEHR Recommended Parameters
Algorithm	FBP	Iterative (OSEM)	
Reconstruction Filter	10th Order, 0.85cm^{-1} cutoff	—	
Iterations	—	96 (6 iterations, 16 subsets)	
Resolution Recovery	—	Depth Dependent	
Attenuation Correction	—	CT AC	
Scatter Correction	—	TEW	CDRM
Postfilter	—	Gaussian 7mm	
Calibration Factor	—	—	0.84
Scheme Name	FBP(L)	TEW(L)	CDRM(L)

Table 13.5: Reconstruction parameters for the ^{123}I-DaTSCAN™ patient study
The recommended parameters by Dickson [30] relate to the optimisation of relative quantification of ^{123}I-DaTSCAN™ studies. The parameters for LEHR data were recommended based on quantitative image quality measures as summarised in Section 9.1 of this thesis.

After reconstruction, the same reorientation was applied to all three reconstructions for each patient study such that transverse slices were in the same plane. The axial thickness of each reconstructed slice was 3.3mm.

Image prints of the reconstructed data were generated which displayed transverse slices in a 4x3 grid. The four transverse slices with the highest uptake were arranged across the middle of the grid, and a display zoom of 143% applied to match current clinical practice. All three methods of reconstruction were displayed using the same colour table. An example of the data presented is shown in Figure 13.11.

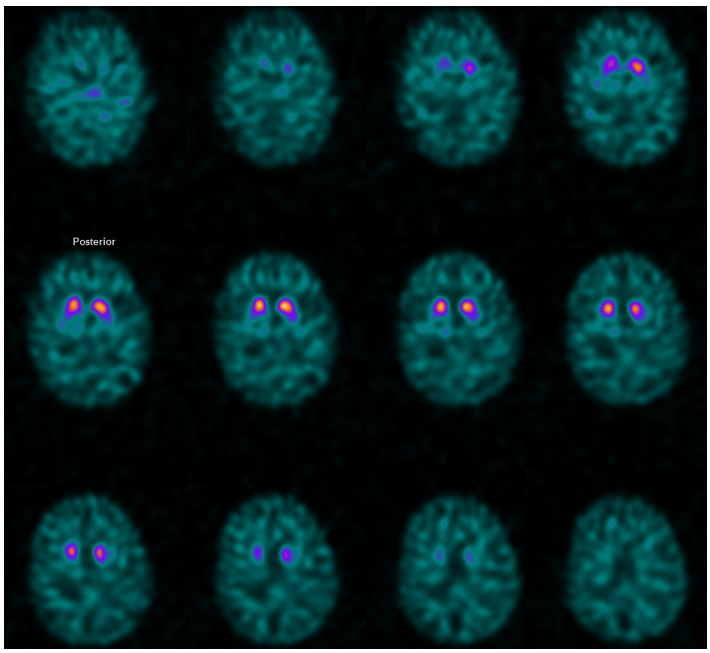

Figure 13.11: Example of a 4x3 print of an ^{123}I-DaTSCAN™ study used in the patient observer study

The FBP(L) and OOSC(L) reconstructions were displayed using relative scaling to the maximum pixel value for each patient study. The CDRM(L) reconstructions were displayed with an absolute scale normalised to a colour table with an upper threshold of 12.8g/ml, as determined in Section 12.3.2.1.

13.3.1.4 Observer Analysis

Two observers assessed the patient images. Due to the observers' previous experience in reporting ^{123}I-DaTSCAN™ clinical studies, no training cases were made available before the study. The observers evaluated the image prints of 50 patient studies, each reconstructed with the three schemes described in Table 13.5 (150 image prints in total). One observer evaluated the data set twice to assess intra-observer variability.

Patient Study Image Quality

Observers were asked to rate overall image quality on an ordinal scale of 1 to 5 with 1 being very poor, 5 being excellent and 3 being neutral.

Diagnosis of Patient Studies

Observers were asked to indicate whether they perceived the images to be normal or abnormal. They also rated their confidence in diagnosis on a continuous scale from 0-100 with 100 indicating complete confidence in their diagnosis. ^{123}I-DaTSCAN™ studies with either normal or abnormal appearance can be divided into subgroups. Observers were not asked for this additional differentiation as it can often require clinical history and

consultation with alternative modalities. Therefore, further differentiation was not appropriate for this study which focussed on quality of ^{123}I-DaTSCAN™ images alone. Examples of normal and abnormal ^{123}I-DaTSCAN™ studies are shown in Figure 13.12.

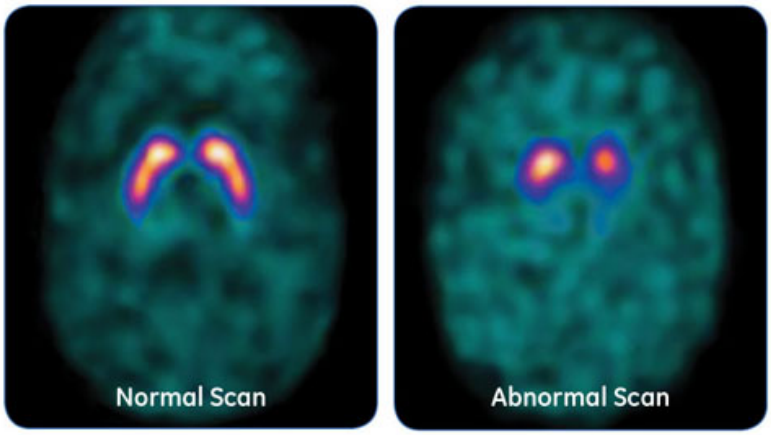

Figure 13.12: An example of a normal (left) and an abnormal (right) ^{123}I-DaTSCAN™ patient study [124]

Participants were also asked for any additional comments regarding image quality or diagnosis.

Statistical Analysis of Patient Observer Study

Similar to the approach described in Section 13.2.1.3, a Friedman test was used to determine statistical difference between image quality ratings of the reconstruction methods. Again, a Kruskal-Wallis followed by a post-hoc Dunn's test was used when the Friedman test indicated significance. The same method of analysis was used for comparing observers' confidence score between reconstruction methods.

A Kappa coefficient is a statistical measure which can be used to assess agreement between observers [227]. A Kappa analysis was used to compare inter and intra-observer agreement of image quality. The Kappa coefficient is measured on a scale of 0 to 1 where 1 is perfect agreement, and 0 is what would be expected due to chance. Kappa coefficients were determined and cross-referenced using two online Kappa calculators: GraphPad [213] and VasserStats [214]. The coefficient was categorised according to Table 13.6.

Kappa	Agreement
< 0	Less than chance
0.01-0.20	Slight
0.12-0.40	Fair
0.41-0.60	Moderate
0.61-0.80	Substantial
0.81-0.99	Almost perfect

Table 13.6: Categorised interpretation of Kappa coefficients [227]

Furthermore, Kappa analysis was used to assess inter and intra-observer agreement for the diagnosis of normal or abnormal for each reconstruction method.

Of the 50 patient studies examined, 36 studies had sufficient clinical follow-up to assess the accuracy of diagnosis. The categorisation of these patient studies as normal or abnormal, based on follow-up, is described in Section 12.2.1.1. From this categorisation, the sensitivity, specificity and diagnostic accuracy were determined for each reconstruction method for both observers. Sensitivity indicates the proportion of True Positives (TP) identified. Specificity indicates the proportion of True Negatives (TN) identified. Diagnostic accuracy indicates the proportion of correctly determined TP and TN in the total population. Sensitivity, specificity and diagnostic accuracy were determined using Equations 12.2, 12.3 and 12.4 respectively.

13.3.2 ^{123}I-DaTSCAN™ Patient Observer Study Results

13.3.2.1 Patient Study Results: Overall Image Quality

As with the phantom observer study, a bubble chart has been used to display image quality scores. The scores for each reconstruction method are shown in Figure 13.13.

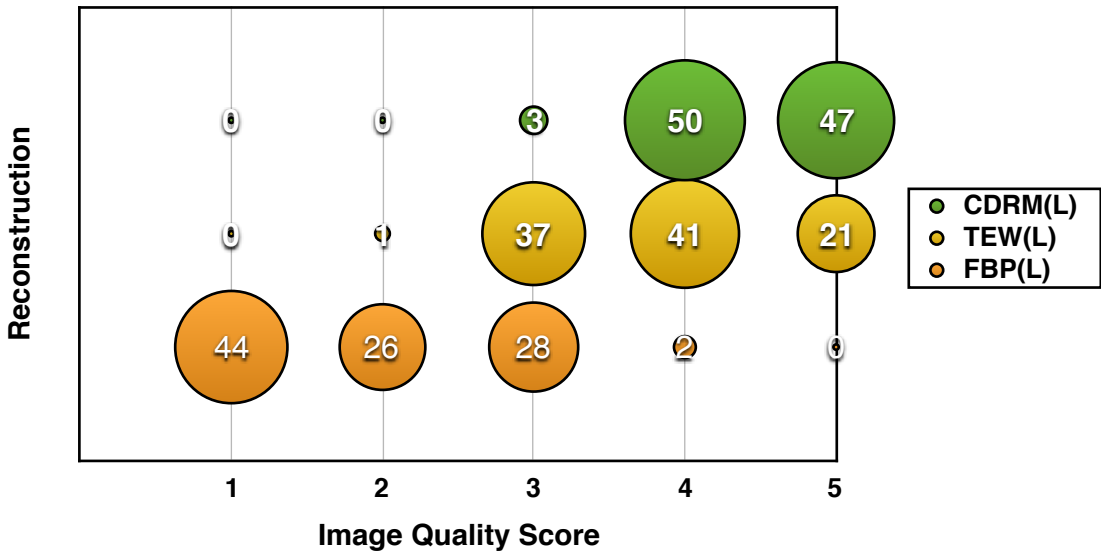

Figure 13.13: Image quality scores for three imaging methodologies of ^{123}I-DaTSCAN™ patient studies
An image quality score of 1 indicates very poor quality, 3 is a neutral response and 5 indicates excellent image quality

Image quality scores for the ^{123}I-DaTSCAN™ patient observer study show that 97% of CDRM(L) images were rated as better than neutral (4 or 5). This compares with 62% for the TEW(L) method of reconstruction and 2% for the FBP(L) reconstruction. There is a statistically significant difference in image quality score between all individual comparisons between the three methods of reconstruction (all p-values <0.01).

The Kappa coefficient for inter-observer agreement of image quality was 0.364 which is considered “fair” according to Table 13.6. The calculation of Kappa was linear weighted which accounts for how far apart observations are. The reason the level of agreement between observers is not stronger than “fair” can be explained by one observer grading image quality higher relative to the other. This disparity in personal opinion can be seen when comparing each observer’s median value for each reconstruction method (Table 13.7).

Reconstruction	Observer 1	Observer 2
CDRM(L)	5	4
TEW(L)	4	3
FBP(L)	3	1

Table 13.7: Median image quality score for observers

The Kappa coefficient for intra-observer agreement of image quality was 0.754 which is considered “substantial” according to Table 13.6.

13.3.2.2 Confidence in Diagnosis

Figure 13.14 demonstrates that the CDRM(L) reconstruction had the highest observer confidence in the diagnosis.

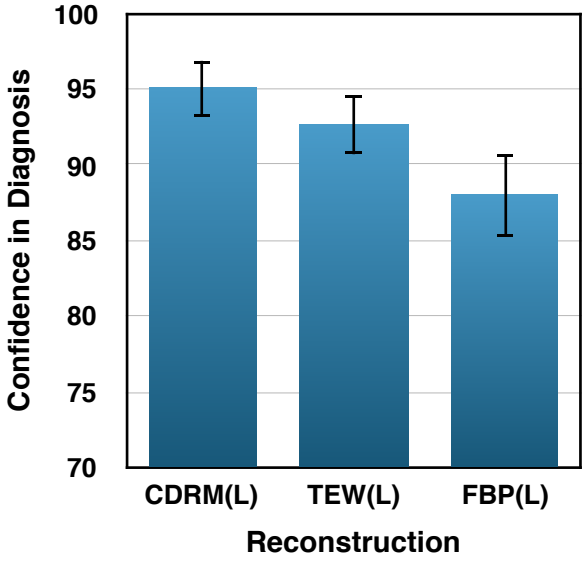

Figure 13.14: Observers' confidence in diagnosis of ^{123}I-DaTSCAN™ patient studies

Although the error bars in the Figure 13.14 overlap, there is a statistically significant difference between the reconstruction methods (Table 13.8) as confidence scores are paired.

	CDRM(L)	FBP(L)
FBP(L)	<0.001	—
TEW(L)	0.004	0.017

Table 13.8: p-values from a test for statistically significant differences in confidence of diagnosis

13.3.2.3 Inter and Intra-Observer Agreement of Diagnosis

The two observers disagreed on the diagnosis in only 4% of cases when viewing CDRM(L) images. This proportion compares with 10% and 18% of cases for the TEW(L) and FBP(L) reconstructions respectively. Although categorisation of Kappa coefficient demonstrates substantial agreement between observers for the TEW(L) and FBP(L) reconstructions, the CDRM(L) reconstruction demonstrated almost perfect agreement. This information is summarised in Table 13.9.

	Cases in Disagreement	Kappa	Kappa CI	Level of Agreement
CDRM(L)	4%	0.913	0.796 to 1.000	Almost perfect
TEW(L)	10%	0.675	0.412 to 0.939	Substantial
FBP(L)	18%	0.640	0.441 to 0.839	Substantial

Table 13.9: Inter-observer agreement on diagnosis of ^{123}I-DaTSCAN™ studies

Intra-observer agreement on diagnosis was considered "substantial" by Kappa analysis for all three methods of reconstruction (Table 13.10).

	Kappa	Kappa CI	Level of Agreement
CDRM(L)	0.745	0.555 to 0.936	Substantial
TEW(L)	0.729	0.478 to 0.980	Substantial
FBP(L)	0.760	0.580 to 0.940	Substantial

Table 13.10: Intra-observer agreement on diagnosis of ^{123}I-DaTSCAN™ studies

13.3.2.4 Diagnostic Performance of Observers

Table 13.11 shows the sensitivity, specificity and diagnostic accuracy for observers' diagnosis of normal or abnormal for 36 patient studies based on one-year clinical follow-up.

		CDRM(L)	TEW(L)	FBP(L)
Sensitivity	**Observer 1**	95.7%	100%	100%
	Observer 2	95.7%	95.7%	78.3%
Specificity	**Observer 1**	92.3%	61.5%	76.9%
	Observer 2	92.3%	53.8%	92.3%
Diagnostic Accuracy	**Observer 1**	94.4%	86.1%	91.7%
	Observer 2	94.4%	80.6%	83.3%

Table 13.11: Sensitivity, specificity and diagnostic accuracy for both observers' diagnoses versus one-year clinical follow-up

The sensitivity of all three methods was comparable, aside from Observer 2's poorer sensitivity with FBP(L). The sensitivity results indicate that all reconstruction methods evaluated are good at the discrimination of true abnormal patients. However, the TEW(L) and FBP(L) reconstructions have a relatively poorer specificity than the CDRM(L) reconstruction, which suggests these methods are poorer for discrimination of true normal patients. Consequently, the diagnostic accuracy was higher for the CDRM(L) reconstruction for both observers compared to the TEW(L) and FBP(L) reconstructions.

Both observers' sensitivity, specificity and diagnostic accuracy results match for the CDRM(L) reconstruction. This finding supports the almost perfect inter-observer agreement found with Kappa coefficient analysis.

13.3.3 Patient Observer Study Discussion

The CDRM(L) method of reconstruction, displayed on an absolute scale, provided the best image quality for ^{123}I-DaTSCAN™ studies, with a statistically significant difference over the alternative methods of reconstruction which were displayed using a relative scale. Observers' confidence in diagnosis was also highest for CDRM(L) reconstructions, again with a statistically significant difference.

Patients who present with Parkinsonian Syndrome symptoms and are referred for an ^{123}I-DaTSCAN™ study typically have a reduction in nigrostriatal nerve terminals of 50% or more [26, 117]. Therefore, it would be anticipated that this proportion of deficit would result in high observer agreement between abnormal and normal cases. However, a review of 5 multi-centre ^{123}I-DaTSCAN™ clinical trials by Seibyl [228] reported that Kappa coefficient can vary from 0.59 to 1.00. This finding by Seibyl indicates that the differentiation of normal or abnormal is not as binary as the extent of nigrostriatal reduction would suggest.

In the current study, the CDRM(L) reconstruction and display method demonstrated an inter-observer variability resulting in an almost perfect level of agreement (0.913). This result was in contrast with the Kappa coefficient between observers for the FBP(L) (0.640) and TEW(L) (0.675) reconstructions, which indicated substantial agreement. However, the level of substantial agreement is in consensus with that found by Kahraman [229], who determined a Kappa coefficient of 0.70-0.74 for three observers assessing 195 patients. Soderlund [230] found a similar level of agreement with a Kappa coefficient of 0.76-0.85 for visual evaluation of 54 patients using the TEW(L) method of reconstruction and display.

Observer interpretation will have been influenced by both the method of reconstruction and the display of CDRM(L) images using a normalised colour table. Figure 13.15 shows two patient examples where observers disagreed with each other on diagnosis based on the TEW(L) reconstruction and display but agreed with each other based on the CDRM(L) reconstruction and display.

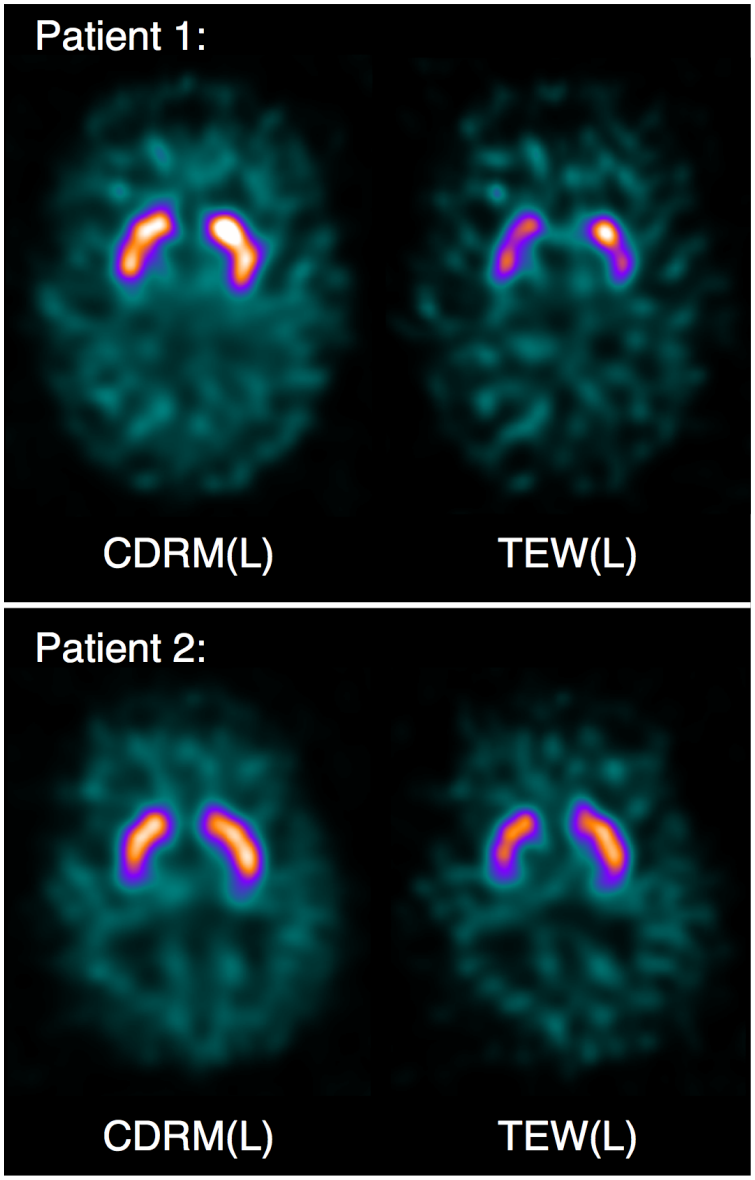

Figure 13.15: Two examples of patient studies where observers agreed on diagnosis based on the CDRM(L) reconstruction but disagreed based on the TEW(L) reconstruction

The image quality of the FBP(L) reconstructions was considered to be better than neutral in only 2% of the images. Additional comments by observers specifically noted “poor quality”, “noisy” or “horrible” images in 30% of the FBP(L) studies. No similar comments were noted for any studies reconstructed with TEW(L) or CDRM(L). This finding suggests that the image quality can be substantially improved compared with the method of reconstruction recommended by the radiopharmaceutical manufacturer.

The low count density torso phantom observer study demonstrated that the performance of the TEW(L) imaging method was poorer than the FBP(L). However, in the neurology patient observer study, which has a higher count density, the TEW(L) reconstruction had higher observer confidence, with a statistically significant difference, and a higher image quality score than the FBP(L) reconstruction. This finding suggests that the TEW scatter

correction method is not appropriate for low count data sets, due to further count subtraction, but may be more suited to higher count studies.

Definitive patient outcomes are difficult to determine due to the often slow progression of disease in the patient population under investigation. An ideal gold standard would be histopathology at autopsy to determine loss of nigrostriatal nerve terminals, as performed by Seibyl [207]. Such a study would require long term follow-up of patients imaged with SPECT-CT and is, therefore, outside the scope of this thesis. However, based on one-year clinical follow-up, the CDRM(L) reconstruction and display method demonstrated higher diagnostic accuracy than the TEW(L) and FBP(L) methods of reconstruction and display.

13.4 Conclusions

The phantom observer study has demonstrated that an MELP acquisition of low count density oncology studies is superior to LEHR acquisitions, even with CDRM reconstruction. Therefore, MELP collimators should be used for ^{123}I-mIBG studies acquired 24 hours post injection.

CDRM is the preferred option of reconstruction for low count density ^{123}I SPECT data acquired with LEHR collimators. Low count data should not have TEW scatter correction applied.

The neurology patient study has demonstrated that the CDRM(L) reconstruction and display method has superior image quality when compared with TEW(L) and FBP(L) reconstructions. The study also demonstrated an improvement in observer confidence in diagnosis and almost perfect inter-observer agreement on diagnosis. Therefore, the CDRM(L) method should be used for reconstruction and display of ^{123}I-DaTSCAN™ studies.

Where CDRM(L) is not available, TEW(L) reconstruction should be used for ^{123}I-DaTSCAN™ studies in preference to reconstruction parameters recommended by the radiopharmaceutical manufacturer (FBP(L)).

Chapter 14: Conclusions and Future Work

14.1 Introduction

The aim of this thesis was to investigate the optimisation and clinical application of advanced third party SPECT reconstruction algorithms with regard to the absolute quantification of ^{123}I.

To achieve this aim, the quality of images reconstructed with advanced correction schemes were quantitatively assessed to determine optimum reconstruction parameters. The evaluation demonstrated that Collimator and Detector Response Modelling (CDRM) greatly improved the accuracy of image quantification for data acquired with LEHR collimators. The quantitative accuracy of the images obtained from optimised CDRM reconstruction was demonstrated by activity concentration measurements in a striatal phantom study. Absolute quantification using the CDRM algorithm facilitated Standardised Uptake Value (SUV) measurements in ^{123}I-DaTSCAN patient studies, a novel development which could enhance clinical performance.

The current investigation is timely in light of the increasing interest in SUV measurements for clinical SPECT. Furthermore, there has been less focus on the absolute quantification of ^{123}I SPECT than, for example, ^{99m}Tc due to the more complex emission scheme of ^{123}I. Therefore, this thesis addresses a clear gap in knowledge with regard to the care required to establish accurate quantification in a number of routine clinical practices.

14.2 Original Contributions to ^{123}I SPECT Quantification

The work in this thesis has demonstrated the substantial groundwork necessary to determine the optimum parameters which are required to facilitate accurate quantification of ^{123}I. In the optimisation of reconstruction parameters, novel methods for the quantification of image quality were also presented. One such novel approach was the evaluation of perturbation methods for the assessment of clinical SPECT spatial resolution

in Chapter 5. A simple perturbation method was shown to be a useful method for the estimation of SPECT spatial resolution when using iterative reconstruction.

The spatial resolution investigation was used to determine if data acquired with MELP collimators were appropriate for ^{123}I neurology studies when using advanced reconstruction correction schemes. The evaluation demonstrated that data acquired with MELP collimators and reconstructed with depth-dependent Resolution Recovery (RR) was not sufficient for neurology studies. The optimal FWHM of the MELP reconstruction was inferior to the optimal LEHR reconstruction with both a statistical and clinically significant difference.

Although discounted for neurology studies, for further image quality measures MELP data reconstructed with the Object Only Scatter Correction (OOSC) algorithm presented the optimum performance of all correction schemes examined. More specifically, this scheme demonstrated higher contrast recovery, greater spatial uniformity, less noise and superior scatter suppression than alternative methods.

For the same four metrics, LEHR data reconstructed with the CDRM correction scheme exhibited superior performance compared with alternative LEHR correction schemes. The results from the quantification of phantom data in Chapters 4-8 were summarised in Chapter 9 with the optimised parameters shown in Table 14.1.

	Collimator	
	LEHR	**MELP**
Iterations	96 (6 iterations, 16 subsets)	
Resolution Recovery	Yes	
Attenuation Correction	CT	
Scatter Correction	CDRM*	OOSC
Reconstruction Time	~6min 30sec	~2min 11sec

Table 14.1: Recommended reconstruction parameters for ^{123}I SPECT
(*) TEW to be used where CDRM is unavailable

The CDRM correction scheme was the most accurate method of ^{123}I SPECT reconstruction for absolute quantification of neurology data acquired with LEHR collimators. A striatal phantom study demonstrated an accuracy in activity concentration measurements of within ±10% of true concentration. This finding could have a substantial impact on clinical neurology applications. Absolute quantification of data reconstructed with CDRM is, therefore, recommended in these clinical scenarios.

The CDRM correction scheme was subsequently applied to clinical ^{123}I-DaTSCAN data acquired using LEHR collimators. It was shown that the mean SUV measured in the putamen had the highest diagnostic accuracy of the quantitative measures assessed. Furthermore, the mean SUV in the putamen demonstrated higher diagnostic accuracy than the commercially available BRASS™ application. The former method has the advantage of not requiring a normal patient database for comparison. Again, this novel finding could have a significant impact on patient studies.

In addition to quantitative accuracy, an observer study showed that CDRM reconstruction of patient ^{123}I-DaTSCAN studies showed improved image quality, confidence in diagnosis and inter-observer agreement compared to alternative reconstructions. Furthermore, the reconstructions which included CDRM were presented to observers in SUV units on an absolute colour scale, which is a novel approach to ^{123}I-DaTSCAN reporting. This methodology was shown to provide significant improvements over current clinical practice. An example of three patients studies, comparing ^{123}I-DaTSCAN images in relative and absolute scale (previously presented in Chapter 12), is reproduced here for reference (Figure 14.1).

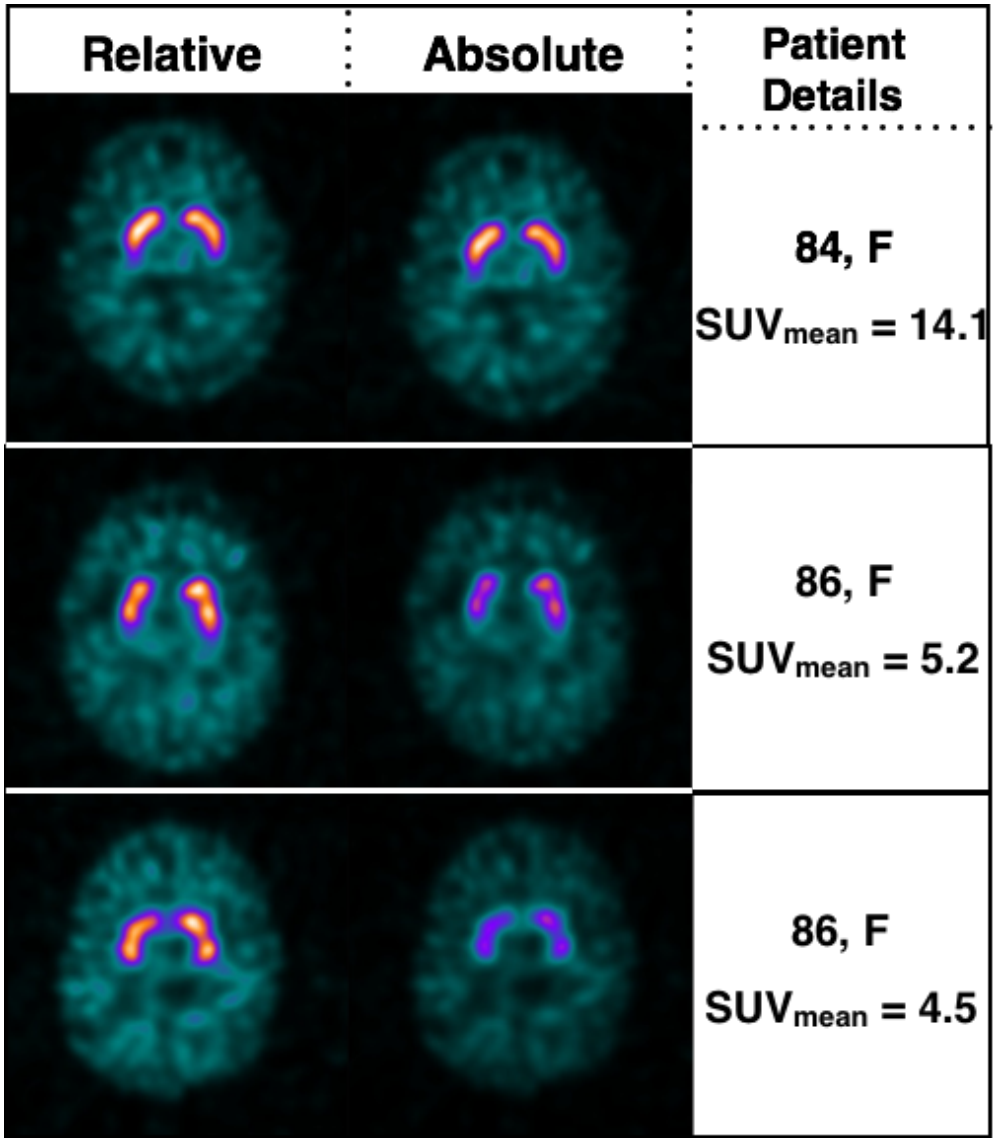

Figure 14.1: Three patient examples which compare ^{123}I-DaTSCAN images in relative and absolute scale

In relation to body imaging, the quantitative accuracy of reconstructed images demonstrated that intra-patient serial studies may be feasible. In these instances, data acquired with MELP collimators and reconstructed with Object Only Scatter Correction (OOSC) was shown to be the most accurate method (±6% for spheres ≥22mm in diameter). However, accuracy was shown to be dependent on lesion location within the FOV, due to variable rates of convergence. Therefore, absolute quantification is not recommended for inter-patient comparison.

A torso phantom observer study demonstrated improved image quality and lesion detection performance for MELP data reconstructed with OOSC compared with the optimum method of reconstructing LEHR data. Therefore, this scheme is recommended for acquisition and reconstruction of ^{123}I-mIBG oncology studies, particularly where serial quantification is necessary.

In summary, the novel CDRM algorithm improves quantitative accuracy compared with alternative corrections for LEHR data. The most appropriate application for this methodology is for ^{123}I-DaTSCAN studies. Quantification of the mean SUV in the putamen leads to more accurate diagnosis of ^{123}I-DaTSCAN studies compared with BRASS™. Furthermore, unlike BRASS™, the SUV approach is not dependent on a normal database.

In relation to oncology applications, quantification of MELP data reconstructed with the OOSC correction scheme has greater quantitative accuracy, with increased image quality and lesion detection performance than the optimal LEHR reconstruction. Therefore, MELP collimators with OOSC should be used for ^{123}I-mIBG studies.

14.3 Methodological Issues

An aim of this work was to evaluate the routine clinical use of novel third party software reconstruction correction schemes for quantification of ^{123}I SPECT. This thesis has focussed on data acquisition using a Siemens Symbia gamma camera. The Siemens LEHR collimators are more susceptible to high energy septal penetration compared with alternative manufacturers' low energy collimators. Therefore, the practical investigations presented the 'worst case scenario' for ^{123}I quantification. The aim of these practical investigations was to establish whether advanced software corrections could provide an adequate solution for this worst case scenario. However, the results demonstrated that accurate quantification in body section imaging remains challenging and a hardware approach is advised in these circumstances.

Assessment of specialist hardware has not been performed in this study. However, Siemens have recently released a Low Energy Low Penetration (LELP) collimator designed for radionuclides with energy photopeaks slightly higher than the 140keV of the commonly used ^{99m}Tc, making it potentially more suitable for ^{123}I. It should be noted, however, that it is the high energy emissions of ^{123}I that substantially affect sensitivity with distance from the detector, rather than the 159keV photons. Nevertheless, the Siemens LELP collimator could be investigated with a view to improving the accuracy of ^{123}I SPECT quantification.

Ringing artefacts were shown to reduce quantitative accuracy (Chapter 11) and cause visual artefacts in the reconstruction of MELP data (Chapter 4). Alternative novel iterative reconstruction algorithms are available which use anatomical prior information from

sequentially acquired CT images and have been shown to reduce ringing artefacts [97]. However, with regard to ^{123}I-DaTSCAN imaging, these algorithms may be inappropriate as there is poor structure delineation of the striatum from CT imaging. Therefore, the correction schemes evaluated in the current study are more appropriate for the clinical scenario.

The focus of clinical evaluation in this thesis was ^{123}I-DaTSCAN studies. In the patient study the clinical outcomes were based on one year follow-up and interpretation of clinical notes. This is not an ideal standard and is recognised as a limitation of the study. A superior gold standard would be to use an extended follow-up or histology/autopsy. These methods are beyond the scope of this thesis. Similarly, the patient cohort was relatively small (36 patients had suitable follow-up). Therefore, conclusions should be viewed as preliminary findings.

14.4 Future Role of ^{123}I SPECT Quantification

This work has shown that measuring the mean SUV in the putamen of ^{123}I-DaTSCAN patient studies may aid visual reporting without the need for comparison with a normal database. An aim of future work will be to establish the benefits of the technique by increasing the patient cohort examined and including longer patient follow-up. It will also be of interest to expand the technique to other imaging centres with alternative hardware.

Currently, the local clinical protocol for ^{123}I-mIBG patient studies is to acquire data with LEHR collimators. However, the torso phantom study has shown that MELP data reconstructed with the OOSC correction scheme can significantly improve image quality and lesion detectability. Therefore, it would be of particular interest to perform an observer study with patient data acquired using both LEHR and MELP collimators. Furthermore, as oncology applications would benefit from the quantification of serial patient studies to investigate the response to therapy, a patient study using the optimum reconstruction of MELP data would be of interest.

The clinical count density of ^{123}I-mIBG considered in this thesis has been that of the local clinical protocol, which is a SPECT acquisition at 24 hour post injection. The aim of this 24 hour acquisition protocol is to maximise uptake to background contrast ratio, particularly in abdominal areas. However, advanced reconstruction correction schemes with optimised contrast recovery may sufficiently improve images acquired 4 hours post injection. This approach would increase count density which may improve lesion detection and be a

more convenient protocol for patients. An observer study would be necessary to validate this approach.

Although thyroid imaging was beyond the scope of this thesis, optimised ^{123}I images with improved image quality may allow for more accurate subtraction of ^{123}I-Iodide from ^{99m}Tc-MIBI in dual-isotope parathyroid imaging, potentially enabling greater detection efficiency of small disease. Again, an observer study would allow evaluation of this likely improvement for clinical practice.

It is hoped that the optimisation of ^{123}I SPECT image quality and the quantitative accuracy demonstrated in this thesis can provide a platform for improving diagnostic accuracy for a number of routine clinical procedures in the future.

Appendix A — The Southampton Method

Introduction

Image analysis techniques have employed relatively large Regions of Interest (ROIs), compared to the structure under observation, which removes partial volume effect from the measurement. One such technique, The Southampton Method, was proposed by Fleming [121] for use in radionuclide imaging. Fleming further described specific application in dopamine receptor and thyroid SPECT studies.

The Southampton Method for Specific Binding Index Measurement

This Section details the method described by Fleming [121] for relative quantification of ^{123}I-DaTSCAN™ images and also provides a simplistic example of the method. The illustration given here describes the use of 2D ROIs. However, the same technique is equally applicable to 3D Volumes of Interest (VOIs).

A relatively large ROI is used to ensure that all the counts from the Structure of Interest (SOI) are measured, which includes counts outside the physical volume of the SOI, thus accounting for partial volume effect. A further reference ROI is placed in an area of non-specific uptake.

The counts which originate from the SOI (C_{TSOI}) are calculated by subtracting the non-specific uptake from the total in the large ROI (Equation A1):

$$C_{TSOI} = C_{TROI} - C_{MBG} * V_{ROI} \qquad \textbf{Equation A1}$$

Where C_{TSOI} is the total counts in the SOI, C_{TROI} is the total counts in the large ROI, C_{MBG} is the mean counts in the background, and V_{ROI} is the volume of the striatal VOI.

To illustrate this calculation, Figure A1 shows an example of a true activity distribution in a large analysis region, the same activity distribution with partial volume effect, and the activity distribution in a uniform uptake region.

2	2	2	2	2	2	2
2	2	2	2	2	2	2
2	2	5	5	5	2	2
2	2	5	5	5	2	2
2	2	5	5	5	2	2
2	2	2	2	2	2	2
2	2	2	2	2	2	2

2	2	2	2	2	2	2
2	2.6	2.7	3	2.7	2.6	2
2	2.7	3	4	3	2.7	2
2	3	4	5	4	3	2
2	2.7	3	4	3	2.7	2
2	2.6	2.7	3	2.7	2.6	2
2	2	2	2	2	2	2

2	2	2	2	2
2	2	2	2	2
2	2	2	2	2
2	2	2	2	2
2	2	2	2	2

Figure A1: True activity distribution in a large Region of Interest (ROI) (left), activity distribution in the same ROI demonstrating partial volume effect (middle), and a ROI of activity distribution in a region of non-specific uptake (right)
The C_{TROI} of the activity distribution is 125. C_{MBG} is 2 and V_{ROI} is 49 (pixels). Therefore, using Equation A1, C_{TSOI} is 27. This corresponds to the increase in uptake in the activity distributions of the SOI compared to non-specific uptake.

Fleming [121] described a Specific Uptake Size Index (SUSI), which is the specific uptake divided by the mean concentration per unit volume.

$$SUSI = \frac{C_{TSOI}}{C_{MBG}} \qquad \textbf{Equation A2}$$

Therefore, in the example given in Figure A1, the SUSI is 13.5.

If the volume of the SOI is known (V_{SOI}) then the Specific Binding Ratio (SBR) can be found using Equation A3

$$SBR = \frac{SUSI}{V_{SOI}} = \frac{\left(\frac{C_{TSOI}}{C_{MBG}}\right)}{V_{SOI}} = \frac{\left(\frac{C_{TROI}}{C_{MBG}}\right) - V_{ROI}}{V_{SOI}} \qquad \textbf{Equation A3}$$

In the example given in Figure A1, the SBR can be determined as shown in Equation A4:

$$SBR = \frac{\left(\frac{125}{2}\right) - 49}{9} = \frac{3}{2} \qquad \textbf{Equation A4}$$

In the example, the SBR calculation has correctly determined the ratio of additional uptake (3) to non-specific uptake (2).

Fleming [121] applied this methodology to ^{123}I-DaTSCAN™ imaging where V_{SOI} was taken to be 11.2ml, which is assumed to be a standard striatal volume described in the literature [231]. The assumption is not critical as V_{SOI} is only a scaling factor in Equation A3.

The Southampton Method for Activity Concentration Measurement

The method described above, as proposed by Fleming, relates to determination of a specific uptake ratio. An amendment to the method is required for direct measurement of activity concentration from a structure with known volume.

The reference region provides a suitable measure of non-specific uptake and the volume of both the SOI and the large ROI are known. Therefore, the contribution of the non-specific counts to the ROI can be subtracted from the total counts in the ROI (C_{TROI}) (Equation A5).

$$C_{AC} = C_{TROI} - \left(C_{MBG} \times \left(V_{ROI} - V_{SOI}\right)\right) \qquad \textbf{Equation A5}$$

where C_{AC} is the counts in the SOI. This method has previously been used by Lagerburg [21].

Using the values from the example shown in Figure A1, the total counts in the SOI are calculated to be 45 (Equation A6), which indicates a mean count of 5 in the SOI.

$$C_{AC} = 125 - \left(2 \times \left(49 - 9\right)\right) = 45 \qquad \textbf{Equation A6}$$

These counts from the SOI (C_{AC}) are converted to activity concentration using a suitable gamma camera sensitivity conversion factor.

List of References

1. Bailey, D.L. and K.P. Willowson, An evidence-based review of quantitative SPECT imaging and potential clinical applications. J Nucl Med, 2013. **54**(1): p. 83-9.
2. Dewaraja, Y.K., et al., MIRD pamphlet No. 23: quantitative SPECT for patient-specific 3-dimensional dosimetry in internal radionuclide therapy. J Nucl Med, 2012. **53**(8): p. 1310-25.
3. Cherry, S.R., J.A. Sorenson, and M.E. Phelps, *Physics in Nuclear Medicine*. 2003: Saunders (W.B.) Co Ltd. 544.
4. Sprawls, P., The Physical Principles of Medical Imaging: Second Edition. 1987: Lippincott Williams and Wilkins.
5. Lawson, R., *The Gamma Camera: A Comprehensive Guide*. 2013: Institute of Physics and Engineering in Medicine.
6. Shepp, L.A. and Y. Vardi, Maximum likelihood reconstruction for emission tomography. IEEE Trans Med Imaging, 1982. **1**(2): p. 113-22.
7. Hudson, H.M. and R.S. Larkin, Accelerated image reconstruction using ordered subsets of projection data. IEEE Trans Med Imaging, 1994. **13**(4): p. 601-9.
8. Greaves, C. and K.A. Goatman, *Mathematical Techniques in Nuclear Medicine*. 2011: Institution of Physics & Engineering in Medicine & Biology.
9. Zaidi, H. and W.D. Erwin, Quantitative Analysis in Nuclear Medicine Imaging. Journal of Nuclear Medicine, 2007. **48**(8): p. 1401.
10. Ritt, P., et al., *Absolute quantification in SPECT.* Eur J Nucl Med Mol Imaging, 2011. **38 Suppl 1**: p. S69-77.
11. Saha, G.B., *Performance Parameters of Gamma Cameras*, in *Physics and Radiobiology of Nuclear Medicine*. 2006, Springer New York: New York, NY. p. 118-138.
12. Graham, L.S., et al., Quantitation of SPECT performance: Report of Task Group 4, Nuclear Medicine Committee. Med Phys, 1995. **22**(4): p. 401-9.
13. Kangasmaa, T.S., et al., Multicenter evaluation of single-photon emission computed tomography quantification with third-party reconstruction software. Nucl Med Commun, 2016. **37**(9): p. 983-7.
14. Koral, K.F., A. Yendiki, and Y.K. Dewaraja, Recovery of total I-131 activity within focal volumes using SPECT and 3D OSEM. Phys Med Biol, 2007. **52**(3): p. 777-90.
15. Bolmsjo, M.S., B.R. Persson, and S.E. Strand, Imaging 123I with a scintillation camera. A study of detection performance and quality factor concepts. Phys Med Biol, 1977. **22**(2): p. 266-77.
16. Macey, D.J., et al., Comparison of low- and medium-energy collimators for SPECT imaging with iodine-123-labeled antibodies. J Nucl Med, 1986. **27**(9): p. 1467-74.
17. Geeter, F.D., et al., Optimal collimator choice for sequential iodine-123 and technetium-99m imaging. Eur J Nucl Med, 1996. **23**(7): p. 768-74.
18. Paras, P., et al. *The Developing Role of Short-lived Radionuclides in Nuclear Medical Practice: Proceedings of a Symposium*. 1982. Pan American Health Organization Building, Washington, D.C.: Office of Scientific and Technical Information, U.S. Department of Energy.
19. Dobbeleir, A.A., A.S. Hambye, and P.R. Franken, Influence of high-energy photons on the spectrum of iodine-123 with low- and medium-energy collimators: consequences for imaging with 123I-labelled compounds in clinical practice. Eur J Nucl Med, 1999. **26**(6): p. 655-8.
20. Small, A.D., et al., Downscatter correction and choice of collimator in 123I imaging. Phys Med Biol, 2006. **51**(17): p. N307-11.
21. Lagerburg, V., et al., A comparison of different energy window subtraction methods to correct for scatter and downscatter in I-123 SPECT imaging. Nucl Med Commun, 2012. **33**(7): p. 708-18.
22. Cot, A., et al., Study of the point spread function (PSF) for 123I SPECT imaging using Monte Carlo simulation. Physics in Medicine and Biology, 2004. **49**(14): p. 3125-3136.
23. Tanaka, M., et al., Monte Carlo simulation of energy spectra for (123)I imaging. Phys Med Biol, 2007. **52**(15): p. 4409-25.

24. Crespo, C., et al., Quantification of dopaminergic neurotransmission SPECT studies with 123I-labelled radioligands. A comparison between different imaging systems and data acquisition protocols using Monte Carlo simulation. Eur J Nucl Med Mol Imaging, 2008. **35**(7): p. 1334-42.
25. Larsson, A., et al., Dopamine D2 receptor SPECT with (123)I-IBZM: evaluation of collimator and post-filtering when using model-based compensation-a Monte Carlo study. Phys Med Biol, 2010. **55**(7): p. 1971-88.
26. Tatsch, K. and G. Poepperl, Nigrostriatal dopamine terminal imaging with dopamine transporter SPECT: an update. J Nucl Med, 2013. **54**(8): p. 1331-8.
27. Darcourt, J., et al., EANM procedure guidelines for brain neurotransmission SPECT using (123)I-labelled dopamine transporter ligands, version 2. Eur J Nucl Med Mol Imaging, 2010. **37**(2): p. 443-50.
28. Cot, A., et al., Absolute quantification in dopaminergic neurotransmission SPECT using a Monte Carlo-based scatter correction and fully 3-dimensional reconstruction. J Nucl Med, 2005. **46**(9): p. 1497-504.
29. Varrone, A., et al., European multicentre database of healthy controls for [(123)I]FP-CIT SPECT (ENC-DAT): age-related effects, gender differences and evaluation of different methods of analysis. Eur J Nucl Med Mol Imaging, 2013. **40**(2): p. 213-27.
30. Dickson, J.C., et al., The impact of reconstruction method on the quantification of DaTSCAN images. Eur J Nucl Med Mol Imaging, 2010. **37**(1): p. 23-35.
31. Tossici-Bolt, L., et al., Quantification of [123I]FP-CIT SPECT brain images: an accurate technique for measurement of the specific binding ratio. Eur J Nucl Med Mol Imaging, 2006. **33**(12): p. 1491-9.
32. Plotkin, M., et al., Combined 123I-FP-CIT and 123I-IBZM SPECT for the diagnosis of parkinsonian syndromes: study on 72 patients. J Neural Transm, 2005. **112**(5): p. 677-92.
33. Gilland, D.R., et al., Volume and activity quantitation with iodine-123 SPECT. J Nucl Med, 1994. **35**(10): p. 1707-13.
34. Bombardieri, E., et al., 131I/123I-metaiodobenzylguanidine (mIBG) scintigraphy: procedure guidelines for tumour imaging. Eur J Nucl Med Mol Imaging, 2010. **37**(12): p. 2436-46.
35. Hardman, J.G., *Oxford Handbook of Clinical Medicine.* BJA: British Journal of Anaesthesia, 2007. **98**(6): p. 849-850.
36. Chen, J.J., et al., Single photon emission computed tomography of the thyroid. J Clin Endocrinol Metab, 1988. **66**(6): p. 1240-6.
37. Wanet, P.M., A. Sand, and J. Abramovici, Physical and clinical evaluation of high-resolution thyroid pinhole tomography. J Nucl Med, 1996. **37**(12): p. 2017-20.
38. Krausz, Y., et al., Role of high-resolution pinhole tomography in the evaluation of thyroid abnormalities. Thyroid, 1997. **7**(6): p. 847-52.
39. Chirumamilla, A. and M.I. Travin, Cardiac applications of 123I-mIBG imaging. Semin Nucl Med, 2011. **41**(5): p. 374-87.
40. Rosenthal, M.S., et al., Quantitative SPECT imaging: a review and recommendations by the Focus Committee of the Society of Nuclear Medicine Computer and Instrumentation Council. J Nucl Med, 1995. **36**(8): p. 1489-513.
41. McKeighen, R.E., G. Muehllehner, and R.A. Moyer, Gamma camera collimator considerations for imaging 123I. J Nucl Med, 1974. **15**(5): p. 328-31.
42. Inoue, Y., et al., Physical characteristics of low and medium energy collimators for 123I imaging and simultaneous dual-isotope imaging. Nucl Med Commun, 2003. **24**(11): p. 1195-202.
43. Leong, L.K., M.K. O'Connor, and D.M. Maraganore, Quantitation of iodine-123-beta-CIT dopamine receptor uptake in a phantom model. J Nucl Med Technol, 1999. **27**(2): p. 117-22.
44. Mueller, S.P., et al., Collimator selection for SPECT brain imaging: the advantage of high resolution. J Nucl Med, 1986. **27**(11): p. 1729-38.
45. Madsen, M.T., W. Chang, and R.D. Hichwa, Spatial resolution and count density requirements in brain SPECT imaging. Phys Med Biol, 1992. **37**(8): p. 1625-36.
46. Chen, J., et al., Improved quantification in 123I cardiac SPECT imaging with deconvolution of septal penetration. Nucl Med Commun, 2006. **27**(7): p. 551-8.

47. Rault, E., et al., Comparison of image quality of different iodine isotopes (I-123, I-124, and I-131). Cancer Biother Radiopharm, 2007. **22**(3): p. 423-30.
48. Van Laere, K., et al., EANM procedure guidelines for brain neurotransmission SPECT/PET using dopamine D2 receptor ligands, version 2. Eur J Nucl Med Mol Imaging, 2010. **37**(2): p. 434-42.
49. Djang, D.S., et al., SNM practice guideline for dopamine transporter imaging with 123I-ioflupane SPECT 1.0. J Nucl Med, 2012. **53**(1): p. 154-63.
50. Taieb, D., et al., EANM 2012 guidelines for radionuclide imaging of phaeochromocytoma and paraganglioma. Eur J Nucl Med Mol Imaging, 2012. **39**(12): p. 1977-95.
51. Tossici-Bolt, L., et al., Calibration of gamma camera systems for a multicentre European (1)(2)(3)I-FP-CIT SPECT normal database. Eur J Nucl Med Mol Imaging, 2011. **38**(8): p. 1529-40.
52. Flotats, A., et al., Proposal for standardization of 123I-metaiodobenzylguanidine (MIBG) cardiac sympathetic imaging by the EANM Cardiovascular Committee and the European Council of Nuclear Cardiology. Eur J Nucl Med Mol Imaging, 2010. **37**(9): p. 1802-12.
53. Maebatake, A., et al., An anthropomorphic phantom study of brain dopamine transporter SPECT images obtained using different SPECT/CT devices and collimators. J Nucl Med Technol, 2015. **43**(1): p. 41-6.
54. James, G., Producing an Accurate Standard for 123I Thyroid Uptake Studies: British Nuclear Medicine Society 42nd Annual Meeting Harrogate 11-14 May 2014. Nuclear Medicine Communications, 2014. **35**(5): p. 541-584.
55. Ross, J., I123 Collimators, Presentation, 18/11/2016
56. Lee, T.C., et al., Multipinhole collimator with 20 apertures for a brain SPECT application. Med Phys, 2014. **41**(11): p. 112501.
57. Park, M.A., et al., Performance of a high-sensitivity dedicated cardiac SPECT scanner for striatal uptake quantification in the brain based on analysis of projection data. Med Phys, 2013. **40**(4): p. 042504.
58. Sohlberg, A., H. Watabe, and H. Iida, Acceleration of Monte Carlo-based scatter compensation for cardiac SPECT. Phys Med Biol, 2008. **53**(14): p. N277-85.
59. Hutton, B., Angular sampling necessary for clinical SPECT. J Nucl Med, 1996. **37**(11): p. 1915-6.
60. Takahashi, Y., et al., Evaluation of the number of SPECT projections in the ordered subsets-expectation maximization image reconstruction method. Ann Nucl Med, 2003. **17**(7): p. 525-30.
61. Stamos, J.A., et al., Object-dependent performance comparison of two iterative reconstruction algorithms. Nuclear Science, IEEE Transactions on, 1988. **35**(1): p. 611-614.
62. Llacer, J. and E. Veklerov, Feasible images and practical stopping rules for iterative algorithms in emission tomography. IEEE Trans Med Imaging, 1989. **8**(2): p. 186-93.
63. Liow, J.S. and S.C. Strother, The convergence of object dependent resolution in maximum likelihood based tomographic image reconstruction. Phys Med Biol, 1993. **38**(1): p. 55-70.
64. Brambilla, M., et al., Characterization of ordered-subsets expectation maximization with 3D post-reconstruction Gauss filtering and comparison with filtered backprojection in 99mTc SPECT. Ann Nucl Med, 2005. **19**(2): p. 75-82.
65. Hutton, B.F., H.M. Hudson, and F.J. Beekman, A clinical perspective of accelerated statistical reconstruction. Eur J Nucl Med, 1997. **24**(7): p. 797-808.
66. Hutton, B.F., I. Buvat, and F.J. Beekman, Review and current status of SPECT scatter correction. Phys Med Biol, 2011. **56**(14): p. R85-112.
67. Brown, S., et al., Investigation of the relationship between linear attenuation coefficients and CT Hounsfield units using radionuclides for SPECT. Appl Radiat Isot, 2008. **66**(9): p. 1206-12.
68. Zaidi, H. and B. Hasegawa, Determination of the attenuation map in emission tomography. J Nucl Med, 2003. **44**(2): p. 291-315.
69. Van Laere, K., et al., Non-uniform versus uniform attenuation correction in brain perfusion SPET of healthy volunteers. Eur J Nucl Med, 2001. **28**(1): p. 90-8.
70. Warwick, J.M., et al., The Role of CT-Based Attenuation Correction and Collimator Blurring Correction in Striatal Spect Quantification. Int J Mol Imaging, 2011. **2011**: p. 195037.

71. Stodilka, R.Z., et al., The relative contributions of scatter and attenuation corrections toward improved brain SPECT quantification. Phys Med Biol, 1998. **43**(10): p. 2991-3008.
72. Bailey, D.L., Transmission scanning in emission tomography. Eur J Nucl Med, 1998. **25**(7): p. 774-87.
73. Zaidi, H. Optimizing attenuation correction in clinical cerebral 3D PET: which method to use? 2001.
74. Zaidi, H., M.L. Montandon, and D.O. Slosman, Attenuation compensation in cerebral 3D PET: effect of the attenuation map on absolute and relative quantitation. Eur J Nucl Med Mol Imaging, 2004. **31**(1): p. 52-63.
75. Fleming, J.S., A technique for using CT images in attenuation correction and quantification in SPECT. Nucl Med Commun, 1989. **10**(2): p. 83-97.
76. Lange, C., et al., CT-based attenuation correction in I-123-ioflupane SPECT. PLoS One, 2014. **9**(9): p. e108328.
77. Lapa, C., et al., Influence of CT-based attenuation correction on dopamine transporter SPECT with [(123)I]FP-CIT. Am J Nucl Med Mol Imaging, 2015. **5**(3): p. 278-86.
78. Yokoyama, K., et al., Computed-tomography-guided anatomic standardization for quantitative assessment of dopamine transporter SPECT. Eur J Nucl Med Mol Imaging, 2016.
79. Hutton, B.F., Cardiac single-photon emission tomography: is attenuation correction enough? Eur J Nucl Med, 1997. **24**(7): p. 713-5.
80. Hesse, B., et al., EANM/ESC procedural guidelines for myocardial perfusion imaging in nuclear cardiology. Eur J Nucl Med Mol Imaging, 2005. **32**(7): p. 855-97.
81. Ogawa, K., et al., A practical method for position-dependent Compton-scatter correction in single photon emission CT. IEEE Trans Med Imaging, 1991. **10**(3): p. 408-12.
82. Ichihara, T., et al., Compton scatter compensation using the triple-energy window method for single- and dual-isotope SPECT. J Nucl Med, 1993. **34**(12): p. 2216-21.
83. Narita, Y., et al., Monte Carlo and experimental evaluation of accuracy and noise properties of two scatter correction methods for SPECT. Phys Med Biol, 1996. **41**(11): p. 2481-96.
84. Beekman, F.J., C. Kamphuis, and E.C. Frey, Scatter compensation methods in 3D iterative SPECT reconstruction: a simulation study. Phys Med Biol, 1997. **42**(8): p. 1619-32.
85. Kadrmas, D.J., et al., Fast implementations of reconstruction-based scatter compensation in fully 3D SPECT image reconstruction. Phys Med Biol, 1998. **43**(4): p. 857-73.
86. Xiao, J., et al., Evaluation of 3D Monte Carlo-based scatter correction for 99mTc cardiac perfusion SPECT. J Nucl Med, 2006. **47**(10): p. 1662-9.
87. Sohlberg, A.O. and M.T. Kajaste, Fast Monte Carlo-simulator with full collimator and detector response modelling for SPECT. Ann Nucl Med, 2012. **26**(1): p. 92-8.
88. O'Mahoney, E. and I. Murray, Evaluation of a matched filter resolution recovery reconstruction algorithm for SPECT-CT imaging. Nucl Med Commun, 2012.
89. Sheehy, N., et al., Pediatric 99mTc-DMSA SPECT performed by using iterative reconstruction with isotropic resolution recovery: improved image quality and reduced radiopharmaceutical activity. Radiology, 2009. **251**(2): p. 511-6.
90. Stansfield, E.C., et al., Pediatric 99mTc-MDP bone SPECT with ordered subset expectation maximization iterative reconstruction with isotropic 3D resolution recovery. Radiology, 2010. **257**(3): p. 793-801.
91. Venero, C.V., et al., A multicenter evaluation of a new post-processing method with depth-dependent collimator resolution applied to full-time and half-time acquisitions without and with simultaneously acquired attenuation correction. J Nucl Cardiol, 2009. **16**(5): p. 714-25.
92. DePuey, E.G., et al., A comparison of the image quality of full-time myocardial perfusion SPECT vs wide beam reconstruction half-time and half-dose SPECT. J Nucl Cardiol, 2011. **18**(2): p. 273-80.
93. Kangasmaa, T.S., et al., Half-time myocardial perfusion SPECT imaging with attenuation and Monte Carlo-based scatter correction. Nucl Med Commun, 2011. **32**(11): p. 1040-5.
94. Armstrong, I.S., et al., Reduced-count myocardial perfusion SPECT with resolution recovery. Nucl Med Commun, 2012. **33**(2): p. 121-9.

95. Müller, S.P., et al., Maximum-likelihood estimation: a mathematical model for quantitation in nuclear medicine. Journal of nuclear medicine : official publication, Society of Nuclear Medicine, 1990. **31**(10): p. 1693-1701.
96. Kalantari, F., H. Rajabi, and M. Saghari, Quantification and reduction of the collimator-detector response effect in SPECT by applying a system model during iterative image reconstruction: a simulation study. Nucl Med Commun, 2012. **33**(3): p. 228-38.
97. Kangasmaa, T., A. Sohlberg, and J.T. Kuikka, Reduction of collimator correction artefacts with bayesian reconstruction in spect. Int J Mol Imaging, 2011. **2011**: p. 630813.
98. Armstrong, I.S. and S.A. Hoffmann, Activity concentration measurements using a conjugate gradient (Siemens xSPECT) reconstruction algorithm in SPECT/CT. Nucl Med Commun, 2016. **37**(11): p. 1212-7.
99. Erlandsson, K., et al., A review of partial volume correction techniques for emission tomography and their applications in neurology, cardiology and oncology. Phys Med Biol, 2012. **57**(21): p. R119-59.
100. Siemens Medical Solutions USA, Symbia TruePoint SPECT-CT System Specifications. 2005.
101. Smith, S.W., Digital Signal Processing: A Practical Guide for Engineers and Scientist. 2003: Newnes Books.
102. Kojima, A., et al., Effect of spatial resolution on SPECT quantification values. J Nucl Med, 1989. **30**(4): p. 508-14.
103. Norberg, P., et al., Evaluation of reconstruction techniques for lung single photon emission tomography: a Monte Carlo study. Nucl Med Commun, 2007. **28**(12): p. 929-36.
104. Olsson, A., et al., Evaluation of reconstruction techniques in regional cerebral blood flow SPECT using trade-off plots: a Monte Carlo study. Nucl Med Commun, 2007. **28**(9): p. 719-25.
105. Bouwens, L.R., et al., Resolution recovery for list-mode reconstruction in SPECT. Phys Med Biol, 2001. **46**(8): p. 2239-53.
106. Knoll, P., et al., Comparison of advanced iterative reconstruction methods for SPECT/CT. Z Med Phys, 2012. **22**(1): p. 58-69.
107. Grootjans, W., et al., Performance of 3DOSEM and MAP algorithms for reconstructing low count SPECT acquisitions. Z Med Phys, 2016. **26**(4): p. 311-322.
108. Oloomi, S., et al., A New Approach for Scatter Removal and Attenuation Compensation from SPECT/CT Images. Iran J Basic Med Sci, 2013. **16**(11): p. 1181-9.
109. Tuzlukov, V., Signal Processing Noise. 2002: CRC Press.
110. Tong, S., A.M. Alessio, and P.E. Kinahan, Noise and signal properties in PSF-based fully 3D PET image reconstruction: an experimental evaluation. Phys Med Biol, 2010. **55**(5): p. 1453-73.
111. van Gils, C.A., et al., Impact of reconstruction parameters on quantitative I-131 SPECT. Phys Med Biol, 2016. **61**(14): p. 5166-82.
112. Bailey, D.L. and A. Kalemis, Externally triggered gating of nuclear medicine acquisitions: a useful method for partitioning data. Phys Med Biol, 2005. **50**(7): p. N55-62.
113. Schmidtlein, C.R., et al., Using an external gating signal to estimate noise in PET with an emphasis on tracer avid tumors. Phys Med Biol, 2010. **55**(20): p. 6299-326.
114. Carlier, T., et al., (90)Y -PET imaging: Exploring limitations and accuracy under conditions of low counts and high random fraction. (0094-2405 (Print)).
115. Gantet, P., et al., Iterative three-dimensional expectation maximization restoration of single photon emission computed tomography images: application in striatal imaging. Med Phys, 2006. **33**(1): p. 52-60.
116. National Electrical Manufacturers Association, Performance Measurements of Positron Emission Tomographs. NEMA Standards Publication, 2007(NU 2-2007).
117. Albert, N.L., et al., Implementation of the European multicentre database of healthy controls for [(123)I]FP-CIT SPECT increases diagnostic accuracy in patients with clinically uncertain parkinsonian syndromes. Eur J Nucl Med Mol Imaging, 2016. **43**(7): p. 1315-22.
118. Chen, J., et al., Heart-to-mediastinum ratios measured from I-123 mIBG SPECT distinguish patients with heart failure from controls. European Heart Journal Supplements, 2011. **13**(A): p. A73-A73.

119. Ortega Lozano, S.J., et al., Diagnostic accuracy of FP-CIT SPECT in patients with parkinsonism. Rev Esp Med Nucl, 2007. **26**(5): p. 277-85.
120. Bolt, L., et al., 4. Quantifying DaTSCANTM images: how automation reduces operator variability. Nucl Med Commun, 2003. **24**(4): p. 445.
121. Fleming, J.S., et al., The specific uptake size index for quantifying radiopharmaceutical uptake. Phys Med Biol, 2004. **49**(14): p. N227-34.
122. Koch, W., et al., Clinical testing of an optimized software solution for an automated, observer-independent evaluation of dopamine transporter SPECT studies. J Nucl Med, 2005. **46**(7): p. 1109-18.
123. Nobili, F., et al., Automatic semi-quantification of [123I]FP-CIT SPECT scans in healthy volunteers using BasGan version 2: results from the ENC-DAT database. Eur J Nucl Med Mol Imaging, 2013. **40**(4): p. 565-73.
124. GE Healthcare. *DaTQUANT - Nuclear Imaging Agents - Products*. [cited 2017 07/09/2017]; Available from: http://www3.gehealthcare.com/en/products/categories/nuclear_imaging_agents/datquant.
125. Dickson, J.C., et al., Proposal for the standardisation of multi-centre trials in nuclear medicine imaging: prerequisites for a European 123I-FP-CIT SPECT database. Eur J Nucl Med Mol Imaging, 2012. **39**(1): p. 188-97.
126. Buchert, R., et al., Reduction in camera-specific variability in [(123)I]FP-CIT SPECT outcome measures by image reconstruction optimized for multisite settings: impact on age-dependence of the specific binding ratio in the ENC-DAT database of healthy controls. Eur J Nucl Med Mol Imaging, 2016. **43**(7): p. 1323-36.
127. Bailey, D.L. and K.P. Willowson, Quantitative SPECT/CT: SPECT joins PET as a quantitative imaging modality. Eur J Nucl Med Mol Imaging, 2014. **41 Suppl 1**: p. S17-25.
128. He, B., et al., A Monte Carlo and physical phantom evaluation of quantitative In-111 SPECT. Phys Med Biol, 2005. **50**(17): p. 4169-85.
129. Shcherbinin, S., et al., Accuracy of quantitative reconstructions in SPECT/CT imaging. Phys Med Biol, 2008. **53**(17): p. 4595-604.
130. Willowson, K., D.L. Bailey, and C. Baldock, Quantitative SPECT reconstruction using CT-derived corrections. Phys Med Biol, 2008. **53**(12): p. 3099-112.
131. Koral, K.F., et al., Determining total I-131 activity within a VoI using SPECT, a UHE collimator, OSEM, and a constant conversion factor. IEEE Transactions on Nuclear Science, 2004. **51**(3): p. 611-618.
132. Zeintl, J., et al., Quantitative accuracy of clinical 99mTc SPECT/CT using ordered-subset expectation maximization with 3-dimensional resolution recovery, attenuation, and scatter correction. J Nucl Med, 2010. **51**(6): p. 921-8.
133. Kangasmaa, T.S., et al., Multicenter evaluation of single-photon emission computed tomography quantification with third-party reconstruction software. Nuclear Medicine Communications, 2016. **37**(9): p. 983-987.
134. Iida, H., et al., Multicenter evaluation of a standardized protocol for rest and acetazolamide cerebral blood flow assessment using a quantitative SPECT reconstruction program and split-dose 123I-iodoamphetamine. J Nucl Med, 2010. **51**(10): p. 1624-31.
135. Du, Y., B.M. Tsui, and E.C. Frey, Model-based compensation for quantitative 123I brain SPECT imaging. Phys Med Biol, 2006. **51**(5): p. 1269-82.
136. Kinahan, P.E. and J.W. Fletcher, Positron emission tomography-computed tomography standardized uptake values in clinical practice and assessing response to therapy. Semin Ultrasound CT MR, 2010. **31**(6): p. 496-505.
137. Wahl, R.L., et al., From RECIST to PERCIST: Evolving Considerations for PET response criteria in solid tumors. J Nucl Med, 2009. **50 Suppl 1**: p. 122S-50S.
138. Vanderhoek, M., S.B. Perlman, and R. Jeraj, Impact of the definition of peak standardized uptake value on quantification of treatment response. J Nucl Med, 2012. **53**(1): p. 4-11.
139. Armstrong, I.S., et al., Impact of point spread function modelling and time of flight on FDG uptake measurements in lung lesions using alternative filtering strategies. EJNMMI Phys, 2014. **1**(1): p. 99.

140. Armstrong, I.S., et al., The assessment of time-of-flight on image quality and quantification with reduced administered activity and scan times in 18F-FDG PET. Nucl Med Commun, 2015. **36**(7): p. 728-37.
141. Lodge, M.A., M.A. Chaudhry, and R.L. Wahl, Noise considerations for PET quantification using maximum and peak standardized uptake value. J Nucl Med, 2012. **53**(7): p. 1041-7.
142. Bolster, A.A., et al., Gamma Camera Performance : Technical Assessment Protocol : Report. 1996.
143. National Electrical Manufacturers Association, Performance Measurements of Gamma Cameras - NEMA Standards Publication NU 1-2012. 2013.
144. Armstrong, I.S., et al., *Report 111: Quality Control of Gamma Cameras and Nuclear Medicine Computer Systems*. Institute of Physics and Engineering in Medicine (IPEM) Report Series, ed. E. Eadie. 2015, UK: The Charlesworth Group. 190.
145. Walpole, R.E. and R.H. Myers, Probability and statistics for engineers and scientists. 1978, New York: Macmillan.
146. Albin, T.J. and P. Vink, A method superior to adding percentiles when only limited anthropometric data such as percentile tables are available for design models. Appl Ergon, 2014. **45**(6): p. 1392-8.
147. Staelens, S., et al., Monte Carlo simulations of a scintillation camera using GATE: validation and application modelling. Phys Med Biol, 2003. **48**(18): p. 3021-42.
148. Holstensson, M., et al., The effect of energy and source location on gamma camera intrinsic and extrinsic spatial resolution: an experimental and Monte Carlo study. Phys Med Biol, 2010. **55**(6): p. 1735-51.
149. Kappadath, S.C., W.D. Erwin, and R.E. Wendt, 3rd, Observed inter-camera variability of clinically relevant performance characteristics for Siemens Symbia gamma cameras. J Appl Clin Med Phys, 2006. **7**(4): p. 74-80.
150. Cot, A., et al., Study of the point spread function (PSF) for 123I SPECT imaging using Monte Carlo simulation. Phys Med Biol, 2004. **49**(14): p. 3125-36.
151. Hsu, B.-L., et al., Energy-based correction of I-123 high-energy contaminants degrading gamma camera uniformity. J Nucl Med Meeting Abstracts, 2006. **47**: p. 193.
152. Galt, J., et al., Gamma camera uniformity correction in I-123 imaging using low energy collimators. J Nucl Med Meeting Abstracts, 2006. **47**: p. 381.
153. Siemens Medical Solutions USA and C. Toussaint, *Signature Series: Principle of Operation and QC*. 2008.
154. Collier, D., Query Regarding Siemens Symbia Uniformity of I123 with LEHR Collimators, E-mail, 04/02/2015
155. Hughes, A. and P.F. Sharp, The sensitivity of objective indices to changes in gamma camera non-uniformity. Physics in Medicine and Biology, 1989. **34**(7): p. 885.
156. Cox, N.J. and B.L. Diffey, A numerical index of gamma-camera uniformity. The British Journal of Radiology, 1976. **49**(584): p. 734-735.
157. Jenkins, L., I131 SPECT reconstruction, Email, 01/09/2017
158. Sohlberg, A., H. Watabe, and H. Iida, Three-dimensional SPECT reconstruction with transmission-dependent scatter correction. Ann Nucl Med, 2008. **22**(7): p. 549-56.
159. Kangasmaa, T., J. Kuikka, and A. Sohlberg, Optimisation of simultaneous tl-201/tc-99m dual isotope reconstruction with monte-carlo-based scatter correction. Int J Mol Imaging, 2012. **2012**: p. 695632.
160. Jenkins, L., Lengthy Reconstruction Times for HybridRecon, Email, 28/10/2015
161. Leong, L.K., R.L. Kruger, and M.K. O'Connor, A Comparison of the Uniformity Requirements for SPECT Image Reconstruction Using FBP and OSEM Techniques. Journal of Nuclear Medicine Technology, 2001. **29**(2): p. 79-83.
162. Choi, J.M., et al., Software development for quality assurance using ACR SPECT phantom. Journal of Nuclear Medicine, 2012. **53**(supplement 1): p. 2530.
163. Rana, N., et al., Evaluation of external beam hardening filters on image quality of computed tomography and single photon emission computed tomography/computed tomography.

Journal of Medical Physics / Association of Medical Physicists of India, 2015. **40**(4): p. 198-206.

164. Squires, G.L., *Practical Physics*. 2001: Cambridge University Press.
165. Li, Y., Correlation imaging with arbitrary sampling trajectories. Magn Reson Imaging, 2014. **32**(5): p. 551-62.
166. NIST. *NIST Physical Reference Data - H2O*. [cited 2014 16/08/2014]; Available from: http://physics.nist.gov/cgi-bin/ffast/ffast.pl?Formula=H2O&gtype=5&range=U&lower=&upper=&density=1.0.
167. Liu, S. and T.H. Farncombe, Collimator-Detector Response Compensation in Quantitative SPECT Reconstruction, in IEEE Nuclear Sciences Symposium Conference. 2007.
168. Sohlberg, A., Thoughts on a MELP SPECT Edge Artefact, Email, 22/02/2016
169. Maebatake, A., et al., Evaluation of Iterative Reconstruction Method and Attenuation Correction in Brain Dopamine Transporter SPECT Using an Anthropomorphic Striatal Phantom. Asia Ocean J Nucl Med Biol, 2016. **4**(2): p. 72-80.
170. Badger, D. and L. Barnden, Spatial resolution is dependent on image content for SPECT with iterative reconstruction incorporating distance dependent resolution (DDR) correction. Australas Phys Eng Sci Med, 2014. **37**(3): p. 551-7.
171. Erlandsson, K., et al., Performance evaluation of D-SPECT: a novel SPECT system for nuclear cardiology. Phys Med Biol, 2009. **54**(9): p. 2635-49.
172. Rumsey, D.J., Statistics For Dummies. 2003: Wiley.
173. McCrum-Gardner, E., Which is the correct statistical test to use? Br J Oral Maxillofac Surg, 2008. **46**(1): p. 38-41.
174. Rockwood, A. *What number of points is required to fit Gaussian Distributions?* 2014 [cited 2017 29/08/2017]; Available from: https://www.researchgate.net/post/What_number_of_points_is_required_to_fit_Gaussian_Distributions.
175. Kappadath, S.C., Effects of voxel size and iterative reconstruction parameters on the spatial resolution of 99mTc SPECT/CT. J Appl Clin Med Phys, 2011. **12**(4): p. 3459.
176. Armstrong, I.S., Gibbs Edge Enhancement in NEMA Phantom, Email, 21/11/2016
177. Brown, C., Is SPECT contrast recovery of the PET NEMA IEC Body phantom dependent on sphere positioning?: British Nuclear Medicine Society 41st Annual Meeting Brighton 21-24 April 2013, in Nuclear Medicine Communications. 2013. p. 362-411.
178. Bomanji, J., et al., Uptake of iodine-123 MIBG by pheochromocytomas, paragangliomas, and neuroblastomas: a histopathological comparison. J Nucl Med, 1987. **28**(6): p. 973-8.
179. Chatfield, M. and A. Mander, The Skillings-Mack test (Friedman test when there are missing data). Stata J, 2009. **9**(2): p. 299-305.
180. Sohlberg, A., Unpredictable nature of full collimator response algorithm, Email, 03/02/2015
181. Aldridge, M.D., et al., Clinical evaluation of reducing acquisition time on single-photon emission computed tomography image quality using proprietary resolution recovery software. Nucl Med Commun, 2013. **34**(11): p. 1116-23.
182. Brown, C., Can an ECG simulator be used to generate reduced count SPECT data?: British Nuclear Medicine Society 41st Annual Meeting Brighton 21-24 April 2013, in Nuclear Medicine Communications. 2013. p. 362-411.
183. National Electrical Manufacturers Association, Performance Measurements of Positron Emission Tomographs. NEMA Standards Publication, 2013(NU 2-2012).
184. Larsson, A., et al., Correction for scatter and septal penetration using convolution subtraction methods and model-based compensation in 123I brain SPECT imaging-a Monte Carlo study. Phys Med Biol, 2006. **51**(22): p. 5753-67.
185. Gilland, D.R., et al., Quantitative SPECT reconstruction of iodine-123 data. J Nucl Med, 1991. **32**(3): p. 527-33.
186. Bettinardi, V., et al., Physical performance of the new hybrid PETCT Discovery-690. Med Phys, 2011. **38**(10): p. 5394-411.
187. El Fakhri, G., et al., Relative impact of scatter, collimator response, attenuation, and finite spatial resolution corrections in cardiac SPECT. J Nucl Med, 2000. **41**(8): p. 1400-8.

188. Lyra, M. and A. Ploussi, Filtering in SPECT Image Reconstruction. Int J Biomed Imaging, 2011. **2011**: p. 693795.
189. Vandenberghe, S., et al., Iterative reconstruction algorithms in nuclear medicine. Comput Med Imaging Graph, 2001. **25**(2): p. 105-11.
190. Dickson, J., Query regarding the post-filter choice for ENC-DAT reconstruction, Email, 07/09/207
191. Dickson, J., et al., ENCDAT Database of I123 FP-CIT Healthy Controls: Options for Implementation, in Annual Congress of the European Association of Nuclear Medicine. 2011: Birmingham.
192. Sohlberg, A., full collimator modelling for I123 imaging, Email, 21/03/2013
193. Diemling, M., HERMES Camera Correction for the ENCDAT database using DaTscan. 2016, Hermes Medical Solutions,.
194. Winz, O.H., et al., Image quality and data quantification in dopamine transporter SPECT: advantage of 3-dimensional OSEM reconstruction? Clin Nucl Med, 2012. **37**(9): p. 866-71.
195. Jarritt, P.H., et al., UK audit of single photon emission computed tomography reconstruction software using software generated phantoms. Nucl Med Commun, 2002. **23**(5): p. 483-91.
196. Koch, W., et al., Cross-camera comparison of SPECT measurements of a 3-D anthropomorphic basal ganglia phantom. Eur J Nucl Med Mol Imaging, 2006. **33**(4): p. 495-502.
197. Du, Y., B.M. Tsui, and E.C. Frey, Partial volume effect compensation for quantitative brain SPECT imaging. IEEE Trans Med Imaging, 2005. **24**(8): p. 969-76.
198. Zeintl, J., et al. Towards Quantitative SPECT: Error Estimation of SPECT OSEM with 3D Resolution Recovery, Attenuation Correction and Scatter Correction. in IEEE Nuclear Science Symposium Conference Record. 2008.
199. Jenkins, L., HERMES SUV-SPECT® User Guide. 2015.
200. Sanders, J.C., et al., Quantitative SPECT/CT Imaging of (177)Lu with In Vivo Validation in Patients Undergoing Peptide Receptor Radionuclide Therapy. Mol Imaging Biol, 2015. **17**(4): p. 585-93.
201. Hofheinz, F., et al., Effects of cold sphere walls in PET phantom measurements on the volume reproducing threshold. Phys Med Biol, 2010. **55**(4): p. 1099-113.
202. Data Spectrum Corporation, K.L. Greer, and T. Perry, *NEMA IEC Body Phantom Set User's Manual*. 2006.
203. Snyder, D.L., et al., Noise and edge artifacts in maximum-likelihood reconstructions for emission tomography. IEEE Trans Med Imaging, 1987. **6**(3): p. 228-38.
204. Shaoying, L. and T.H. Farncombe. Collimator-detector response compensation in quantitative SPECT reconstruction. in 2007 IEEE Nuclear Science Symposium Conference Record. 2007.
205. Hokama, H., et al., Caudate, putamen, and globus pallidus volume in schizophrenia: a quantitative MRI study. Psychiatry Res, 1995. **61**(4): p. 209-29.
206. Pitcher, T.L., et al., Reduced striatal volumes in Parkinson's disease: a magnetic resonance imaging study. Transl Neurodegener, 2012. **1**(1): p. 17.
207. Seibyl, J., et al., The molecular basis of dopaminergic brain imaging in Parkinson's disease. Q J Nucl Med Mol Imaging, 2012. **56**(1): p. 4-16.
208. Koch, W., et al., Extended studies of the striatal uptake of 99mTc-NC100697 in healthy volunteers. J Nucl Med, 2007. **48**(1): p. 27-34.
209. Altman, D.G. and J.M. Bland, Diagnostic tests. 1: Sensitivity and specificity. BMJ, 1994. **308**(6943): p. 1552.
210. Simundic, A.M., Measures of Diagnostic Accuracy: Basic Definitions. EJIFCC, 2009. **19**(4): p. 203-11.
211. Baratloo, A., et al., Part 1: Simple Definition and Calculation of Accuracy, Sensitivity and Specificity. Emerg (Tehran), 2015. **3**(2): p. 48-9.
212. Keeble, C., et al., Methods for the analysis of ordinal response data in medical image quality assessment. Br J Radiol, 2016. **89**(1063): p. 20160094.

213. GraphPad Software Inc. *Quantify agreement with kappa*. 2017 [cited 2017 24/07/2017]; Available from: https://graphpad.com/quickcalcs/kappa1/.
214. Lowry, R. *Kappa as a Measure of Concordance in Categorical Sorting*. 2017 [cited 2017 24/07/2017]; Available from: http://vassarstats.net/kappa.html.
215. Suwijn, S.R., et al., The diagnostic accuracy of dopamine transporter SPECT imaging to detect nigrostriatal cell loss in patients with Parkinson's disease or clinically uncertain parkinsonism: a systematic review. EJNMMI Res, 2015. **5**: p. 12.
216. Yokoyama, K., et al., Computed-tomography-guided anatomic standardization for quantitative assessment of dopamine transporter SPECT. Eur J Nucl Med Mol Imaging, 2017. **44**(3): p. 366-372.
217. Thompson, J.D., et al., A free-response evaluation determining value in the computed tomography attenuation correction image for revealing pulmonary incidental findings: a phantom study. Acad Radiol, 2014. **21**(4): p. 538-45.
218. Verdun, F.R., et al., Image quality in CT: From physical measurements to model observers. Phys Med, 2015. **31**(8): p. 823-43.
219. Chakraborty, D.P., Recent advances in observer performance methodology: jackknife free-response ROC (JAFROC). Radiat Prot Dosimetry, 2005. **114**(1-3): p. 26-31.
220. Chakraborty, D.P., A brief history of free-response receiver operating characteristic paradigm data analysis. Acad Radiol, 2013. **20**(7): p. 915-9.
221. Chakraborty, D.P. and X. Zhai, Analysis of Data Acquired Using ROC Paradigm and Its Extensions,
222. Chakraborty, D.P. RJafroc: Analysis of Data Acquired Using the Receiver Operating Characteristic Paradigm and Its Extensions. 2015 [cited 2017 28/07/2017]; Available from: https://cran.r-project.org/web/packages/RJafroc/.
223. Chakraborty, D.P., et al., Digital and conventional chest imaging: a modified ROC study of observer performance using simulated nodules. Radiology, 1986. **158**(1): p. 35-9.
224. Chakraborty, D.P. and L.H. Winter, Free-response methodology: alternate analysis and a new observer-performance experiment. Radiology, 1990. **174**(3 Pt 1): p. 873-81.
225. Chakraborty, D.P., Analysis of location specific observer performance data: validated extensions of the jackknife free-response (JAFROC) method. Acad Radiol, 2006. **13**(10): p. 1187-93.
226. Gregory, R.A., et al., Objective comparison of lesion detectability in low and medium-energy collimator iodine-123 mIBG images using a channelized Hotelling observer. Phys Med Biol, 2017. **62**(1): p. 17-30.
227. Viera, A.J. and J.M. Garrett, Understanding interobserver agreement: the kappa statistic. Fam Med, 2005. **37**(5): p. 360-3.
228. Seibyl, J.P., et al., Individual-Reader Diagnostic Performance and Between-Reader Agreement in Assessment of Subjects with Parkinsonian Syndrome or Dementia Using 123I-Ioflupane Injection (DaTscan) Imaging. J Nucl Med, 2014. **55**(8): p. 1288-1296.
229. Kahraman, D., et al., 123I-FP-CIT SPECT imaging of the dopaminergic state. Visual assessment of dopaminergic degeneration patterns reflects quantitative 2D operator-dependent and 3D operator-independent techniques. Nuklearmedizin, 2012. **51**(6): p. 244-51.
230. Soderlund, T.A., et al., Value of Semiquantitative Analysis for Clinical Reporting of 123I-2-beta-Carbomethoxy-3beta-(4-Iodophenyl)-N-(3-Fluoropropyl)Nortropane SPECT Studies. J Nucl Med, 2013. **54**(5): p. 714-22.
231. Aylward, E.H., et al., Basal ganglia volume in adults with Down syndrome. Psychiatry Res, 1997. **74**(2): p. 73-82.

"In case I don't see ya: good afternoon, good evening, and good night!"
— The Truman Show, 1998